
Fatigue and Fracture Toughness- CRYOGENIC BEHAVIOR

STP 556



AMERICAN SOCIETY FOR TESTING AND MATERIALS

FATIGUE AND FRACTURE TOUGHNESS— CRYOGENIC BEHAVIOR

A symposium
presented at the
Seventy-sixth Annual Meeting
AMERICAN SOCIETY FOR
TESTING AND MATERIALS
Philadelphia, Pa., 24—29 June 1973

ASTM SPECIAL TECHNICAL PUBLICATION 556
C. F. Hickey, Jr., and R. G. Broadwell
symposium cochairmen

List price \$20.25
04-556000-30



AMERICAN SOCIETY FOR TESTING AND MATERIALS
1916 Race Street, Philadelphia, Pa. 19103

© by *American Society for Testing and Materials* 1974
Library of Congress Catalog Number: 74-76067

NOTE

The Society is not responsible, as a body,
for the statements and opinions
advanced in this publication.

Printed in Baltimore, Md.
July 1974

Foreword

This special technical publication consists of eight papers presented during the symposium on Fatigue and Fracture Toughness of Metallic Materials at the Seventy-sixth Annual Meeting of the American Society for Testing and Materials held in Philadelphia, Pa., 24-29 June 1973. The symposium was sponsored by the Low Temperature Panel of the American Society for Testing and Materials, American Society of Mechanical Engineers, and Metal Properties Council Joint Committee on the Effect of Temperature on the Properties of Metals. C. F. Hickey, Jr., Army Materials and Mechanics Research Center, and R. G. Broadwell, Titanium Metals Corporation of America, presided as symposium cochairmen.

Related ASTM Publications

**Fracture Toughness Testing at Cryogenic Temperature, STP 496 (1971), \$5.00
(04-496000-30)**

**Fracture Toughness Evaluation by R-Curve Methods, STP 527 (1973), \$9.75
(04-527000-30)**

**Progress in Flaw Growth and Fracture Toughness Testing, STP 536 (1973),
\$33.25 (04-536000-30)**

Contents

Introduction	1
Fracture Toughness of High-Strength Alloys at Low Temperature—<i>J. E. Campbell</i>	
Aluminum Alloys	4
Titanium Alloys	7
Steels	8
Inconel Alloy 718	15
Fatigue Crack Growth Rate Data	15
The Challenge for the Future	16
Discussion	21
Alloy, Texture, and Microstructural Effects on the Yield Stress and Mixed Mode Fracture Toughness of Titanium—<i>H. W. Rosenberg and W. M. Parris</i>	26
Procedures	28
Experimental Results	31
Discussion	34
Conclusions	41
Flexural Fatigue Testing of Titanium Forging Material in Liquid Hydrogen—<i>N. R. Adsit, P. Dessau, and W. E. Witzell</i>	44
Material	45
Procedure	46
Results	49
Statistical Treatment of the Data	49
Comparison of Results	54
Toughness Data for Monolithic High-Hardness Steel—<i>C. F. Hickey, Jr.</i>	55
Materials	56
Test Procedure	56
Results and Discussion	59
Conclusions	66
Fatigue and Fracture Characteristics of High-Hardness, Laminar Composite Steel—<i>R. Chait, C. F. Hickey, Jr., and C. H. Curll</i>	68
Materials and Test Procedure	69
Results and Discussion	72
Summary and Conclusions	82
Investigation of the Plastic Fracture of High-Strength Aluminum Alloys—<i>R. H. Van Stone, R. H. Merchant, and J. R. Low, Jr.</i>	93
Materials	94

Fractographic Study	96
Failure of the Large Second Phase Particles	97
Quantitative Metallography of Second-Phase Particles	105
Identification of the Second Phase Particles	108
Transmission Electron Microscopy	111
Discussion	115
Conclusions	123
Large-Scale Fracture Toughness Tests of Thick 5083-0 Plate and 5183 Welded Panels at Room Temperature, -260 and -320°F—<i>J. G. Kaufman, F. G. Nelson, and R. H. Wygonik</i>	125
Material	126
Weld Preparation and Qualification	126
Test Procedure	128
Results	137
Conclusions	156
Fatigue Crack Growth in Aluminum Alloy 5083-0 Thick Plate and Welds for Liquefied Natural Gas Tanks—<i>R. A. Kelsey, G. E. Nordmark, and J. W. Clark</i>	159
Material	161
Compact Tension Specimens	162
Surface-Flawed Plate Specimens	168
Predicting Growth of Cracks Under Spectrum Loading	176
Predicted Flaw Growth in Test Specimens	183
Summary and Conclusions	184

Introduction

The symposium was organized to document the current state of the art in fatigue and fracture toughness of aluminium, steel, and titanium alloys at room and cryogenic temperatures. Included are previously unpublished original papers and reviews. Of particular importance to metallurgists, design engineers and researchers, this volume relates directly to both current and future applications, such as liquefied natural gas pressure vessels, armor plate, and airframe hardware. It is a notable contribution to the literature.

The Campbell paper reviews the effect of test temperature on the toughness of materials. For many aluminum alloys, the fracture toughness tends to increase or remain generally constant as the testing temperature is decreased. Titanium alloys tend to have lower toughness as the testing temperature is decreased, but the effect is influenced by the alloy content and heat treatment. Alloy steels normally exhibit decreasing fracture toughness as the testing temperature is decreased through the transition temperature range, when the structure contains ferrite or tempered martensite. In the Rosenberg-Parris paper the mixed mode fracture toughness, K_Q , behavior of alpha-beta titanium alloys was examined in terms of: (1) alloy effects of aluminum, oxygen, and beta stabilizer, (2) processing effects of hot roll and anneal temperatures, and (3) test direction. Qualitatively, the oxygen, texture, and microstructural effects on K_Q parallel findings in the literature on titanium alloys regarding the effects of these variables on K_{IC} . The paper by Adsit et al presents data on the high cycle fatigue behavior of Ti-5Al-2.5Sn. Tests were run in a liquid hydrogen environment and showed no directionality effect. The Hickey and Chait et al papers present data that characterize the static and dynamic mechanical properties of high hardness monolithic and laminar steel composites. It was found that toughness properties vary as a function of specimen orientation and that fatigue properties are maximized with improved as-received material surface and lowered humidity during testing. Low et al studied plastic fracture in five high-strength aluminum

2 FATIGUE AND FRACTURE TOUGHNESS—CRYOGENIC BEHAVIOR

alloys (2014, 2024, 7075, and 7079). Their results show that ductility and fracture toughness are affected primarily by the size and volume fraction of the larger (1 to 10 μm) second-phase particles which contain iron or silicon or both. The Kaufman et al and Kelsey et al papers present data at cryogenic temperatures on the fracture toughness and fatigue crack growth rates for the aluminum alloys 5083-0 and 5183. Both of these materials are contenders for LNG applications; thus, the data presented in their papers are of considerable current interest.

Two other presentations that do not appear in this volume were made at the symposium:

1. Flow Growth Behavior During Proof Testing; by F. R. Schwartzberg; Martin-Marietta Corp., Denver, Colo.
2. Review of Soviet Titanium Alloys for Cryogenic Applications; by R. A. Wood; Battelle Columbus Labs., Columbus, Ohio.

Interested persons are referred to the authors for copies of the manuscripts.

In behalf of the Low Temperature Panel, the Chairmen wish to acknowledge the sincere interest and cooperation of Miss Jane B. Wheeler, managing editor of ASTM. Her assistance in the organizing of the symposium and in the publishing of this STP is greatly appreciated.

C. F. Hickey, Jr.

Metallurgist, Metals Division,
Army Materials and Mechanics Research Center,
Watertown, Mass. 02172;
symposium cochairman.

R. G. Broadwell

Manager, Aerospace Market Development,
TIMET, Division of TMCA,
West Caldwell, N. J. 07006;
symposium cochairman.

J. E. Campbell¹

Fracture Toughness of High-Strength Alloys at Low Temperature—A Review

REFERENCE: Campbell, J. E., "Fracture Toughness of High-Strength Alloys at Low Temperature—A Review," *Fatigue and Fracture Toughness—Cryogenic Behavior*, ASTM STP 556, American Society for Testing and Materials, 1974, pp. 3–25.

ABSTRACT: According to available information on the fracture toughness of high-strength alloys at low temperatures, the effect of low temperatures on toughness is generally dependent on the alloy base. For many aluminum alloys, the fracture toughness tends to increase or remain generally constant as the testing temperature is decreased. Titanium alloys tend to have lower toughness as the testing temperature is decreased, but the effect is influenced by the alloy content and heat treatment. Certain titanium alloys retain good toughness at very low temperatures. Alloy steels normally exhibit decreasing fracture toughness as the testing temperature is decreased through the transition temperature range, when the structure contains ferrite or tempered martensite. The transition temperature is influenced by the alloy content, grain size, and heat treatment. Low temperatures apparently have little effect on the fracture toughness of Inconel Alloy 718. These trends are reviewed based on current state-of-the-art information. Limited information on the fatigue crack growth rates of 2219-T87 aluminum alloy and Ti-6Al-4V alloy indicate that the slope of the da/dN curves is changed as the testing temperature is decreased.

KEY WORDS: fracture properties, cryogenics, mechanical properties, fracture tests, toughness, temperature, cryogenics, aluminum alloys, titanium alloys, alloy steels, nickel containing alloys, crack propagation

Current and developing applications for materials at low temperatures include structures, vehicles, and pipeline equipment for arctic environments; storage and transport equipment for liquefied fuel gases, oxygen, and nitrogen; and superconducting machinery, devices, and electrical transmission systems. Most of these applications relate to the production and distribution of energy and have attained greater prominence because of the current energy shortage.

¹ Staff metallurgist, Battelle-Columbus Laboratories, Columbus, Ohio 43201.

4 FATIGUE AND FRACTURE TOUGHNESS—CRYOGENIC BEHAVIOR

The effects of low temperatures on the tensile and impact properties of many structural materials are well known, but information on the fracture toughness of these same materials at cryogenic temperatures is very limited. The objective of this review is to indicate what fracture toughness data are available on structural metals at low temperatures and to show trends in the data for several classes of alloys. With this information, we can obtain some general concepts regarding potentially suitable materials based on fracture mechanics criteria and damage tolerance at certain temperature levels within the low-temperature regime.

Much of the available low-temperature fracture toughness data were presented at a previous workshop session of the Low-Temperature Panel in June of 1970 [1].² Available data for low-temperature fracture toughness of high-strength alloys also have been compiled in the *Damage Tolerant Design Handbook* [2]. The alloy classes that are included in this review are aluminum alloys, titanium alloys, steels, and one nickel-base alloy—Inconel Alloy 718.

Testing methods for determining plane-strain fracture-toughness data and criteria for determining the validity of the data have been developed over the past ten years. Most of the data referenced in this review were obtained before the 1972 version of the test method (ASTM Test for Plain-Strain Fracture Toughness of Metallic Materials (E 399-72)) was published. Therefore, they may not necessarily comply with all of the requirements of the most recent version. However, if the data are valid based on the test method applicable at the time the tests were conducted, the data are indicated as valid for this review. Data that apparently are not valid by the foregoing criteria are designated as K_Q values. Such data are considered only if they are useful in showing a significant trend.

Fracture toughness data obtained on part-through surface-crack specimens are designated as K_{IE} values to distinguish them from data obtained by the standard method. The validity of these data have been established by the original authors, although there are no consensus criteria for establishing validity.

Aluminum Alloys

In considering the cryogenic properties of aluminum alloys, we are well aware of the fact that many of the alloys retain good ductility with increased strength at very low temperatures. This favorable characteristic is attributed to the face-centered cubic (fcc) crystalline structure of the aluminum alloys. Low-temperature K_{IC} data for some of the aluminum alloys in the 2000 series as plate are shown in Fig. 1. These data were obtained from tests on bend or compact specimens of the type described in ASTM Method E 399 and represent valid

² The italic numbers in brackets refer to the list of references appended to this paper.

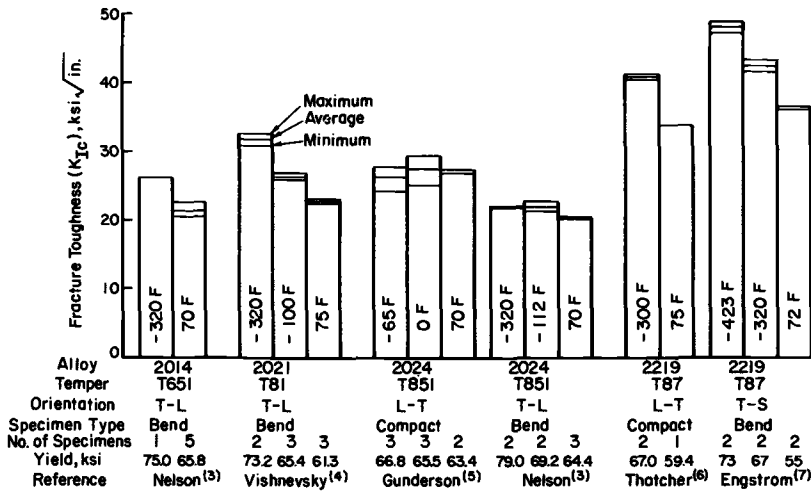


FIG. 1—Effect of temperature on fracture toughness of 2000-series aluminum alloys as plate.

data. The trend is for increased toughness as the testing temperature is decreased. In recent years, the 2219-T87 alloy has been studied extensively for use in aerospace cryogenic tankage and represents an alloy with a good combination of properties including strength, toughness, and weldability for use at cryogenic temperatures. Fracture toughness data obtained on part-through surface-crack specimens of 2014-T6 and 2219-T87 alloys are shown in Fig. 2. The 2014-T6 alloy plate and welds represent the material used in the Saturn S-IVB stage for the liquid hydrogen (LH_2) tankage. The weld metal has lower toughness than the parent metal, but the toughness was not reduced by exposure to LH_2 .

Results of tests on part-through surface-crack specimens of 2219-T87 alloy from the two sources in Fig. 2 show the same trend as is shown in Fig. 1 for tests down to $-423^\circ F$.

Available valid data on the fracture toughness for some of the 7000 series alloys, shown in Fig. 3, indicate that many of the alloys in this series, which have good toughness at room temperature, experience very little change in toughness as the testing temperature is decreased. For room-temperature applications, some of the 7000 series alloys have better combinations of strength and toughness than those in the 2000 series. However, at cryogenic temperatures, further studies are needed to determine the strongest contender of the 7000 series based on combined strength and toughness at low temperatures to compete with 2219-T87.

6 FATIGUE AND FRACTURE TOUGHNESS-CRYOGENIC BEHAVIOR

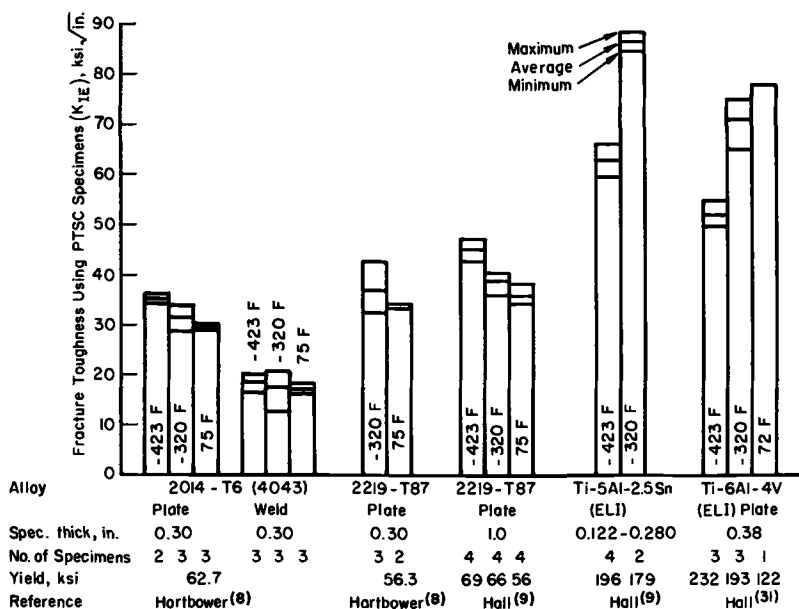


FIG. 2—Effect of temperature on fracture toughness of aluminum and titanium alloys using part-through surface-crack specimens.

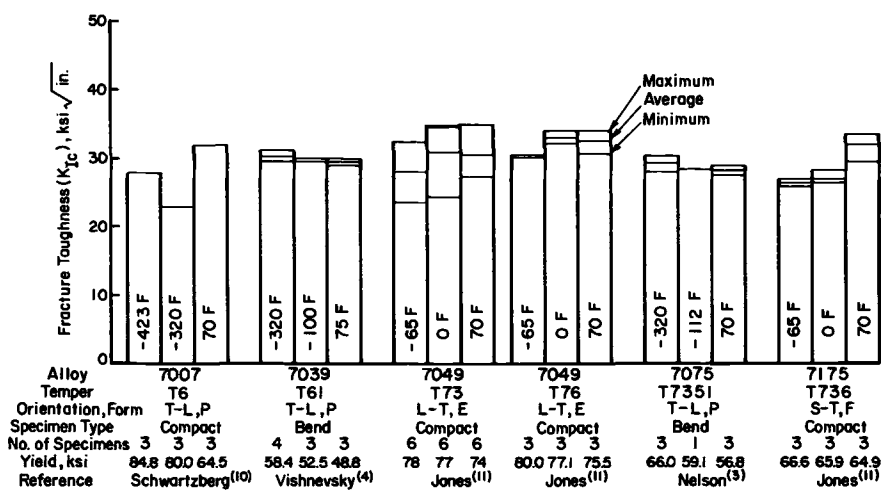


FIG. 3—Effect of temperature on fracture toughness of 7000-series aluminum alloys. Note: P = plate, E = extrusions, and F = forging.

Titanium Alloys

Only limited fracture toughness data are available from tests at cryogenic temperatures on titanium alloys using the standard bend or compact specimens. Test data reported by Vishnevsky and Steigerwald [4] indicate that the K_{Ic} values for beta-processed Ti-6Al-4V alloy in the solution-treated-and-aged condition (150 ksi yield strength) drops from about $45 \text{ ksi}\sqrt{\text{in.}}$ at 75°F to about $36 \text{ ksi}\sqrt{\text{in.}}$ at -320°F (227 ksi yield strength) when using 1-in.-thick bend specimens. Results representing valid test data by Hall [9] on compact specimens of annealed Ti-5Al-2.5Sn (ELI) at -320 and -423°F indicate that the K_{Ic} values were in the same range as the K_{IE} values shown in Fig. 2.

Figure 4 shows results of valid K_{Ic} tests for a few specimens of Ti-6Al-4V alloy in the recrystallized annealed condition. Fracture toughness data for specimens of Ti-6Al-6V-2Sn in two solution treated and aged (STA) conditions also are shown in Fig. 4. Because of the limited number of specimens, the results are of limited significance, but the trend is for the toughness to decrease as the testing temperature is decreased. Data for the latter alloy were obtained before ASTM Method E 399 was available and are therefore assigned K_Q values.

Results of fracture toughness tests using part-through surface-crack specimens of annealed Ti-5Al-2.5Sn (ELI) and Ti-6Al-4V (ELI) to -423°F , shown in Fig. 2, indicate that the Ti-5Al-2.5Sn alloy has better toughness at each testing temperature in the cryogenic range than the Ti-6Al-4V alloy. The interesting feature about these two titanium alloys is that the yield strength at -423°F is

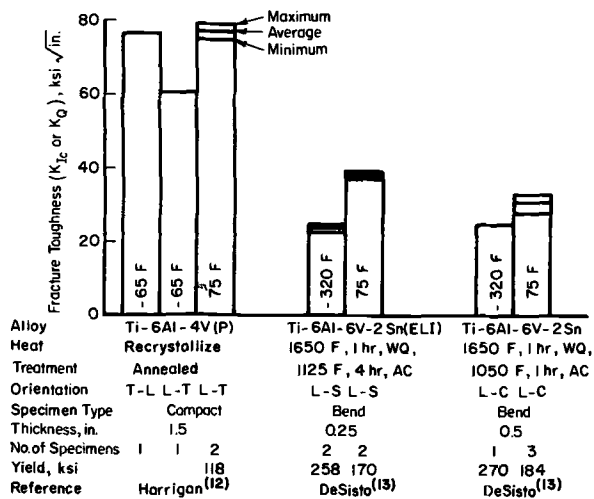


FIG. 4—Effect of temperature on K_{Ic} or K_Q values for titanium alloys.

8 FATIGUE AND FRACTURE TOUGHNESS—CRYOGENIC BEHAVIOR

nearly twice that at room temperature, yet they retain high toughness in the cryogenic temperature range.

Various modifications of notched and precracked specimens of Ti-5Al-2.5Sn and Ti-6Al-4V alloys have been used in evaluating variations in mixed-mode and plane-stress fracture toughness of these alloys in sheet thicknesses to -423°F and lower at NASA-Lewis[14], McDonnell Douglas[15], Boeing[16], Battelle[17], Martin-Marietta, and other laboratories. This is an appropriate place to recognize the efforts of the investigators on these programs, because this is a very difficult and sometimes hazardous area of investigation. However, these studies involve special applications of fracture toughness measurements, and the detailed results are beyond the scope of this review.

The decision to use one of the aluminum or titanium alloys at very low temperatures must be based on a complete analysis of the application. For example, Tiffany has noted that since Ti-5Al-2.5Sn alloy exhibits lower toughness as the temperature is decreased, pressure vessels of this alloy should be proof tested at temperatures equal to or below the lowest service temperature[16]. On the other hand, the toughness of 2219-T87 aluminum alloy increases as the testing temperature is decreased. Therefore, under certain circumstances, it may be advantageous to proof test cryogenic pressure vessels of 2219-T87 aluminum alloy at temperatures above the lowest service temperature.

Steels

Carbon and low-alloy steels represent body-center-cubic (bcc) atomic lattices and exhibit toughness transition temperature ranges either above, at, or below room temperature depending on a number of factors. At temperatures above the transition temperature, the alloy has substantially better toughness than at lower temperatures. Furthermore, the lower strength steels generally are strain-rate sensitive, while the higher strength steels are not strain-rate sensitive. The effect of strain rate on the transition temperature of ship plate from tests on precracked bend specimens is shown in Fig. 5. Ship plate is not a high-strength alloy, but the results of these tests show that the transition temperature is much higher under conditions of dynamic loading than for static loading because of the strain rate sensitivity. Only the lower portions of the transition curves could be obtained under plane-strain conditions. For strain-rate sensitive alloys, the results of the dynamic fracture toughness tests are more significant than those for the static tests.

Figures 6 through 9 show transition temperature curves for several ASTM steels for static loading conditions from tests on precracked bend or compact specimens. The curves for parent metal and welds in ASTM A517F steel plate in Fig. 6 indicate that the weld metal and heat-affected zones in these specimens had lower transition temperatures than the parent metal. However, the weld metal in the specimens of A542 steel had higher transition temperatures than the

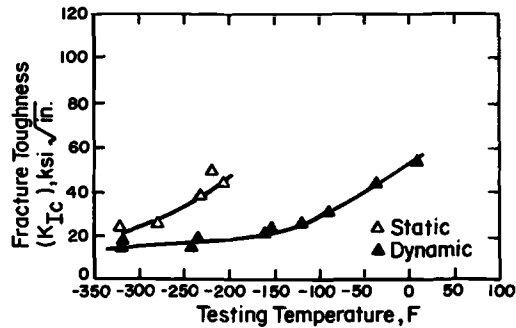


FIG. 5—Static and dynamic fracture toughness of ABS-C steel at low temperatures[18].

parent metal as shown in Fig. 7. The fracture toughness data in Fig. 8 are for A533 Grade B Class 1 steel from 12-in.-thick plate. This steel type has been studied extensively for nuclear reactor pressure vessels. The data points indicate that for testing temperatures above about -100°F , the toughness increases substantially as the testing temperature is increased. Thus the required thickness of the specimens must be increased in order to increase the constraint that is necessary at the crack tip to simulate plane-strain conditions at the initiation of fracture. For these tests, a specimen thickness of 12 in. was required for valid K_{IC} data at 50°F . The second curve is for the yield strength which increases as the testing temperature is decreased. The NDT is the nil ductility temperature which is obtained on a dynamic test.

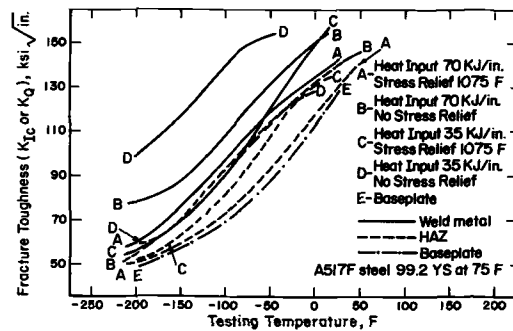


FIG. 6—Effect of temperature on fracture toughness of ASTM A517F steel plate and welds for precracked bend specimens 2 in. thick[19]. Note: Only the data obtained at the lower temperatures are valid K_{IC} values.

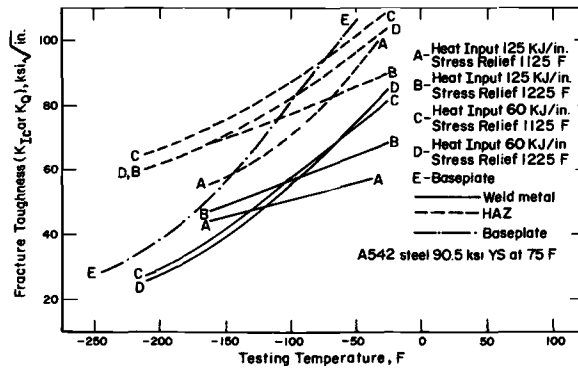


FIG. 7—Effect of temperature on fracture toughness of ASTM A542 steel plate and welds for precracked bend specimens 2 in. thick [19]. Note: only the data obtained at the lower temperatures are valid K_{IC} values.

Results of fracture toughness tests on three ASTM forging steels, as reported by Greenberg et al, are shown in Fig. 9 [21]. The general trends in the toughness data may be similar, but the compositions, grain sizes, and other factors have marked effects on the transition temperatures. Figure 10 shows both static K_{IC} and dynamic K_{ID} data by Shoemaker for HY-130 steel at temperatures down to -320°F [19]. These data indicate that this steel, in the temperature range tested, is not strain-rate sensitive.

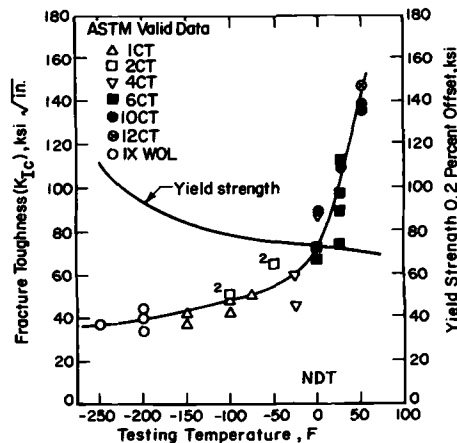


FIG. 8—Fracture toughness at low temperatures for ASTM A533 Grade B, Class I steel plate 12 in. thick [20].

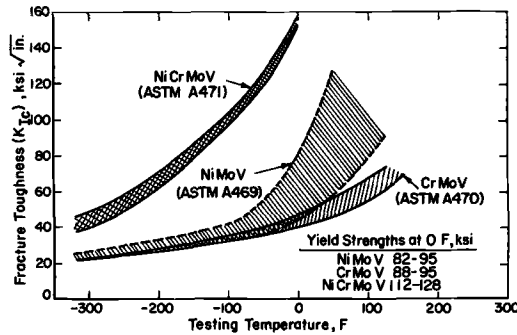


FIG. 9—Effect of temperature on fracture toughness for several heats from each of three types of forging alloys for turbine-generator rotors[21].

These steels are not intended for use at temperatures in or below the transition temperature range, and there is no accepted method for indicating the specific transition temperature from a transition temperature curve. Furthermore, there is no accepted method for relating the transition temperature to a safe minimum service temperature for structural components. However, if K_{IC} data are obtained for a given alloy at low temperatures, the critical crack sizes may be estimated in the low-temperature range at the maximum service stress of the structure.

Vishnevsky studied the effects of variations in composition on a series of Ni-Cr-Mo-V steels to show the effects of the alloying elements on the low-temperature fracture toughness[22]. Bars of these steels were quenched and tempered to about 170 ksi yield strength and tested as precracked bend

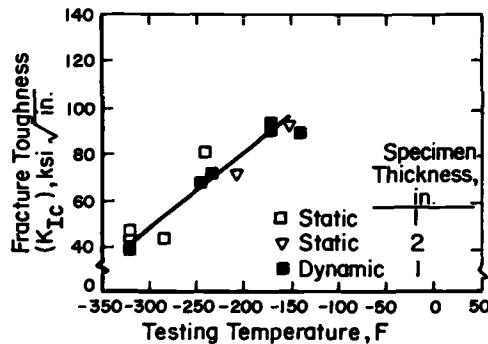


FIG. 10—Static and dynamic fracture toughness of HY-130 (T) alloy steel at low temperatures[18].

12 FATIGUE AND FRACTURE TOUGHNESS—CRYOGENIC BEHAVIOR

specimens. The effects of carbon content and nickel content were the most significant. An increase in carbon content from 0.28 to 0.41 raised the transition temperature based on K_Q data as shown in Fig. 11. Increasing the nickel content from 1.26 to 6.23 percent decreased the K_Q transition temperature as shown in Fig. 12. This represents one of the major attributes of nickel additions to the alloy steels.

The effect of a range of testing temperatures on the toughness of D6ac steel specimens of the compact design tested in various conditions of toughness is shown in Fig. 13. The specimens were austenitized at about 1650°F, furnace cooled to 975°F, and quenched in oil or molten salt according to several different procedures, to simulate quenching of the welded forgings that comprise the F111 wing carry-through structure. The high-toughness specimens were quenched in oil, while the medium-toughness specimens were quenched in salt. Regardless of the quench, the yield strength of the specimens was approximately 217 ksi after tempering twice at 1000 to 1025°F. The fracture toughness tests were very sensitive indicators of the effect of the variation in quenching rate on the toughness. The specimens that had the highest toughness at room temperature also had the highest toughness at -65°F.

Available fracture toughness data at low temperatures for other alloy steels: AISI 4340, 300M, HP9-4-20, HP9-4-25, and 18 Ni (200) maraging steel, are shown in Fig. 14. The trend usually is for decreasing toughness as the testing temperature is decreased. The one exception is HP9-4-25 in the temperature range +75 to -75°F. At lower temperatures, the expected trend would be for

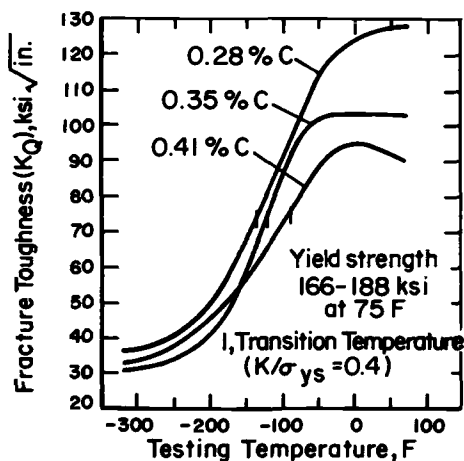


FIG. 11—Effect of carbon content on fracture toughness of Ni-Cr-Mo-V steels at low temperatures from tests on precracked bend specimens[22].

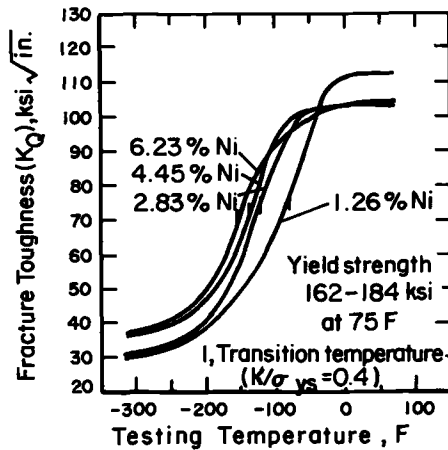


FIG. 12—Effect of nickel content on fracture toughness of Ni-Cr-Mo-V steels at low temperatures from tests on precracked bend specimens[22].

the toughness to drop as indicated for HP9-4-20 in the range from -100 to -320°F . The data obtained by Steigerwald for AISI 4340 steel and by Wessel for the HP9-4-20 alloy steel were obtained before ASTM Method E 399 was available and are designated as K_Q values.

The 18Ni (200) grade maraging steel (Fig. 14) also exhibits considerable reduction in toughness as the testing temperature is reduced from -100 to

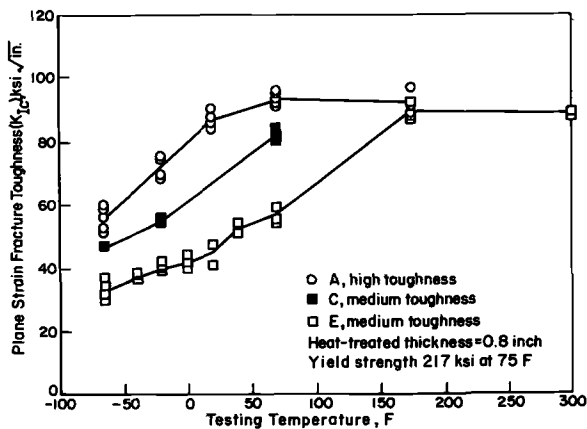


FIG. 13—Effect of testing temperature on the fracture toughness of D6AC steel for compact specimens of plate for three heat-treatment conditions[23].

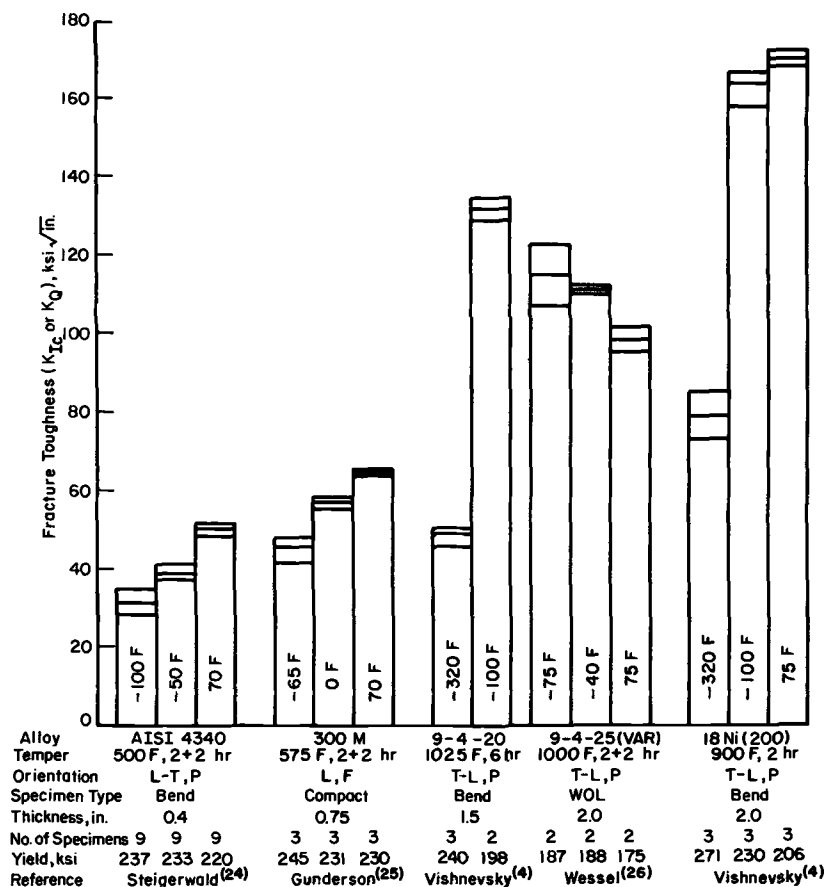


FIG. 14—Effect of temperature on fracture toughness of alloy steels.

–320°F, but at –320°F, this heat of the 200 grade retained a toughness of about 80 ksi√in. From limited information on the toughness of the 200 grade, it appears that there is a considerable range in results of K_{IC} tests at room temperature. This level of toughness at –320°F probably can be achieved only if the alloy has a toughness of about 160 ksi√in. or over at 75°F.

The effect of low temperatures on the static and dynamic fracture toughness of bend specimens of 18Ni (250) maraging steel is shown in Fig. 15. There apparently is a straight line relationship between the K_{IC} values and the testing temperature in the range from 75 to –320°F. At –320°F, the K_{IC} value was about 40 ksi√in., and the alloy is not strain-rate sensitive in the low-temperature range.

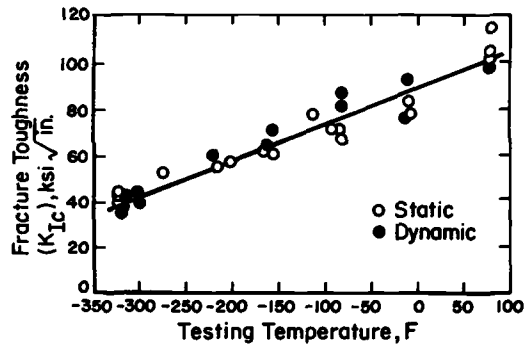


FIG. 15—Static and dynamic fracture toughness of 18Ni (250) maraging steel at low temperatures[18].

Results of tests by Killpatrick on part-through surface-crack specimens of 200 grade maraging steel are shown in Fig. 16[27]. These heats had high toughness at 75°F and also retained relatively good toughness at -320°F. With optimum welding conditions, the weld metal also retains good strength and toughness at -320°F.

Inconel Alloy 718

Results of fracture toughness tests by Pettit et al on part-through surface-crack specimens of Inconel Alloy 718, a nickel-base alloy, also are shown in Fig. 16[28]. These test data indicate that the toughness is nearly insensitive to testing temperatures as low as -423°F, when the alloy is evaluated as sheet. Toughness of the weld metal is somewhat lower than for the parent metal for the testing conditions reported, but it also is unaffected by temperatures to -423°F. This alloy has been used extensively for liquid oxygen tankage in spacecraft.

Fatigue Crack Growth Rate Data

Fatigue crack growth rate data based on stress intensity criteria have been obtained on only a few alloys at low temperatures. The results of the fatigue tests by Hall and Bixler are plotted on da/dN versus ΔK coordinates in Fig. 17 for 2219-T87 aluminum alloy at 72, -320, and -423°F for various flaw shapes in part-through surface-crack specimens[29]. The test data at lower temperatures tend to show a decrease in the slope of the curves when plotted according to the method shown. However, in the ΔK range of 35 to 40 ksi√in., the points overlap. Additional studies are needed to demonstrate the maximum ΔK value that may be applied to the specimen on cyclic loading for which no detectable flaw growth would occur, at each testing temperature.

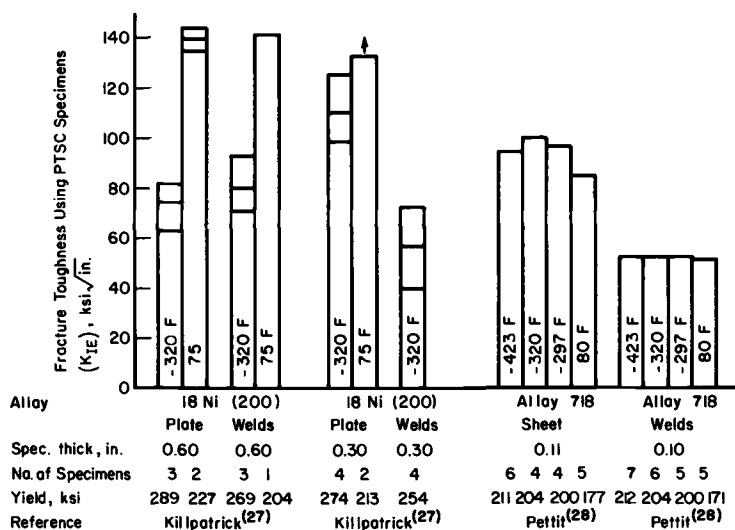


FIG. 16—Effect of temperature on fracture toughness of 18Ni (200) maraging steel plate and welds and Alloy 718 sheet and welds using part-through surface-crack specimens.

As shown in Fig. 18, fatigue crack growth rate tests have been conducted at temperatures to -200°F in hydrogen atmospheres by Pittinato to determine the effect of hydrogen on the crack growth rate in Ti-6Al-4V alloy [30]. The tests were on ELI grade alloy in the solution-treated-and-aged condition. This series of curves shows: (1) that in an inert environment, the slope of the curves is decreased slightly as the temperature is decreased, and (2) that the effect of the hydrogen environment is decreased as the testing temperature is decreased. The trend is similar in specimens of welded Ti-6Al-4V alloy in which the crack is located in weld metal.

The Challenge for the Future

The challenge for the future in evaluating fracture toughness and mechanical properties of materials in general at cryogenic temperatures will be for superconducting machinery and transmission systems and for liquefied fuel gas systems. This includes studies of the properties of materials at liquid helium temperature and at higher temperatures within the cryogenic range. Not all materials of construction for superconducting systems are exposed to superconducting temperatures, but maximum efficiency of the systems can be realized only if optimum materials are used in the critical components of such systems.

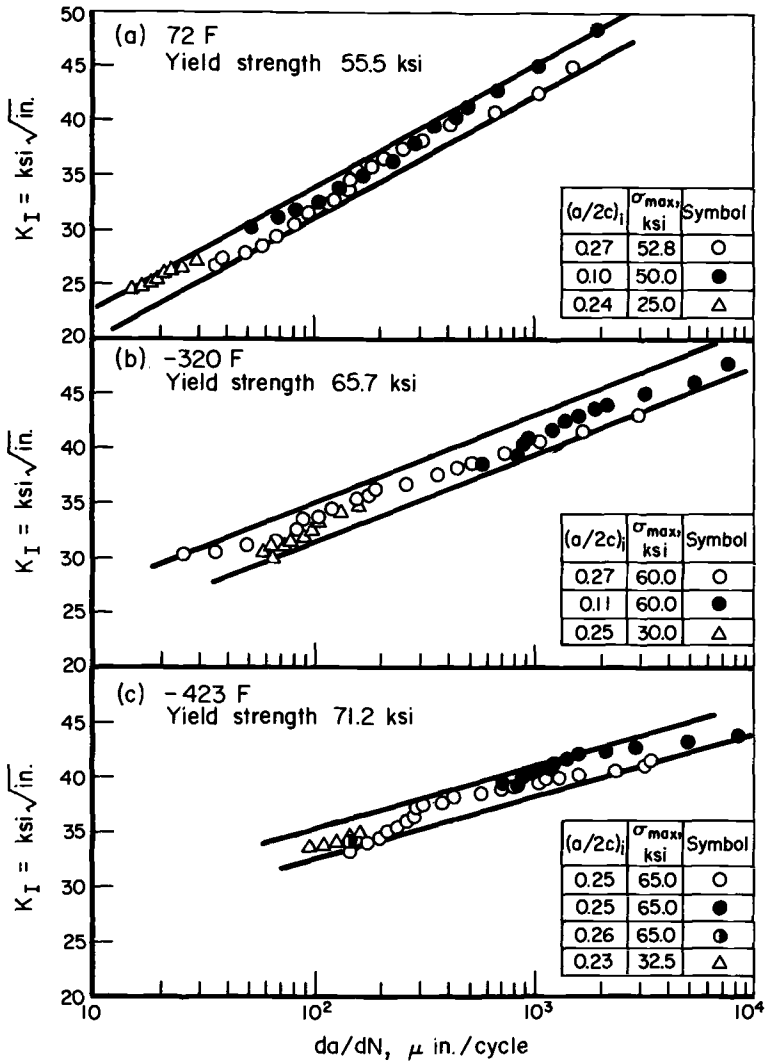


FIG. 17—Fatigue crack-growth rates at 72, -320, and -423° F for part-through surface-crack specimens of 2219-T87 aluminum plate for T-S orientation [29].

18 FATIGUE AND FRACTURE TOUGHNESS—CRYOGENIC BEHAVIOR

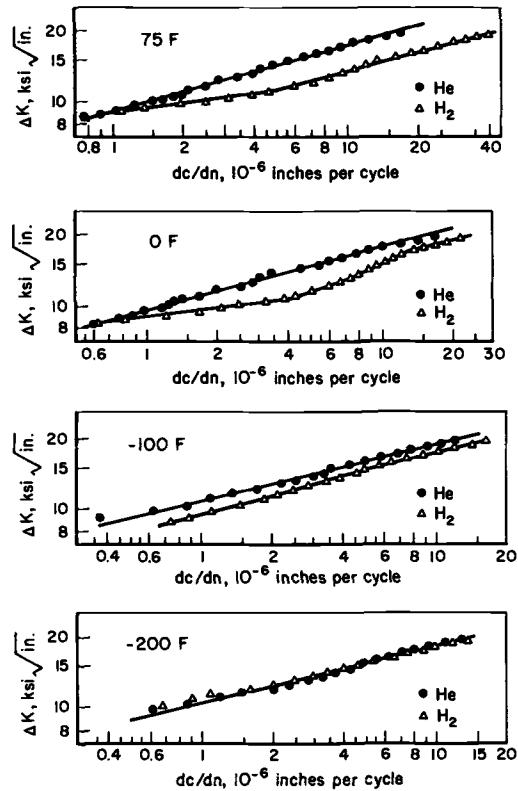


FIG. 18—Fatigue crack-growth rate curves for parent metal in Ti-6Al-4V (STA) specimens in helium and hydrogen environments from 75 to -200°F [30].

References

- [1] *Fracture Toughness Testing at Cryogenic Temperatures*, ASTM STP 496, American Society for Testing and Materials, Aug. 1971.
- [2] Campbell, J. E., Berry, W. E., and Feddersen, C. E., *Damage Tolerant Design Handbook*, MCIC HB-01, Metals and Ceramics Information Center, Battelle-Columbus Laboratories, Columbus, Ohio, Dec. 1972 (along with the First Supplement for the Handbook of Sept. 1973).
- [3] Nelson, F. G. and Kaufman, J. G. in *Fracture Toughness Testing at Cryogenic Temperature*, ASTM STP 496, American Society for Testing and Materials, 1971, pp. 27-39.
- [4] Vishnevsky, C. and Steigerwald, E. A. in *Fracture Toughness Testing at Cryogenic Temperatures*, ASTM STP 496, American Society for Testing and Materials, 1971, pp. 3-26.
- [5] Gunderson, A. W., "Tensile, Fracture and Fatigue Properties of 2024-T851 Aluminum Thick Plate," Report No. LA 72-24, Air Force Materials Laboratory, Wright-Patterson Air Force Base, Ohio, 26 May 1972.

- [6] Thatcher, C. S., "Fracture of Aluminum Alloy 2219-T87," Report SD72-SH-0129, North American Rockwell, Space Division, Nov. 1972.
- [7] Engstrom, W. L., "Determination of Design Allowable Properties, Fracture of 2219-T87 Aluminum Alloy," NASA CR-115388, The Boeing Company, Aerospace Group, Seattle, Wash., Contract NAS 9-10364, March 1972.
- [8] Hartbower, C. E., Reuter, W. G., Morais, C. F., and Crimmins, P. P., "Correlation of Stress-Wave-Emission Characteristics with Fracture in Aluminum Alloys," NASA Report CR-2072, Aerojet Solid Propulsion Company, Sacramento, Calif., Contract No. NAS 8-21405, July 1972.
- [9] Hall, L. R. and Finger, R. W., "Investigation of Flaw Geometry and Loading Effects on Plane Strain Fracture in Metallic Structures," NASA Report CR-72659, The Boeing Company, Seattle, Wash., Contract NAS 3-12026, 18 Dec. 1971.
- [10] Schwartzberg, F. R., Keys, R. D., and Kiefer, T. F., "Cryogenic Alloy Screening," NASA Report CR-72733, Martin Marietta Corporation, Denver, Colo., Contract NAS 3-11203, Nov. 1970.
- [11] Jones, R. E., "Mechanical Properties of 7049-T73 and 7049-T76 Aluminum Alloy Extrusions at Several Temperatures," Report AFML-TR-72-2, University of Dayton Research Institute, Dayton, Ohio, Contract F33615-71-C-1054, Feb. 1972.
- [12] Harrigan, M. J., "B-1 Fracture Mechanics Data for Air Force Handbook Usage," Report TFD-72-501, North American Rockwell, Los Angeles Division, Los Angeles, Calif., 21 April 1972.
- [13] DeSisto, T. S. and Hickey, Jr., C. F. in *Proceedings*, Vol. 65, American Society for Testing and Materials, 1965, pp. 641-653.
- [14] Orange, T. W., Sullivan, T. L., and Calfo, F. D., "Fracture of Thin Sections Containing Through and Part-Through Cracks," NASA Report TN D-6305, Lewis Research Center, Cleveland, Ohio, April 1971.
- [15] Eitman, D. A. and Rawe, R. A., "Plane Stress Cyclic Flaw Growth of 2219-T87 Aluminum and 5Al-2.5Sn ELI Titanium Alloys at Room and Cryogenic Temperatures," NASA Report CR-54956, Douglas Aircraft Company, Santa Monica, Calif., Contract NAS 3-4192, 1 Sept. 1966.
- [16] Tiffany, C. F., Lorenz, P. M., and Shah, R. C., "Extended Loading of Cryogenic Tanks," NASA Report CR-72252, The Boeing Company, Seattle, Wash., Contract NAS 3-6290, July 1967.
- [17] Hoeppner, D. W., Pettit, D. E., Feddersen, C. E., and Hyler, W. S., "Determination of Flaw Growth Characteristics of Ti-6Al-4V Sheet in the Solution-Treated and Aged Condition," NASA Report CR-65811, Battelle-Columbus Laboratories, Columbus, Ohio, Contract NAS 9-6969, 1 Jan. 1968.
- [18] Shoemaker, A. K. and Rolfe, S. T., *Journal of Basic Engineering, Transactions*, American Society of Mechanical Engineers, Sept. 1969, pp. 512-518.
- [19] Gentilcore, V. J., Pense, A. W., and Stout, R. D., *Welding Journal, Welding Research Supplement*, Aug. 1970, pp. 341-s to 353-s.
- [20] Seman, D. J., Kallenberg, G. P., and Towner, R. J., "Fracture Toughness of Low Strength Steels," Report WAPD-TM-895, Bettis Atomic Power Laboratory, Pittsburgh, Pa., May 1971.
- [21] Greenberg, H. D., Wessel, E. T., and Pryle, W. H., *Engineering Fracture Mechanics*, Vol. 1, 1970, pp. 653-674.
- [22] Vishnevsky, C. and Steigerwald, E. A., *Transactions*, American Society for Metals, Vol. 62, 1969, pp. 305-315.
- [23] Feddersen, C. E. et al, "Crack Behavior in D6AC Steel," Report MCIC 72-04, Metals and Ceramics Information Center, Battelle-Columbus Laboratories, Columbus, Ohio, Jan. 1972.
- [24] Steigerwald, E. A., "Plane Strain Fracture Toughness for Handbook Presentation," Report AFML-TR-67-187, TRW Inc., Cleveland, Ohio, Contract AF33(615)-5001, July 1967.
- [25] Gunderson, A. W. and Harmsworth, C. L., "MAAE Engineering and Design Data,

20 FATIGUE AND FRACTURE TOUGHNESS—CRYOGENIC BEHAVIOR

- Material 300M," Test Memo No. MAAE 70-5, Air Force Materials Laboratory, Wright-Patterson Air Force Base, Ohio, 24 Sept. 1970.
- [26] Wessel, E. T. et al, "Engineering Methods for the Design and Selection of Materials Against Fracture," Final Technical Report, Westinghouse Research Laboratories, Pittsburgh, Pa., Contract DA-30-069-AMC-602(T), 24 June 1966.
- [27] Killpatrick, D. H., Corn, D. L., and Stoeckinger, G. R., "Cryogenic Fracture Toughness of 18 Nickel 200-Grade Maraging Steel Plate and Welds," MDAC Paper WD 2030, McDonnell Douglas Astronautics Company-West, McDonnell Douglas Corporation, Huntington Beach, Calif., presented to American Society for Metals 1973 Western Conference, Los Angeles, Calif., 12 March 1972.
- [28] Pettit, D. E., Feddersen, C. E., and Mindlin, H., "Flaw Growth Behavior of Inconel 718 at Room and Cryogenic Temperature," NASA Report CR-101942, Battelle-Columbus Laboratories, Columbus, Ohio, Contract NAS 9-7689, 1969.
- [29] Hall, L. R. and Bixler, W. D., "Subcritical Crack Growth of Selected Aerospace Pressure Vessel Materials," NASA Report CR-120834, The Boeing Company, Seattle, Wash., Contract NAS 3-12044, Dec 1972.
- [30] Pittinato, G. F., "Hydrogen-Enhanced Fatigue Crack Growth in Ti-6Al-4V ELI Weldments," *Metallurgical Transactions*, Vol. 3, No. 1, Jan. 1972, pp. 235-242.
- [31] Hall, L. R. and Finger, R. W., "Fracture and Fatigue Growth of Partially Imbedded Flaws," The Boeing Company, Seattle, Wash., paper presented at the Air Force Conference on Fatigue of Aircraft Structures and Materials, Miami Beach, Fla., 15-18 Dec. 1969.

DISCUSSION

J. L. Shannon, Jr.,¹ and W. F. Brown, Jr.,¹ (written discussion)— Mr. Campbell has presented an interesting compilation of fracture toughness data for a variety of alloys tested over a wide range of temperatures. Some of these data also appear in the *Damage Tolerant Design Handbook* published by MCIC for the Air Force. One important object of compilations of this kind is to provide the designer with information which will enable him to select alloys for particular applications where crack propagation is a critical factor in determining the safety of the structure. In order to meet this objective we must be reasonably certain that differences in testing technique or data analysis do not obscure the real differences in toughness among the materials under consideration. Assurance in this respect can only be obtained if there is a sound physical basis for the tests employed and there is a generally accepted way of conducting the tests and reducing the data. This is, of course, why the ASTM E-24 Committee on Fracture Testing of Metals has issued a standard (E 399) for plane strain fracture toughness (K_{Ic}) tests. Certain details of this test method have changed since its inception in draft form in *ASTM STP 410* issued in 1966, but the major criteria for validity, namely, the size requirements have remained unchanged.

Nearly all of the data shown by Mr. Campbell originated from investigations reported after 1966, and, therefore, it would seem reasonable to assume that the size requirements were met in nearly all cases he reports. However, a brief examination of Refs 19 and 22 reveals that the size requirements were not met for some of the data shown in Figs. 6, 7, 11, and 12. For example, in Fig. 6 the data defining the *B* and *D* curves above about -150°F are designated in Ref 19 as invalid according to the size requirements. Other curves in Figs. 6 and 7 have been extrapolated through test results not meeting the size requirements. A value of $82 \text{ ksi-in.}^{1/2}$ is the maximum K_{Ic} that can be measured with the specimen size used by the authors of the data shown in Fig. 11. This value is based on the highest yield strength of 188 ksi. By this conservative estimate one would have to discard nearly all the data above the transition temperature. The same observations can be made for Fig. 12. It would be helpful if the author would identify for the remainder of the data shown in his paper, those that are valid according to the ASTM Method E 399 size requirements.

Of the various validity requirements given in ASTM Method E 399, the size

¹ National Aeronautics and Space Administration-Lewis Research Center, Cleveland, Ohio 44135.

22 FATIGUE AND FRACTURE TOUGHNESS—CRYOGENIC BEHAVIOR

requirements are probably the most important for they ensure that the toughness values meet the conditions of small-scale yielding and plane strain that characterize the crack mechanics analysis that underlies the method. There is a great temptation to use specimens that are undersize or to extrapolate K_{IC} data outside the range where the size requirements have been met. These procedures can lead to completely erroneous results when comparing materials in regard to their plane strain fracture toughness. An example of how far one can go wrong in making a judgement of relative toughness on the basis of subsize specimens is provided by the previously published results of Jones and Brown.² These are summarized in Fig. 19 which shows the K_Q values for both tempered 4340 and overaged 18Ni maraging steel as a function of yield strength level. The range of valid K_{IC} values is shown by the shaded bands, and it is quite evident that the maraging steel possess a superiority in toughness throughout the yield strength range investigated. The results for the subsize specimens are shown as data points. These specimens were cut from the center of the broken K_{IC} specimens. Note that the results for the subsize specimens indicate the plane strain toughness of these two alloys to be the same at 180 ksi yield strength, when in

² Jones, M. H. and Brown, W. F., Jr., in *Review of Developments in Plane Strain Fracture Toughness Testing*, ASTM STP 463, American Society for Testing and Materials, 1970, pp. 63-101.

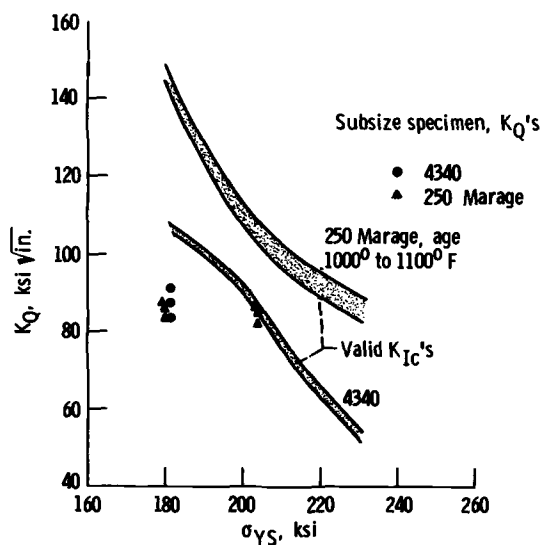


FIG. 19— K_Q values for subsize specimens and the range of valid K_{IC} as a function of yield strength for 4340 and overaged 250 grade maraging steels (footnote 2).

fact they are very substantially different. The subsize specimen results also indicate that the toughness of the maraging steel remains unchanged over the yield strength range from 180 to 203 ksi when in fact the K_{IC} values decrease by nearly one third in this range of strength levels.

Mr. Campbell has reported data from part-through surface crack specimens in Figs. 2 and 16 of his paper. The toughness values are designated as K_{IE} to distinguish them from the values obtained from standardized tests. Mr. Campbell states that "The validity of these data have been established by the original authors, although there are no consensus criteria for establishing validity." This is an incongruous statement. Validity has meaning only if it implies judgement of worth by a generally acceptable authority or standard. If we accept each investigators judgment of the "validity" of his data, we can have as many toughness values for a given material as there are tests to measure this quantity. It was to avoid such a situation that ASTM Committee E-24 established the K_{IC} test method. The problem of reducing surface crack data to K_{IE} values lies in the fact that even for brittle materials the calculated stress intensity values at maximum load may not be independent of the geometry of the crack and the thickness of the piece containing the crack. The results obtained by Corn and Mixon³ for a brittle steel, Fig. 20, illustrate the problem. Note that the K_{IE}

³ Corn, D. L. and Mixon, W. V., "Interim Report on the Effect of Crack Shape on Fracture Toughness," Report No. SM-44671, The Douglas Aircraft Company, 27 April 1964.

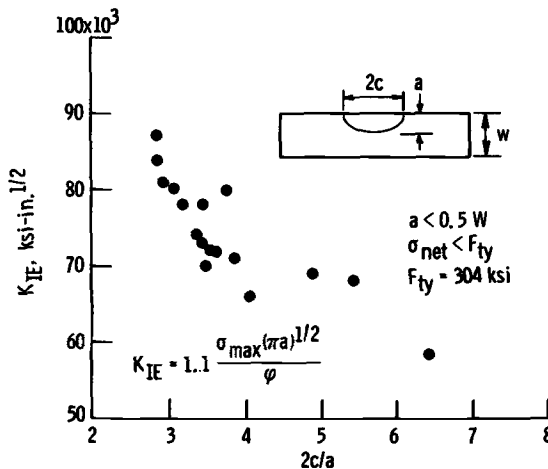


FIG. 20—Influence of crack shape on apparent fracture toughness, K_{IE} of fully aged 300 grade maraging steel part-through surface-crack specimens (footnote 3).

values decrease substantially with increasing eccentricity ($2c/a$). All the K_{IE} data shown in Fig. 20, except the highest, correspond to ratios of net stress to yield strength less than 0.7, so there was little point in making a "plasticity" correction. If one does, the situation is not improved. Similar problems with the correlation of surface crack data on the basis of K_{IE} have been reported by Brown and Srawley⁴ and by Randall.⁵ Keeping these problems in mind it is evident that comparisons among materials on the basis of surface crack data are reliable only if the crack sizes, crack geometries, and specimen dimensions are the same. It would be helpful to the reader if the author would give some indication of the variations in these parameters for the data shown in Figs. 2 and 16.

There are two situations where it would be unwise to use the increased plane strain fracture toughness of some aluminum alloys at cryogenic temperatures as justification for substitution of a room temperature proof test for a cryogenic proof test: (1) if the maximum expected operating stress is based on the cryogenic yield strength it may be impossible to proof the structure at ambient temperature without exceeding the yield stress in all or part of the structure, and (2) if structural failure is controlled by mixed mode toughness, as it might well be in thin sections of relatively tough materials, the trend of K_{IC} with test temperatures may be misleading if used to judge the effect of temperature on mixed mode fracture behavior.

J. E. Campbell (author's closure)—The comments by Messrs. Shannon and Brown are indeed "valid." In Figs. 6, 7, 11, and 12, the toughness parameter represents valid K_{IC} values only at the lower testing temperatures. As indicated in the introduction, only the results of plane-strain fracture-toughness tests that were reported to be valid based on the version of the test method that was applicable at the time (but not earlier than 1968) are identified as K_{IC} values. Otherwise they are designated as K_Q values in the text and in the figures. The transition curves in Figs. 6, 7, 11, and 12 were extended into the invalid range only to show the trends at testing temperatures between the valid range and room temperature in the original references.

The purpose of measuring fracture toughness criteria by means of part-through surface-crack (ptsc) specimens is to provide an evaluation of the toughness in L-S and T-S orientations on sections which are not thick enough for evaluation by precracked bend or compact specimens. When naturally occurring flaws and small fatigue cracks occur in primary structures or pressure

⁴ Brown, W. F., Jr., and Srawley, J. E., *Plain Strain Crack Toughness Testing of High Strength Metallic Materials*, ASTM STP 410, American Society for Testing and Materials, 1966.

⁵ Randall, P. N., discussion to *Plane Strain Crack Toughness Testing of High Strength Metallic Materials*, ASTM STP 410, American Society for Testing and Materials, 1966, pp. 88-128.

vessels, they usually occur as surface defects. Part-through surface cracks in panel-type tension specimens may represent certain idealized forms of the naturally occurring defects when evaluating pressure vessel alloys.

In spite of the apparent disagreement in regard to the stress intensity analysis for the use of ptsc specimens, they have been used for evaluating pressure vessel alloys since the beginning of the fracture mechanics era. They represent a design of specimen that may be used in a cryostat without a compliance gage, since the measured load is usually the maximum load to cause fracture. If I had ignored the extensive amount of information that is available on the effect of low temperatures on the fracture toughness of metals as determined by tests on ptsc specimens, I would have omitted an important contribution to the state of the art. In selecting the K_{IE} data that are plotted in Figs. 2 and 16 for ptsf specimens, I not only selected data for specimens in which the crack depth was less than half the thickness and in which the maximum gross stress was less than 90 percent of the yield stress, but I selected data for specimens that were the thickest in their respective series to best show the trends discussed previously.

Data presented in Ref 9 show the effect of specimen thicknesses and crack size ratios ($a/2c$), and indicate that for ptsc specimens of 2219-T87 that are over about 0.3 in. in thickness the K_{IE} value is independent of specimen thickness. As a result of the same study, K_{IE} data obtained at -320°F on ptsc specimens of Ti-5Al-2.5Sn (ELI) over about 0.150 in. in thickness also are independent of thickness. Variations in the ratio $a/2c$ theoretically would cause minor variations in the stress intensity calculations, but for the range or ratios used in obtaining the K_{IE} data in Figs. 2 and 16 the spread in K_{IE} data was less than might be expected considering the range in $a/2c$ ratios. In all cases the crack depth (a) was less than half the thickness. The K_{IE} data from the ptsc specimens discussed in Ref 9 fall within the scatter band for K_{IC} data from compact and bend specimens of the same materials when tested at the same testing temperatures. Because of the usefulness of ptsc specimens for measuring fracture toughness, a consensus standard is needed for conducting these tests.

Alloy, Texture, and Microstructural Effects on the Yield Stress and Mixed Mode Fracture Toughness of Titanium

REFERENCE: Rosenberg, H. W. and Parris, W. M., "Alloy, Texture, and Microstructural Effects on the Yield Stress and Mixed Mode Fracture Toughness of Titanium," *Fatigue and Fracture Toughness—Cryogenic Behavior*, ASTM STP 556, American Society for Testing and Materials, 1974, pp. 26-43.

ABSTRACT: The mixed mode fracture toughness, K_Q , behavior of alpha-beta titanium alloys was examined in terms of: (1) alloy effects of aluminum, oxygen, and beta stabilizer, (2) processing effects of hot-roll and anneal temperatures, and (3) test direction. In the Ti-4V alloy system, alloying and processing effects interact in their influence on K_Q in a complex manner. In the Ti-2Mo alloy system, oxygen depresses K_Q after alpha-beta rolling, whereas aluminum has a similar effect after beta rolling; in each case the alloy effect dominates that of yield strength. In the overall analysis, texture as implied by a test direction effect, significantly influences K_Q . The oxygen, texture, and microstructural effects on K_Q were shown by statistical methods to qualitatively parallel findings in the literature on titanium alloys regarding the effects of these variables on K_{Ic} .

KEY WORDS: fracture properties, fracture (materials), texture, mechanical properties, evaluation, titanium containing alloys, microstructure, titanium alloys, Widmanstätten structure, statistical analysis, interstitial solutions, toughness, cryogenics

In exploratory alloy research there are two kinds of errors to be made, rejecting a good alloy or accepting a bad one. To reduce each error simultaneously to essentially zero is to pay a prohibitive price in terms of cost and time. Even with a data bank, exploratory work often necessarily starts on a qualitative basis. The qualitative guidelines are then ideally quantified as the composition scope narrows and the evaluation deepens. Although titanium has now been employed in engineering structures for some two decades a number of

¹ Supervisor, Metallurgical Research, and senior research metallurgist, respectively, Henderson Technical Laboratories, TIMET, Henderson, Nev. 89015.

technological problems remain to be quantified. Among these is fracture toughness in alpha-beta titanium.

A general problem in fracture mechanics, aside from methodology, lies in relating toughness variations to the underlying metallurgy. For example, it is well known that fracture toughness results are sensitive to microstructure[1-6],² strain rate[7-15], texture[16-17], and interstitial content[4,5,16,18,19], but the interrelations among these quantities have been too little studied. A further problem has been the use of diverse methods to determine fracture toughness. Although specimens of quite different configurations tested at different rates in tension or bend may produce results that intercorrelate to some degree[13-15,20,21], there are no *a priori* reasons known why they should. Further data are obviously needed. A primary purpose of this paper is to establish the effects of certain metallurgical variables on K_Q of alpha-beta titanium so as to facilitate later quantification of these variables on K_{Ic} .

The use of K_Q specimens for qualitative trend work is justified primarily on economic grounds. However K_Q screen testing is further justified by evidence in the literature that structural effects on K_Q in Ti-6Al-4V[6], Ti-4Al-3Mo-1V[6], and Ti-6Al-6V-2Sn[1] parallel those on K_{Ic} in Ti-6Al-2Sn-4Zr-6Mo[3]. Similarly, the effect of oxygen on K_Q in Ti-(6.5-7.0) Al-1.5Mo-0.5V[19] parallels the trend of oxygen effect on K_{Ic} in Ti-6Al-4V[18]. Finally, May[22], in a study of the Hylite 50 titanium alloy, found that, so long as either or both specimen thickness and crack length are within K_{Ic} requirements, the differences between K_Q and K_{Ic} are not large. This author also found that K_Q values drop abruptly at thicknesses below about 0.5 cm. Although these results have not been confirmed, prudence would dictate the use of K_Q specimens of constant dimensions and thicker than 0.5 cm.

It is well known that titanium alloys may be subject to subcritical crack growth[11,23]. Galda and Munz[23] showed the minimum stress concentration to initiate crack growth in Ti-6Al-4V is thickness dependent even though specimen dimensions to provide valid K_{Ic} data are met. To the extent subcritical crack growth contributes to K_Q , prudence again dictates the use of constant specimen thickness.

It is certain also that K_Q cannot yet be regarded as being quantitatively predictive of K_{Ic} . In a study of 4340 and a maraging steel, Jones and Brown[24] found specimen size exerts different effects on K_Q in these quite different alloys. These authors also found K_Q for the maraging steel to be essentially independent of strength over a significant range. Apparently the "size effect" is "strength dependent." The effect is superficial, however, because strength is a dependent variable in the same sense that K_Q (or K_{Ic}) is; each depends on variables such as alloy, structure, and texture. For the maraging steel these

² The italic numbers in brackets refer to the list of references appended to this paper.

authors studied, the metallurgical variables are compensating in their effect on K_Q but not in their effect on strength or K_{Ic} . This is not true of their 4340, and from the literature cited previously it is quite unlikely to be true of alpha-beta titanium alloys. A methodology that defines, independently of strength, the effects various metallurgical variables have on fracture toughness is needed. With these features established qualitatively in terms of K_Q , the later optimization of alloy and its processing in terms of K_{Ic} is facilitated. This paper is intended to provide some of these guidelines.

The alloy variables considered here were oxygen, aluminum, and beta stabilizer. The beta stabilizer effect was qualitative only, 4V being compared with 2Mo in the alloy formulations. Structure as manifest by roll temperature and texture as reflected by test direction as well as annealing temperature were additional variables studied. The experimental plan was a full factorial so that variance and correlational analyses could be used to disclose trends not self evident in the data and to give proper weight to the realities and magnitudes of main effects and interactions. Specimens of constant dimensions were used so as to minimize size effects.

This work is to be regarded, therefore, as a first tier effort toward determining some of the metallurgical variables affecting mixed mode fracture toughness in alpha-beta titanium.

Procedures

All alloys were formulated from commercial Kroll titanium sponge and master alloy materials and consumable arc melted twice under vacuum into 20-lb ingots. These were converted to nominal 0.71 cm (0.28 in.) plate using a laboratory press and rolling mill. After heat treatment, single edge-notch specimens were machined according to Fig. 1. About 8×10^5 stress cycles per centimeter were used to propagate the last millimeter of crack. All tests were performed in tension. The modified secant method of Srawley et al[25] was used to calculate K_Q (K_{Ic}). Within each experiment, specimens of constant thickness and configuration were used so as to facilitate comparisons among alloys or conditions even though K_{Ic} requirements were not always met. For engineering purposes, the data are valid only for the plate thickness and conditions employed. Tensile data, as averaged from duplicate tests, were generated from 2.5-cm gage length specimens. All testing was carried out on a Riehle Model PS-60 tensile machine.

Heat numbers and chemical analyses appear in Table 1. Processing and heat treatment were independent variables and are so indicated in the text. The processing was designed to give significantly different textures and microstructures. The alloys were hot rolled at two temperatures, beta transus plus 42 K(75°F) (beta rolling) or beta transus minus 42 K(75°F) (alpha-beta rolling). Beta rolling yielded transformed microstructures, whereas alpha-beta rolling

NOTES- 1. NOTCH SHOULD BE PROPAGATED TO .63 TO .79 cm BEFORE TESTING.
2. SPECIMEN THICKNESS MUST FALL IN RANGE .711 TO 1.422 cm.

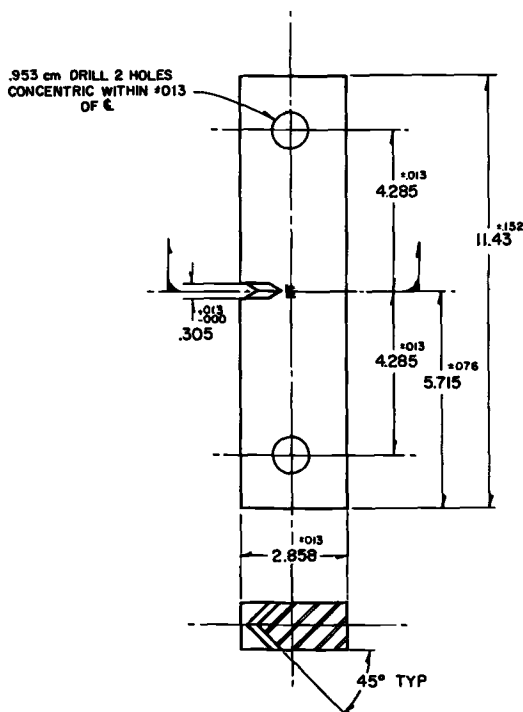


FIG. 1—Illustration of fracture toughness specimen used. All dimensions in centimeters.

produced microstructures having various degrees of equiaxed and stringy primary alpha.

Test direction was also a variable. Crack propagation was in the long transverse direction for longitudinal specimens and vice versa.

Statistical methods were used to analyze the data, the experiments being designed to facilitate such analyses. The least squares (regression) methods used are those described by Brownlee for one or two independent random variables[26]. Such correlations are assumed to have the forms $z = a + bx$ and $z = a + bx + cy$ where x and y are independent variables, a , b , and c are coefficients while z is the dependent variable.

The procedure for two independent variables is convenient when trying to decide if oxygen influences fracture toughness independently of yield strength. Oxygen level and yield strength are not metallurgically independent variables as

30 FATIGUE AND FRACTURE TOUGHNESS—CRYOGENIC BEHAVIOR

TABLE 1—Heat numbers and chemical analyses of alloys used.^a

Heat No.	Weight Percent					
	Al	V	Mo	O	N	Fe
V-3645	4.51	4.12		0.15	0.006	0.072
V-3646	4.49	4.12		0.08	0.006	0.077
V-3647	5.14	4.08		0.15	0.005	0.068
V-3648	5.15	4.12		0.07	0.005	0.067
V-3649	5.94	3.98		0.16	0.005	0.063
V-3650	6.00	4.00		0.07	0.005	0.065
V-3693	4.58		1.87	0.14	0.005	0.057
V-3694	4.57		1.87	0.07	0.006	0.067
V-3695	5.18		1.88	0.14	0.005	0.066
V-3687	5.26		1.84	0.07	0.007	0.071
V-3686	6.12		2.01	0.15	0.004	0.056
V-3685	6.20		2.07	0.07	0.003	0.050

^a Carbon < 0.03 weight percent.

assumed in linear regression theory. However, if oxygen affects toughness only through its effect on the flow stress, the correlation between yield strength and fracture toughness should dominate the correlation statistically. This is because an indirect effect on the average will be attenuated relative to a direct effect. Any significant variance in toughness attributable to oxygen after subtracting out that due to the yield strength must arise through a mechanism not linearly related to yield strength.

It should be mentioned, however, that the normal equations used to solve for the regression coefficients are assumed to correlate independent variables that are normally distributed with dependent variables that are known without error. This is not the exact case where yield strength and K_Q are considered as dependent variables. Both have associated experimental errors. Nevertheless, the regression method will be used with the reservation that results will be first approximations.

The variance analysis methods used are those to be found in Brownlee[26] and Winer[27]. The independent variables used were fixed; that is, increments between levels were uniform or else there was a qualitative difference such as alloy or rolling direction. A subtlety with variance analysis is that the dependent variable ideally should exhibit a normal distribution of experimental error and have an error variance not related to the absolute level of the variable. In the case of fracture toughness, however, error variance is related to the toughness level so the distribution is skewed. Logarithmic transformations, therefore, were used in all variance analyses.

Student's t test was used to determine the significance of difference between means[26].

In deciding whether or not a given effect or interaction is significant, a level of $p = 0.05$ was selected as giving a reasonable balance between the possible errors of rejecting a real effect or accepting a false one. Here p is the probability that a given observation is due to chance alone (experimental error).

Experimental Results

Within the standard errors of the various chemical analyses, the compositional variables employed in this study were fixed and equal to the nominal values. The experimental plan for each alloy was a full factorial in which oxygen, aluminum, rolling temperature, annealing temperature, and test direction were the independent variables. Tables 2 and 3 present the tensile and mixed mode fracture data. Table 4 gives the complete analysis of variance where yield strength is the dependent variable. Aluminum and oxygen are strong main effects, whereas rolling temperature, test direction, and beta stabilizer all appear in significant interactions.

Breaking down the data by alloy, rolling temperature, and test direction, it is possible to estimate the individual strengthening effects of aluminum and oxygen for each condition. In titanium-aluminum alloys, aluminum is known to strengthen linearly and athermally [28]. From the literature [29,30] oxygen is known to strengthen titanium thermally according to \sqrt{c} . The strengthening rate regression coefficients for aluminum and oxygen were calculated by least squares technique on these bases. The coefficients and their standard errors along with variance ratios, F , and residuals are given in Table 5. The significant annealing effect is relatively small and was pooled with the residual in these data. The main effects of aluminum and oxygen are highly significant in this analysis also. The strengthening rates in each case are consistent in magnitude with data in the literature.

Table 6 presents the complete overall analysis of variance for $\log K_Q$. Annealing temperature is insignificant. Only test direction among the main effects is significant against the four significant interactions involving the other main effects. These data were broken down as shown in Tables 7 and 8. From these tables, it is obvious that alloying effects depend generally on rolling temperature and in one case on test direction. When it exists, the effect of oxygen on K_Q is negative. Beta rolling, however, negates any oxygen effect. However, aluminum has a significant effect on K_Q in beta rolled Ti-2Mo. The Ti-4V system analysis in Table 7 is complicated by interactions involving aluminum, oxygen, and test direction. Breaking down the alpha-beta rolled Ti-4V data by test direction, shows the oxygen-aluminum interaction dominates the main effects, see Table 8. Trends associated with these features are shown in Fig. 2. Alloying effects clearly depend on microstructure and to a less extent on texture as manifest by an interaction with test direction. The latter dependence is a function of the data field considered. Overall, texture is a significant main

TABLE 2—Results of yield strength factorial units, MNm^{-2} , strain rate, $8.3 \times 10^{-5} \text{ s}^{-1}$ alloy compositions nominal.

Roll Temperature	Beta Alloy	Anneal ^a Temperature	Direction	4.5Al ^b		5.25Al		6.0Al	
				0.08 O ₂	0.16 O ₂	0.08 O ₂	0.16 O ₂	0.08 O ₂	0.16 O ₂
α/β	4V	950 K	L	721	807	779	885	844	922
α/β	4V	950 K	T	791	903	870	954	919	991
α/β	4V	978 K	L	702	788	757	862	826	890
α/β	4V	978 K	T	780	873	838	940	892	956
α/β	4V	1006 K	L	699	786	758	847	823	885
α/β	4V	1006 K	T	800	878	837	948	884	966
α/β	2Mo	950 K	L	692	755	706	801	777	843
α/β	2Mo	950 K	T	753	872	777	936	957	999
α/β	2Mo	978 K	L	659	717	701	763	778	847
α/β	2Mo	978 K	T	720	884	835	897	893	969
α/β	2Mo	1006 K	L	648	742	714	784	766	843
α/β	2Mo	1006 K	T	691	872	835	915	848	967
β	4V	950 K	L	690	763	735	807	789	852
β	4V	950 K	T	742	790	774	866	809	878
β	4V	978 K	L	696	771	727	800	786	847
β	4V	978 K	T	722	793	735	836	802	856
β	4V	1006 K	L	673	764	707	779	764	815
β	4V	1006 K	T	715	794	726	892	806	853
β	2Mo	950 K	L	679	737	739	821	744	887
β	2Mo	950 K	T	690	779	753	803	777	931
β	2Mo	978 K	L	683	718	725	801	763	838
β	2Mo	978 K	T	665	733	730	780	792	843
β	2Mo	1006 K	L	654	707	714	772	772	872
β	2Mo	1006 K	T	667	761	701	793	771	822

^a 950 K = 1250 °F

978 K = 1300 °F

1006 K = 1350 °F

^b 1 ksi = 6.895 MNm⁻¹

TABLE 3—Results of K_Q toughness factorial units $MNm^{-3/2}$.
Alloy compositions nominal

Roll Temperature	Beta Alloy	Anneal ^a Temperature	Direction	4.5Al ^b				5.25Al				6.0Al			
				0.08 O ₂	0.16 O ₂	0.08 O ₂	0.16 O ₂	0.08 O ₂	0.16 O ₂	0.08 O ₂	0.16 O ₂	0.08 O ₂	0.16 O ₂	0.08 O ₂	0.16 O ₂
α/β	4V	950 K	L	59	53	55	49	59	49	59	41 ^c	59	41 ^c		
α/β	4V	950 K	T	58	61	67	46 ^c	57	46 ^c	57	40 ^c	57	40 ^c		
α/β	4V	978 K	L	52	53	52	51	53	51	53	44	53	44		
α/β	4V	978 K	T	62	59	69	47	61	47	61	45 ^c	61	45 ^c		
α/β	4V	1006 K	L	50	53	56	49	59	49	59	41 ^c	59	41 ^c		
α/β	4V	1006 K	T	59	56	65	50	51	50	51	43 ^c	51	43 ^c		
α/β	2Mo	950 K	L	66	64	53	41	61	41	61	51	61	51		
α/β	2Mo	950 K	T	76	57	63	50	70	50	70	46 ^c	70	46 ^c		
α/β	2Mo	978 K	L	57	43	60	43	52	43	52	54	52	54		
α/β	2Mo	978 K	T	65	58	58	51	51	51	51	64	51	64		
α/β	2Mo	1006 K	L	53	57	53	43	59	43	59	52	59	52		
α/β	2Mo	1006 K	T	58	49	71	50	50	50	50	56	50	56		
β	4V	950 K	L	53	61	63	69	76	69	76	65	76	65		
β	4V	950 K	T	60	71	75	69	77	69	77	67	77	67		
β	4V	978 K	L	56	63	73	64	60	64	60	66	60	66		
β	4V	978 K	T	59	61	71	61	69	61	69	71	69	71		
β	4V	1006 K	L	55	66	70	60	68	60	68	67	68	67		
β	4V	1006 K	T	64	69	66	69	66	69	66	64	66	64		
β	2Mo	950 K	L	50	52	69	70	69	70	69	63	69	63		
β	2Mo	950 K	T	65	69	60	68	66	68	66	50	66	50		
β	2Mo	978 K	L	65	61	63	59	62	59	62	73	62	73		
β	2Mo	978 K	T	46	56	73	63	76	63	76	77	76	77		
β	2Mo	1006 K	L	59	60	64	70	61	70	61	64	61	64		
β	2Mo	1006 K	T	50	66	59	71	67	71	67	65	67	65		

^a See footnote ^a Table 2.^b ksi $\sqrt{\text{in.}} = 1.10 \text{ MNm}^{-3/2}$ ^c K_{Ic} validity requirements nominally met. All other results are K_Q .

TABLE 4—Analysis of variance for yield strength.

Variable	Degrees Freedom	Mean Square	Significance ^a
Oxygen (O)	1	5043.37	< 0.001
Aluminum (A)	2	2752.28	< 0.001
Roll temperature (R)	1	2652.25	... ^b
Test direction (D)	1	2679.79	... ^c
Beta stabilizer (B)	1	671.67	... ^d
Anneal (T)	2	155.38	< 0.001
RD interaction	1	1150.34	< 0.001
RB interaction	1	86.49	0.01
Residual	133	9.26	...

^a Values given are probabilities that observations are due to chance.

^b Not significant against RD interaction and indeterminate because roll temperature is involved in two significant interactions.

^c Not significant against RD interaction.

^d Not significant against RB interaction.

effect. Microstructural effects are important but not simple. Overall, K_Q for beta rolled product averages about $9.9 \text{ MNm}^{-3/2}$ higher than for alpha-beta rolled product. This difference means little *per se* because of the three interactions. However, considering only the data for Ti-6Al-4V, beta rolling leads to significantly higher K_Q values at each oxygen level. In Tables 7 and 8, the data for the three anneals were considered as simple replications so as to allow calculations of test error and high order interactions.

Correlation coefficients were calculated in order to obtain first approximations of the degrees to which oxygen and aluminum influence K_Q independently of yield strength in the Ti-2Mo system. These analyses appear in Table 9. The Ti-2Mo system was chosen because in these alloys only aluminum and oxygen, among the variables studied, were significant effects according to the breakdown in Table 7.

In no case did the effect of yield strength on K_Q reach the 0.05 level of significance. This is so regardless of whether yield strength is considered alone (simple r) or in combination with oxygen or aluminum (partial r'). From this, one draws the tentative conclusion for the data fields examined here that either K_Q or yield strength correlates with alloy content more highly than they do with each other. These results are first approximations to be sure but are nevertheless interesting enough to justify further work and analysis.

Discussion

The significant effect of test direction on K_Q relates to crystallographic texture effects. Considering only the data for alpha-beta rolling, which develops basal plane textures of twofold symmetry, transverse specimens averaged some

TABLE 5—Statistical analyses of data appearing in Tables 2 and 3 where yield strength depends on variables shown.

Alloy	Roll Temperature	Test Direction	Strengthening Rate ^a			F(Al), <i>b,c</i>	F(O), <i>b,d</i>	Residual ^e
			Aluminum MNm ⁻² c ⁻¹	Oxygen MNm ⁻² c ^{-1/2}				
Ti-xAl-4V	α/β	L	76 \pm 6	723 \pm 63	163	133	243	
Ti-xAl-4V	α/β	T	62 \pm 6	736 \pm 66	96	123	273	
Ti-xAl-4V	β	L	55 \pm 5	598 \pm 57	102	110	202	
Ti-xAl-4V	β	T	50 \pm 7	640 \pm 68	58	87	290	
Ti-xAl-2Mo	α/β	L	72 \pm 6	622 \pm 59	161	112	214	
Ti-xAl-2Mo	α/β	T	92 \pm 12	944 \pm 130	56	53	1034	
Ti-xAl-2Mo	β	L	78 \pm 8	643 \pm 86	89	56	458	
Ti-xAl-2Mo	β	T	71 \pm 10	663 \pm 108	48	38	713	

^a c is solute concentration in weight percent \pm values are standard errors for effect.^b (1,15) degrees of freedom.^c F ratio for aluminum effect on yield strength.^d F ratio for oxygen effect on yield strength.^e Contains the significant effect of annealing temperature.

TABLE 6—Analysis of variance for $\log K_Q$.

Variable	Degrees Freedom	Mean Square	Significance ^a
Oxygen (O)	1	0.03377	... ^b
Aluminum (A)	2	0.00087	... ^b
Roll temperature (R)	1	0.20437	... ^b
Test direction (D)	1	0.01589	0.01
Beta stabilizer (B)	1	0.00000	... ^c
Anneal (T)	1	0.00221	NS ^d
OA interaction	2	0.02420	0.01
OR interaction	1	0.05527	< 0.001
AR interaction	2	0.05799	< 0.001
RB interaction	1	0.01048	0.05
Residual	131	0.00177	...

^a Values given are probabilities that observations are due to chance.

^b Indeterminant because variable involved in two or more interactions.

^c Variable not significant but involved in the RB interaction.

^d NS = not significant.

4.0 MNm^{-3/2} (3.6 ksi $\sqrt{\text{in.}}$) higher in K_Q than did longitudinal specimens. Crack propagation is more difficult parallel to basal planes than perpendicular to them according to Harrigan et al [17], and results here are consistent on that basis. In this work, areas of high basal pole intensity were bilaterally disposed about the rolling direction after alpha-beta rolling.

The oxygen:aluminum interactions arising from the K_Q analyses of variance of the Ti-4V system are of considerable phenomenological interest. The effect of one element on K_Q depends on the concentration of the other. Such a result may indicate an association between oxygen and aluminum atoms in the lattice such that the effect of either solute species would be compounded in the presence of the other. Their free energies of oxide formation and individual effects on lattice parameters are consistent with an "association mechanism." Other work on the activation partials of alpha titanium alloyed with aluminum suggests the same possibility [28].

No interactions were found in the Ti-2Mo system. This may be a result of the large residuals appearing in the analysis of variance of these alloys rather than a complete lack of an aluminum-oxygen interaction.

That alloying can affect mixed mode fracture toughness independently of yield strength in alpha-beta titanium is also evident. Further work would be necessary, however, to demonstrate the practical significance of this result and whether alloying elements that strengthen thermally (oxygen) do indeed influence fracture toughness in a manner different from alloying elements that strengthen athermally (aluminum). The preliminary analysis of the Ti-2Mo alloy system indicates that perhaps they do.

In any case this work has shown that it is dangerous to consider only small domains of data. For example, alloy content, microstructure, and perhaps

TABLE 7—Analyses of variance for log K_Q broken down by alloy and roll temperature and pooling heat treatment for replication purposes.

Variable	Degrees Freedom	4V			2Mo		
		α/β Roll		β Roll		α/β Roll	
		Mean Square	Significance ^a	Mean Square	Significance	Mean Square	Significance
Oxygen (O)	1	0.2704	...	0.002	NS ^f	0.1936	0.01
Aluminum (A)	2	0.0623	... ^b	0.0375	...	0.0311	NS
Test direction (D)	1	0.0361	... ^{c,d}	0.0196	...	0.0560	0.05
OA interaction	2	0.0620	...	0.0290	0.05	0.0279	NS
OD interaction	1	0.0114	...	0.0013	NS	0.0001	NS
AD interaction	2	0.0090	NS	0.0025	NS	0.0148	NS
OAD interaction	2	0.0171	0.05	0.0006	NS	0.0064	NS
Residual	24	0.0028	(0.0036) ^e	0.0045	(0.0039) ^e	0.0142	(0.0164) ^e
						0.0134	(0.0119) ^e

^a Values given are probabilities that observations are due to chance.^b Indeterminant, variable involved in two interactions.^c Not significant against OAD interaction.^d Not significant against OA interaction.^e Residual after pooling nonsignificant variances.^f NS = not significant.

38 FATIGUE AND FRACTURE TOUGHNESS—CRYOGENIC BEHAVIOR

TABLE 8—Analyses of variance for $\log K_Q$ for Ti-4V, α/β rolled, broken down by test direction and pooling heat treatment for replication purposes.

Variable	Degrees Freedom	Longitudinal		Transverse	
		Mean Square	Significance ^a	Mean Square	Significance ^a
Oxygen (O)	1	0.0854	... ^b	0.1964	... ^b
Aluminum (A)	2	0.0147	... ^b	0.0593	... ^b
OA interaction	2	0.0332	0.01	0.0430	0.01
Residual	12	0.0026		0.0029	

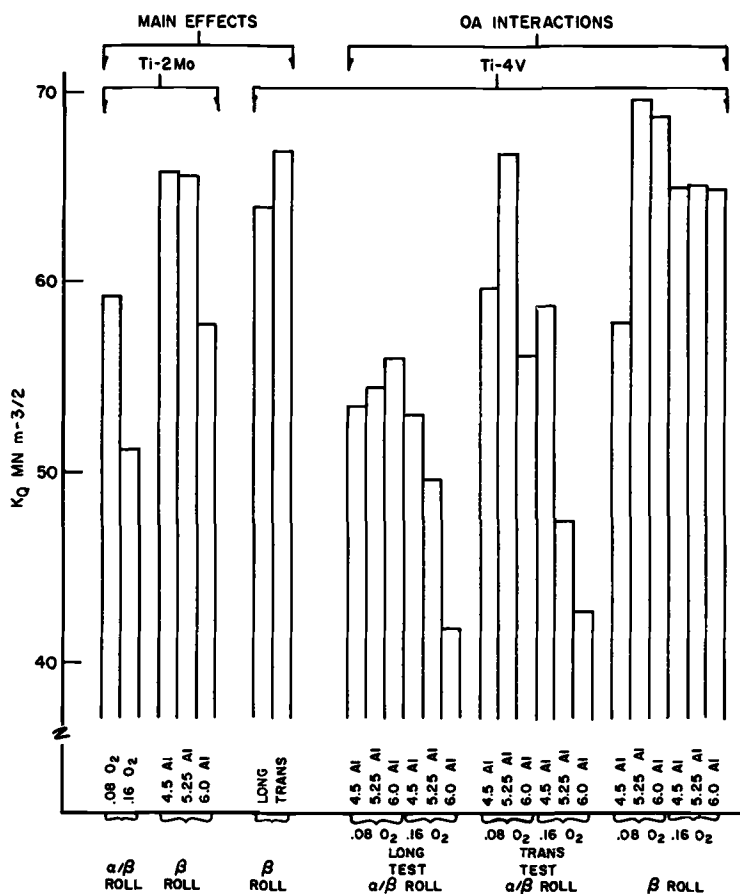
^a Values given are probabilities that observations are due to chance.^b Not significant against OA interaction.

FIG. 2—Bar graph summarizing main effects and interactions appearing in Tables 7 and 8.

TABLE 9—Correlational analyses of Ti-2Mo system data for relative magnitudes of alloying and yield strength correlations with K_Q .^a

Correlation Coefficient	α/β Roll ^b		β Roll ^b	
	L	T	L	T
Simple (16 degrees of freedom)				
$r(O_2)$	-0.51 (0.05)	-0.54 (0.02)	0.09 (NS) ^c	0.15 (NS)
$r(Al)$	-0.10 (NS)	-0.21 (NS)	0.52 (0.05)	0.39 (NS)
$r(YS)$	-0.28 (NS)	-0.41 (0.10)	0.41 (0.10)	0.30 (NS)
Partial (15 degrees of freedom)				
$r'(O_2)$	-0.45 (0.10)	-0.39 (NS)		
$r'(YS)$	0.06 (NS)	-0.10 (NS)		
$r'(Al)$			0.36 (NS)	0.26 (NS)
$r'(YS)$			0.04 (NS)	0.05 (NS)

^a Correlations are with K_Q directly, use of $\log K_Q$ makes no essential difference.

^b Correlation coefficients with sign of effect given and probability that observed correlation is due to chance given in parenthesis.

^c NS = not significant.

strength may be mutually dependent in their effects on K_Q . Alloys of dissimilar textures also would not give comparable results.

In an attempt to evaluate the shear lip effect, load readings were taken on duplicate specimens at the point of visual propagation of the crack or point at which the crack tip dimpled inward (indicating internal crack propagation) whichever came first. The results did not correlate well with data generated by the secant method. Variance analyses also disclosed a high experimental error for the optical method. This precluded effective statistical treatment. The fraction of shear lip was not constant for these specimens, and this undoubtedly contributed to error variance.

To some extent this is also true for data determined by the secant method. The variance analysis accounts for this, however. Whatever variance can be attributed independently to the relative proportion of shear fracture at the 5 percent secant intercept can only appear in the residual. Tests for significance are ultimately against the residual. It must be recognized also that the amount of shear fracture at a given secant may depend in turn on some other variable. The power of variance analysis is such, however, that significant effects would be still more significant if the independent variance due to shear fraction could be subtracted out. The main effects and interactions would be more clearly shown in that event. This would amount to partitioning the variance of effects between plane strain and plane stress modes. So far this has not been possible.

Whatever effects the use of subsize specimens have on the analyses, findings here are nevertheless qualitatively consistent with the literature on K_{Ic} . The

texture effect, as implied by the test direction effect, parallels findings of Harrigan et al[17] on Ti-6Al-2Sn-4Zr-6Mo where tests were performed in accordance with ASTM Test for Plane-Strain Fracture Toughness of Metallic Materials (E 399). Considering only the alpha-beta rolled Ti-6Al-4V alloy data in this study, the negative effect of oxygen on K_Q is significant to $p < 0.001$ according to a correlated pairs t test. This result parallels the findings of Hieronymus[18], who employed K_{Ic} tests on alpha-beta rolled commercial Ti-6Al-4V of various oxygen levels. Microstructural effects (as a result of rolling temperature) found here are consistent with trends noted by Hall et al[3] who employed K_{Ic} specimens and found K_{Ic} to increase with the volume fraction of relatively coarse acicular alpha in Ti-6Al-2Sn-4Zr-6Mo. Hall and Pierce[1] earlier found a similar trend in K_Q for Ti-6Al-6V-2Sn.

Taken together, these results confirm the probability discussed in the introduction that the metallurgical variables in alpha-beta titanium are not compensating in terms of their effects on K_Q . Nevertheless, whenever K_Q and K_{Ic} data in a given alloy system can each be shown to correlate even qualitatively with certain metallurgical variables, reaching the goals of alloy optimization and K_{Ic} design type data generation becomes an expeditious matter.

Results here for the dependence of K_Q on oxygen in Ti-6Al-4V also parallel the findings of Gerberich and Baker[4] who found a dependence on interstitials for precracked Charpy toughness in that alloy. At a low interstitial level, these authors showed the same microstructural effect found here. However, the high oxygen material used by these authors also contained higher iron, nitrogen, and carbon which led to yield strengths higher than observed here. These may have masked any microstructural effect on toughness in their material at high interstitial levels. Judy et al[5] also found that drop weight tear resistance depends on oxygen and microstructure in Ti-6Al-4V.

A further point to be made from this study is that while previous authors have correctly identified several variables that affect fracture toughness in titanium alloys, a more comprehensive experimental plan amenable to statistical analyses yields additional insight as to how variables interact. How the effect of one variable may be influenced by the level of another is an important aspect of alloy design. Similar knowledge is important when one's concern is to modify some property of existing alloys. Finally such knowledge is important to an understanding of the underlying metallurgy. A note of caution in this regard, however: statistical correlations are correlations and do not demand a cause and effect relation between variables; there may be a third variable "causing" them both. Moreover, interactions may not always require some mutual dependence of effects although that may often be the case. For instance, it may happen that two variables are additive toward some critical limit beyond which neither has any effect. Upon exceeding that limit, where "increasing" one variable "negates" the effect of the other, an interaction may appear in the variance analysis. Proper

experimental design will take account of this eventuality and disclose such situations for what they are. Conventional metallurgical analyses, of course, are quite helpful in deducing the underlying meaning of statistical results.

Conclusions

1. Alloying effects on K_Q in alpha-beta titanium alloys depend on microstructure.

2. There is a strong interaction effect between oxygen and aluminum on K_Q in Ti-4V alloys.

3. To a first approximation, oxygen and aluminum affect K_Q in Ti-2Mo independently of yield strength.

4. Texture, as implied by a significant effect of test direction, influences K_Q . The direction most nearly paralleling the basal planes gives the highest K_Q value, in agreement with the literature on K_{IC} in Ti-6Al-2Sn-4Zr-6Mo.

5. The negative effect of oxygen on K_Q in alpha-beta rolled Ti-6Al-4V is qualitatively similar to that in the literature on K_{IC} in this alloy.

6. In Ti-6Al-4V, at low iron, carbon, and nitrogen levels, transformed microstructures containing platelet alpha provide generally higher K_Q values than do microstructures containing equiaxed or stringy primary alpha. This effect occurs at both 0.08 and 0.16 percent oxygen, and qualitatively agrees with the literature on K_{IC} in Ti-6Al-2Sn-4Zr-6Mo.

7. Statistical methods have been shown to be quite useful in the study of fracture toughness.

Acknowledgment

A. J. Hatch, formerly with TIMET, designed and supervised the experimental work.

References

- [1] Hall, J. A. and Pierce, C. M., "Improved Properties of Ti-6Al-6V-2Sn Through Microstructure Modification," Technical Report AFML-TR-70-312, Air Force Materials Laboratories, Wright-Patterson Air Force Base, Ohio, Feb. 1971.
- [2] Greenfield, M. A. and Margolin, H., *Metallurgical Transactions*, Vol. 2, March 1971, pp. 841-847.
- [3] Hall, J. A., Pierce, C. M., Ruckle, D. L., and Sprague, R. A., "Property-Microstructure Relationships in Titanium Alloy Ti-6Al-2Sn-4Zr-6Mo," Technical Report AFML-TR-71-206, Air Force Materials Laboratories, Wright-Patterson Air Force Base, Ohio, Nov. 1971.
- [4] Gerberich, W. W. and Baker, G. S. in *Applications Related Phenomena in Titanium Alloys*, ASTM STP 432, American Society for Testing and Materials, 1968, pp. 80-99.
- [5] Judy, R. W. Jr., Goode, R. J., and Huber, R. W., "Effects of Heat Treatment Below the Beta Transus on the Fracture Resistance of Ti-6Al-4V," NRL Memorandum Report 2345, Naval Research Laboratory, Washington, D. C., Sept. 1971.
- [6] Curtis, R. E. and Spurr, W. F., *Transactions*, American Society for Metals, Vol. 61, 1968, pp. 115-127.
- [7] Gross, B., Srawley, J. E., and Brown, W. F., "Stress-Intensity Factors for a

- single-Edge-Notch Tension Specimen by Boundary Collocation of a Stress Function," NASA TN D-2395, National Aeronautics and Space Administration, Washington, D. C., Aug. 1964.
- [8] Krafft, J. M. and Irwin, G. R. in *Fracture Toughness Testing and Its Applications, ASTM STP 381*, American Society for Testing and Materials, April 1965, pp. 114-129.
 - [9] Tetelman, A. S. and McEvily A. J., Jr., *Fracture of Structural Materials*, Wiley, New York, 1967, p. 82.
 - [10] Shoemaker, A. K. and Rolfe, S. T., "The Static and Dynamic Low-Temperature Crack-Toughness Performance of Seven Structural Steels," AD 846 126 L, Nov. 1968, (available from Defense Documentation Center).
 - [11] Meyn, D. A., "A Procedure for Investigating the Effect of Hydrogen Content on Toughness and Sustained Load Cracking Resistance of Titanium Alloys With Some Results for Ti-6Al-4V," NRL Memorandum Report 2461, Naval Research Laboratory, Washington, D. C., June 1972.
 - [12] Wood, R. A., Boyd, J. D., Williams, D. N., and Jaffee, R. I., "The Effect of Alloy Composition on the Mechanism of Stress-Corrosion Cracking of Titanium Alloys in Aqueous Environments," Battelle Annual Summary Report 11 June 1971-10 June 1972) to National Aeronautics and Space Administration, June 1972.
 - [13] Barsom, J. M. and Rolfe, S. T. in *Impact Testing of Metals, ASTM STP 466*, American Society for Testing and Materials, 1970, pp. 281-302.
 - [14] Sailors, R. H. and Corten, H. T. in *Fracture Toughness*, Proceedings of the 1971 National Symposium on Fracture Mechanics, Part II, *ASTM STP 514*, American Society for Testing and Materials, 1972, pp. 164-191.
 - [15] Ronald, M. F., Hall, J. A., and Pierce, C. M., *Metallurgical Transactions*, Vol. 3, April 1972, pp. 813-818.
 - [16] Hatch, A. J., "Mechanical Metallurgy and Fracture Toughness of Titanium Alloys," paper given at the Titanium Technical Conference, Air Force Materials Laboratory and University of Dayton, Ohio, Nov. 1967.
 - [17] Harrigan, M. J., Sommer, A. W., Reimers, P., and Alers, G. A. in *Titanium Science and Technology*, Plenum Press, New York, 1973, pp. 1297.
 - [18] Hieronymous, W. S., *Aviation Week and Space Technology*, 26 July 1971, pp. 42-45.
 - [19] Boyd, J. D., "The Influence of Interstitials, Particularly Hydrogen, in Titanium Behavior," Titanium Course, New York University, 8-11 Sept. 1969.
 - [20] Rolfe, S. T. and Novak, S. R. in *Review of Developments in Plane Strain Fracture Toughness Testing, ASTM STP 463*, American Society for Testing and Materials, 1970, pp. 124-159.
 - [21] Judy, R. W., Freed, C. N., and Goode, R. J., "A Characterization of the Fracture Resistance of Thick-Section Titanium Alloys," NRL Report 7427, Naval Research Laboratory, Washington, D. C., July 1972.
 - [22] May, M. J. in *Review of Developments in Plane Strain Fracture Toughness Testing, ASTM STP 463*, American Society for Testing and Materials, 1970, pp. 41-62.
 - [23] Galda, K. H. and Munz, D., *International Journal of Fracture Mechanics*, Vol. 8, 1972, pp. 472-474.
 - [24] Jones, M. H. and Brown, W. F., Jr., in *Review of Developments in Plane Strain Fracture Toughness Testing, ASTM STP 463*, American Society for Testing and Materials, 1970 pp. 77-82.
 - [25] Srawley, J. E., Jones, M. H., and Brown, W. F., *Materials Research and Standards*, June 1967, pp. 262-266.
 - [26] Brownlee, K. A., *Industrial Experimentation*, Chemical Publishing Company, New York, 1953, pp. 36-80.
 - [27] Winer, B. J., *Statistical Principles in Experimental Design*, second edition, McGraw-Hill, New York, 1971.
 - [28] Rosenberg, H. W., "Deformation Mechanics of Alpha Titanium Alloys," PhD

dissertation, Department of Materials Science, Stanford University, Stanford, Calif., May 1971.

[29] Conrad, H., *Acta Metallurgica*, Vol. 14, 1966, pp. 1631.

[30] Covington, L. C., "A Correlation of the Effects of Impurities on the Hardness of Titanium," Titanium Metals Corporation of America, Project 47-31, Progress Report No. 6, Oct. 1959.

N. R. Adsit,¹ P. Dessau,² and W. E. Witzell¹

Flexural Fatigue Testing of Titanium Forging Material in Liquid Hydrogen

REFERENCE: Adsit, N. R., Dessau, P., and Witzell, W. E., "Flexural Fatigue Testing of Titanium Forging Material in Liquid Hydrogen," *Fatigue and Fracture Toughness—Cryogenic Behavior*, ASTM STP 556, American Society for Testing and Materials, 1974, pp. 44–54.

ABSTRACT: The program described is the fatigue testing of titanium 5Al-2.5Sn material cut from production forgings. The high-cycle fatigue testing was carried out in a liquid hydrogen environment. Forging from two different mills were used, and these were tested in various directions.

A cantilever beam type specimen tapered to provide constant stress across the length was used throughout this program. A special cryostat was made and adapted to standard fatigue testing machines.

There was a sizeable amount of scatter in the data, but 50 percent survival curves were constructed. There was no evidence of directionality, but there was a large difference between materials. This difference may be explained by the metallurgical structure.

KEY WORDS: fracture properties, fatigue tests, liquid hydrogen, forgings, metallographic structures, titanium, cantilever beams, stresses, cryogenics

Although a large amount of cryogenic data has been generated for sheet materials under conventional tensile load conditions, less data are available for forging materials, particularly at liquid hydrogen temperatures. Similarly, because of the difficulty in adapting conventional fatigue machines to use with the potentially explosive liquid hydrogen, less fatigue data are available at -423°F .

This program was designed to determine the behavior of a material designated for use in a cryogenic fluid pump at its lowest service temperature. Operating conditions of the pump required the material to be subjected to stress reversals at frequent intervals. Consequently, it was prudent to examine the material under cyclic conditions while immersed in liquid hydrogen.

¹ Senior engineering metallurgist and design specialist, respectively, Convair Aerospace Division, General Dynamics Corp., San Diego, Calif. 92138.

² Chief metallurgist, AIRCO Viking, Verdi, Nev. 89439, formerly of Aerojet Nuclear Systems Co.

This program was performed by General Dynamics/Convair Aerospace, in San Diego, under the direction of the Aerojet General Corporation.

Material

Since the material to be used was a titanium forging, two forging blanks were produced, and the data were acquired from these simulated production products. The material was Ti-5Al-2.5Sn in the ELI grade. The chemistry of these are given in Table 1.

The forgings were produced by Wyman-Gordon and by Carlton in the form of pancakes. They were then vacuum annealed at 1400°F for 1 h. Since it was not known if the direction would influence the behavior, specimens from both the radial direction and the tangential direction were fabricated. They were numbered in the following manner:

<i>XYZ</i>		<i>Designation</i>
X ((Wyman-Gordon Forming	...
	(Carlton forming	C
	(
Y (Radial direction	R
	Tangential direction	T
Z (Serial number of specimen	1 to 15

Thus, the Carlton radial specimen No. 7 was identified as CR-7. The tests were numbered sequentially, and the specimen identification maintained at all times. The specimens from each forging were randomized, that is, the specimens to be run at each stress were chosen randomly. A photomicrograph of a failed specimen is shown as Fig. 1. This is from the Carlton forging; visual examination of the Wyman-Gordon showed that it had a substantially larger grain size.

TABLE 1—Chemical composition of material.

Element	Content	
	Wyman-Gordon	Carlton
C	0.009/0.011	0.02
Mn	< 0.01	...
Fe	0.14	0.12
Al	5.44	5.4
Sn	2.47	2.5
H ₂	0.0094	90 ppm
O ₂	0.083	0.10
N ₂	0.009	0.01
Ti	balance	balance



FIG.1—*Photograph of failed specimen CT-7 (×6).*

Procedure

In order to test the specimen in a fully reversed stress field, a flexure type specimen was chosen. The most simple type of flexure test is a cantilever beam which has the disadvantage that the stress is not uniform along the section. To remedy this, a constant stress cantilever beam specimen was designed and is shown in Fig. 2. The test section on this specimen has a constant stress. The specimens were machined from blanks and had a surface finish of 16 rms or better.

The testing on this program was carried out in a BLH SF 1-U fatigue testing machine. The specimen was installed in a special cryostat mounted on the machine, as shown in Fig. 3. The cryostat was fitted with a double Teflon seal on the bottom and the space between the seals purged with helium gas so that the loading rod would not ice up and cause errors in the load.

All specimens were tested using an R value ($\sigma_{\min}/\sigma_{\max}$) of -1.0 . This means that no static load was applied during the test.

To ascertain that the bending beam formula give the correct stresses on the test specimens, the first specimen was strain gaged. This specimen was calibrated using the bending fixture that was later installed in the liquid hydrogen (LH_2) cryostat. The specimen was then installed in the fatigue machine and loaded statically. This check assured the investigators that the calculated stresses were equal to the actual stresses.

The first specimen tested failed because of fretting damage at the point of contact with the fixture. To prevent this type of failure, two actions were taken. First, the specimen was coated with a thin layer of zinc chromate; second, the fixture itself was coated with a tough layer of Teflon. These actions prevented metal-to-metal contact, and no further fretting damage was observed. Some failures were observed at the bolt holes because of two factors. First, the specimen rocked at the large (fixed) end; second, because of the tendency to

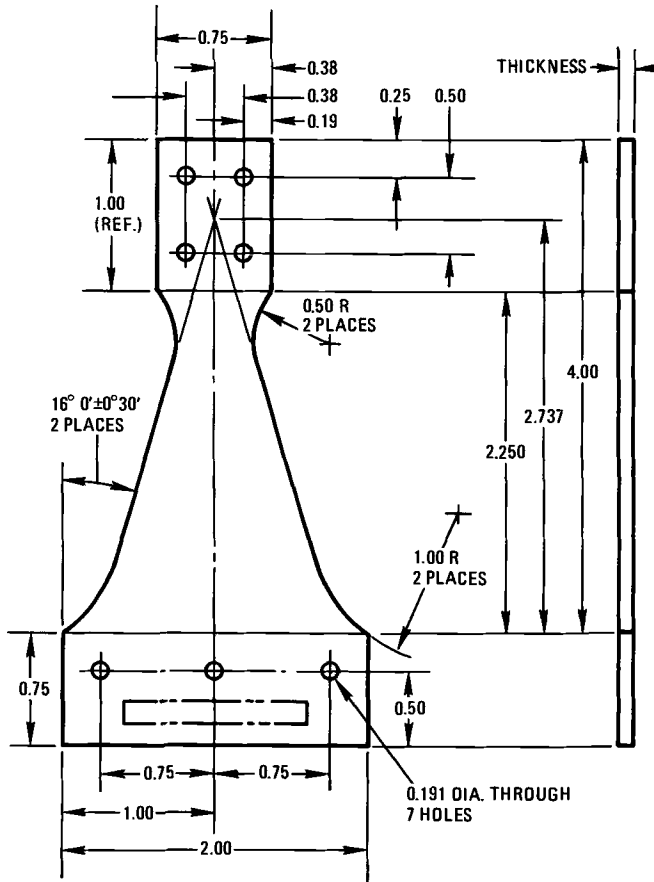


FIG. 2—Constant stress cantilever beam specimen.

rock, the Teflon coating was extruded and slightly increased the amount of rocking. Periodically, the Teflon was stripped off and a new flat smooth layer was applied.

The procedure for installing specimens was as follows: the specimen was secured to the fixture, as shown in Fig. 4. The load was applied through a rod coming through the bottom of the cryostat. To ensure that no static preload was applied, the system had a link which was removable. (This link also served to ensure that no lateral motion was transmitted to the rod through the seals.) The bottom bolt in the link was left out while the specimen was installed. The loading rod was then positioned so that the bolt slipped into position and did

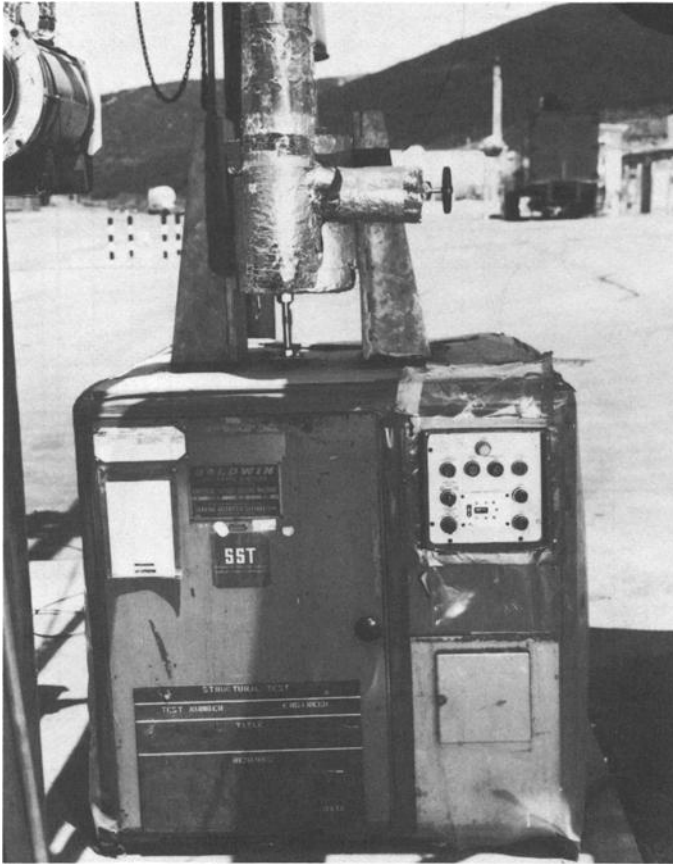


FIG. 3—Fatigue test machine with LH_2 chamber installed.

not cause a static load. The bolt had a positive locking mechanism to keep it in place during testing. After the specimen was secured, the top lid was installed, the chamber was purged with helium gas, and was finally filled with liquid hydrogen. A thermocouple was installed on top of the test fixture to measure the temperature (-423°F), and the specimen was submerged in the liquid at all times during the test ensuring a test temperature of -423°F . The calculated load was set on the dynamic scale, and the machine was turned on, brought up to speed, and allowed to run. The test was terminated at failure, or 2 000 000 cycles, whichever came first. A few specimens were allowed to continue cycling for up to 10 000 000 cycles.

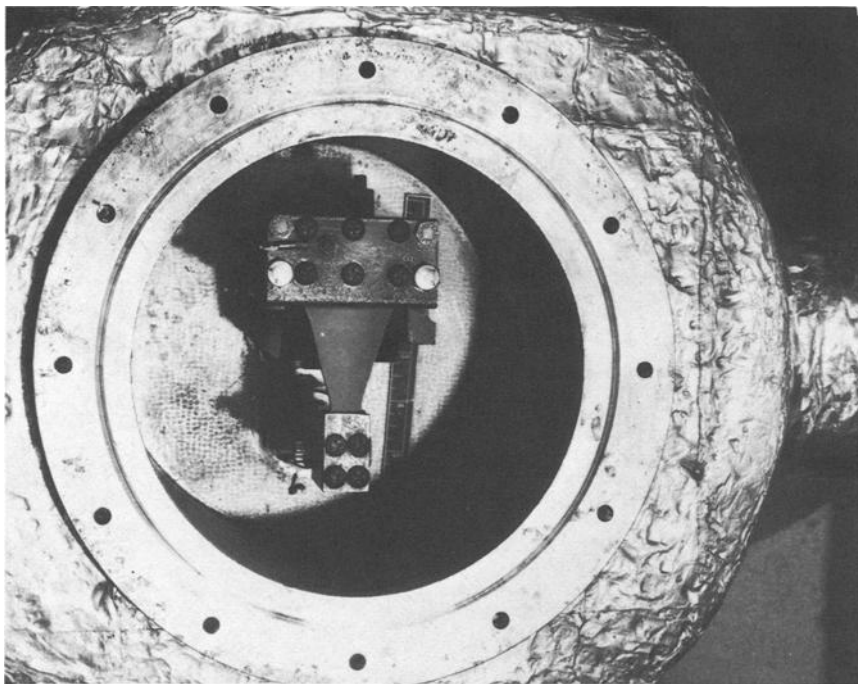


FIG. 4—Titanium flexure fatigue specimen installed in LH_2 cryostat.

Results

The results of the tests performed during this program are given in Table 2. The data have been tabulated by the material supplier, and stresses leveled to facilitate reading. Tensile test data at room temperature and at $-423^{\circ}F$ are given in Table 3. These data were not part of this program but are included for comparison.

Statistical Treatment of the Data

Test schemes for fatigue are presented in *ASTM STP 91-A, A Guide for Fatigue Testing and the Statistical Analysis of Fatigue Data*. For reasons of economy and time, a more elaborate test program was not practical for the present study. In fact, fatigue testing at $-423^{\circ}F$ is quite uncommon, and comparative data are unknown.

Some of the techniques of *STP 91A* were applied to the present program. As in all fatigue testing, a relatively large amount of scatter was observed. The statistical approaches of *STP 91A* were used to try to provide 99 percent probability curves for the test performed. The results were not entirely

TABLE 2--*Test results.*

Specimen No.	Maximum Stress, ksi	Cycles to Failure × 10 ³ Cycles
CT-12	90	210 ^a
CT-7	90	164
CR8	90	138
CR11	90	142 ^a
T-14	90	64
R-11	90	40
R-5	90	37
R-9	90	17
CR-5	80	137 ^a
CT-6	80	78 ^a
CT-5	80	162 ^a
CT-2	72	327
CT-3	72	440
CR4	72	1 137
CT9	72	449
CR-1	72	353
R4	72	84
R3	72	75
T11	72	67
T-16	72	81
R3	72	61
R2	72	61
CT-10	60	1 329
CR10	60	2 000 ^b
CR7	60	408
CR6	60	112
CT11	60	1 232
CT14	60	2 020 ^b
CR3	60	229
CR9	60	6 340
CR2	60	319
T-17	60	201
T-13	60	189
R-14	60	128
R10	60	95
R1	60	106
R6	40	390
R8	40	635
R12	40	302
T15	40	1 042
T9	40	541
CR4	40	2 000 ^b
CT8	40	10 000 ^b
T-10	30	2 000 ^b
R-7	30	2 000 ^b
T-12	30	1 394
T-7	30	6 949

^a Broke at bolt line.^b No failure.

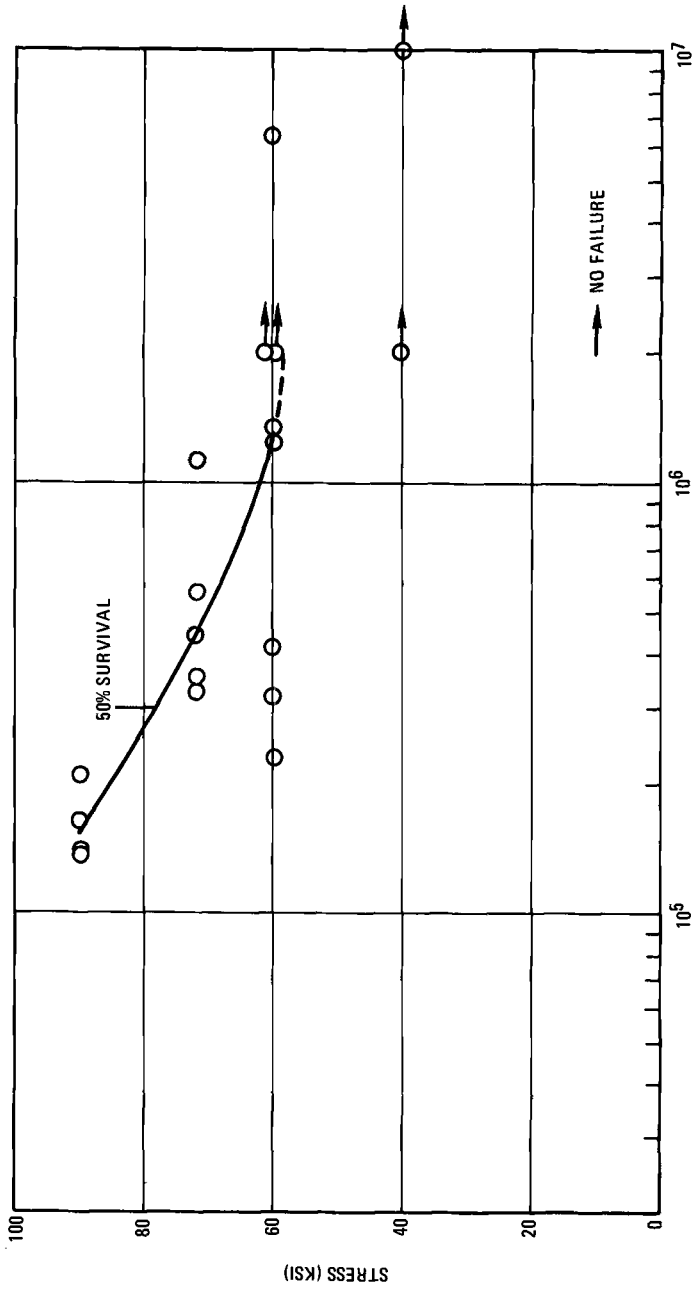


FIG. 5—S-N curve for the Carlton forging Ti-5Al-2.5Sn tested at -423°F .

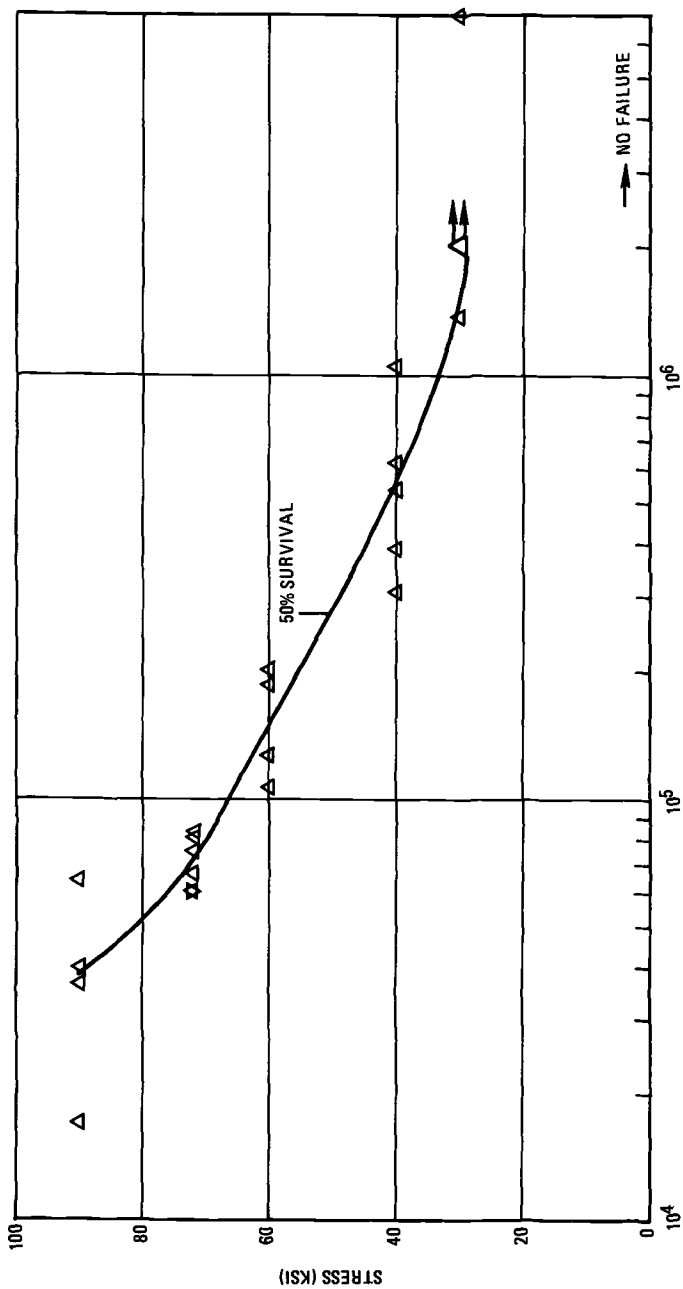


FIG. 6—S-N curve for the Wyman-Gordon forging Ti-5Al-2.5Sn tested at -423°F .

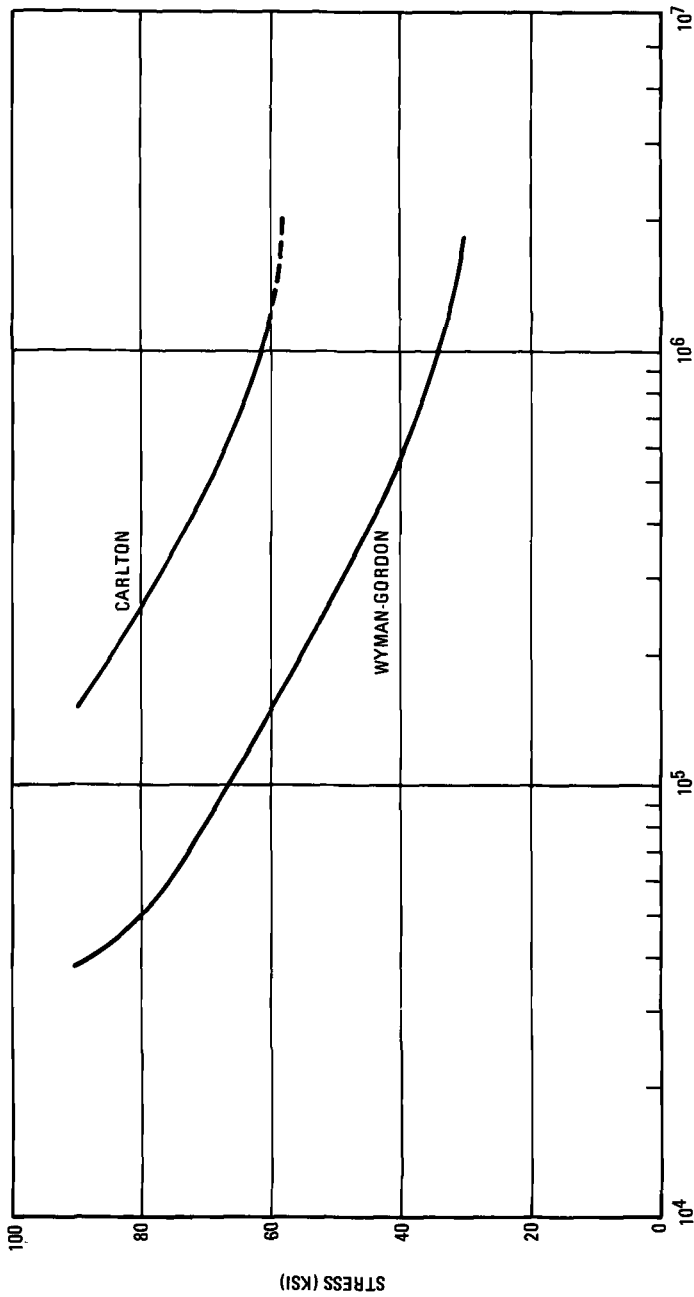


FIG. 7 - 50 percent survival curves for the two forgings of Ti-5Al-2.5Sn tested at -423°F.

TABLE 3—*Tensile test properties.*

Temperature	Forging, avg	Wyman-Gordon, ksi	Carlton, ksi
RT	ultimate tensile strength	120	
	yield strength	108	
-423°F	ultimate tensile strength	209	211
	yield strength	189	187

satisfactory. The combination of large scatter and insufficient sampling in most cases invalidated 99 percent probability limits; hence, only median values are presented for further discussion. For the Carlton forgings (Fig. 5) the normal 50 percent survival or median curve is plotted.

The 50 percent survival curve (median) for the Wyman-Gordon forging is plotted in Fig. 6.

Comparison of Results

The 50 percent survival curves for both forgings are shown in Fig. 7. In this context, the Carlton forging with the smaller grain size shows a marked advantage. A point-by-point examination shows the following:

1. Despite the scatter at 60 ksi, all test points of the Carlton forgings fall to the right of the Wyman-Gordon 50 percent survival curve. In fact, the lowest point on the Carlton curve is higher than the highest point on the Wyman-Gordon curve.

2. It is relatively certain that the fatigue strength of the Carlton forging exceeds 40 ksi.

Less certain is the fatigue strength of the Wyman-Gordon forging at 2 million cycles of approximately 30 ksi.

While it cannot be proven that the grain size is the reason the Carlton forging gives higher results than the Wyman-Gordon forging, it does seem to be logical and does fit a consistent pattern.

There does not seem to be any clear trends due to directionality in these limited data. At 72 ksi, the Carlton forging has a higher average cycles to failure in the radial direction, but at 60 ksi the higher average cycles to failure is in the tangential direction. The Wyman-Gordon forging has virtually the same cycles to failure in both directions at 72 ksi, while at 60 ksi, the higher value is in the tangential direction.

C. F. Hickey, Jr.¹

Toughness Data for Monolithic High-Hardness Armor Steel

REFERENCE: Hickey, C. F., Jr., "Toughness Data for Monolithic High-Hardness Armor Steel," *Fatigue and Fracture Toughness—Cryogenic Behavior*, ASTM STP 556, American Society for Testing and Materials, 1974, pp. 55–67.

ABSTRACT: The purpose of this program was to generate meaningful toughness parameter data that could be incorporated into existing high-hardness steel armor specifications.

Various toughness parameters, including Charpy V-notch impact, pre-cracked Charpy toughness (W/A) and fracture toughness (K_{IC}), were explored for defining the toughness characteristics of monolithic high-hardness armor steels. Materials from three producers were investigated in thicknesses ranging from 0.125 to 0.750 in. The equivalent energy-area criterion was utilized to relate the toughness data obtained from subsize and standard size Charpy V-notch impact specimens.

Results of this investigation show that the energy requirements, as set forth in the military specification for high-hardness armor steels, are met by each producer's material when the plate thickness is sufficient to use the standard size Charpy V-notch impact specimen. The equivalent energy-area criterion represents a usable approach for the interpretation of data obtained from subsize impact specimens and should now suffice to define an interim specification for the subsize Charpy test. The other toughness parameter results, plus hardness and tensile properties, are presented and discussed.

KEY WORDS: fracture properties, toughness, impact, armor plate, mechanical properties, hardness, high strength steels, test temperature

An examination of current armor specifications[1,2]² indicated a need for additional toughness parameter data for monolithic and dual-hardness steel armor. A minimum Charpy V-notch impact value of 10 ft·lb at -40°C for the transverse direction (WR orientation) is stipulated in Ref 1; however, sufficient toughness data have not been generated to verify this as an acceptable toughness level. Also, due to a limitation in plate thickness, the standard size Charpy bar

¹ Metallurgist, Army Materials and Mechanics Research Center, Watertown, Mass. 02172.

² The italic numbers in brackets refer to the list of references appended to this paper.

cannot always be used. In addition, it may be possible that other toughness parameters such as precracked Charpy toughness (W/A) and fracture toughness (K_{Ic}) can be utilized to further characterize armor materials.

This program pertains to the generation of Charpy impact, precracked Charpy toughness, fracture toughness, and hardness and tensile data for monolithic high-hardness steel armor.³ The work has been coordinated with in-house fatigue-crack propagation and stress corrosion cracking programs on the same materials. An earlier investigation[3] has provided a background as to the mechanical testing of armor materials, and the current program should act as a beginning study which should result in the ventual incorporation of more meaningful toughness data into existing armor specifications.

Materials

The high-hardness armor steels, all of which are representative of air-melting practice, were supplied by three producers in thicknesses ranging from 0.125 to 0.750 in. The sources are designated by a letter code, and the chemical composition for each producer's material is shown in Table 1. Typical microstructures of the thickest plate from each producer, consisting of tempered martensite, are shown in Fig. 1.

Test Procedure

Charpy transition curves were established on 26 plates of high-hardness steel. In addition to the conventional transverse orientation (WR), a limited number of transition curves were obtained using specimens from a longitudinal orientation (RW). Precracked Charpy toughness and fracture toughness data were generated from selected plates utilizing specimens in WR and RW orientations.

Standard size Charpy V-notch specimens were used for plates having a thickness of 0.450 in. or greater, and subsize specimens were used for obtaining toughness data from the plates less than 0.450 in. in thickness. The slow-bend type fracture toughness specimen was utilized for obtaining fracture toughness data. A ManLabs machine, Model FCM-300B, was used for fatigue cracking the impact specimens from which the W/A results were obtained. All impact specimens (transition and precracked type) were broken in a 217 ft·lb Mouton machine. The fracture toughness specimens were fatigue cracked in a Sonntag SF-1-U machine and tested in accordance with the Tentative Method of Test for Plane-Strain Fracture Toughness of Metallic Materials (E 399-70T) of the ASTM Committee E-24 on Fracture Testing of Metals. The fatigue crack for both types of specimens was extended approximately 0.050 in.

³ This program was conducted in accordance with requirements consistent with AR 37-100-72, "2122020 Operation and Maintenance, Army," Section VIII, Code 728012.12000 (Production Engineering for Stock Fund Items), 12 Nov. 1970.

TABLE 1—Chemical composition, weight percent.

Source	Thickness, in.	C	Mn	P	S	Si	Cr	Mo	Zr	B	Cu	Ni
A	0.125	0.29	0.86	0.017	0.016	0.60	0.62	0.20	0.07	0.0010		
	0.250	0.27	0.86	0.015	0.020	0.53	0.65	0.19	0.13	0.0009		
	0.312	0.31	0.82	0.014	0.020	0.55	0.63	0.19	0.09	0.0011		
	0.400	0.29	0.80	0.012	0.025	0.50	0.62	0.22	0.08	0.0011		
	0.450	0.28	0.85	0.015	0.016	0.63	0.61	0.21	0.14	0.0006		
	0.500	0.28	0.94	0.010	0.025	0.66	0.59	0.21	0.14	0.0014		
	0.625	0.27	0.85	0.009	0.017	0.54	0.60	0.21	0.09	0.0009		
	0.750	0.28	0.91	0.015	0.015	0.63	0.63	0.20	0.14	0.0010		
B	0.125 to including 0.500	0.30	1.20	0.012	0.020	0.24		0.21			0.23	
	0.550 to including 0.700	0.30	1.55	0.012	0.020	0.20		0.14			0.26	
C	0.125 to 0.700	0.29	0.83	0.007	0.010	0.60	0.49	0.41	0.16			1.05

NOTE—Chemical analyses provided by producer.



FIG. 1—Typical microstructure of high-hardness armor steels. Etchant: Picral ($\times 1000$).

Results and Discussion

Hardness

Military Specification AMMRC PD-100[1] states the acceptable Brinell hardness range for armor steels is from 477 to 534. Based upon the SAE-ASM-ASTM hardness conversion, this would correspond to a Rockwell C range of approximately 49.5 to 54.5.

Surface hardness in Rockwell C units is presented as a function of plate thickness for all investigated materials in Table 2. Of the 26 plates investigated, there were only two plates (0.625 and 0.750 of Material A) where the hardness was outside the converted harness acceptability range. Hardness data supplied by the producer showed a minimum of 495 BHN for these two thicknesses. As noted in Table 2, all plate thicknesses for Material C came from the same heat.

Transition Curves

Impact transition curves are shown in Fig. 2 for plate thicknesses of 0.450 in. and greater, using the standard size Charpy V-notch specimen. Specimen blanks were machined from a plate surface position and ground approximately 0.025 in. prior to finish machining. The most significant aspect of these results is that

TABLE 2—Surface hardness as a function of plate thickness for high-hardness armor steels.

Thickness in.	Specimen Identification ^a	SH	Specimen Identification ^b	SH	Specimen Identification ^c	SH
0.125	A1	52.9	B1	50.2		
0.187					CA	53.5
0.250	A3	50.9	B3	51.4	CB	51.3
0.300			B5	52.7		
0.312	A5	51.5			CC	50.6
0.350			B7	50.9		
0.375					CD	50.5
0.400	A7	50.7	B9	49.8		
0.450	A9	50.3	B11	51.2		
0.500	A11	50.0	B13	51.7	CE	50.3
0.550			B15	52.0		
0.600			B17	51.1		
0.625	A13	48.7			CF	50.1
0.650			B19	49.5		
0.700			B21	49.7	CG	49.8
0.750	A15	49.0				

NOTE—SH = surface hardness, Rockwell C.

^a All thickness plates from different heats.

^b Two heats—0.125 to 0.500 in.; 0.500 to 0.700 in.

^c All thickness plates from same heat.

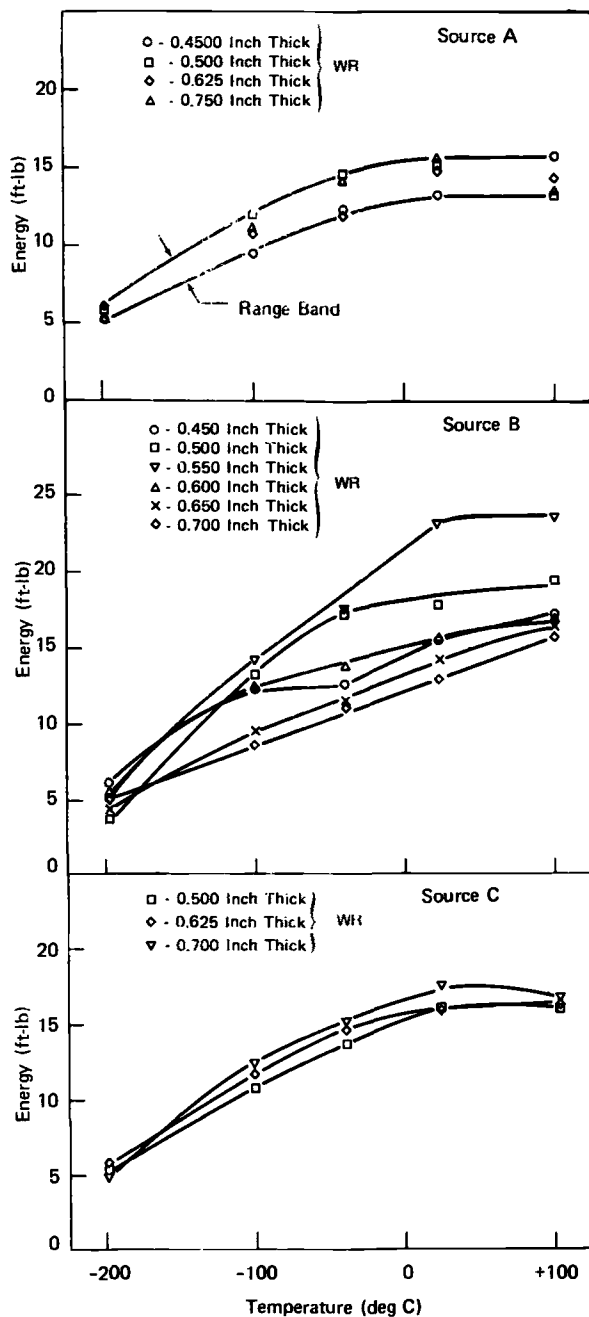


FIG. 2—Transition curves as a function of plate thickness using the standard size impact specimen.

plates within this thickness range from all three producers surpassed the *WR* toughness criterion of 10 ft·lb at -40°C . The material from producer B exhibited the greatest toughness variation as a function of plate thickness.

Processing history and chemical composition are the likely factors in the degree of energy variation. For example, the energy variation at -40°C for B was 11.2 to 17.1 ft·lb, for A 12.1 to 14.7 ft·lb, and for C 14.9 to 15.5 ft·lb. In general, this trend existed over the entire investigated temperature range of -196 to $+100^{\circ}\text{C}$.

Fibrosity values are also plotted normally as part of energy transition curves. In these high-hardness armor steels it was impossible to obtain an accurate assessment of fibrosity, and only approximate values were supplied for many temperatures. Thus, the transition plots are restricted to energy data.

Transition Curves as a Function of Orientation

Figure 3 contains a plot of transition curves for the three materials with specimens in *RW* and *WR* orientations. Standard size impact specimens were machined from 0.500-in.-thick plates from each of the three producers and tested. An examination of the plots clearly shows that the *RW* orientations result in substantially higher energy values and greatly exceed the minimum value of 12 ft·lb at -40°C as stated in the specification[1]. Specific energy values for the *RW* orientation for specimens tested at -40°C ranged from 15.5 ft·lb for Material C to 25.2 ft·lb for Material B.

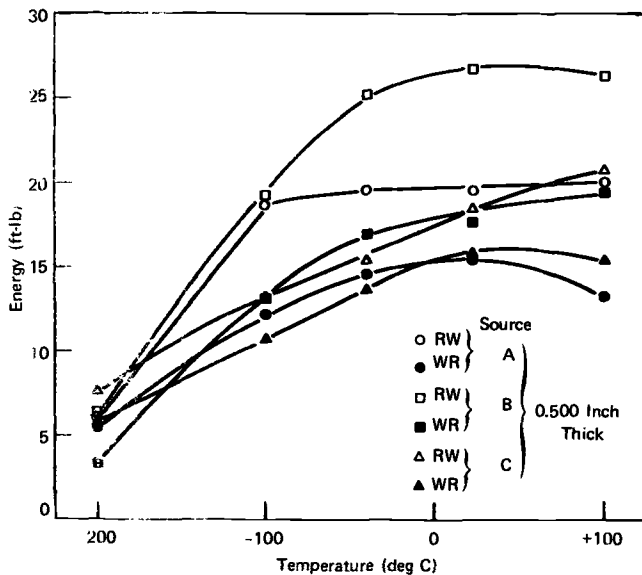
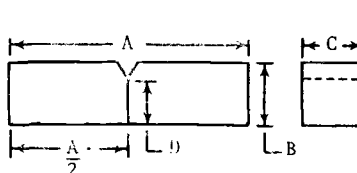


FIG. 3—Transition curves as a function of orientation using the standard size impact specimen.

Subsize Charpy Impact Specimen Relationship

A number of investigators, including Curl[4] and Fahey and Kula[5], have attempted to correlate the energy of subsize with standard Charpy impact specimens. These previous results have shown that the energy to fracture a reduced width, standard depth specimen is proportional to the specimen width at zero and 100 percent fibrosity. The correlation also appears to be valid in the transition temperature range, provided comparisons are made at the same fibrosity (not test temperature). The transition temperature decreases for specimens having a width of less than 0.197 in.; thus, the data for the 0.098 in. spacing may be erroneous[5].

In this investigation it was impossible to obtain an accurate assessment of the fibrosity values; therefore, the subsize data were analyzed solely on an equivalent energy-area basis. Tables 3 and 4 contain actual and converted energy values for all plate thicknesses tested at -40°C and as a function of test temperature. Charpy V-notch specimens, Types C1-2 and C1-5, were utilized with the variable in the area factor being the width dimension as indicated below.



Type	A	B	C	D	Area Factor
C1 2	2.165	0.394	0.394	0.315	1.0
C1 3	2.165	0.394	0.295	0.315	1.34
C1 4	2.165	0.394	0.197	0.315	2.0
C1 5	2.165	0.394	0.098	0.315	4.0

Results of the converted energy values are very encouraging. For example, converted values from 12 of the 13 plates having a thickness of 0.400 in. or less fell within a scatter band of ± 2.1 ft·lb and met the specification criterion of 10 ft·lb for the *WR* orientation. Based upon these results and previous studies[5,6], the equivalent energy-area criterion should now suffice to define an interim subsize Charpy test for PD-100[1].

Since the data in Tables 3 and 4 are representative of only one test, a statistical survey, using approximately 25 specimens per plate thickness, appears advisable. If the results from such a program are reflective of those obtained in this program, the equivalent energy-area criterion should be considered for permanent incorporation into steel armor specifications.

Precracked Charpy Toughness (W/A)

Precracked Charpy toughness data as a function of temperature and orientation utilizing the standard size impact specimen are plotted in Fig. 4. This

TABLE 3—Equivalent energy of standard and subsize impact specimens based on area factor at -40°C .

Specimen <i>WR</i> Orientation				Energy, ft·lb	
No.	Type	Width, in.	Area Factor	Actual	Converted
A1	Cl 5	0.098	4.0	3.0	12.0
A3	4	0.197	2.0	6.4	12.8
A5	3	0.295	1.34	8.1	10.9
A7	3	0.295	1.34	8.1	10.9
A9	2	0.394	1.0	12.4	12.4
A11	2	0.394	1.0	14.7	14.7
A13	2	0.394	1.0	12.1	12.1
A15	2	0.394	1.0	14.2	14.2
CA	5	0.098	4.0	3.4	13.6
CB	5	0.197	2.0	5.4	10.8
CC	3	0.295	1.34	9.7	13.0
CD	3	0.295	1.34	9.2	12.3
CE	2	0.394	1.0	13.9	13.9
CF	2	0.394	1.0	14.9	14.9
CG	2	0.394	1.0	15.2	15.2
B1	5	0.098	4.0	2.1	8.4
B3	4	0.197	2.0	6.2	12.4
B5	4	0.197	2.0	6.0	12.0
B7	3	0.295	1.34	8.4	11.3
B9	3	0.295	1.34	11.5	15.4
B11	2	0.394	1.0	12.7	12.7
B13	2	0.394	1.0	17.0	17.0
B15	2	0.394	1.0	17.1	17.1
B17	2	0.394	1.0	13.9	13.9
B19	2	0.394	1.0	11.5	11.5
B21	2	0.394	1.0	11.2	11.2

is also an energy-area criterion. The specimen is precracked approximately 0.050 in. and then broken in an impact machine. The breaking energy is then divided by the specimen areas beneath the fatigue crack and the results expressed as W/A in units of inch pounds per square inch.

As indicated, the data in Figs. 3 and 4 came from the same thickness of plate, and it is evident that a similar trend exists at most of the testing temperatures for both the impact and W/A tests. Based upon a larger data differential, the W/A method appears to offer a more discriminatory acceptance criterion for high-hardness steel armor. Unfortunately, because of time and possible difficulties encountered in fatigue cracking of the W/A type specimen, the practicality of the test when compared to the impact test is questioned. It should also be noted that this is a more discriminatory test than plane-strain fracture toughness testing, Table 5.

64 FATIGUE AND FRACTURE TOUGHNESS—CRYOGENIC BEHAVIOR

TABLE 4—Equivalent energy of various thickness impact specimens as a function of testing temperature.

Temperature, °C	Material Designation—WR Orientation										
	A1	A3	A5	A7	A9	A11	A13	A15			
−196	4.4	5.6	4.6	4.0	5.2	5.7	6.0	5.4			
−100	7.2	12.0	10.0	9.4	9.5	12.1	10.9	11.2			
−40	12.0	12.8	10.8	10.8	12.4	14.7	12.1	14.2			
+22	12.0	15.0	10.8	11.9	13.3	15.5	14.9	15.5			
+100	16.8	16.1	11.5	11.5	15.9	13.3	14.5	13.6			
	CA	CB	CC	CD	CE	CF	CG				
−196	4.4	4.2	5.9	5.6	5.7	6.2	5.2				
−100	10.0	9.4	8.6	10.3	10.9	11.8	12.7				
−40	13.6	10.8	13.0	12.3	13.9	14.9	15.2				
+22	16.0	12.0	13.0	15.0	15.9	15.8	17.1				
+100	17.6	14.0	14.6	16.6	15.5	16.2	16.5				
	B1	B3	B5	B7	B9	B11	B14	B15	B17	B19	B21
−196	4.4	5.6	3.6	4.0	5.8	6.0	3.4	5.0	5.4	4.4	5.0
−100	6.0	11.4	8.8	11.2	13.4	12.1	13.3	14.2	12.4	9.5	8.9
−40	8.4	12.4	12.0	11.2	15.3	12.7	17.0	17.1	13.9	11.5	11.2
+22	9.2	13.4	12.8	12.2	18.1	15.5	17.8	23.3	15.8	14.2	13.0
+100	10.0	14.6	14.0	14.5	19.3	17.1	19.4	23.6	17.1	16.2	15.8

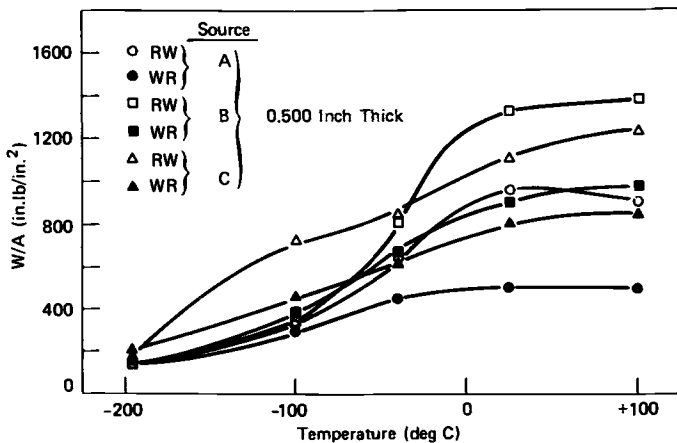


FIG. 4—Precracked Charpy toughness as a function of orientation using the standard size impact specimen.

TABLE 5—Plane-strain fracture toughness of high-hardness armor steels.

Material and Orientation	Specimen Thickness B , in.	Specimen Width W , in.	Crack Depth a , in.	Fracture Toughness, K_{Ic} ksi $\sqrt{\text{in.}}$
A11-WR	0.495	1.000	0.513	78.5
	0.500	1.000	0.512	78.9
	0.496	1.000	0.520	76.1
				77.8 avg
A11-RW	0.496	1.001	0.551	87.5
	0.495	1.001	0.501	88.8
	0.508	1.001	0.543	89.9
				88.7 avg
B13-WR	0.501	1.000	0.550	98.2 ^a
	0.501	1.000	0.524	90.0
	0.501	1.001	0.456	93.9 ^a
				94.0 avg
B13-RW	0.501	1.000	0.548	104.9 ^a
	0.501	1.000	0.520	102.1 ^a
	0.501	0.905	0.434	105.1 ^a
				104.0 avg
CE-WR	0.512	1.001	0.524	84.0
	0.512	1.001	0.522	89.3
	0.512	1.001	0.516	73.8
				82.4 avg
CE-RW	0.511	1.001	0.499	96.6 ^a
	0.512	1.001	0.508	98.1 ^a
	0.512	1.001	0.552	94.1 ^a
				96.3 avg

^a Specimen thickness $< 2.5 \left(\frac{K_Q^2}{\sigma_{ys}} \right)$

Specimen length $\equiv 4.4$ in.

Fracture Toughness

Room temperature fracture toughness values were obtained as a function of orientation from 0.500-in. plate of each producer. Specimen dimensions, crack depth, and plane-strain fracture toughness data are presented in Table 5. Results of some tests must be considered invalid because they did not meet the specimen thickness criterion as set forth in ASTM Tentative Method E 399-70 T. Such tests are noted in Table 5, and the data must be expressed as K_Q rather than K_{Ic} . Mechanical property data for the materials are given in Table 6.

Results of the fracture toughness tests (Table 5) show that Material A exhibits the lowest values, and Material B the highest for both the *RW* and *WR*

TABLE 6—*Mechanical properties of high-hardness armor steels.*

Material	Orien- tation	Yield Strength 0.2%, ksi	Tensile Strength, ksi	Elonga- tion, %	Reduction of Area, %
A-11	L	208	262	13.5	49.8
	T	216	253	10.5	39.8
B-13	L	207	255	13.3	51.8
	T	209	256	11.5	45.5
C-E	L	201	231	11.5	47.8
	T	204	241	11.0	44.0

NOTE—Data are average of two tests.

orientations. Respective RW values ranged from 88.7 to 104 $\text{ksi}\sqrt{\text{in.}}$, whereas corresponding WR values ranged from 77.8 to 94.0 $\text{ksi}\sqrt{\text{in.}}$. In general, there was very good consistency for the triplicate tests for each condition, and the values indicate that these materials exhibit fair-to-good fracture toughness.

As previously stated, the fracture toughness portion of the program was coordinated with an in-house stress corrosion cracking investigation. Results to date indicate that K_{ISCC} data for Material B range between 14 and 19 $\text{ksi}\sqrt{\text{in.}}$, and there is little orientation effect[6]. These values indicate a high susceptibility to stress corrosion cracking for this material.

Mostovoy and Ripling[7] have published recently the results of a fracture toughness and stress corrosion cracking susceptibility study of four plates of high-hardness armor steel. Three of the four plates had "bad" histories, that is, they cracked either in room temperature service or storage, whereas the fourth was representative of "good" plate produced by the most recent fabrication procedures. Results of their work indicated that the fracture toughness type test could not distinguish between the good and bad plates, whereas data from the stress corrosion cracking susceptibility test did show large differences between the two qualities of plate.

The materials considered in this investigation should be good in nature. The plates were produced by recent fabrication procedures and cracking was not observed.

Conclusions

1. All plate thicknesses from each producer, with the exception of two which had marginal values, met the hardness criterion as set forth in MIL AMMRC PD-100.

2. All plates from each producer having a thickness of 0.450 in. or greater met the -40°C transverse (WR) toughness criterion of 10 $\text{ft}\cdot\text{lb}$ based upon impact data obtained from the standard size impact specimen. Longitudinal

(*RW*) values obtained from 0.500-in. material from each producer also met the specification requirements of 12 ft·lb at -40°C .

3. Based on an equivalent energy-area criterion for the subsize impact specimens, 12 of the 13 plates having a thickness of 0.400 in. or less met the *WR* toughness specification at -40°F . Thus, these results, plus those from former investigations, should suffice to define an interim subsize Charpy test for high-hardness Armor Steels.

4. The precracked Charpy test is more discriminatory than the fracture toughness test and possibly more so than the Charpy impact test. However, because of fatigue cracking, it is more time consuming than the Charpy test.

Acknowledgment

The author wishes to express his appreciation to T. S. DeSisto for his valuable contributions to this program.

References

- [1] *Steel Armor Plate, Wrought, High-Hardness*, Army Materials and Mechanics Research Center, AMMRC PD-100, 14 Nov. 1968.
- [2] *Steel Armor Plate, Roll-Bonded, and Dual-Hardness*. MIL-S-46099A, 15 Nov. 1966.
- [3] Hickey, C. F., Jr., "Mechanical Properties and Bonding Efficiency of Steel Composites," Army Materials and Mechanics Research Center, AMRA TR67-12, May 1967; also *Journal of Materials*, Vol. 3, No. 1, March 1968, p. 3.
- [4] Curll, C. H., "Subsize Charpy Correlation with Standard Specimens," Army Materials and Mechanics Research Center, MS-28, May 1961; also *Materials Research and Standards*, Vol. 1, No. 2, Feb. 1961, p. 91.
- [5] Fahey, N. H. and Kula, E. B. in *Proceedings*, American Society for Testing and Materials, Vol. 63, 1963, p. 1147.
- [6] Dawson, D., "Development of a Stress Corrosion Cracking Test for Armor Alloys," Army Materials and Mechanics Research Center, AMMRC PTR 72-1, June 1972.
- [7] Mostovoy, S. and Ripling, E. J. "The Feasibility of Using Fracture Mechanics for Evaluating High-Hardness Armor Steel," U.S. Army Tank-Automotive Command, TACOM Technical Report No. 10580, June 1969.

R. Chait,¹ C. F. Hickey, Jr.,¹ and C. H. Curll¹

Fatigue and Fracture Characteristics of High-Hardness, Laminar Composite Steel

REFERENCE: Chait, R., Hickey, C. F., Jr., and Curll, C. H., "Fatigue and Fracture Characteristics of High-Hardness, Laminar Composite Steel," *Fatigue and Fracture Toughness—Cryogenic Behavior, ASTM STP 556*, American Society for Testing and Materials, 1974, pp. 68–92.

ABSTRACT: The purpose of the present paper is to characterize static and dynamic mechanical properties of high-hardness laminar composite steel. Tensile, compressive, and shear properties were obtained. Fatigue properties were also investigated including the effect of minimum:maximum stress (*R*) ratio, humidity, and surface condition. Improving the as-received surface led to increased values of the fatigue limit. Fatigue resistance was lowered markedly by humidity. For a given value of maximum stress increasing the *R* ratio increased the number of cycles to failure. Orientation had a pronounced effect on the toughness of cracked and uncracked Charpy specimens, that is, *RW* orientation exhibited greater toughness than did *WR*. There is some evidence to indicate that constraint has caused the hard-soft interfacial bond to delaminate. Lastly, examination of the fracture surfaces of the tensile, fatigue, and Charpy specimens revealed that in most instances crack initiation phase of fracture takes place on the hard side of the composite.

KEY WORDS: fracture properties, laminates, composite materials, steels, toughness, compressive strength, tensile properties, fatigue behavior, environmental effects, temperature effects

High-hardness laminar composite steel consists of a high-carbon frontal portion metallurgically bonded to a softer, lower carbon steel backup portion. The resulting laminar composite offers excellent resistance to ballistic penetration[1].² In addition, such material could be used possibly in load-carrying capacity[2], thus satisfying the desire to make more efficient use of existing armor materials. From a design viewpoint, this requires full characterization of the material. Since the thought of using laminar composite steel in a structural

¹ Chief, Materials Properties Branch, metallurgist, and engineer, respectively, Army Materials and Mechanics Research Center, Watertown, Mass. 02172.

² The italic numbers in brackets refer to the list of references appended to this paper.

capacity is relatively new, there is need for pertinent mechanical property data. To date there have been some fabrication studies which have focused on cutting, forming, and finishing[3,4]. Hickey[5], in an earlier study, investigated hard-soft side interfacial integrity resulting from ballistic damage, and correlated the results with tensile properties. In follow-on efforts, Anctil and Kula[6] studied fatigue crack propagation behavior. In both of these studies, the differences in behavior between the hard and soft portion became apparent.

In the present paper, additional static and dynamic mechanical properties are presented. Investigated are the response to uniaxial tension and compression loading. The shear strength of the bond formed between the hard and soft side is determined. *S-N* (maximum stress—number of cycles to failure) curves were obtained for several minimum:maximum stress ratios. The influence of environment and surface condition on fatigue behavior was also studied. Toughness is investigated as a function of orientation and test temperature using Charpy specimens in two conditions—standard notched and fatigue cracked. Lastly, through-the-thickness hardness traverses were taken to provide information on surface decarburization and the extent of the transition zone between the hard and soft portion of the composite.

Additional studies have been conducted which have focused on the behavior of ballistically damaged material[7-9]. It is the intent of this paper to highlight the mechanical property behavior of undamaged material rather than the ballistic capabilities or response, the latter being covered in another publication[7,9]. Properties of ballistically damaged material will only be mentioned so that appropriate comparison can be made to initial undamaged properties.

Materials and Test Procedure

Material

As noted earlier, the laminar composite steel consists of a hard frontal portion metallurgically bonded to a softer, approximately equal thickness, backup portion by means of a roll bonding process that takes place at 1150 to 1260°C. The material is later oil-quenched from about 815°C and tempered at 120 to 167°C. The desired hardness levels on the frontal and backup portion are HRC 60 and 50, respectively. The difference in hardness stems mainly from a higher carbon level in the frontal portion than in the backup portion. Carbon contents in the hard layer usually range from 0.52 to 0.62 percent carbon, while the level in the soft layer is about one half as much. It should be noted that additional alloying elements (nickel, chromium, molybdenum) are present, usually in about the same amounts on both sides. The amounts of the alloying elements depend on the producer involved and the melting procedure that is employed.

In the present study material processed by conventional air melting (AM) and vacuum induction melting (VIM) techniques are investigated. Both are nominally

0.220 in. thick and were composed of hard and soft layers that were approximately of equal thickness. The composition of each layer for each material together with an average hardness is given in Table I. It should be noted that the hardness readings are representative of a ground surface to eliminate decarburization. To determine the extent of decarburization as well as the width of the transition zone between the hard and soft side, hardness readings were taken across the section of several specimens with a Knoop hardness indenter using a 1-kg load. These readings were then converted to Rockwell hardness, C scale, using appropriate conversion tables.

Material for the present study was supplied from the producer in plate form from which the test specimens outlined next were machined. Preliminary information from the producer indicated that the material was cross rolled during fabrication and that the long direction of the plate was the primary rolling direction. Unless otherwise noted, specimens were taken in the direction of primary rolling. As will be discussed further, toughness tests substantiated the information from the producer. To preclude edge cracking which can result from improper cutting procedures[10], an electrical discharge machining (EDM) procedure was used. EDM techniques were also used to machine pin holes in the tension specimens as well as in some fatigue specimens. Additional details of each phase of the testing are given next.

Tension and Compression Tests

Pin-loaded tension specimens having an 0.5-in.-wide, 1.0-in.-long gage section were utilized. These specimens were tested in a 120 000-lb capacity Baldwin Universal testing machine. Strain gages were mounted on both the hard and soft side, and readings averaged to provide a more accurate indication of the 0.2 percent offset yield strength. In addition to the 0.2 percent yield strength, tensile strength, reduction of area, and elongation were measured. Also, notch strength values (maximum load divided by original cross-sectional area) were obtained on specimens having $K_t = 2.0$. Compressive yield strengths were

TABLE 1—Chemistry and hardness.

Material	C	Mn	P	S	Si	Ni	Cr	Mo	Al	Average Hardness
<i>Air melt:</i>										
Hard side	0.62	0.47	0.008	0.008	0.32	3.30	0.07	0.40	0.02	HRC 61
Soft side	0.28	0.48	0.008	0.010	0.29	3.33	0.11	0.42	0.03	HRC 50
<i>Vacuum induction melt:</i>										
Hard side	0.53	0.87	0.006	0.005	0.27	1.12	0.76	0.50	0.05	HRC 58
Soft side	0.28	0.87	0.006	0.007	0.27	1.11	0.75	0.52	0.03	HRC 48

obtained with a specially designed test fixture to ensure against buckling during compressive deformation. Additional details of the fixture are given in Ref 11.

S-N and Corrosion Fatigue Behavior

Axially loaded fatigue tests were conducted on a Satec SF-10U fatigue machine to determine the number of cycles to failure for various applied stress levels. To obtain higher load levels, a 5:1 multiplying fixture was employed. The specimen dimensions for this test were approximately the same as the tension specimen noted previously. With this apparatus it was possible to obtain positive R ratios (minimum:maximum stress ratio) of $R = 0.1$ and 0.5 to evaluate AM material in the as-received surface condition. For comparison to as-received material, $R = 0.1$ was used to evaluate a machine ground surface condition. To provide an additional R ratio for evaluation, an SF-1U Satec fatigue machine was used to study behavior under fully reversed loading ($R = -1.0$) for both AM and VIM material in the as-received and machine ground surface condition. In addition, corrosion fatigue behavior was investigated ($R = -1.0$) for both AM and VIM material by testing in a chamber containing a 100 percent humidity environment.

Toughness Variation with Temperature and Orientation

VIM material was used to establish the effect of temperature on the toughness. Subsize Charpy V-notch impact specimens of standard notch depth (0.079 in.) and geometry having a thickness equal to the thickness of the plate were tested over a temperature range of -196 to $+175^{\circ}\text{C}$ in both the WR and RW orientation. In this instance R is the primary rolling direction. A 217-ft·lb capacity Mouton impact machine was used for these tests. A more detailed investigation for the fracture toughness characterization of the AM material is currently underway and will be discussed in a future publication.

Precracked Charpy bars of the foregoing dimensions were utilized to provide an additional means of examining toughness variation with temperature and orientation. Here, the fracture energy is divided by the area beneath the fatigue crack and the result expressed as W/A in units of inch pounds per square inch. The specimens were precracked approximately 0.050 in. in a ManLabs machine (Model FCM-300B) and broken in a Mouton impact machine noted previously. An improved precracking procedure [12] was utilized which involved initiating the crack with a compressive load and extending it in tension to obtain a more uniform crack front.

Bond Shear Strength

Shear strength tests of the bond between the hard and soft side were conducted on AM material utilizing a $\frac{1}{2}$ in. diameter disk having the nominal 0.220 in. thickness. The disks were placed in a shear fixture which secured the

specimen such that shear would occur at the center of the transition zone between the hard and soft side as determined by the hardness traverse. The fixture was used in conjunction with a 120 000-lb-capacity Baldwin Universal testing machine to conduct the test. Ultimate shear strength based on maximum load was determined. In addition, it was possible to obtain approximate yield strength in shear by recording load as a function of crosshead displacement and noting the first indication of a deviation from linearity.

Results and Discussion

Chemistry, Microstructure, and Hardness

The chemistry corresponding to the hard and soft side is shown in Table 1. Ladle analyses supplied by the producer agreed well with these compositions. Note that the major difference between the hard and soft side lies in the carbon content. The microstructures, consisting primarily of tempered martensite, are shown in Fig. 1. Earlier it was noted that the target hardness levels of the hard and soft side were HRC 60 and 50, respectively. Preliminary hardness check readings of incoming plate material failed to meet the target hardness levels unless a small surface layer was removed by grinding. The reason is a decarburized surface layer that is revealed by the microhardness tranverse across the section shown in Fig. 2. The existence of the decarburized layer is shown on both the hard and soft side and extends about 0.010 to 0.015 in. from the surface. The reading in the decarburized region can be as much as 5 HRC points lower than target hardness levels.

The extent of the transition region is also revealed by the microhardness traverse shown in Fig. 2. The zone, approximately 0.045 in. wide, is representative of the type of gradual transition that can be expected from a metallurgical bond formed by diffusion. In the diffusion or transition region between the hard and soft side the hardness level undergoes a change of approximately 10 HRC points.

Tensile, Compressive, and Shear Properties

Room temperature tensile properties for both AM and VIM are shown in Table 2. It is interesting to note that depending on projectile velocity and applied load at impact, residual strength values obtained from ballistically damaged specimens are between 10 to 30 percent of the ultimate tensile strengths shown in Table 2. Primarily due to a higher percent carbon, the AM material exhibits a higher yield strength than the VIM material. The yield strength values for both materials are lower than expected probably due to retained austenite[5]. Note that the increased ductility of VIM materials results in a higher maximum load and, hence, an increased value of the ultimate tensile strength. The same factor probably accounts for the superior notch tensile

TABLE 2—Room temperature tensile, compressive and shear properties.

Test	Material	Yield Strength, ^a ksi	Ultimate Strength, ksi	Elongation, %	Reduction in Area, %
Tensile					
Smooth	air melt	197	261	1.0	3.0
	vacuum induction melt	184	285	5.0	7.0
Notch ^b	air melt	...	242
	vacuum induction melt	...	275
Compressive	air melt	239
	vacuum induction melt	189
Shear ^c	air melt	113	175

^a All yield strength values are 0.2 percent offset except in shear where proportional limit was used.

^b $K_T = 2.0$.

^c At hard-soft side bond.

properties of the VIM material. For comparison to the smooth section tensile properties shown in Table 2, low temperature tests were conducted on AM material at -196°C . Yield strength and ultimate tensile strength values at this temperature were 257 and 333 ksi, respectively. The ductility values were about the same as those obtained at room temperature.

As shown in Table 2, the compressive yield strength values exceed the corresponding values determined in tension. Such behavior has been detailed for high-strength steels[13] and is referred to as the strength differential (SD) effect[14]. It has been suggested that the SD of as-quenched martensite can be interpreted in terms of a solute/dislocation model, where nonlinear elastic strains resulting from the distortion of the lattice around the interstitial atom lead to a greater interstitial-dislocation binding energy in compression than in tension[14]. Precipitation of carbon from solution during the tempering process does not negate its application to tempered martensite microstructures, since the interaction may now involve carbon atmosphere adsorbed at dislocations[14].

Shear properties at the interface between the hard and soft side were determined on five specimens. The average shear yield strength and ultimate shear strength are given in Table 2. The surface of a typical shear fracture is shown in Fig. 3 along with the tensile fracture surface. Note in the latter that the fracture initiates on the hard side. This is consistent with the observation of tensile fracture initiation in an earlier investigation[5]. This behavior probably results from the higher flow stress that exists on the hard side as shown schematically in Fig. 4. For example, by changing the soft:hard side thickness ratio in conjunction with a technique outlined by Papirno[15,16], it was possible to obtain 0.2 percent yield strength values of 187 and 159 ksi on the hard and soft side of the VIM material, respectively.

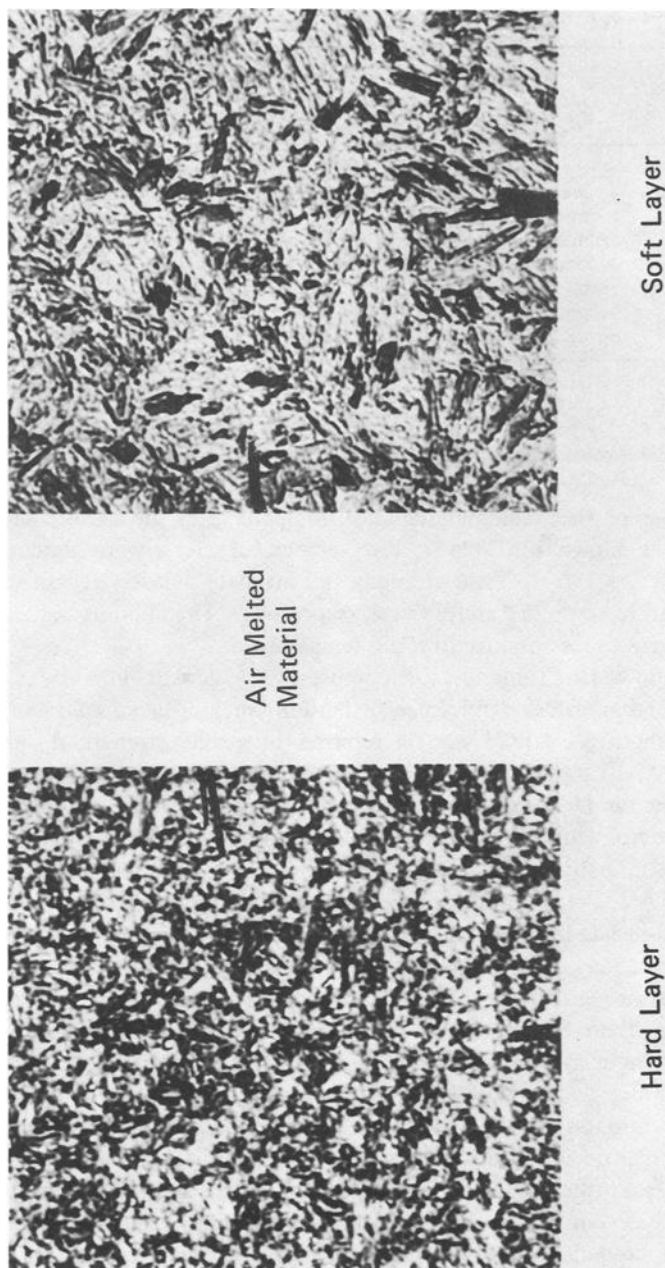




FIG. 1—Microstructure of hard and soft layers for air melted and vacuum induction melted material ($\times 1000$).

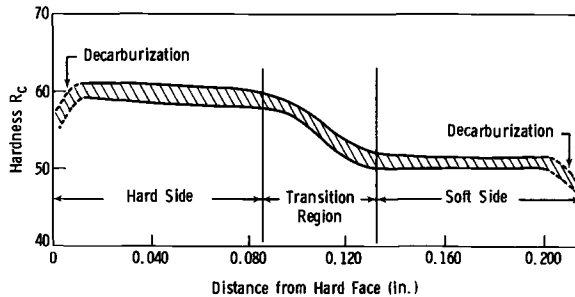


FIG. 2—Microhardness traverse across the section as-received air melted dual hardness steel. HRC readings are converted Knoop hardness numbers.

Fatigue Behavior

S-N Properties—The response of the AM material to cyclic loading is shown in Fig. 5 for $R = 0.1$. The fatigue limit for AM material in the as-received condition is approximately 65 to 70 ksi. For the as-received material, surface condition plays a significant role in the fatigue behavior. As seen in the fractograph, Fig. 6, the surface of the as-received material contains stress raisers which serve as

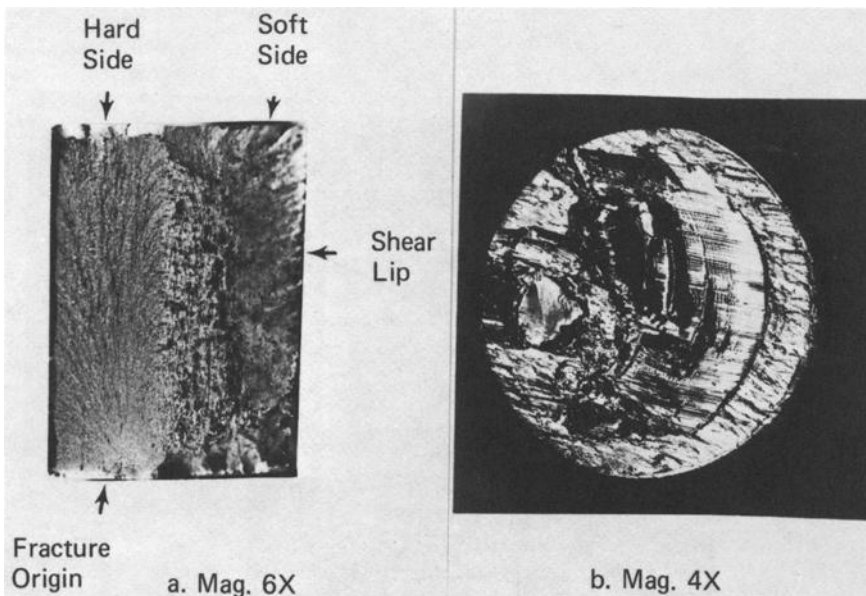


FIG. 3—Fracture surface of (a) tension specimen and (b) shear specimen, both air melted material. Note fracture origin on hard side and presence of shear lip on soft side in (a).

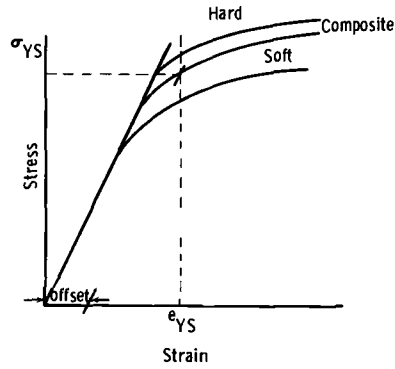


FIG. 4—Schematic diagram showing the contribution of hard and soft side to yield strength of the composite. Note the differing flow stresses of the hard and soft side at a total strain e_{ys} corresponding to 0.2 percent offset yield strength of the composite.

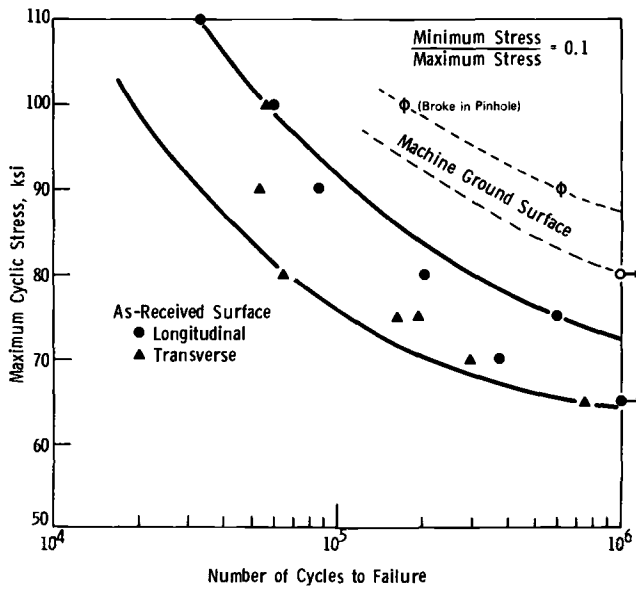


FIG. 5—Fatigue curve for air melted material showing influence of surface condition. Minimum:maximum stress ratio = 0.1.

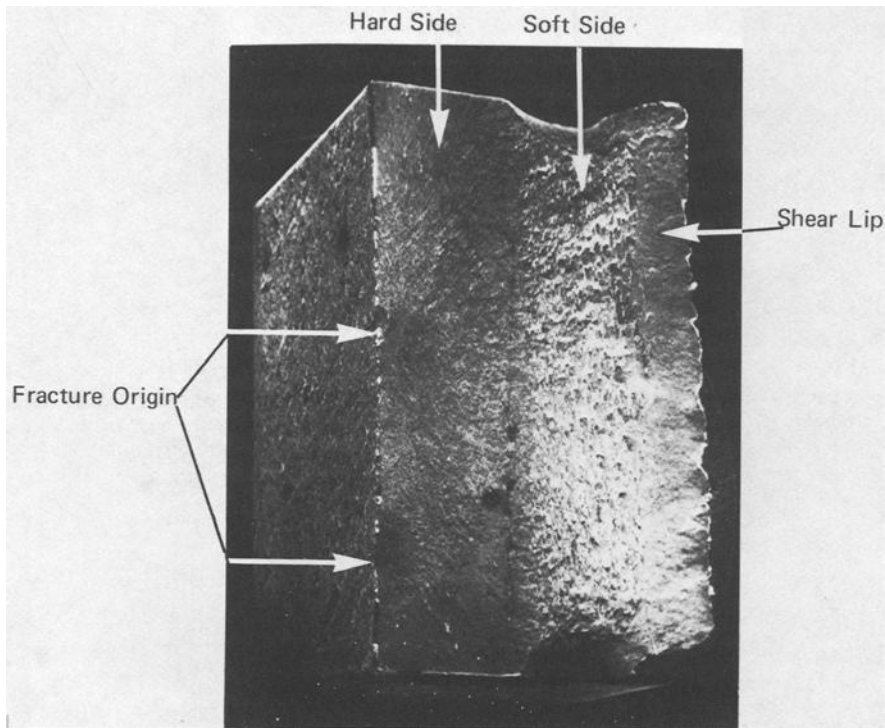


FIG. 6—Scanning electron microscope fractograph of smooth fatigue specimen (air melted material) with as-received surface. Note multiple crack initiation sites on hard side surface ($\times 5.6$).

initiation sites for fatigue failure. Note that the fatigue failure initiated on the hard side, as it did on most of the as-received and machine ground specimens, regardless of the R ratio. Because of the overriding influence of the surface condition and the cross-rolling techniques used during fabrication, orientation does not appear to affect fatigue behavior of the as-received AM material markedly.

Improving the surface finish by machine grinding probably leads to a fatigue limit above 80 ksi. Specimen pin-hole failures precluded a more precise determination. It should be noted that grinding also removed the decarburized layer on both the hard and soft side (Fig. 2), improving the fatigue properties by increasing the strength level of the surface layer. However, this may be offset to some extent by an undesirable residual tensile stress pattern introduced by grinding[17]. Further increase in the fatigue limit can be achieved by combining

metal removal procedures that introduce a more favorable residual stress pattern with a final polishing operation.

Fatigue behavior is also affected by the R ratio. As expected, increasing the R ratio increases the fatigue limit. For $R = 0.5$ the fatigue limit of AM material in the as-received condition is in the vicinity of 80 ksi. Conversely, employing reversed bending, $R = -1.0$, lowers the fatigue limit to approximately 40 ksi for the as-received AM material, as shown in Fig. 7. At $R = -1.0$ machine grinding the as-received surface doubles the fatigue limit to about 80 ksi. Similar behavior for the VIM material is shown in Fig. 8. At $R = -1.0$, the fatigue limit was approximately 30 ksi, slightly lower than for the AM material because of the slightly lower hardness and a rougher as-received surface. Again, machine grinding leads to a significant increase in fatigue limit.

Corrosion Fatigue—An additional factor which influences the fatigue behavior of high-strength steels is a high-humidity environment. Working with heat treated 4140 steel at $R = -1.0$, Lee and Uhlig[18] recently investigated corrosion fatigue for the hardness range HRC 20 to 52. The fatigue limit was

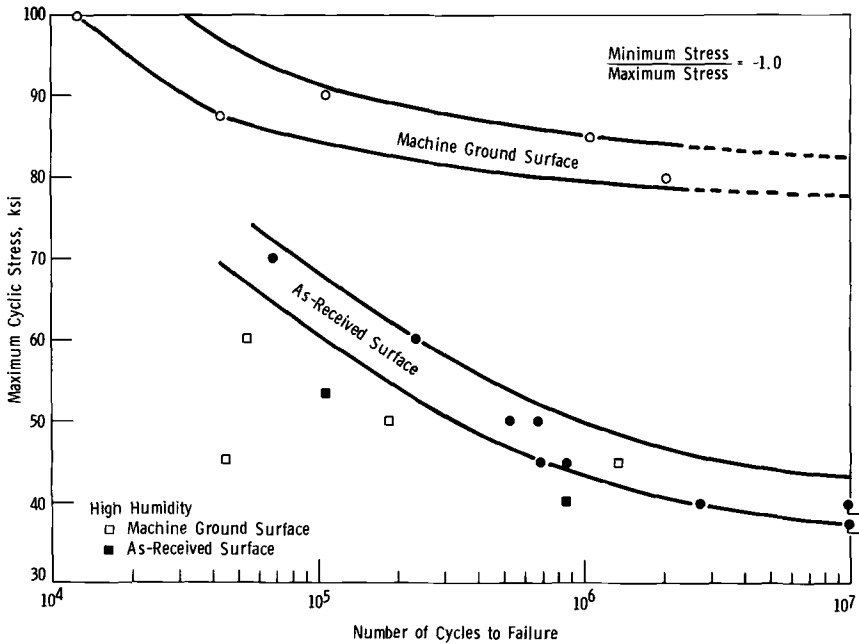


FIG. 7—Fatigue curve for air melted material showing influence of surface condition and environment. Minimum:maximum stress ratio = -1.0 .

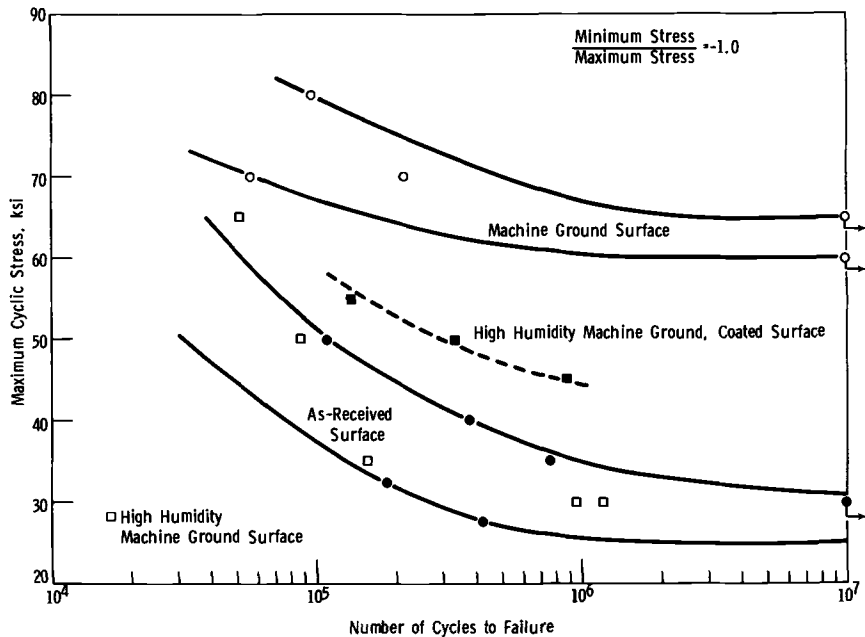


FIG. 8—Fatigue curve for vacuum induction melted material showing influence of surface condition and environment. Minimum:maximum stress ratio = -1.0 .

found to be about one half the ultimate tensile strengths for dry air. In a high-humidity environment the fatigue life is shorter for hardness levels \geq HRC 37. For example, at HRC 52, the fatigue strength for dry air was reduced one third using a high-humidity environment. Therefore it is not surprising to find that a high-humidity environment decreases the fatigue resistance ($R = -1.0$) of both AM and VIM materials by roughly one half. As shown in Fig. 7 for AM material, a high-humidity environment reduces the fatigue resistance of specimens with machine ground surfaces to levels obtained for the as-received material tested under ambient conditions. Similar behavior was obtained for VIM material, Fig. 8. Also shown in Fig. 8 is the effect of coatings on the high-humidity fatigue resistance of machine ground specimens. Specimens coated with a commercially available zinc-chromate primer and top coat of metallic spray paint brought the level of the fatigue curve for machine ground specimens closer to the curve representative of ambient conditions. No additional efforts were made to study more effective coatings; however, their employment should improve the fatigue resistance under high-humidity environments.

Toughness

Transition curves obtained from Charpy impact specimens are shown in Fig. 9 for both the *RW* and *WR* orientation. Higher impact values are noted for the *RW* orientation, that is, a crack propagating in the width direction on the crack plane normal to the direction of primary rolling. For example, at -40°C the energy values for the *RW* and *WR* orientation are 6 and 3.2 ft·lb, respectively. Due to the difference in hardness levels of the hard and soft side, there is a vast

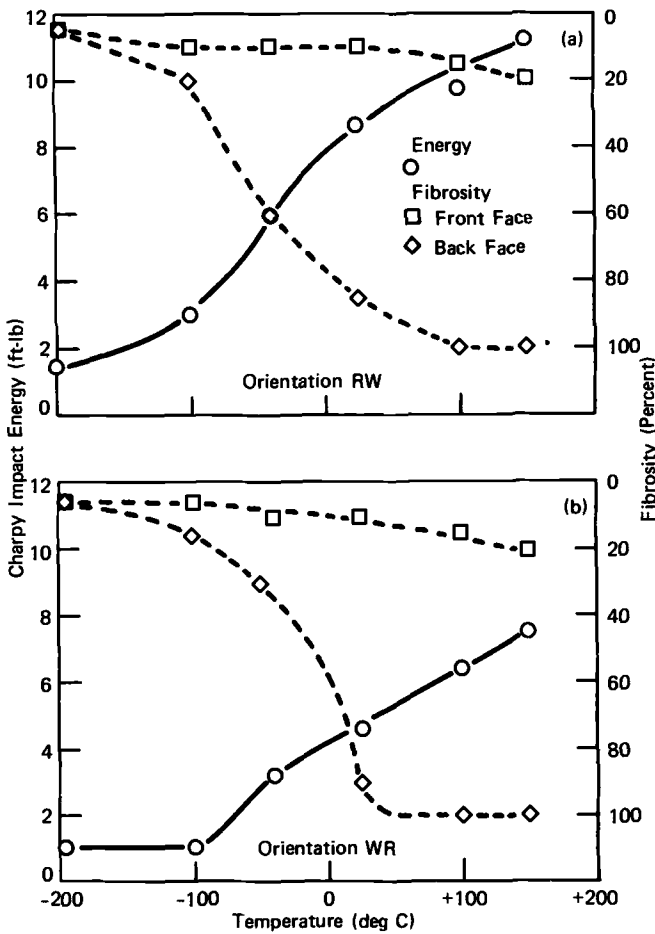


FIG. 9—Charpy impact transition curves for subsize specimens of vacuum induction melted material.

difference in the degree of fibrosity of the two sides. For example, the soft side is 100 percent fibrous at $+100^{\circ}\text{C}$, while the hard side is only 20 percent fibrous at $+175^{\circ}\text{C}$. Note that over the indicated temperature range the hard side changes little in fracture appearance. An approximation to the transition temperature, therefore, should be based on the appearance of the soft side. For example, if a 50 percent fibrous fracture of the soft side is chosen for a criterion, then the approximate transition temperature of the VIM material using subsize specimens (0.220 in. nominal thickness) are -50 and 0°C for the *RW* and *WR* orientation, respectively.

Precracking the Charpy specimens enabled *W/A* determination as a function of temperature and orientation (Fig. 10). It is evident again that *W/A* values show greater toughness in the *RW* direction. Values for the *RW* and *WR* specimens tested at -40°C were 515 and 216 in·lb/in.², respectively. This would appear to indicate that unlike the fatigue behavior of as-received AM material shown in Fig. 5 and discussed previously, Charpy impact specimens with and without precracking reveal the effect of rolling direction. Toughness data on AM material are currently being obtained to substantiate this observation.

Fractographs of the impact specimen (with and without precracking) for the various test temperatures and accompanying orientation are shown in Figs. 11 to 14. For the Charpy specimens that were not precracked (Figs. 11 and 12), fracture initiated on the hard side, propagated across the hard side, and simultaneously in a radial manner, into the soft side. There is also some evidence of interfacial delamination between the hard and soft side, particularly at the elevated test temperatures. Such delamination has been discussed previously [19] and results from the tendency to relax constraint by interfacial failure.

Summary and Conclusions

Important mechanical properties of high-hardness laminar composite steel have been characterized. Static properties that were studied included hardness, tension, compression, and interfacial shear strength. Fatigue data were obtained which showed the effect of surface condition humidity and minimum stress/maximum stress ratio. Utilizing cracked and uncracked Charpy impact bars the effect of temperature and orientation was investigated.

The following conclusions can be drawn from this study:

1. From tension tests, yield strength values of 197 and 184 ksi were obtained for AM and VIM material, respectively. Slightly higher values were noted under compressive loading. The VIM material exhibited better ductility and hence higher ultimate tensile strength and notch strength values than the AM material.
2. Surface grinding to improve the as-received surface and remove the decarburization markedly improved fatigue resistance. The effect of high

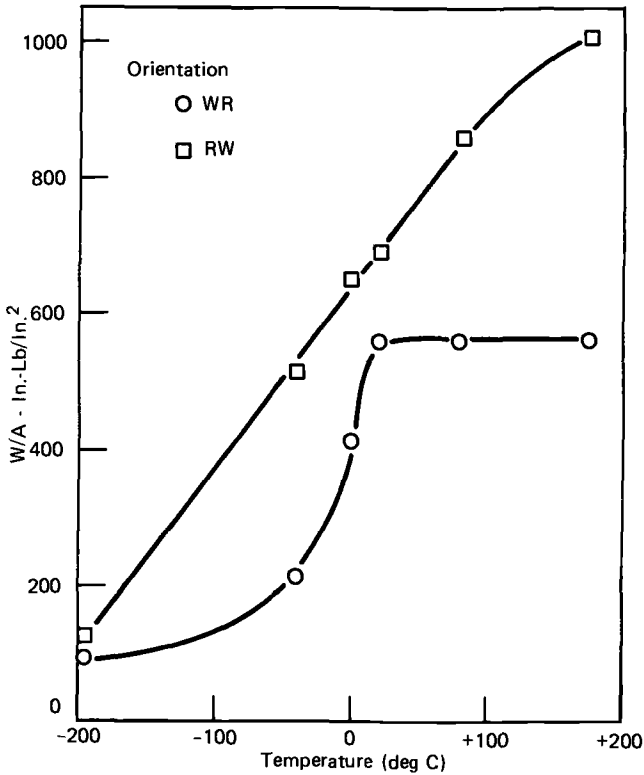
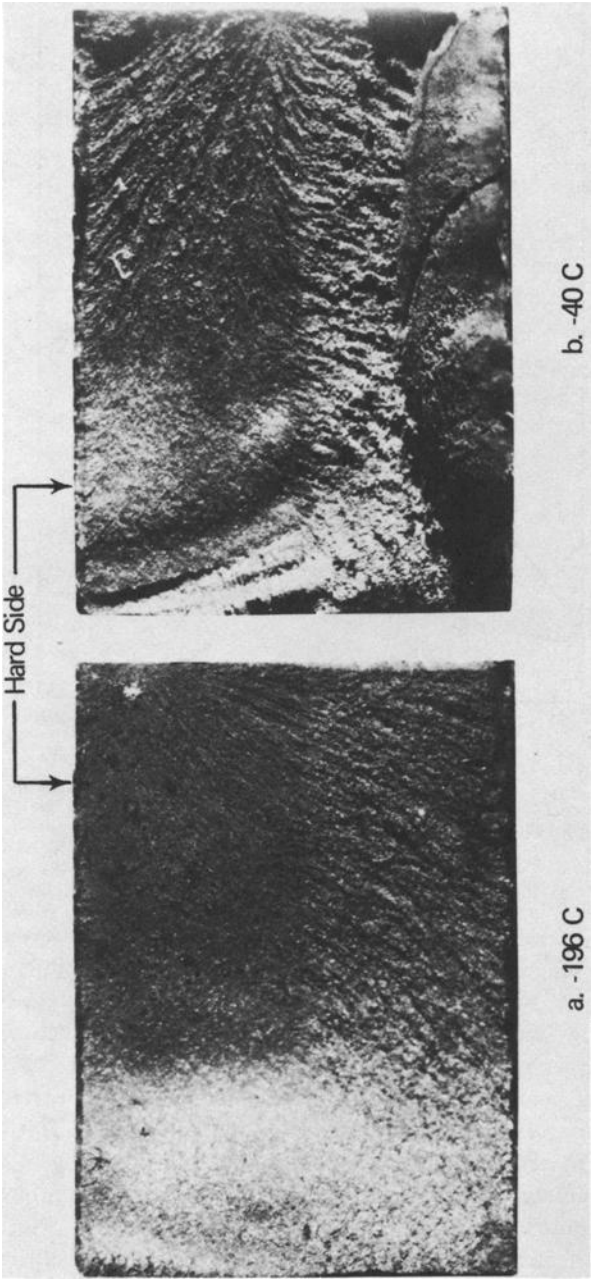


FIG. 10—Preactured Charpy toughness (W/A) as a function of test temperature and orientation for subsize specimens of vacuum induction melted material.

humidity was to offset any improvement in surface condition and lower the number of cycles to failure to levels characteristic of as-received specimens. Increasing the minimum:maximum stress ratio led to higher endurance limits.

3. Based on a 50 percent fibrous fracture criterion, Charpy impact transition curves obtained from subsize specimens (0.220 in nominal thickness) indicate a transition temperature of approximately -50 and 0°C for the *RW* and *WR* orientation, respectively. For a given test temperature the *RW* orientation exhibited a larger energy value than did the *WR* orientation. This behavior was substantiated by testing precracked Charpy bars and obtaining W/A values over the same temperature range. There is evidence of delamination at the hard-soft side interface probably indicating a constraint effect.

4. In most instances of fatigue, tensile, or impact fracture, the crack initiates on the hard side.



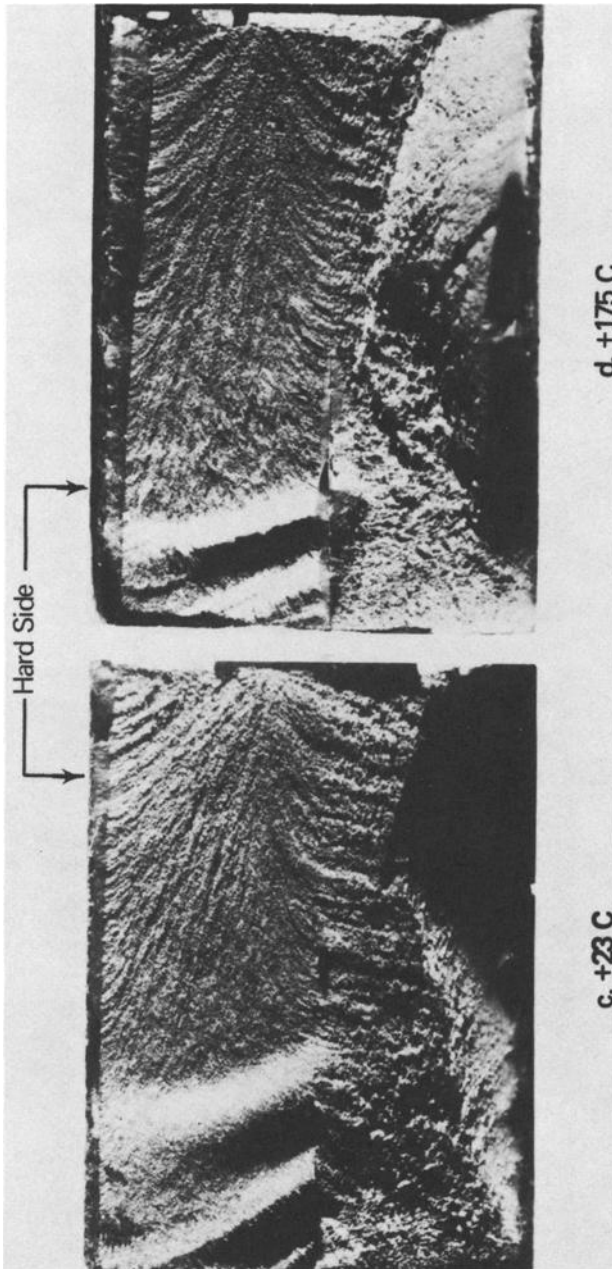
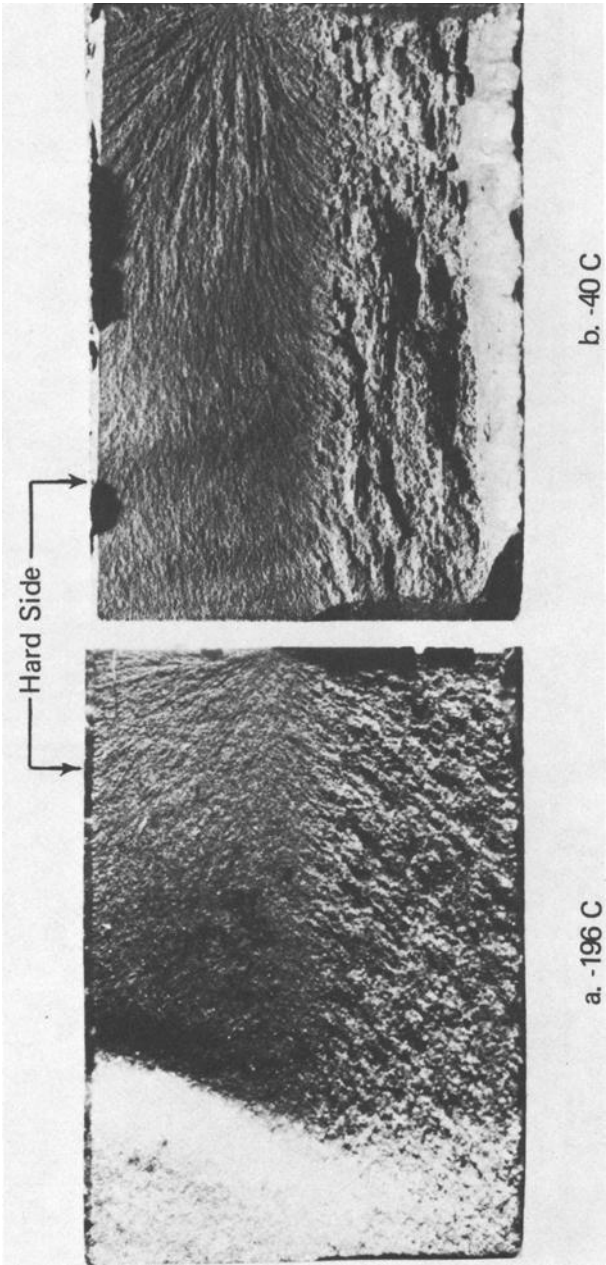


FIG. 11—Fracture surface of Charpy V-notch specimens (vacuum induction melted material) as a function of test temperature for RW orientation (X10).



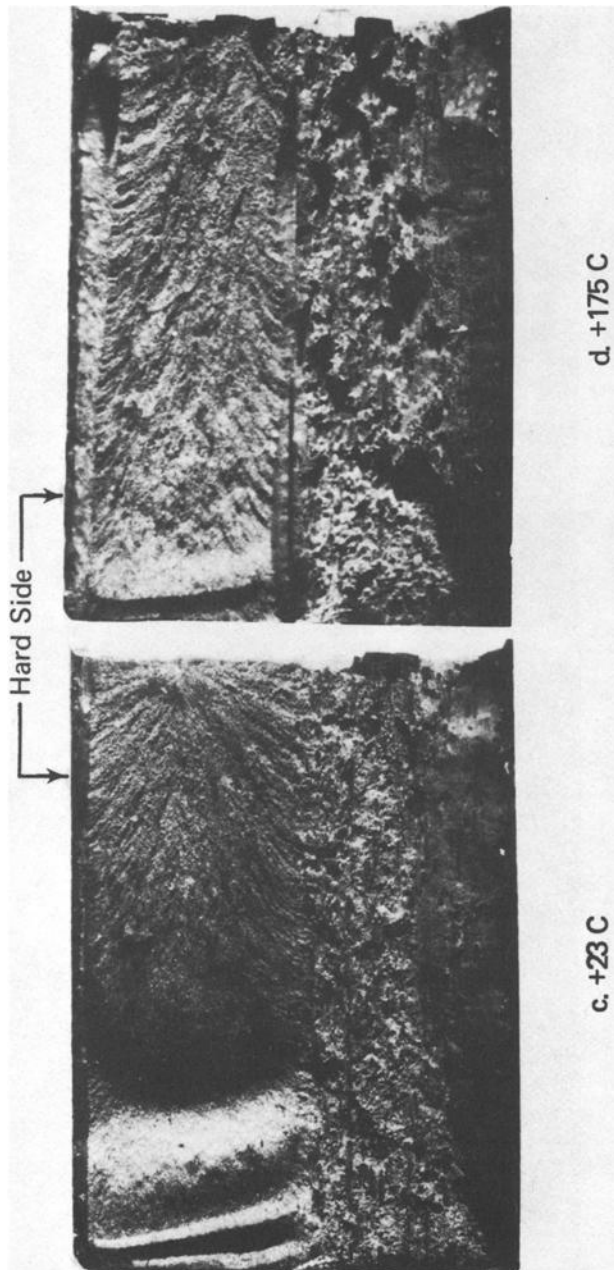
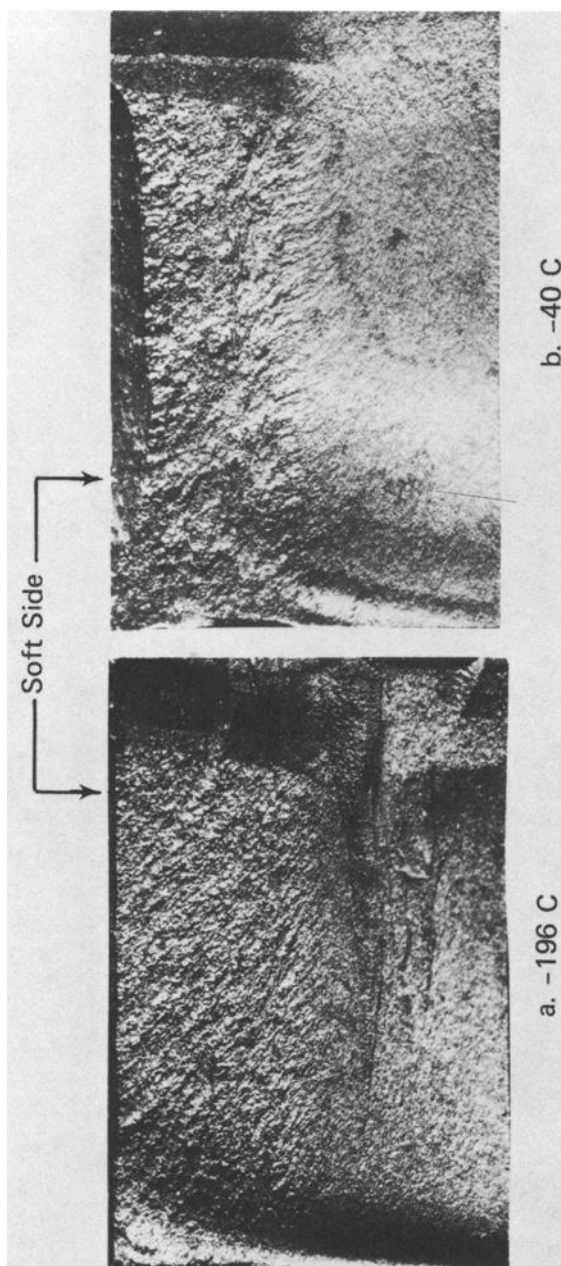


FIG. 12—Fracture surface of Charpy V-notch specimens (vacuum induction melted material) as a function of test temperature for WR orientation ($\times 10$).



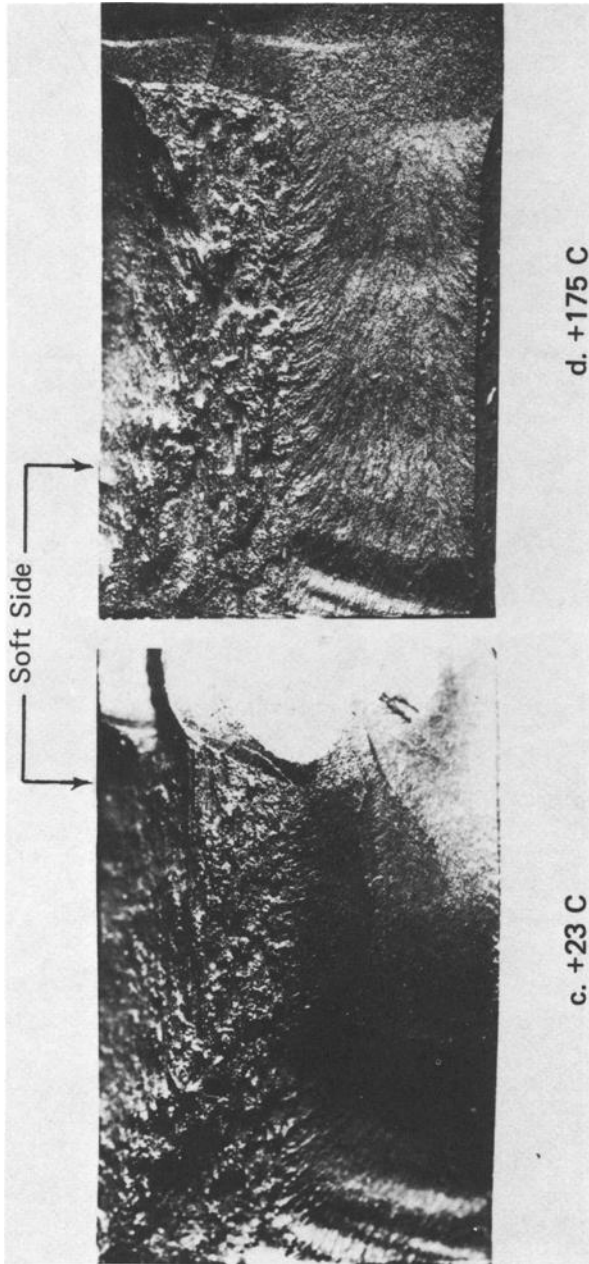
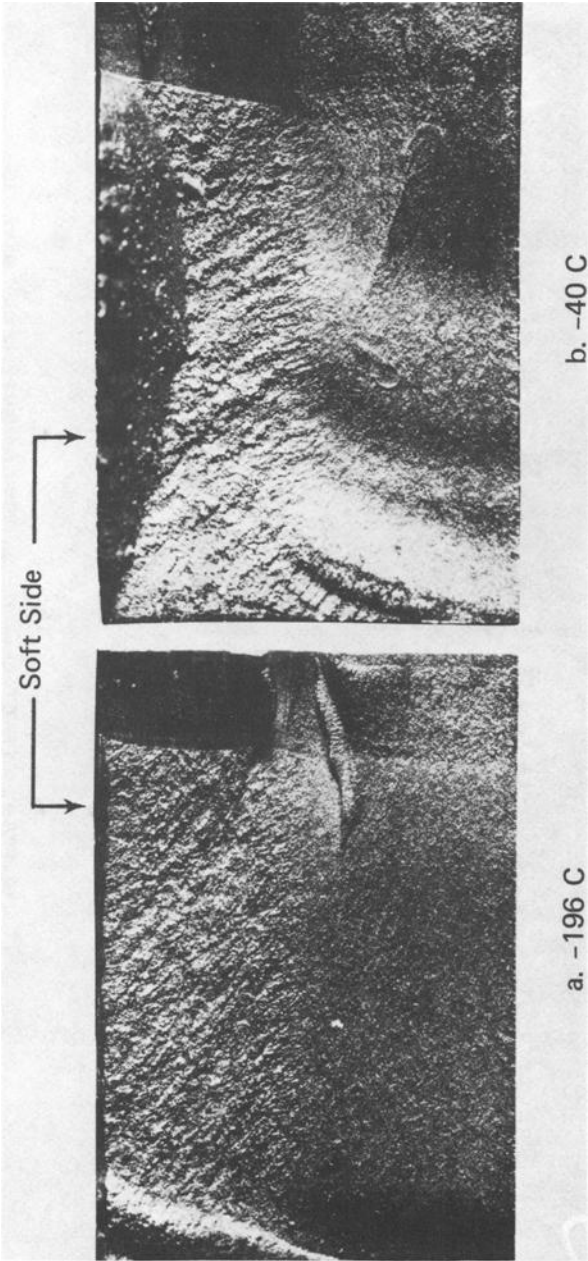


FIG. 13—Fracture surface of precracked Charpy specimens (vacuum induction melted material) as a function of test temperature for WR orientation ($\times 10$).



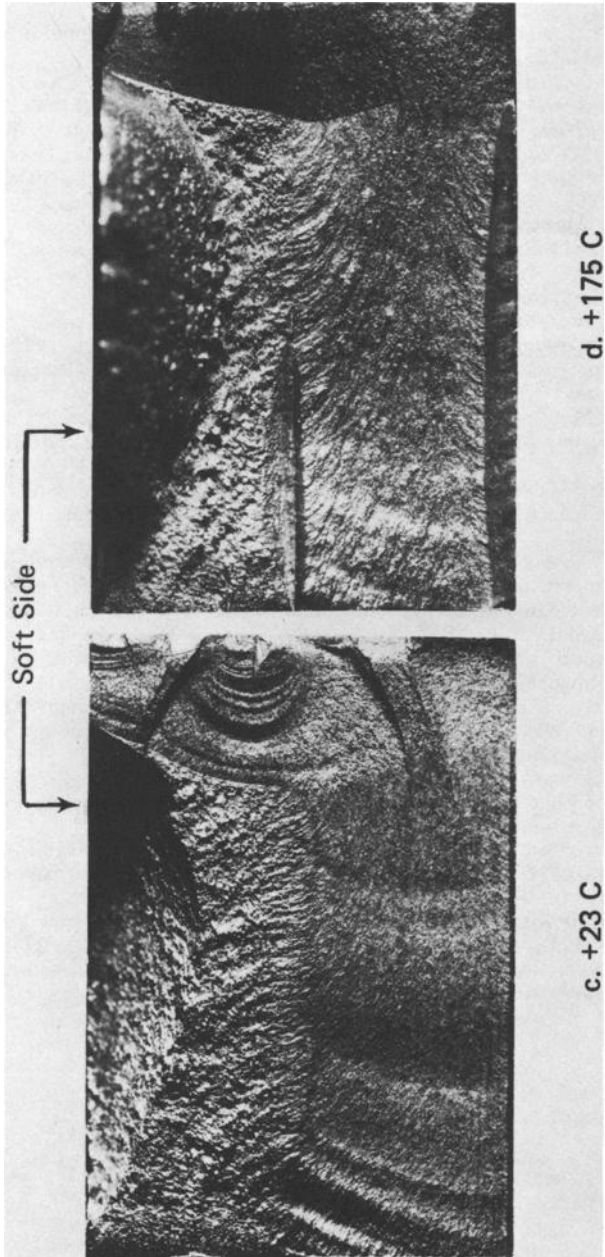


FIG. 14—Fracture surface of precracked Charpy specimens (vacuum induction melted material) as a function of test temperature for RW orientation ($\times 10$).

References

- [1] Manganello, S. J. and Abbott, K. H., *Journal of Materials*, Vol. 7, June 1972, p. 231.
- [2] *VertiFlight*, Vol. 16, Dec. 1970.
- [3] Burr, C. W., Degnan, W. G., Grumm, A. W., and McCaul, C. O., "Aerial Armored Fuselage Engineering and Manufacturing Report Part 1 (U) Technical Report AMMRC CR 70-2/1, United Aircraft Corp., East Hartford, Conn., Feb. 1970.
- [4] Greenwood, J. D. and Hill, R. M., "Manufacturing Technology Using Dual-Hardness, Heat-Treatable Steel Armor," Technical Report AMMRC CR 69-09, FMC Corp., San Jose, Calif., 1969.
- [5] Hickey, C. F., *Journal of Materials*, Vol. 3, March 1968, p. 3.
- [6] Anctil, A. A. and Kula, E. B., "Fatigue Crack Propagation in Armor Steels," Technical Report AMMRC TR 69-25, Army Materials and Mechanics Research Center, Watertown, Mass., Nov. 1969.
- [7] Anctil, A. A. et al, "Structural Properties of Dual Hardness Steel Armor," presented at Army Symposium on Solid Mechanics, Ocean City, Md., Oct. 1972; see also Technical Report AMMRC TR 73-6, Army Materials and Mechanics Research Center, Watertown, Mass., Feb. 1973.
- [8] Murphy, T. M., "Aerial Armored Fuselage Materials Evaluation," Confidential Technical Report AMMRC CT 71-11, United Aircraft Corp., East Hartford, Conn., 1971.
- [9] Chait, R., "NDT Evaluation of Ballistically Impacted Laminar Composite Armor Steel," presented at 9th Symposium on Nondestructive Evaluation, San Antonio, Tex., 26 April 1973.
- [10] Swanson, R. A. and Anctil, A. A., "Dual-Hardness Steel Armor—Observations on Material Characteristics and Specimen Preparation," Technical Note AMMRC TN 71-2, Army Materials and Mechanics Research Center, Watertown, Mass., Aug. 1971.
- [11] Curll, C. H. and Lum, P., "Basic Strength Properties of Ti-8Mo-8V-2Fe-3Al Sheet," Technical Report AMMRC PTR 73-7, Army Materials and Mechanics Research Center, Watertown, Mass., June 1973.
- [12] Rollins, K. A. et al, "On the Precracking Procedure for Fracture Toughness Determination," Technical Note AMMRC TN 72-24, Army Materials and Mechanics Research Center, Watertown, Mass., Sept. 1972.
- [13] Chait, R., *Metallurgical Transactions*, Vol. 3, 1972, p. 365.
- [14] Hirth, J. P. and Cohen, M., *Metallurgical Transactions*, Vol. 1, 1970, p. 3.
- [15] Papirno, R., *Experimental Mechanics*, Vol. 11, 1971, p. 446.
- [16] Papirno, R., "In-Situ Component Stress-Strain Measurements in Filamentary Composites," Technical Note AMMRC TN 69-07, Army Materials and Mechanics Research Center, Watertown, Mass., Sept. 1969.
- [17] Hempel, M. R. in *Internal Stresses and Fatigue in Metals*, Elsevier, New York, 1959.
- [18] Lee, H. H. and Uhlig, H. H., *Metallurgical Transactions*, Vol. 3, 1972, p. 2949.
- [19] Almond, E. A. et al in *Interfaces in Composites*, ASTM STP 452, American Society for Testing and Materials, 1969, p. 107.

R. H. Van Stone,¹ R. H. Merchant,¹ and J. R. Low, Jr.¹

Investigation of the Plastic Fracture of High-Strength Aluminum Alloys

REFERENCE: Van Stone, R. H., Merchant, R. H., and Low, J. R., Jr., "Investigation of the Plastic Fracture of High-Strength Aluminum Alloys," *Fatigue and Fracture Toughness—Cryogenic Behavior, ASTM STP 556*, American Society for Testing and Materials, 1974, pp. 93–124.

ABSTRACT: In a study of plastic fracture in five high-strength aluminum alloys (2014, 2024, 2124, 7075, and 7079), it has been shown that fracture toughness is affected primarily by the size and volume fraction of the larger (2 to 10 μm) second-phase particles. Certain of these particles crack at small plastic strains, nucleating voids which, with further plastic strain, coalesce to cause fracture. Not all second-phase particles crack at small plastic strains, and qualitative analysis of those which are primarily responsible for void nucleation shows that they contain iron or silicon or both. This result suggests that a reduction in the iron and silicon impurity content of the alloys should improve fracture toughness without loss of strength.

KEY WORDS: fracture properties, fracture strength, toughness, fractures (materials), rupture (materials), second-phase particles, voids, aluminum alloys, evaluation, tests

The brittle fracture of many high-strength alloys, such as steel, titanium, and aluminum have been shown in most cases to occur by a process called plastic fracture[1].² Plastic fracture is that mode of fracture where microscopic voids form at precipitates or impurity particles, then grow and coalesce to cause the final rupture. Tanaka et al[2] have assessed the role played by second-phase particles in the fracture of a 2014-T6 aluminum alloy. To understand the fracture process in other high-strength aluminum alloys, four additional alloys have been investigated: 2024-T851, 2124-T851, 7075-T7351, and 7079-T651. Fractography, quantitative microscopy, and microprobe studies have helped to determine the roles of the various types of particles and precipitates.

¹ Instructor, research assistant, and professor, respectively, Department of Metallurgy and Materials Science, Carnegie-Mellon University, Pittsburgh, Pa. 15213. Mr. Merchant is now at Queens University, Kingston, Ont., Canada.

² The italic numbers in brackets refer to the list of references appended to this paper.

Materials

In this study, five precipitation-hardened aluminum alloys with commercial thermal-mechanical treatments were investigated. Three of the alloys, 2014-T6, 2024-T851, and 2124-T851, are primarily aluminum-copper alloys, while 7075-T7351 and 7079-T651 are primarily aluminum-zinc-magnesium-copper alloys. Table 1 lists the chemical specifications, chemical analyses of the materials used, and temper designations for the alloys. All the alloys, excluding 2124-T851, are commercial grade materials. Alloy 2124-T851 has the same chemical specification as 2024-T851 except for reduced levels of iron and silicon, as reflected in Table 1.

The 2014-T6 material was the same as that used in the investigation of Tanaka et al[2]. The 2024-T851, 7075-T7351, and 7079-T651 materials were supplied by J.G. Kaufman of Alcoa Research Laboratories in the form of fractured three-point bend, plane-strain fracture toughness specimens. H. Y. Hunsicker of Alcoa Research Laboratories supplied two, 3-in.-thick test blocks of 2124-T851.

For this study, both tension tests and plane-strain fracture toughness tests were conducted. The 2024-T851, 7075-T7351, and 7079-T651 K_{Ic} fracture toughness values are those reported by Kaufman[3]. Some of the fracture toughness tests on 2014-T6 and 2124-T851 were performed at the NASA Lewis Research Center by M. H. Jones and R. T. Bubsey.

Table 2 shows the room temperature 0.2 percent offset yield stress (σ_y), K_{Ic} fracture toughness, and the relative toughness (K_{Ic}/σ_y). Also shown are the strength coefficient (A) and the strain-hardening exponent (n) from the tension flow curve, using a least square fit to the form $\sigma = Ae^n$. In Table 2, the symbols in parentheses represent the specimen orientation

where

- L = principal rolling direction,
- T = transverse direction, and
- S = thickness direction.

The tension tests are characterized by the tensile axis, and the fracture toughness tests are characterized by the normal to the fracture plane (or major tensile axis) followed by the direction of the crack propagation. With the exception of 2014-T6, the fracture planes of both tests are the same. To observe the effect of orientation, both the (LS) and (SL) K_{Ic} were determined for 2124-T851. The 2014-T6 and 2024-T851 alloys have virtually the same toughness, whereas 2124-T851, with decreased iron and silicon content, has a significantly improved fracture toughness while maintaining the same strength as the other 2000 series alloys. The two 7000 series alloys show the usual inverse relationship between strength and toughness; and comparison of 2124-T851 and 7079-T651 illustrates that, at the same toughness level, the 7000 series alloys possess higher strength[1].

TABLE I—Composition and heat treatment of aluminum alloys, weight percent.

Alloy	Si	Fe	Cu	Zn	Mg	Mn	Cr	Ti	V	Al
2014-T6 ¹	0.5 to 1.2	0.7 max	3.9 to 5.0	0.25 max	0.2 to 0.8	0.4 to 1.2	0.10 max	0.15 max	...	balance
Analysis	0.83	0.20	4.67	...	0.51	0.73
2024-T851 ²	0.5 max	0.5 max	3.8 to 4.9	0.25 max	1.2 to 1.8	0.3 to 0.9	0.10 max	balance
Analysis	0.17	0.50	4.2	0.077	1.52	0.59	0.018	0.05	0.018	...
2124-T851 ²	0.2 max	0.3 max	3.8/4.9	0.25 max	1.2 to 1.8	0.3 to 0.9	0.10 max	balance
Specification	0.04	0.05	4.11	0.02	1.41	0.61	0.00+	0.02	0.00+	...
Analysis										
7075-T7351 ³	0.5 max	0.7 max	1.2 to 2.0	5.1 to 6.1	2.1 to 2.9	0.3 max	0.18 to 0.40	0.2 max	...	balance
Specification	0.098	0.22	1.65	5.50	2.48	0.033	0.21	0.033	0.008	...
Analysis										
7079-T651 ⁴	0.3	0.4 max	0.4 to 0.8	3.8 to 4.8	2.9 to 3.7	0.1 to 0.3	0.1 to 0.25	0.1 max	...	balance
Specification	0.11	0.19	0.76	4.60	3.30	0.23	0.17	0.024	0.009	...
Analysis										

Typical heat treatments: (*Aluminum Standards and Data 1970-1971*, Aluminum Association, New York)

- 1. 2014-T6—Solution treatment at 935°F, quenched, age 18 h at 320°F.
- 2. 2024-T851, 2124-T851—Solution treatment at 920°F, quenched, stress-relieved by stretching, age 12 h at 375°F.
- 3. 7075-T7351—Solution treatment at 900°F, quenched, stress-relieved by stretching, age 6 to 8 h at 225°F, followed by 24 to 30 h age at 325°F.
- 4. 7079-T651—Solution treatment at 830°F, stress-relieved by stretching, age 5 days at room temperature, followed by 48 h age at 240°F.

TABLE 2—Mechanical test results.

Alloy	Yield Stress σ_y , ksi	K_{Ic} , ksi $\sqrt{\text{in.}}$	K_{Ic}/σ_y , $\sqrt{\text{in.}}$	Flow Curve $\sigma = A\epsilon^n$	
				A, ksi	n
2014-T6	63.5 (L)	17.7 \pm 0.8 (ST)	0.277	87.1 \pm 0.8	0.064 \pm 0.003
2024-T851	64.4 (L)	18.8 (LS)	0.292	85.5 \pm 0.1	0.051 \pm 0.000+
2124-T851	63.3 (L)	23.8 \pm 0.6 (SL)	0.378	93.6 \pm 1.1	0.074 \pm 0.003
		34.4 (LS)	0.544		
7079-T651	73.0 (L)	24.9 (LS)	0.341	110.0 \pm 1.0	0.074 \pm 0.003
7075-T7351	56.8 (L)	28.1 (LS)	0.495	92.6 \pm 1.1	0.097 \pm 0.004

Fractographic Study

The fracture surface of each alloy was studied with two-stage plastic-carbon replicas. The replicas were taken from fracture toughness specimens near the onset of unstable crack growth. The fracture surfaces of these alloys are characterized by regions of large and small dimples, as illustrated in Fig. 1 for 2024-T851. Region *A* contains large dimples surrounded by areas of small dimples, as shown in Region *B*. The large dimple diameters are of the order of 10 μm and show slip traces known as serpentine glide marks[4]. In the central region of the large dimples, there is often a cracked particle (*C*) whose size is of the order of several microns. When fractographs are viewed as stereo pairs, the regions of small dimples are at large angles to the macroscopic plane of crack propagation and connect planes of large dimple clusters. The size of the small dimples are of the order of 0.1 μm . Figure 2 shows a cracked particle and a region of small dimples in 2124-T851. The cracked particle failed by cleavage, as indicated by the river patterns[5]. Figure 2*b* shows depressions in some of the dimples, indicating that the small voids may form at submicron sized particles by interface decohesion. Fractographs for 2124-T851, 7075-T7351, and 7079-T651 are shown in Figs. 3, 4, and 5, respectively, and have features similar to those of 2024-T851 and 2014-T6[2]. Comparison of these fractographs show that, as the toughness is increased, the large dimples become deeper, and the fracture surface deviates greatly from an ideally flat plane of crack propagation. It also becomes more difficult to distinguish between regions of large and small dimples due to the increased amount of local plastic deformation.

The fractographs for all the alloys except 7075-T7351, the toughest alloy, were characterized quantitatively. The surface roughness of 7075-T7351, as shown in Fig. 5, prohibited accurate fractographic measurements. The following quantities were measured (*m*) or calculated (*c*).

1. Percentage of the area covered by large dimples (*m*) (% LD).
2. Percentage of the area covered by crack particles (*m*) (% CP).
3. Number of large dimples per unit area (*m*).

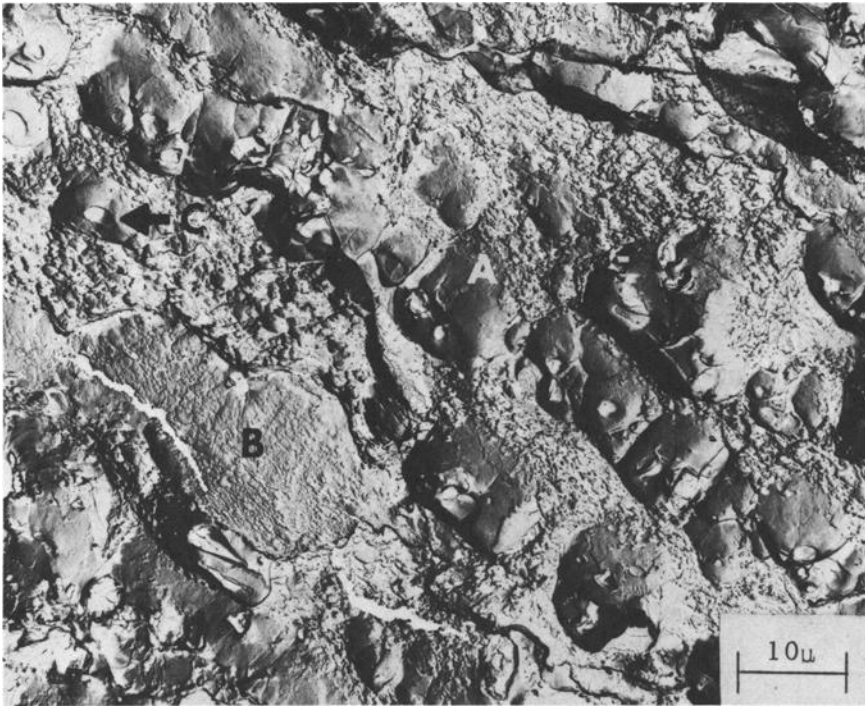


FIG. 1—Fractograph of 2024-T851 showing regions of large dimples (A); regions of small dimples (B); and a cracked particle (C).

4. Number of cracked particles per unit area (m).
5. Average diameter of large dimples (c).
6. Small dimple intercept distance in regions of small dimples (m).
7. (VGP) the void growth parameter (c).

$$\text{VGP} = \sqrt{(\% \text{ LD}) / (\% \text{ CP})} \quad (1)$$

The VGP is equivalent to the ratio of the diameters of large dimples to those of the void initiating particles assuming there is one cracked particle per void. This is not always the case, but in each dimple there is usually one large particle which probably nucleated the dimple. The data are shown in Table 3 and are based on at least five fractographs for each alloy.

Failure of the Large Second Phase Particles

Optical and scanning electron microscopy (SEM) were used to determine the role played by large (2 to 10 μm) second-phase particles. These particles are

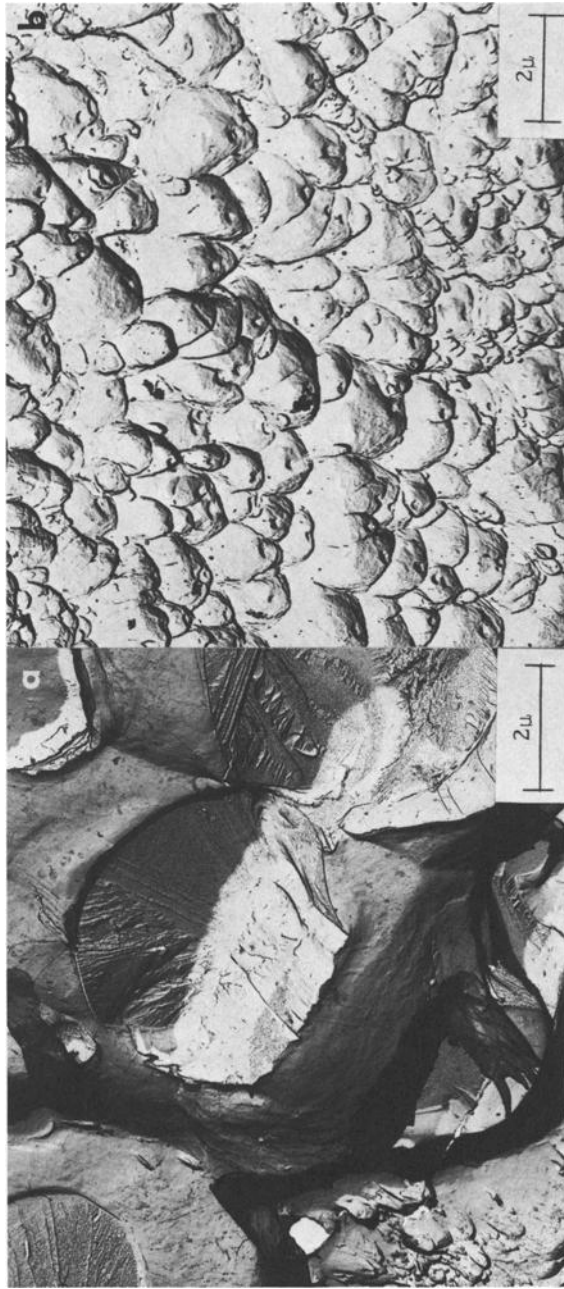


FIG. 2—Detail of fractographs of 2124-T851: (a) cleaved particles with river patterns and (b) regions of small dimples.

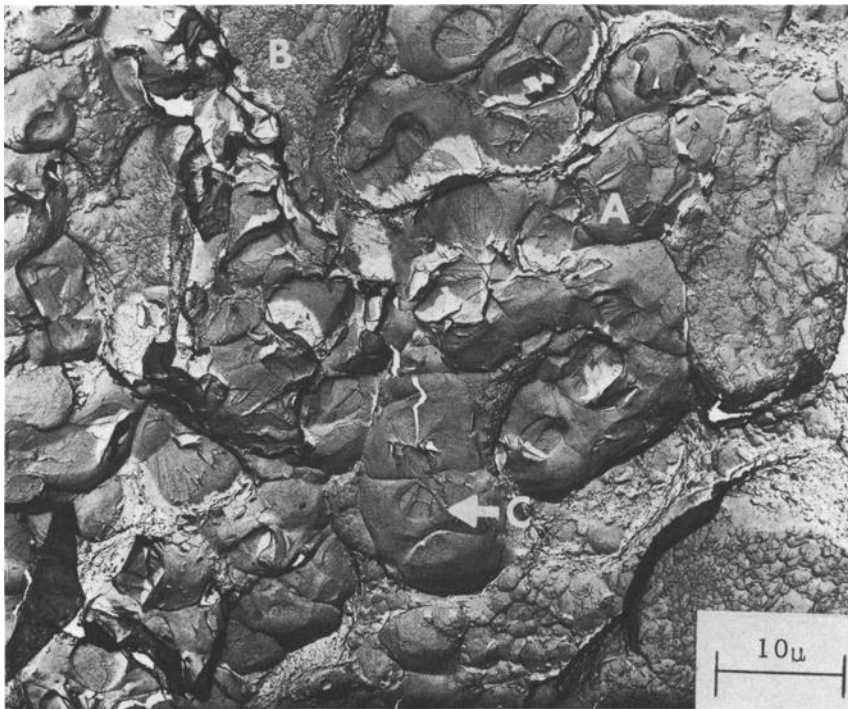


FIG. 3—Fractograph of 2124-T851 showing regions of large dimples (A); regions of small dimples (B); and a cracked particle (C).

TABLE 3—Fractographic data.

Feature	2014-T6	2024-T851	2124-T851	7079-T651
Area covered by large dimples, (%)	57.5	46.9	64.1	43.6
Area covered by cracked particles, %	5.4	2.7	3.4	2.1
Number of large dimples per unit area, $10^5/\text{cm}^2$	8.0	13.4	8.6	11.1
Number of cracked particles per unit area, $10^5/\text{cm}^2$	10.4	18.7	16.3	15.7
Average diameter of large dimples, μm	9.6	6.7	10.6	7.1
Small dimple intercept distance, μm	0.78	0.58	0.84	0.48
Void growth parameter	3.24	4.17	4.35	4.56

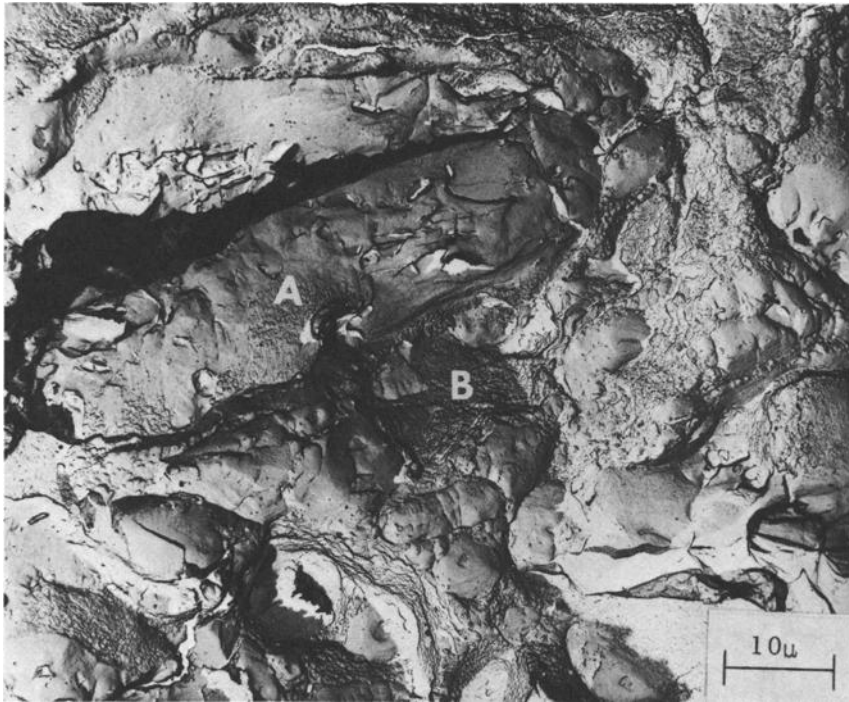


FIG. 4—Fractograph of 7079-T651 showing regions of large (A) and small (B) dimples.

formed during the freezing of the alloys. As in the investigation of Tanaka et al[2], the role of these particles was investigated by straining flat, 0.1-in.-thick tension specimens and observing polished sections at the midplane of the specimen. In most of these alloys, there is more than one type of second-phase particle, and the type which fails first can be noted. The identification of the various types of particles is discussed in a later section.

In order to discuss the effect of strain on the development voids at the second-phase particles, 2124-T851 will be discussed in some detail because it is the only alloy with just one type of particle. Figure 6 shows a series of micrographs of polished longitudinal midplanes of tension specimens at various stages of deformation. In all cases, the axis of applied stress is in the horizontal direction. Figure 6a shows a polished unstrained section, while Fig. 6b and 6c show sections strained 2.5 percent and a region near the fracture surface of a specimen strained 7.9 percent, respectively. In the specimen strained 2.5 percent, only the larger particles are cracked, while in the fractured specimen many of the particles are cracked or have voids associated with them. At first, the particles have fine, hair-line cracks which are perpendicular to the stress axis.

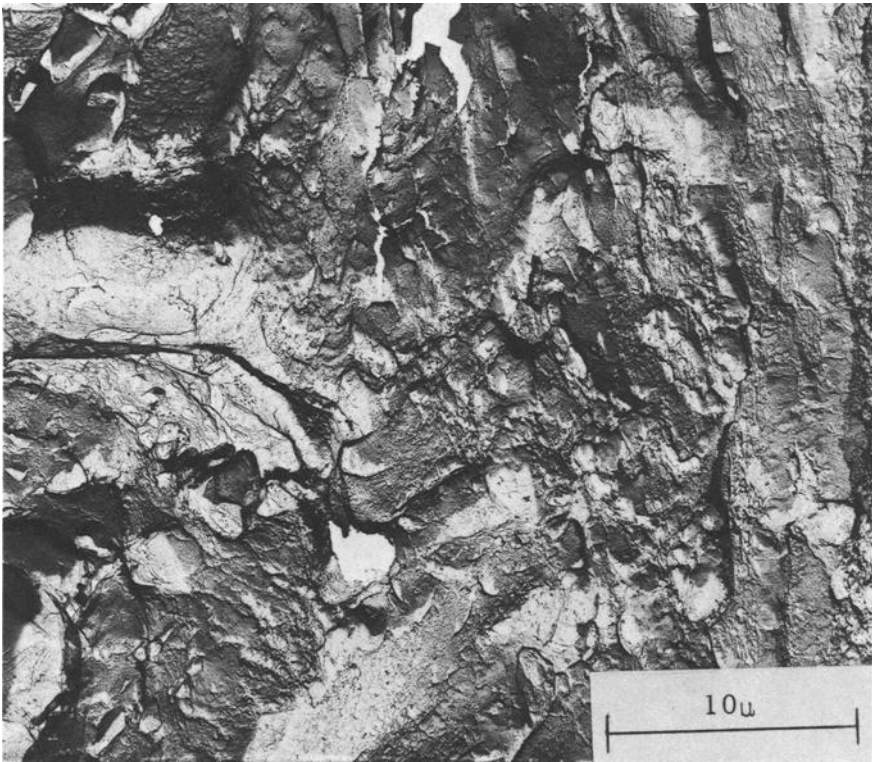


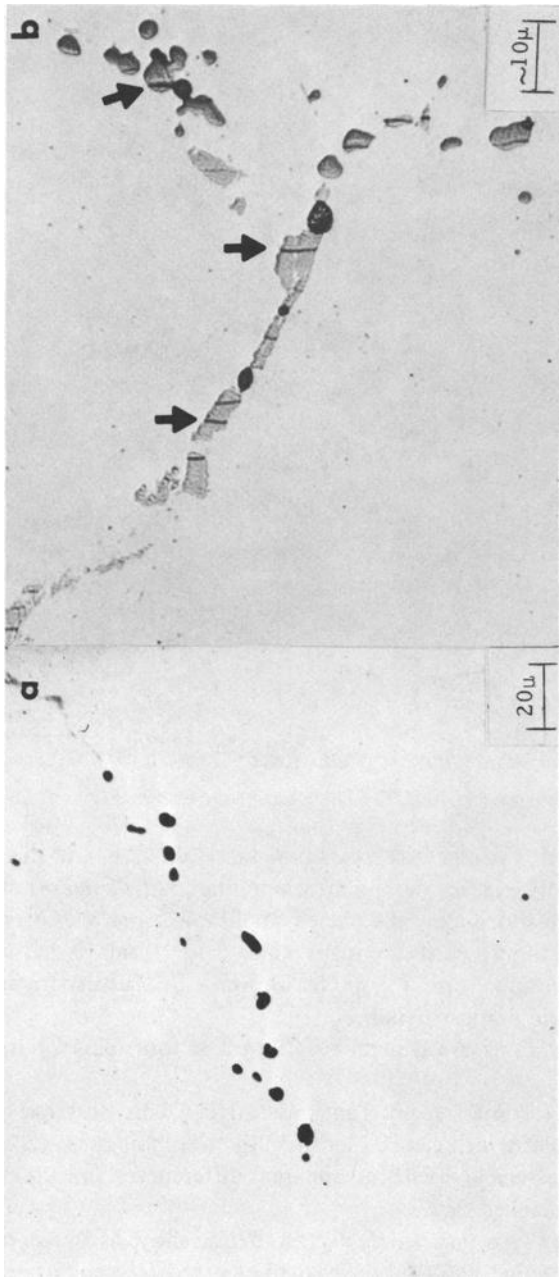
FIG. 5—Fractograph of 7075-T7351 showing large amounts of surface roughness.

As the specimen is strained, the two new faces separate, and the void starts to grow into the matrix to the point where the particle may not be observed because it is above or below the plane of polish. The particles often have several cracks in them. Figure 6c shows many voids 5 to 10 μm in size associated with particles of the same size. Figure 6d shows a SEM micrograph showing the nature of one void in more detail.

These observations are general for the other four alloys and are discussed next:

A. 2014-T6 (as reported by Tanaka et al)[2]—This alloy has clear gray and dark gray particles which can be identified by morphology as well as color. Both types of particles cracked with no apparent difference in cracking behavior. The larger particles cracked first.

B. 2024-T851—An unstrained section of this alloy, as shown in Fig. 7a, has three types of second-phase particles, light (*L*), gray (*G*), and dark (*D*). The light and gray inclusions were observed to crack first; and, at higher strains, the dark



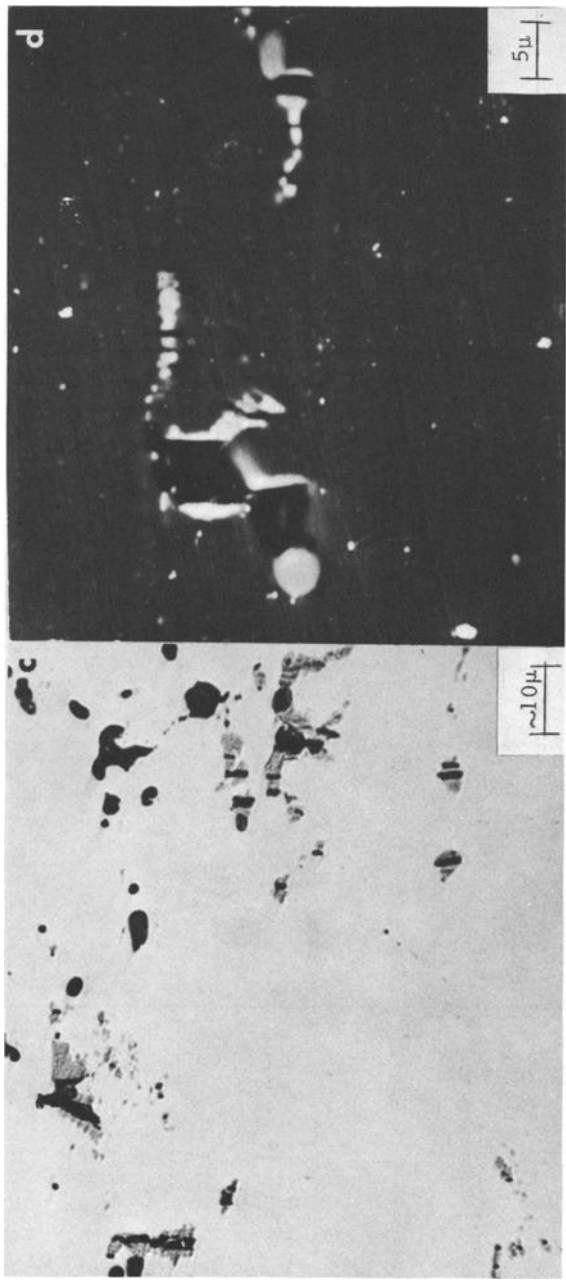


FIG. 6—Formation of voids in 2124-T851: (a) unstrained specimen, (b) specimen strained 2.5 percent, (c) specimen strained 7.9 percent, (d) SEM micrograph of specimen strained 7.9 percent. The stress axis is horizontal.

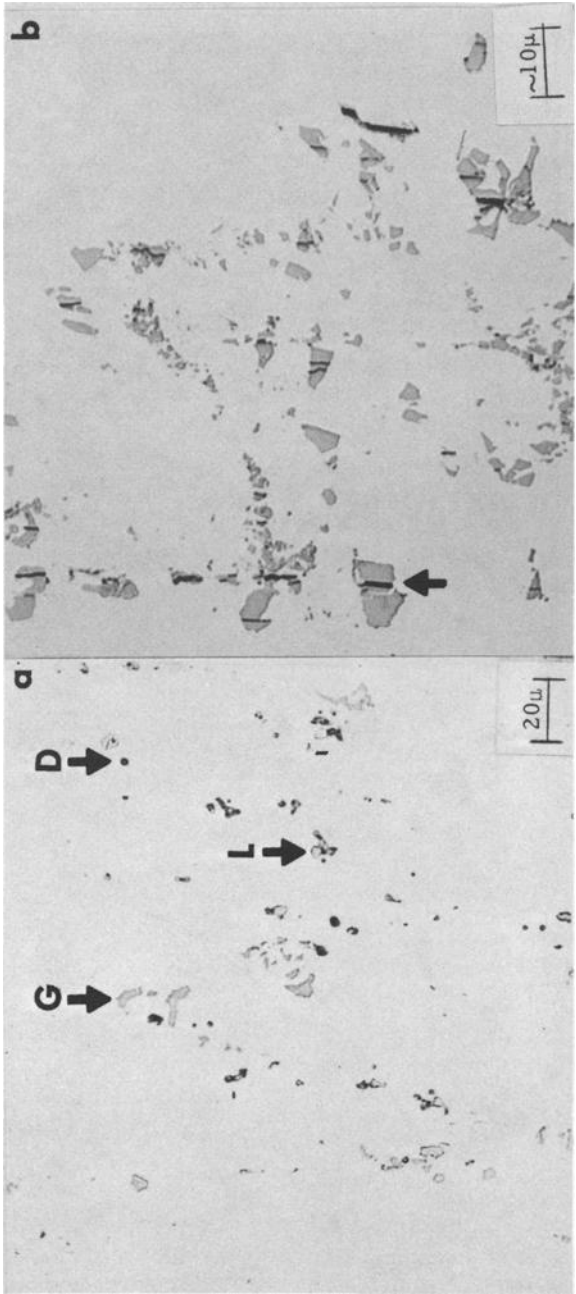


FIG. 7—Formation of voids in 2024-T851: (a) unstrained specimen showing light (L), gray (G), and dark (D) particles; (b) specimen strained to 6.1 percent showing cracks in the light particles. The stress axis is horizontal.

particles also failed. Figure 7b shows the cracking of the light particles at 6.1 percent elongation.

C. 7075-T7351—Figure 8a shows both light (*L*) and dark (*D*) second-phase particles. As shown in Fig. 8b for a specimen strained 6 percent, both sets of particles failed in several places. The light particles were observed to crack at lower strains than the dark particles.

D. 7079-T651—Like 7075-T7351, this alloy has both light (*L*) and dark (*D*) particles, as shown in Fig. 9a. The light particle cracks first and at lower strains than the dark ones. Figure 9b is a SEM micrograph showing the relative sizes of the voids on both types of particles strained 11.6 percent.

As these alloys are strained, one or several of the second-phase particles crack very early in the deformation process to serve as initiation sites for voids. To measure this effect quantitatively, the fraction of particles which have cracks associated with them was noted as a function of strain. Since no particle smaller than 2 μm was observed to crack, using the methods of examination just listed, 2 μm were used as the lower limit for these measurements. The standard deviation of these data was close to 2 percent in all cases. The results for these alloys are shown in Fig. 10. In no case were more than 50 percent of the particles cracked. In all the alloys, the cracking started shortly after the onset of plastic flow, with particles in the aluminum-zinc-magnesium-copper alloys cracking at higher strains than the aluminum-copper alloys. It will be noted that as the strain for the onset of cracking increases, so does the toughness (see Table 2).

Quantitative Metallography of Second-Phase Particles

The size and morphology of each type of second-phase particle in all 5 alloys were determined by quantitative optical metallography. The shape of the particles was very dependent on the plane of polish, probably due to interdendritic solidification and deformation during hot rolling. The particles were characterized using the method of DeHoff[6] for triaxial ellipsoids, with the particle major axes aligned with the rolling, transverse, and thickness directions. The average dimension in the primary rolling (d_R), transverse (d_W), and thickness (d_T) directions and the number of particles per unit volume (N_V) were determined using DeHoff's method. The volume percentage (v/o) was calculated, and three-dimensional center-to-center spacing (λ) was determined from the following equation[7]:

$$\lambda = \frac{0.554}{(N_V)^{1/3}} \quad (2)$$

The data were obtained using a Bausch and Lomb Quantitative Metallurgical System. So that these data could be compared with the particle cracking data, no particle smaller than 2 μm was counted. The results are shown in Table 4. The 2 μm cutoff resulted in exaggerated thickness dimensions. Also shown are

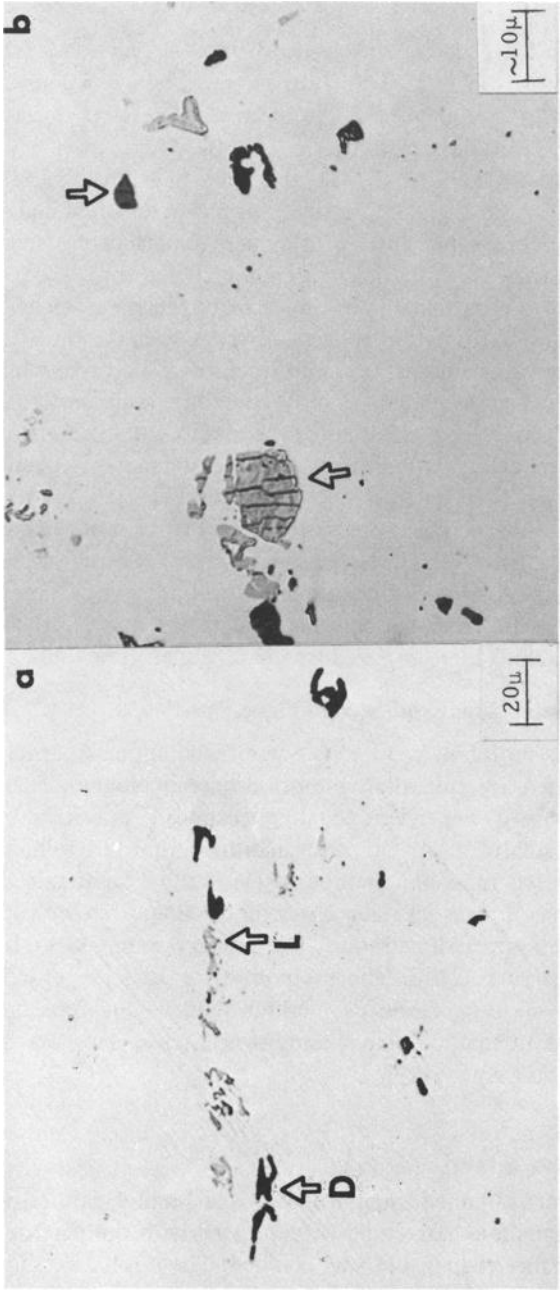


FIG. 8—Void formation in 7075-T7351: (a) unstrained specimen showing light and dark particles and (b) specimen strained 6.0 percent showing cracks in both particles. The stress axis is horizontal.

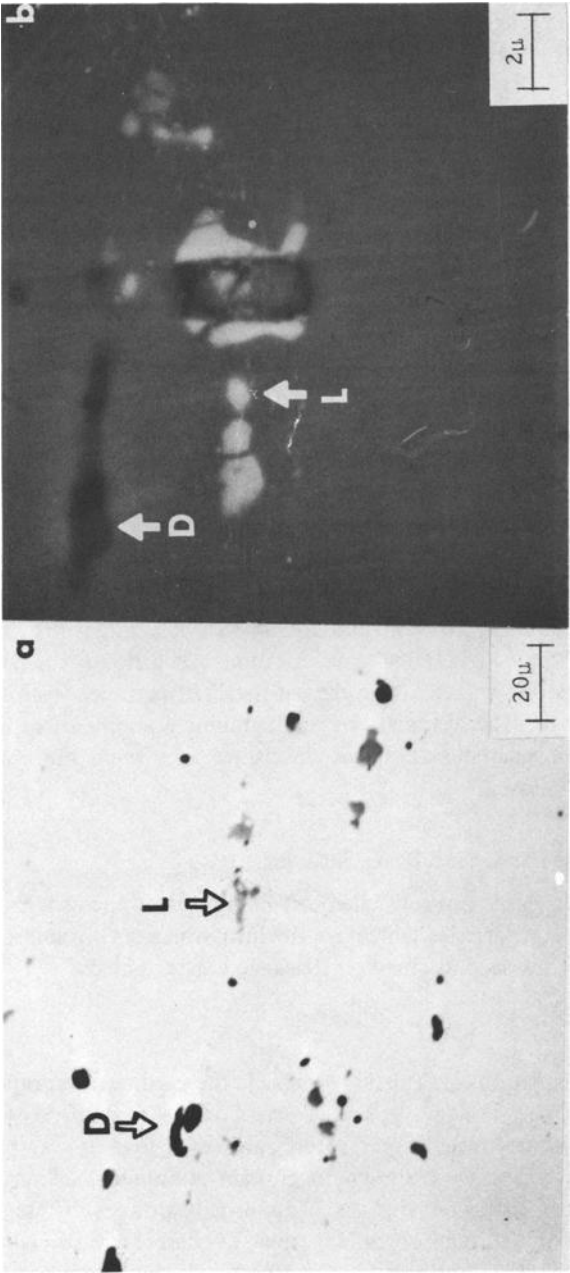


FIG. 9—Void formation in 7079-T651: (a) unstrained specimen showing light (L) and dark (D) particles. (b) SEM micrograph of specimen strained 11.6 percent with cracks in both types of particles. The stress axis is horizontal.

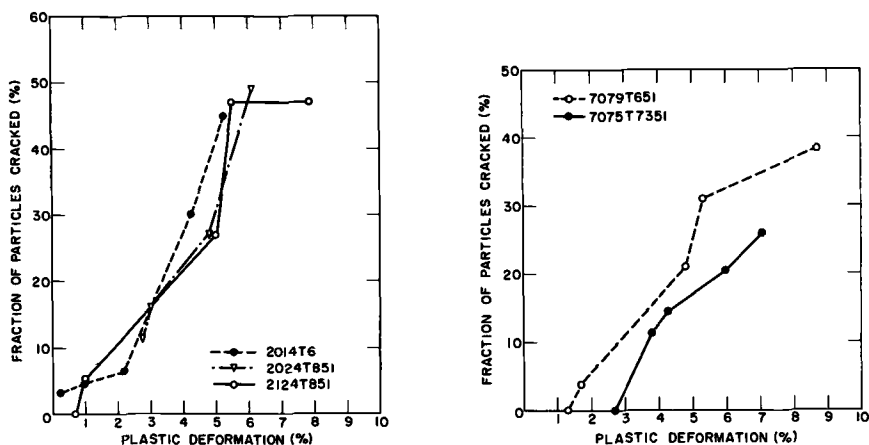


FIG. 10—Fraction of second-phase particles cracked as a function of macroscopic tensile strain: (left) 2000 series alloys and (right) 7000 series alloys.

combined populations identified as void nucleating populations. These are the data from two types of particles if two types of particles were observed to crack at the same strain as in 2014-T6 and 2024-T851. The data for the dark particles in 2024-T851 and 7079-T651 are questionable due to the small number observed. It was impossible to distinguish the light particles from the gray ones in 2024-T851 using the automated metallographic equipment, so both types of particles were measured as a single class since they were the void nucleating particles in that alloy.

Identification of the Second Phase Particles

In order to suggest possible chemical composition changes to decrease the volume fraction of particles which are the initiation sites for voids, the chemical compositions of the second phase particles were determined.

2014-T6

In the investigation of Tanaka et al[2] the authors determined that the composition of the dark gray particle was close to that of $Al_{12}(Fe, Mn)_3Si$ through extraction replicas from fracture surfaces. The clear gray particles could not be extracted but were shown to contain aluminum, silicon, copper, and magnesium by microprobe analysis of polished surfaces. These elements are characteristic of a phase called the Q -phase whose composition is $Al_4CuMg_5Si_4$ [8]. It is not possible to determine if the lighter particle could not

TABLE 4—Quantitative metallography on second-phase particles.

Alloy	Particle Description	Number Per Volume, $10^7/\text{cm}^3$	Volume Fraction, %	Center-to-Center Spacing, μm	d_R (rolling), μm	d_W (transverse), μm	d_T (thickness), μm
2014-T6	clear gray	21.9	1.5	9.2	6.5	4.4	4.6
	dark gray	7.3	1.5	13.3	9.7	9.3	4.7
	clear and dark gray ^a	29.2	2.9	8.4	7.2	5.6	4.6
2024-T851	gray	17.0	0.2	10.0	2.2	0.8	10.6
	dark	0.7	1.7 (?)	28.8	36.6 (?)	13.8 (?)	8.9 (?)
	light and gray ^a	41.6	2.7	7.4	8.8	3.6	3.9
2124-T851	light ^a	21.8	1.0	9.2	4.0	4.1	5.4
7075-T7351	light ^a	9.3	0.4	12.2	5.0	3.1	4.8
	dark	1.4	2.2 (?)	23.0	22.4 (?)	11.7 (?)	11.4 (?)
7079-T651	light ^a	16.0	0.4	10.2	4.5	2.8	3.5
	dark	4.7	0.5	15.3	6.2	4.7	6.4

^a Indicates void nucleating particles.

be extracted because (a) it was not a void-nucleating particle or (b) that the technique was not suitable for its extraction.

In the other four alloys, the extraction replication technique failed, so the elements in the second-phase particles were determined by examining polished surfaces in a scanning electron microscope equipped with an energy-dispersion X-ray detection system. The results are qualitative in nature because the large penetration distance of electrons with respect to the thickness of the second-phase particles cause the results to reflect the composition of the matrix, that is, values for aluminum would be too high while those of iron, silicon, copper, manganese, and magnesium would be too low.

2024-T85

Analysis of the particles in this alloy show that the dark particles contained magnesium and silicon, the light particles contained aluminum, iron, manganese, and copper, while the gray particles contained aluminum and copper. H. Y. Hunsicker et al[8] have suggested that the light, gray, and dark particles are $\text{Al}_2\text{O}_3\text{Cu}_2(\text{Mn}, \text{Fe})_3$, CuAl_2 , and Mg_2Si , respectively. Phase diagrams of these systems support these conclusions[9].

2124-T851

In 2124-T851, the SEM investigation has shown that the single type of second-phase particles contain aluminum, manganese, and copper. Hunsicker et al[8] have identified this phase as $\text{Al}_2\text{O}_3\text{Cu}_2(\text{Mn}, \text{Fe})_3$. Phase diagrams[9] support this conclusion. The silicon content of this alloy is below the solid solubility of silicon in aluminum[9] so no phase containing silicon was observed.

7075-T7351

Surface analysis revealed that the dark particles in this alloy contained magnesium and silicon, while the light particles contained copper, iron, and manganese. Mondolfo[11] has reported that at the iron-to-manganese ratio of this alloy, a nonequilibrium FeAl_6 will form, but it can be stabilized by having manganese and copper replace some of the iron. He also indicates that Mg_2Si will be present. Hunsicker et al[8] and phase diagrams[9] again confirm this conclusion.

7079-T651

The SEM investigation of 7079-T651 showed that the second-phase particles in this alloy contain the same elements as 7075-T7351. At the iron-to-manganese ratio of this alloy, Mondolfo[11] reports that MnAl_6 will form, but iron and copper can replace some of the manganese and aluminum. He reports that Mg_2Si will be present. These results were verified by Hunsicker et al[8] and by phase diagrams[9].

The foregoing results are presented in Table 5. The crystal structure of each phase [9] and indication of the void nucleating particles is also given. The only particles which do not act as void nucleating particles are the face-centered-cubic (fcc) Mg_2Si particles. All the void-nucleating particles except the Q -phase in 2014-T6 and CuAl_2 in 2024-T851 contain iron.

Transmission Electron Microscopy

The strength of these alloys is a result of interference with dislocation motion by precipitates and submicron size particles which are usually called dispersoids [14]. The precipitates form during the aging treatment, but the dispersoids are formed during homogenization, hot-rolling, and solution treatment [12] and are sometimes called "high-temperature precipitates." Tanaka et al [2] suggested that the dispersoid may act as void-nucleating particles for the small dimples in 2014-T6. For this reason, quantitative thin foil transmission electron microscopy (TEM) was used to measure the characteristics of the dispersoids. The method of Cahn and Nutting [13] was used which assumes the particles are spheres and yields particle size and number. The local foil thickness must be known to use this analysis. This was measured by observing the number of extinction contours at a grain boundary, solving the appropriate diffraction pattern, and determining the extinction distance for the appropriate zone axis from standard tables.

Micrographs of the five alloys are shown in Fig. 11. The dispersoids have diameters of the order of $0.1 \mu\text{m}$.

In the 2000 series alloys, the dispersoids were occasionally cylindrically shaped, but they were arbitrarily assumed to be spheres. They have been identified as $\text{Al}_{12}(\text{Mn}, \text{Fe})_3\text{Si}$ [8]. In the background of these micrographs, the acicular θ' precipitate is shown which is a transition phase of CuAl_2 [14].

TABLE 5—Composition of the second-phase particles.

Alloy	Particle Description	Elements in Particle	Presumed Phase Composition	Crystal Structure [9]
2014-T6	clear gray ^a dark gray ^a	Al, Si, Cu, Mg	$\text{Al}_4\text{CuMg}_5\text{Si}_4$ $\text{Al}_{12}(\text{Fe}, \text{Mn})_3\text{Si}$	body-centered cubic cubic
2024-T851	light ^a gray ^a dark	Al, Fe, Mn, Cu Al, Cu Mg, Si	$\text{Al}_{20}\text{Cu}_2(\text{Mn}, \text{Fe})_3$ CuAl_2 Mg_2Si	orthorhombic body-centered tetragonal face-centered cubic
2124-T851	light ^a	Al, Cu, Mn	$\text{Al}_{20}\text{Cu}_2(\text{Mn}, \text{Fe})_3$	orthorhombic
7075-T7351	light ^a dark	Fe, Cu, Mn Mg, Si	$(\text{Fe}, \text{Mn}, \text{Cu})\text{Al}_6$ Mg_2Si	orthorhombic face-centered cubic
7079-T651	light ^a dark	Fe, Cu, Mn Mg, Si	$(\text{Mn}, \text{Fe}, \text{Cu})\text{Al}_6$ Mg_2Si	orthorhombic face-centered cubic

^a Indicates void nucleating particles.

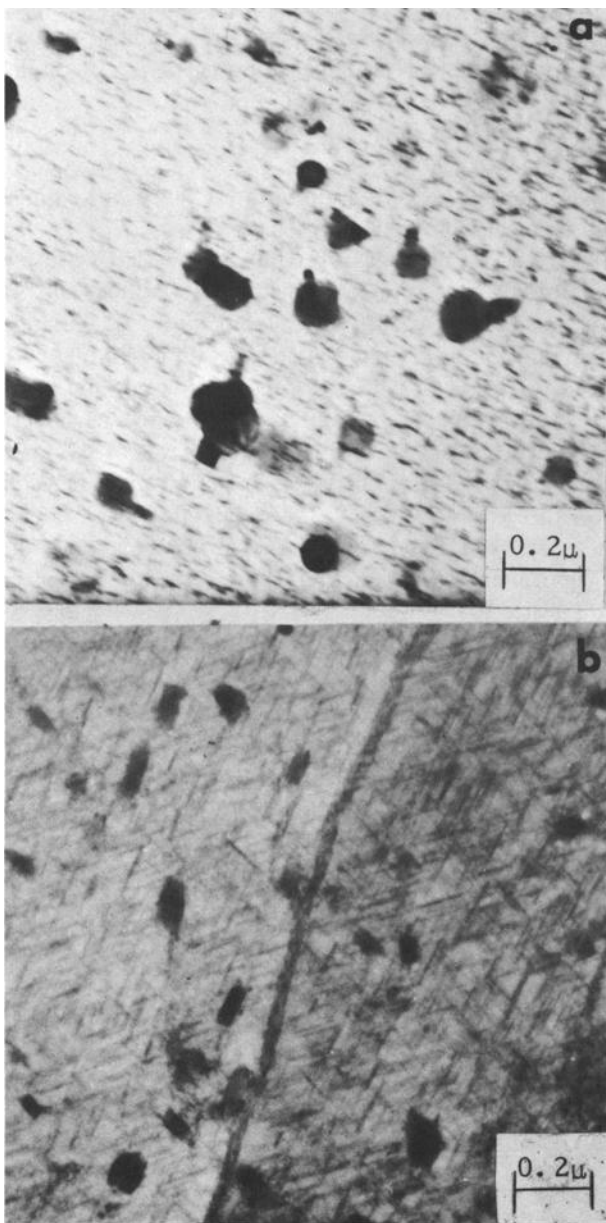


FIG. 11—Transmission electron micrographs showing dispersoids and strengthening precipitates: (a) 2014-T6, (b) 2024-T851, (c) 2124-T851, (d) 7075-T7351, (e) 7079-T651.

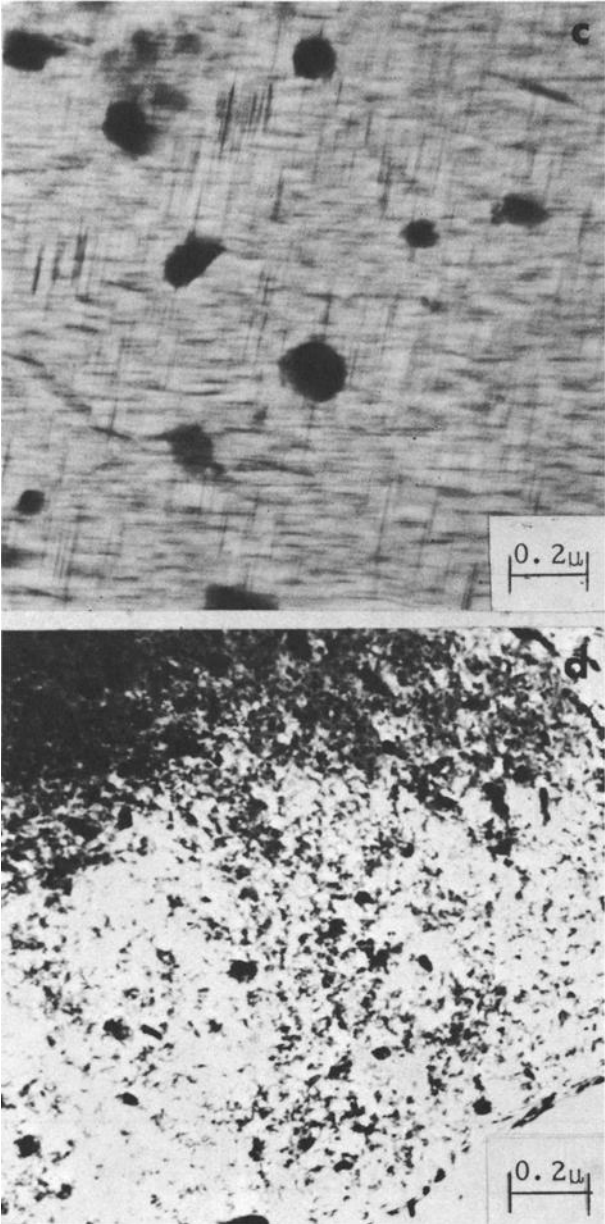


FIG. 11—(Continued)

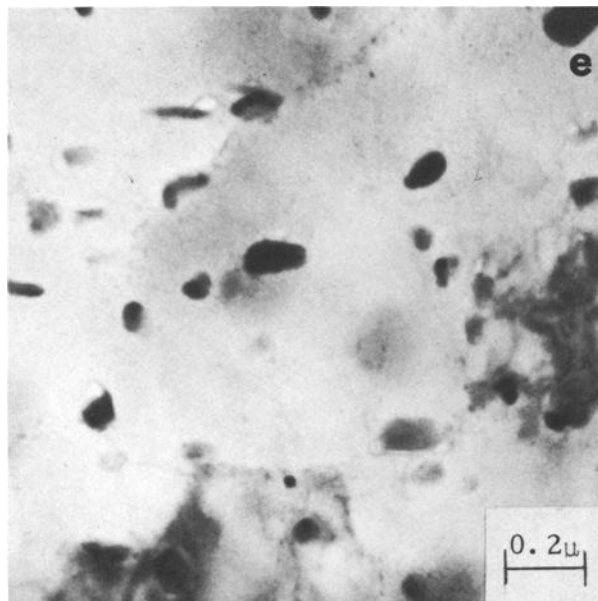


FIG. 11—(Concluded)

The 7000 series spherical dispersoids and diffuse M' ellipsoidal precipitates can be observed in the background of Fig. 11d. The precipitate in 7079-T651 is much smaller than that of 7075-T7351 and thus cannot be observed clearly at this magnification. The dispersoids are similar in size and shape to those identified as $Al_{12}Mg_3Cr_2$ by Hunter and McMillan[15] in 7075-T7351. Hunsicker et al[8] verify this result. The M' precipitate is a transition form of $MgZn_2$ [14,15].

Table 6 gives the results of the quantitative TEM. Also shown in the table is the center-to-center spacing as calculated from Eq 2.

TABLE 6—Dispersoid data.

Alloy	Mean Dispersoid Diameter, Å	Number Per Unit Volume, $10^{12}/cm^3$	Center-to-Center Spacing, μm
2014-T6	930	2.0	0.44
2024-T851	680	10.9	0.25
2124-T851	1010	4.7	0.33
7075-T7351	490	4.9	0.33
7079-T651	760	19.0	0.21

Discussion

From the experimental evidence just described, it is possible to describe qualitatively the fracture processes in these aluminum alloys. First, voids are initiated by the cracking of large second-phase particles. Upon further deformation, the voids grow until a critical ligament size between the voids is reached. The final rupture occurs by the formation of small voids at the dispersoids within the ligaments. Each of these steps will be discussed in detail.

Void Initiation

The second-phase particles in all of these alloys except 2024-T851 can be identified as either iron- or silicon-containing particles. In 2024-T851, one type of particle (CuAl_2) contained only copper and aluminum. The particles with iron cracked first and the ones containing silicon failed at higher strains. It appears that iron is more detrimental to fracture toughness than silicon. This effect has been noted by other investigators in both 2000[10] and 7000[16] series alloys.

Vruggink[10] flattened fracture surfaces of 2024-T851 against a tungsten carbide block and compared microprobe traces on a metallographic specimen with those of the flattened fracture surface. He compared the ratio between the amount of each element detected from the fracture surface to that from the polished surface. The elements listed in order of decreasing ratios are iron, copper, manganese, magnesium, and silicon. The ratio for iron was 5.4, while that of silicon was 1.3. From Table 5 it can be observed that the elements in the phases identified as void nucleating particles in 2024-T851 have a higher ratio. The other particles may participate in the fracture process, but they will be secondary in nature.

Piper et al[16] have investigated aluminum-zinc-magnesium-copper alloys and reported that iron is very detrimental to toughness with little effect on strength. They report that silicon itself improved toughness but only at the expense of strength. Silicon combined with magnesium to form Mg_2Si , so that less of the strengthening precipitate (MgZn_2) was formed. In alloys with equal amounts of magnesium available for the precipitation reaction, silicon reduced toughness, but to a lesser extent than iron. Copper was also observed to reduce toughness, possibly because copper stabilizes the nonequilibrium FeAl_6 [11]. Again, silicon appears to be less detrimental to fracture toughness than iron.

The only particles which are not identified as void-nucleating particles (Mg_2Si) have fcc crystal structure. Kelly et al[17] have shown that several fcc materials do not fail by cleavage because the material will slip before the stress is high enough to initiate cleavage. This may also be the case for Mg_2Si which is a metallic phase. To the authors' knowledge, there has been no work on the deformation or fracture mode in Mg_2Si . During the particle cracking study, the Mg_2Si particles were observed to crack, as shown in Fig. 8b and 9b; but the

fracture mode could not be verified since the Mg_2Si particles did not appear on the fracture surface. More work is required to fully explain the reason for the silicon-contained particles cracking at a later stage than those which contain iron or copper or both.

As just noted, the resistance to particle cracking increases with increasing K_{IC} . Within any one alloy the largest particles always cracked first, so the effect of particle size on the initiation of fracture was investigated. Because the particles have different dimensions in the various plate orientations, the particle size must be defined for each particular orientation. The cracks in the particles have been observed to be perpendicular to the stress axis so the equivalent particle diameter (\bar{d}) will be defined from the dimensions of the particle in the plane normal to the tensile axis as

$$\bar{d} = \sqrt{d_1 d_2} \quad (3)$$

where d_1 and d_2 are the particle dimensions in that plane, as determined from quantitative metallography. Figure 12 shows the strain-size relationship for the void nucleating particles where the strain is the largest strain wherein no particle cracking was observed. As the particle size decreases, the strain necessary to initiate particle cracking increases. To relate the particle size effect to K_{IC} , a crack instability criterion based on stresses at the crack tip rather than strains,

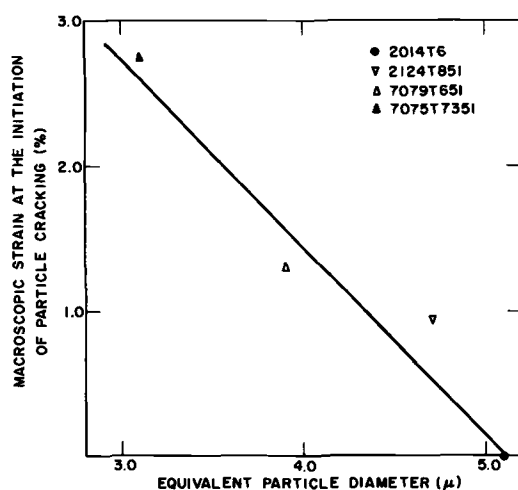


FIG. 12—The plastic strain necessary to initiate particle cracking as a function of the equivalent particle diameter \bar{d} .

the particle size should be related to stress necessary to initiate particle cracking. One such relationship has been proposed by Gurland and Plateau[18] based on the concept that when the elastic strain energy in the particle is greater than the surface energy required to form a crack, the particle will fail. For a spherical particle, this can be expressed as

$$\sigma = \frac{1}{q} \left(\frac{6E\gamma}{d} \right)^{1/2} \quad (4)$$

where

- q = stress concentration factor in the particle,
- E = Young's modulus of the particle,
- γ = surface energy of the particle, and
- d = particle diameter.

In the aluminum alloys under investigation here, the particles failed by cleavage; so, it is unlikely that the particle underwent extensive deformation. Thus, the Gurland and Plateau analysis may be valid for this case. Figure 13 shows the macroscopic stress necessary for cracking plotted against $1/\sqrt{d}$. The line should have a slope of $\sqrt{6E\gamma}/q$ and pass through the origin. The least square

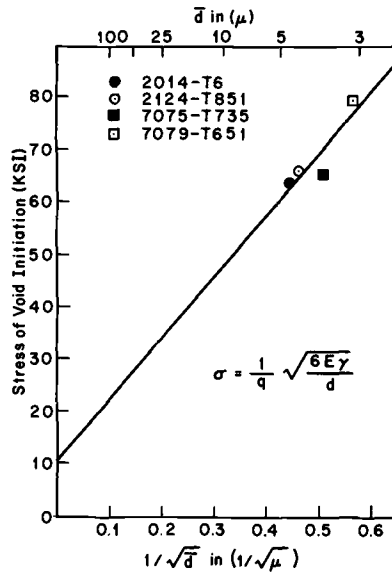


FIG. 13—The effect of equivalent particle diameter (d) on the stress necessary to initiate particle cracking.

fit of these experimental data has a y -axis intercept that falls within one standard deviation of the origin. Using a stress concentration factor of two as suggested by McClintock[19], the value of $E\gamma$ is 4.31×10^{15} dynes²/cm³. No published values of E or γ were known, so the approximation of Rosenfield[20] for γ was used

$$\gamma = \frac{Ea}{75} \quad (5)$$

where

a = interatomic spacing and

E = Young's modulus.

Thus $E\gamma = E^2a/75$ and using an interatomic spacing of 4Å, the elastic modulus was estimated to be 2.84×10^{12} dynes/cm² (41.2×10^6 psi). Through Eq 5, γ was estimated to be 1520 ergs/cm². Both of these values (E and γ) are of the correct order of magnitude, and it is reasonable to expect that the Young's modulus of intermetallic phases to be greater than that of the matrix. For this modulus, the particles would have been strained about ½ percent when cracking occurred.

The importance of Fig. 13 is that for particles of sizes less than 5 μ m a decrease in size of 1 μ m causes a significant increase in the amount of stress necessary to initiate cracking.

This is also reflected in fracture toughness. The toughness of the two orientations of 2124-T851 showed that when the major tensile axis of the specimen was in the rolling direction, the K_{IC} value was almost 50 percent greater than when the major tensile axis is in the plate thickness direction. This can be largely attributed to the orientation of the elongated second-phase particles and the fact that these particles crack perpendicular to the tensile axis. When the tensile axis is in the rolling direction, the equivalent particle diameter will be smaller than when the major tensile axis is in the thickness direction.

Void Growth

McClintock [21] and Rice and Tracey[22] have proposed models of void growth for different geometries. In both cases, void growth was enhanced by triaxial stress states such as one would expect to experience at a crack tip. These models also predict that the diameter of a void under the same strain state is proportional to its initial diameter. For this reason, the VGP as experimentally measured from K_{IC} specimen fractographs was defined as the ratio between the void diameter and diameter of the void nucleating particle.

In these alloys, the VGP varied only from 3.24 to 4.56 but increasing VGP correlates with increasing plane-strain fracture toughness, as shown in Fig. 14. From a microstructural point of view, growth of the large voids should be limited only by the spacing of the second-phase particles which initiate the

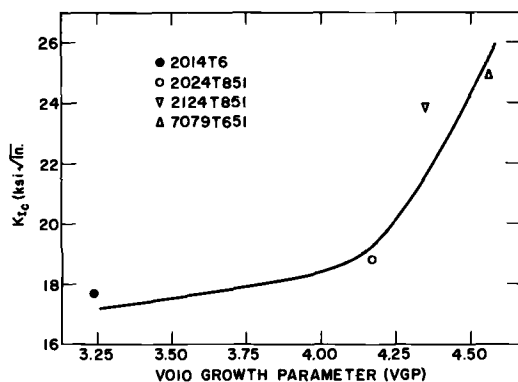


FIG. 14— K_{IC} as a function of the void growth parameter.

voids. Thus, the VGP should be related to λ/d where λ is the particle spacing and d is the particle diameter. Figure 15 shows increasing VGP with larger values of λ/d . The relationship does not have linear slope because the void growth stage is stopped by the void coalescence mechanism which is also dependent on structural parameters to be discussed later. The value of the VGP is greater than that of λ/d because only about half of the void nucleating particles crack, as shown in

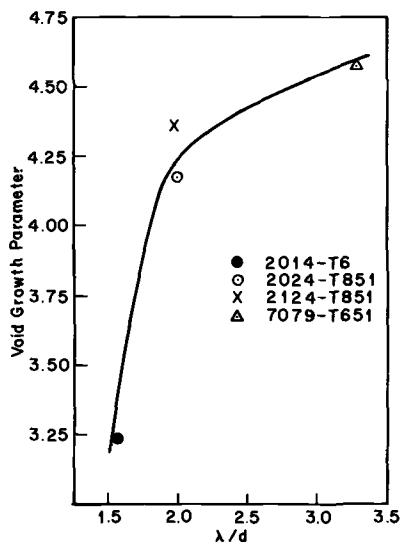


FIG. 15—The effect of the spacing-to-size ratio of the void nucleating particles (λ/d) on the void growth parameter.

Fig. 10, and the VGP is measured from fractographs, whereas λ/d is calculated from quantitative optical metallography which considers all the particles.

Large amounts of void growth were not observed in the tension specimens used in the particle cracking study. This can be attributed to the fact that necked regions of flat tension specimens have very small levels of triaxial tension with respect to those at the crack tip of plane-strain fracture toughness specimens. As just noted, models of void growth[21-22] show that triaxial stress states rapidly increased the rate of void growth.

Void Coalescence

Fractographic evidence indicated that in these aluminum alloys, the small voids form at submicron size particles and tend to connect planes of large dimples with many small open-ended shear dimples. Similar observations have been made in several alloy systems[23,25].

Rogers[23] observed narrow bands of heavy deformation at 45 deg extending from large voids in the necked regions of OFHC tension specimens. Upon further deformation, small voids formed within the deformation bands, hence the name void sheets. Cox and Low[25] have shown that small voids form at cementite particles, about 2000 Å long, in a quenched and tempered 4340 steel. These voids were observed to form void sheets between large voids which were formed at an earlier stage of the deformation process.

Tanaka et al[2] have suggested that the 0.1 μm dispersoids act as the void nucleating particles for the small dimples in 2014-T6. Voids can be nucleated at very small particles, as documented by the work of Palmer et al[24] where voids formed at 50 Å particles in internally oxidized copper. Using TEM, Broek[26] has observed voids to form at dispersoids by interface separation in 2024 aluminum.

No attempt was made to observe the formation of the small dimples, but the center-to-center spacing as measured by quantitative TEM was compared to the small dimple intercept distance as measured from fractographs. The results are shown in Fig. 16 and suggest that the dispersoids act as the void nucleating particles for the small dimples. The linear plot has a slope greater than unity because not every dispersoid acts as a nucleation site for small dimples.

The effect of void coalescence on fracture in these alloys is primarily that of preventing the large voids from growing into one another. If these alloys could accommodate more void growth, it would be expected that their K_{IC} values would increase. Further increases in toughness may be realized by refining the dispersoid size. Ashby[27] has modeled the effect of a spherical particle in a slip band and proposed that the stress acting on particle from the slip band is proportional to the particle diameter. Thus, larger particles would be under higher stresses and would act as void nucleating particles first. This effect has been observed experimentally at the Ni_3Mo strengthening precipitates in maraging steels[28].

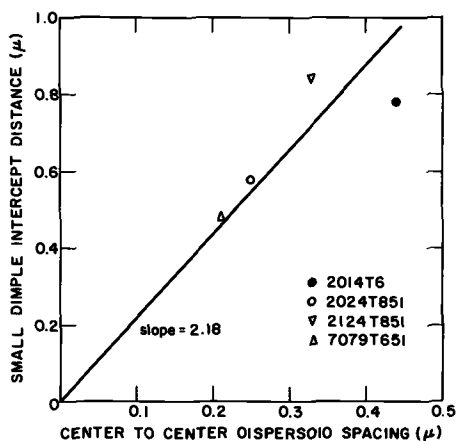


FIG. 16—The relationship between the center-to-center spacing of the dispersoids and the small dimple intercept distance.

It is impossible to verify Ashby's results[27] in these aluminum alloys due to the high fraction of large dimples (~50 percent) on the fracture surfaces. The role of the dispersoids on toughness is further complicated because they also act as strengthening particles[14], so the particle spacing must remain small to maintain the strength levels of these alloys. Further work in special high-purity alloys with very few second-phase particles is required to determine fully the role of size and spacing of the dispersoids on both strength and toughness. It may be possible to increase the toughness of these alloys by reducing the size of the dispersoid which might delay void sheet formation and permit additional void growth before fracture.

The fracture process in high-strength aluminum alloys is largely controlled by the size and spacing of the second-phase particles and the dispersoids. To increase fracture toughness, it would be desirable to simultaneously decrease the size (d), as shown in Fig. 13, and increase the spacing (λ) of the larger void nucleating particles, as shown in Fig. 17. A decrease in the size of the particles would increase the stress necessary to cause void initiation as well as decrease the initial size of a void and thus permit more void growth. It can be shown that the volume fraction of a phase is proportional to the cube of (d/λ) . Thus, the changes just noted effectively reduce the volume fraction of the second-phase particles. Improvement of fracture toughness by decreasing the volume fraction of an impurity phase has been established in many high-strength materials[29]. Figure 18 shows the K_{Ic} of the alloys investigated here plotted against the volume fraction of the particles identified as void nucleating particles. The aluminum-copper alloys have essentially equivalent yield stresses and show a characteristic improvement of toughness with increasing purity. The two

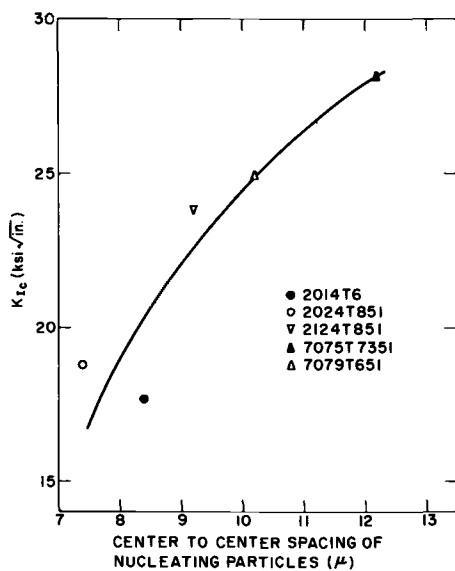


FIG. 17— K_{IC} as a function of the center-to-center spacing of the void nucleating particles.

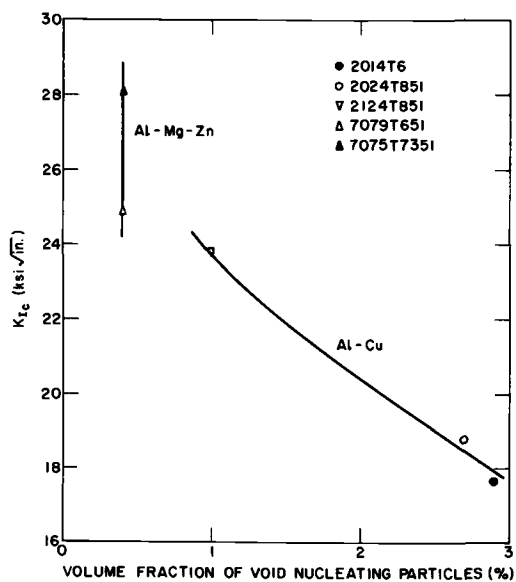


FIG. 18— K_{IC} as a function of the volume fraction of the void nucleating particles.

aluminum-zinc-magnesium-copper alloys have similar impurity levels but have vastly different K_{IC} values largely due to different strength levels.

Conclusions

1. Fracture toughness in aluminum alloys is controlled principally by second-phase particles containing iron or silicon which have only minor effects on strength. The particles containing iron seem to be more detrimental to toughness than those containing silicon.

2. The void initiation stage of fracture is delayed as the second-phase particles decrease in size. Particle size decreases of 1 μm for particles smaller than 5 μm cause significant improvement of the stress necessary to crack the particle.

3. The extent of void growth is controlled by the spacing-to-size ratio of the void-nucleating second-phase particles. Decreasing the particle size decreases the initial void size, while increasing the particle spacing will permit the voids to grow to larger sizes before coalescence and therefore improve toughness.

4. Void coalescence occurs by the formation of void sheets between the large voids and terminates the void growth stage. The small voids appear to form at the submicron dispersoids. Further investigation is required to assess the role of the dispersoid size and spacing on both strength and toughness.

Acknowledgments

This investigation was made possible by a research grant from the National Aeronautics and Space Administration, Research Grant No. NGR 39-087-003. The authors would also like to thank W. G. Fricke and R. H. Stevens for the use of the automated quantitative metallography equipment at the Alcoa Technical Center.

References

- [1] Low, J. R., Jr., *Engineering Fracture Mechanics*, Vol. 1, 1968, p. 47.
- [2] Tanaka, J. P., Pimpillo, C. A., and Low J. R., Jr., in *Review of Developments in Plane Strain Fracture Toughness Testing*, ASTM STP 463, American Society for Testing and Materials, 1970, p. 19.
- [3] Kaufman, J. G., Alcoa Research Laboratories, private communication.
- [4] Beachem, C. D. and Meyn, D. A. in *Electron Fractography*, ASTM STP 436, American Society for Testing and Materials, 1968, p. 59.
- [5] Low, J. R., Jr., *Progress of Materials Science*, Vol. 12, 1963, p. 1.
- [6] DeHoff, R. T. in *Quantitative Microscopy*, R. T. DeHoff and F. N. Rhines, Eds., McGraw-Hill, New York, 1968, p. 145.
- [7] Gurland, J. in *Quantitative Microscopy*, R. T. DeHoff and F. N. Rhines, Eds., McGraw-Hill, New York, 1968, p. 283.
- [8] Hunsicker, H. Y., Anderson, W. A., Fricke, W. G., and Stumpf, H. C., Alcoa Research Laboratory, private communication.
- [9] Wiley, L. A., *Aluminum*, Vol. 1, Kent R. Van Horn, Ed., American Society for Metals, Metals Park, Ohio, 1967, p. 359.
- [10] Vrugink, J. E., "Use of the Microprobe in Fracture Analysis," presented at 1972 Materials Engineering Congress, Cleveland, Ohio, Oct. 1972.

- [11] Mondolfo, L. F., *Metallurgical Reviews*, Vol. 16, 1971, p. 95.
- [12] Boyd, J. D., Drennen, D. C., Martin, D. J., Price, C. W., Rosenfield, A. R., Williams, D. N., and Thompson, D. S., "Research on Synthesis of High-Strength Aluminum Alloys," AFML-TR-72-199, Air Force Avionics Laboratory, Wright-Patterson Air Force Base, Ohio, 1972.
- [13] Cahn, J. W. and Nutting, Jack, *Transactions*, American Institute of Mining, Metallurgical, and Petroleum Engineers, Vol. 215, 1959, p. 526.
- [14] Hunsicker, H. Y., *Aluminum*, Vol. 1, K. R. Van Horn, Ed., American Society for Metals, Metals Park, Ohio, 1967, p. 109.
- [15] Hunter, M. S. and McMillan, J. C. in *Electron Fractography*, ASTM STP 436, American Society for Testing and Materials, 1968, p. 196.
- [16] Piper, D. E., Quist, W. F., and Anderson, W. F., *Application of Fracture Toughness Parameters to Structural Metals*, Metallurgical Society Conference, Vol. 31, Gordon and Breach, New York, 1966, p. 227.
- [17] Kelly, A., Tyson, W. R., and Cottrell, A. H., *Philosophical Magazine*, Vol. 15, 1967, p. 567.
- [18] Gurland, J. and Pleateau, J., *Transactions*, American Society for Metals, Vol. 56, 1963, p. 442.
- [19] McClintock, F. A., *Ductility*, American Society for Metals, Metals Park, Ohio, 1968, p. 255.
- [20] Rosenfield, A. R., *Metallurgical Reviews*, Vol. 13, 1968, p. 29.
- [21] McClintock, F. A., *Journal of Applied Mechanics*, Vol. 35, 1968, p. 363.
- [22] Rice, J. R. and Tracey, D. M., *Journal of Mechanics and Physics of Solids*, Vol. 17, 1969, p. 201.
- [23] Rogers, H. C., *Transactions*, American Society of Mining, Metallurgical, and Petroleum Engineers, Vol. 218, 1960, p. 498.
- [24] Palmer, I. G., Smith, G. C., and Warda, R. D., *Physical Basis of Yield and Fracture*, Institute of Physics and Physical Society Conference, Series No. 4, Oxford, England, Sept. 1966.
- [25] Cox, T. B. and Low, J. R., Jr., "Investigation of the Plastic Fracture of High Strength Steels," NASA Technical Report No. 4, Department of Metallurgy and Materials Science, Carnegie-Mellon University, Pittsburgh, Pa., Oct. 1972.
- [26] Broek, D., "A Study on Ductile Fracture," NRL TR 71021 U, National Aerospace Laboratory, The Netherlands, 1971.
- [27] Ashby, M. F., *Philosophical Magazine*, Vol. 14, 1966, p. 1157.
- [28] Roesch, L. and Henry, G. in *Electron Microfractography*, ASTM STP 453, American Society for Testing and Materials, 1969, p. 3.
- [29] Hahn, G. T. and Rosenfield, A. R., "Relation Between Microstructure and Fracture Toughness of Metals," presented at the Third International Conference on Fracture, Munich, Germany, April 1973.

J. G. Kaufman,¹ F. G. Nelson,¹ and R. H. Wygonik¹

Large-Scale Fracture Toughness Tests of Thick 5083-0 Plate and 5183 Welded Panels at Room Temperature, -260 and -320°F

REFERENCE: Kaufman, J. G., Nelson, F. G., and Wygonik, R. H., "Large-Scale Fracture Toughness Tests of Thick 5083-0 Plate and 5183 Welded Panels at Room Temperature, -260 and -320°F," *Fatigue and Fracture Toughness-Cryogenic Behavior, ASTM STP 556*, American Society for Testing and Materials, 1974, pp. 125-158.

ABSTRACT: The exceptionally high toughness of thick 5083-0 plate and 5183 welded panels at room temperature, -260 and -320°F has been demonstrated by large-scale fracture toughness testing. No evidence of a fracture instability at elastic stresses was observed, even in K_{Ic} tests of 7.7-in.-thick notched bend specimens and in a K_{Ic} test of a 4-in.-thick and 44-in.-square edge-notched tension panel. Ductile tearing was observed in all cases with panels as thick as or thicker than those used in critical structures such as liquefied natural gas tanks. The toughness at -260 and -320°F was as high as or higher than at room temperature by all available indexes. While these conclusions indicate that the application of fracture mechanics to the design of 5083-0 tanks is not very appropriate and may be unduly conservative, some engineering estimates of K_{Ic} and K_{Ic} were made from the results of the fracture tests.

KEY WORDS: fracture properties, toughness, fracture tests, aluminum alloys, liquid nitrogen, tanks (containers), cryogenics

Alloy 5083-0 and welds in that alloy with compatible filler alloy 5183 are the primary structural metals of which containers for storage and transportation of liquefied natural gas (LNG)[1]² are made. These aluminum alloys are not new but have been used for almost 20 years for handling a variety of liquid cryogens such as nitrogen, oxygen, hydrogen, helium, and natural gas[2,3]. The tensile

¹ Manager, senior engineer, and engineer respectively, Engineering Properties and Testing Division, Alcoa Laboratories, Aluminum Company of America, Alcoa Center, Pa. 15069.

² The italic numbers in brackets refer to the list of references appended to this paper.

properties and toughness of these alloys have been well documented in the past[2-9].

Despite the substantial history of use and knowledge about these materials, their application in large spherical tanks for the shipboard transportation of LNG could be implemented only after certain additional tests were made to show that even in extremely thick sections this material still is very fracture resistant. The large spheres employ plate over 1 in. thick even in the thinnest areas and, in some designs of support system, plate nearly 8 in. thick is used to manufacture the equatorial ring. Therefore, some large-scale fracture toughness tests were made in an attempt to measure the condition, if any, under which unstable crack growth might be expected in this material in the large sections in which it would be used in such structures. It is the purpose of this paper to describe those tests and present the results in terms useful to designers.

In addition to the fracture toughness evaluation, the fatigue crack growth resistance of the material was also evaluated; the results of that evaluation are the subject of a separate paper[10]. Both evaluations were carried out at Alcoa Laboratories, sponsored in part by the Quincy Shipbuilding Division of General Dynamics Corporation.

Material

The materials used in this investigation consisted of some 7.0 and 7.7-in.-thick 5083-0 plate. The chemical compositions and tensile properties of these plates are shown in Table 1. All meet the requirements of applicable specifications[11,12].

Weld Preparation and Qualification

Welds in the 7.0-in. plate and one piece of the 7.7-in. plate were made in the vertical position with 5183 IG electrode by the gas metal arc (MIG) method by the Joining Division of Alcoa Laboratories. The edges of the plate were prepared by machining a 60 deg included deep "V" groove with a 3/8 in. root radius and 1/4 in. abutting land. The pieces to be joined were then mounted vertically to represent the normal position in welding the LNG tanks. A semiautomatic procedure was used, in which the spool of electrode and welding gun rise vertically while a weld bead is deposited; the gun is then lowered to the starting position and another pass is initiated. The stronger pass technique was used to provide maximum soundness. From 476 to 640 passes were required to make each weld; the passes were made in layers across the joint, and the panel was rotated 180 deg after each layer of weld was deposited to maintain the required flatness.

The panels were radiographed twice: once when the depth of deposited weld metal was about 3 in., and once when the weld was completed. Each panel met all ASME radiographic requirements (Division 2, Section VIII)[13].

TABLE 1—Composition and tensile properties of some 7.0 and 7.7-in. 5083-0 plate.

Thickness, in.	Composition, element %							
	Si	Fe	Cu	Mn	Mg	Cr	Zn	Ti
7.0	0.10	0.24	0.08	0.78	4.74	0.11	0.04	0.04
7.7								
Plate 1	0.16	0.24	0.07	0.54	4.34	0.07	0.05	0.04
Plate 2	0.11	0.28	0.06	0.66	4.47	0.08	0.07	0.04
Limits ^a								
Max	0.40	0.40	0.10	1.0	4.9	0.25	0.25	0.15
Min	0.40	4.0	0.05

Thickness, in.	Longitudinal Tensile Properties ^b		
	Tensile Strength, ksi	Yield Strength Offset = 0.2%, ksi	Elongation in 4D, %
7.0	45.0	19.7	24.2
Specified min ^a	37	15	14
7.7			
Plate 1	41.2	18.4	21.4
Plate 2	42.6	17.8	20.8
Specified min ^a	36	14	12

^a Aluminum Standards and Data, third edition, Jan. 1972, The Aluminum Association, New York.

^b ½-in.-diameter specimens; T/4 location.

A single lot of 5183 filler wire was used for all welds. The chemical composition (average of three determinations) of the filler wire is shown in Table 2. It is well within the composition limits for 5183 and represents normal commercial quality.

To further check the quality of the weld in the 7.7-in.-thick plate, three cross-weld reduced-section tension specimens were prepared from one panel and tested at room temperature in accordance with Section IX of the ASME Boiler and Pressure Vessel Code[13]. The average cross-weld strength was 40 ksi. As expected, this is on the low side of the range of strengths of welds in thinner plate, but still well above the specified minimum tensile strength of 5083-0 plate of this thickness, 36 ksi. This is further indication that the 5183 welds produced for this program were of good commercial quality.

The results of a metallographic examination of the weld zone in the 7.7-in.-thick plate are shown in Fig. 1. The equivalency of the metallurgical structure in the parent material immediately adjacent to the weld and well away from the weld demonstrates the absence of any significant effects of the heat of

TABLE 2—Chemical composition of 5183 IG electrode.

Elements	Composition		
	Actual ^a	Nominal	Limits ^b
Silicon (Si)	0.08	...	0.40
Iron (Fe)	0.16	...	0.40
Copper (Cu)	0.04	...	0.10
Manganese (Mn)	0.63	0.75	0.5 to 1.0
Magnesium (Mg)	5.03	4.8	4.3 to 5.2
Chromium (Cr)	0.08	0.15	0.05 to 0.25
Zinc (Zn)	0.01	...	0.25
Titanium (Ti)	0.08	...	0.25

^a Based on three determinations.^b Military Specification MIL-E-16053, Electrodes, Welding, Bare, Aluminum Alloys.

Maximum unless shown as a range.

welding. The microstructures in the various regions are considered representative of a 5183 weld in thick 5083-0 plate.

Test Procedure

The tensile properties of the 5083 plate and of the 5183 welds were determined with ½-in.-diameter specimens per ASTM Method E 8, Fig. 8[14]. For the 7.0-in. plate, the specimens were tested at -260°F (LNG temperature) as well as room temperature and -320°F. From the 7.7-in. plate, they were taken at several locations through the thickness (center, midway, and surface), but tested only at room temperature and -320°F. Specimens were taken from several locations in the weld zone (parallel to and across the center of the weld, across the fusion zone, and in the adjacent parent metal); the specific locations were selected by etching the cross-weld section to clearly identify the appropriate regions cut. The tension tests were made in accordance with ASTM Methods E 8[14] and B 557[15]; yield strengths were determined at 0.2 percent offset from autographically plotted load-strain curves.

For comparison with earlier fracture testing of 5083[2-9], tear tests were made of 0.1-in.-thick specimens of the design in Fig. 2 machined from the same locations from which the tension tests of the parent metal and welds; the orientations from which specimens were taken from the welds are shown in Fig. 3. The tear test specimen and testing procedures were as described in Alcoa Technical Paper No. 18[16].

The tension and tear tests at -260 and -320°F were made in exactly the same manner as those at room temperature, except that the specimens and grips were enveloped in (a), for -260°F, the vapors of liquid nitrogen (LN₂) boiling at a controlled rate and (b), for -320°F, in the liquid nitrogen itself. The

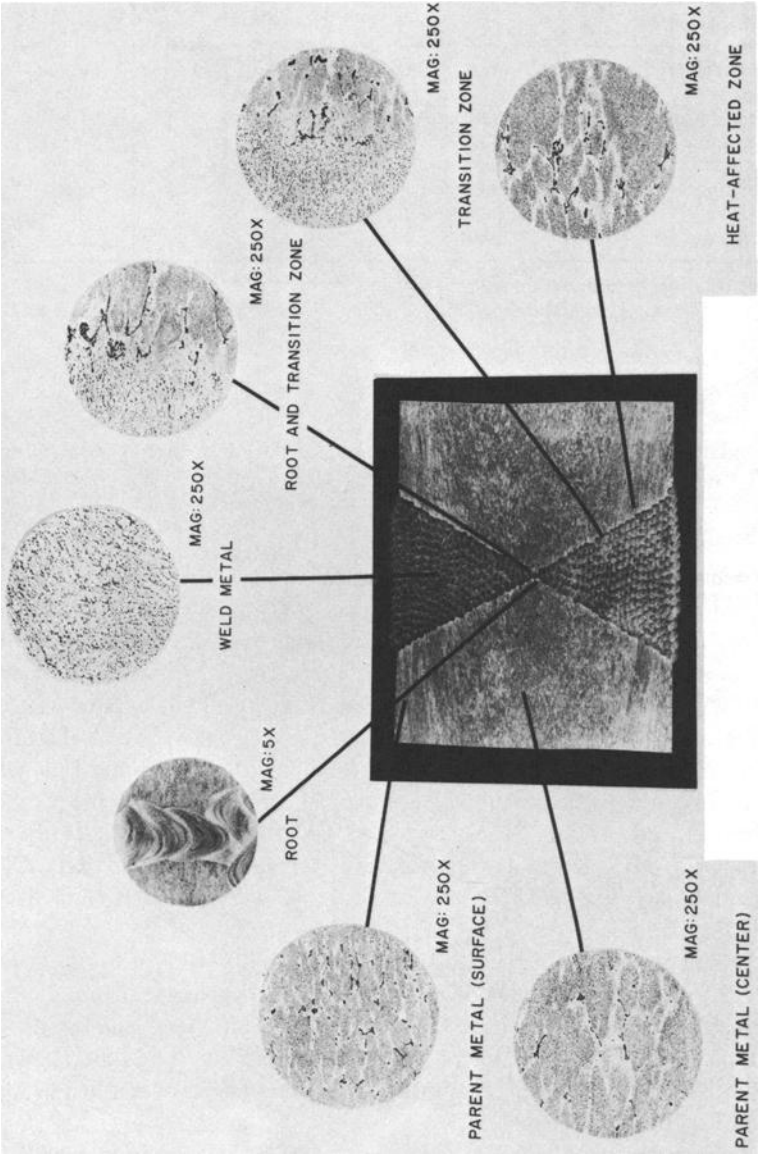


FIG. 1—Metallographic examination of groove weld in 7.7-in.-thick 5083-0 plate made with 5183 filler metal with the gas-metal arc (MIG) method (reduced one third for reproduction).

$$\text{Tear strength, psi} = \frac{P}{A} + \frac{MC}{I} = \frac{P}{bt} + \frac{3P}{bt} = \frac{4P}{bt}$$

$$\text{Unit propagation energy, in.-lb per sq in.} = \frac{\text{energy to propagate a crack}}{bt}$$

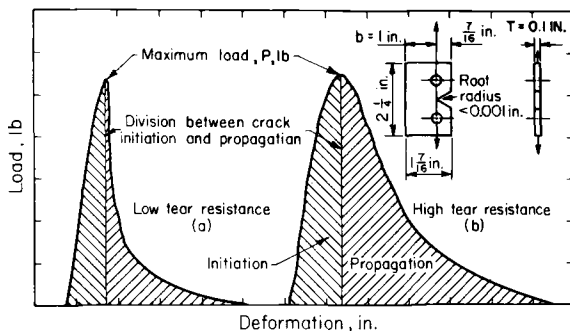


FIG. 2—Tear test specimen and representative tear test curves.

LEGEND FOR WELDS (PLAIN PLATE PER ASTM E399)

FIRST LETTER DESIGNATES CRACK TIP LOCATION: C-CENTER OF WELD
H-HEAT-AFFECTED ZONE
F-FUSION ZONE

SECOND LETTER DESIGNATES DIRECTION OF PRINCIPAL STRESS AT CRACK TIP WITH RESPECT TO WELD: P-PARALLEL
N-NORMAL
T-THROUGH

THIRD LETTER DESIGNATES DIRECTION OF CRACK GROWTH

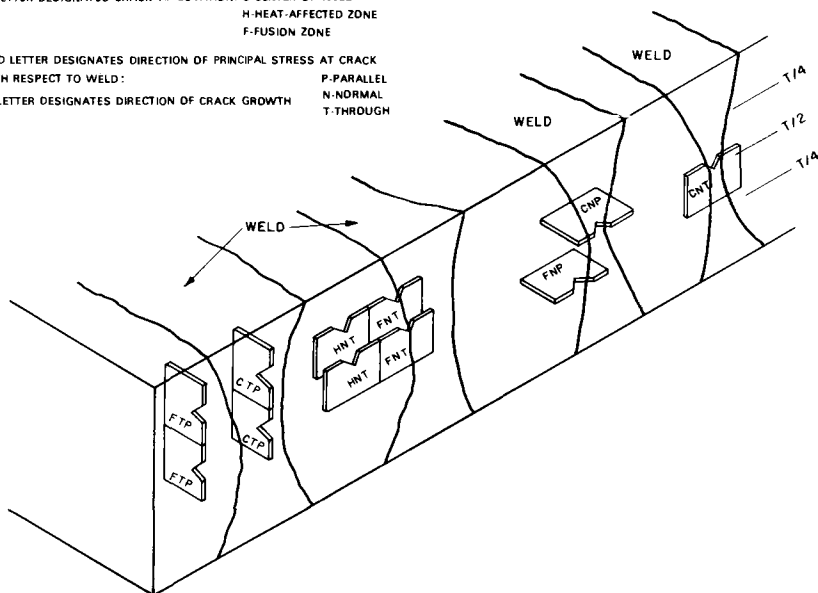


FIG. 3—Tear specimens in welded plate.

autographic tension and tear test load-deformation curves were obtained using a strain transfer device in conjunction with the autographic extensometer.

Fracture Toughness Tests

Three types of fracture toughness specimens were tested as illustrated in Fig. 4:

A. Compact tension fracture toughness tests of specimens from the parent plate and welds (Fig. 5).

B. Notch-bend specimens from the long-transverse, through-thickness, and across-width orientations (T-S, T-L) of the plain plate, and two cross-weld orientations from the welded panel (Fig. 6).

C. One long-transverse (T-L) 4-in.-thick, 44-in.-wide edge-notched tension specimen machined from the center of the thickness of the 7.7-in. plate.

Compact Tension Specimens—Fatigue cracks were initiated in the compact tension specimens in Sonntag SF-6 machines with about 100 000 cycles at a stress intensity of about $20 \text{ ksi}\sqrt{\text{in.}}$, and propagated to the desired length by about 200 000 cycles at a stress intensity of about $16 \text{ ksi}\sqrt{\text{in.}}$ in Krouse fatigue machines.

After fatigue precracking, the specimens were tested in a horizontal-bed Marquardt testing machine to measure K_{Ic} . The setup for the tests at -320°F is shown in Fig. 7. The tests at -320°F were made in exactly the same manner as those at room temperature except that the specimens were immersed almost completely in a tank of LN_2 , so that only the upper surface and the displacement gage were above the LN_2 level. Even though the temperature of the gage was depressed because of its proximity to the LN_2 , its usefulness in obtaining the secant offsets was not affected. The temperature of the specimen was allowed to stabilize for 5 min before testing; the time necessary for stabilization was checked on the first test using a thermocouple embedded in one specimen slightly off-center from the root of the notch.

In each test a load-crack opening displacement curve was obtained on an X - Y plotter, and the curve was analyzed in accordance with ASTM Method E 399[17]. A 5 percent secant offset line was constructed, and, if the basic requirements for validity were met, the load at 5 percent secant intercept was used to calculate the K_Q value (candidate value of K_{Ic}) with the following equation[17]:

$$K_Q = \frac{P_5}{BW^{1/2}} \left[29.6 \left(\frac{a}{W} \right)^{1/2} - 185.5 \left(\frac{a}{W} \right)^{3/2} + 655.7 \left(\frac{a}{W} \right)^{5/2} - 1017.0 \left(\frac{a}{W} \right)^{7/2} + 638.9 \left(\frac{a}{W} \right)^{9/2} \right]$$

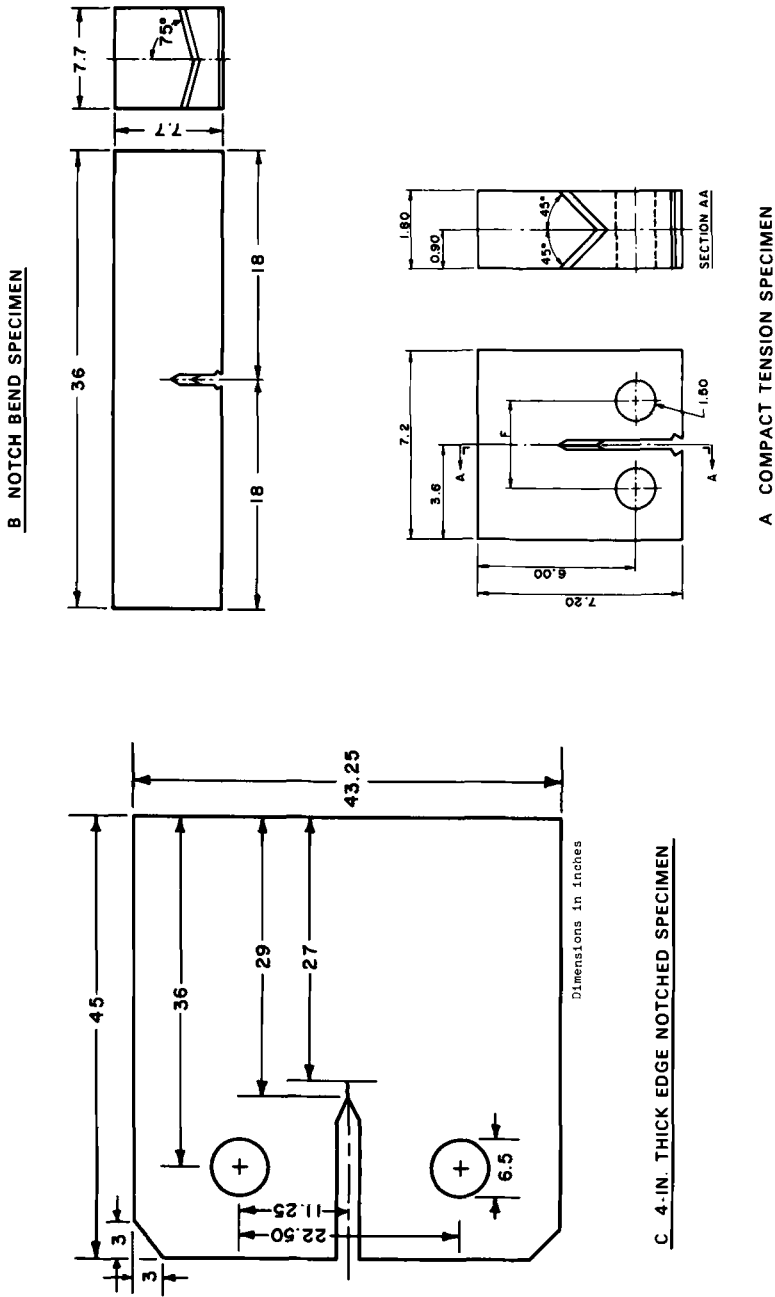


FIG. 4—Fracture toughness specimen.

LEGEND FOR WELDS (PLAIN PLATE PER ASTM E399)

FIRST LETTER DESIGNATES CRACK TIP LOCATION: C-CENTER OF WELD
H-HEAT-AFFECTED ZONE
F-FUSION ZONE

SECOND LETTER DESIGNATES DIRECTION OF PRINCIPAL STRESS AT CRACK TIP WITH RESPECT TO WELD:

P-PARALLEL
N-NORMAL
T-THROUGH

THIRD LETTER DESIGNATES DIRECTION OF CRACK GROWTH

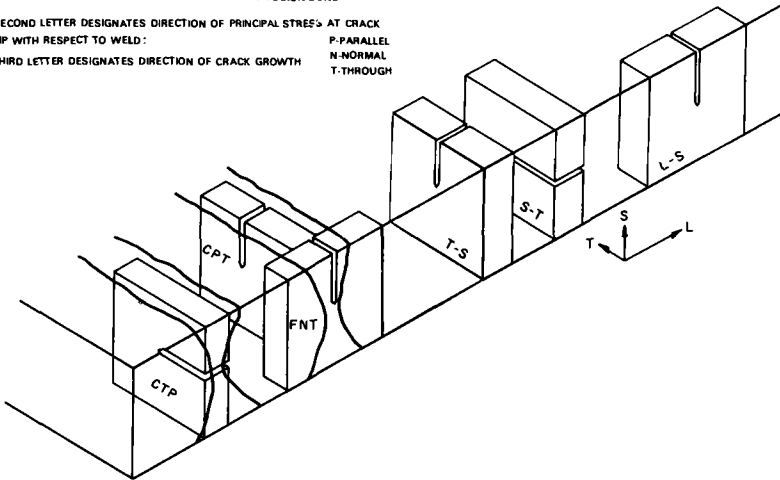


FIG. 5—Compact tension specimens in plain and welded plate.

LEGEND FOR WELDS (PLAIN PLATE PER ASTM E399)

FIRST LETTER DESIGNATES CRACK TIP LOCATION: C-CENTER OF WELD
H-HEAT-AFFECTED ZONE
F-FUSION ZONE

SECOND LETTER DESIGNATES DIRECTION OF PRINCIPAL STRESS AT CRACK TIP WITH RESPECT TO WELD:

P-PARALLEL
N-NORMAL
T-THROUGH

THIRD LETTER DESIGNATES DIRECTION OF CRACK GROWTH

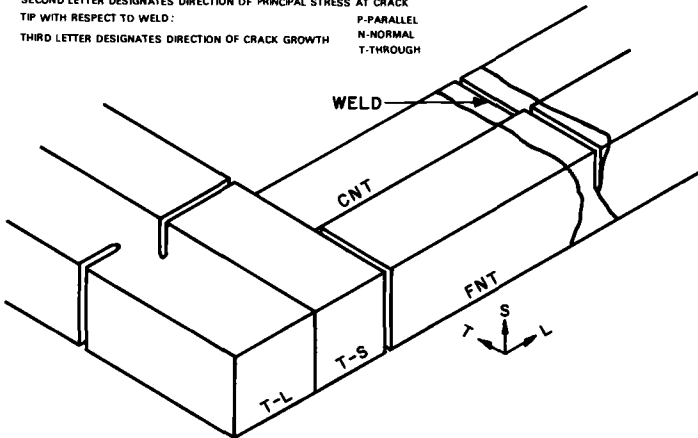


FIG. 6—Notch bend specimens in plain and welded plate.

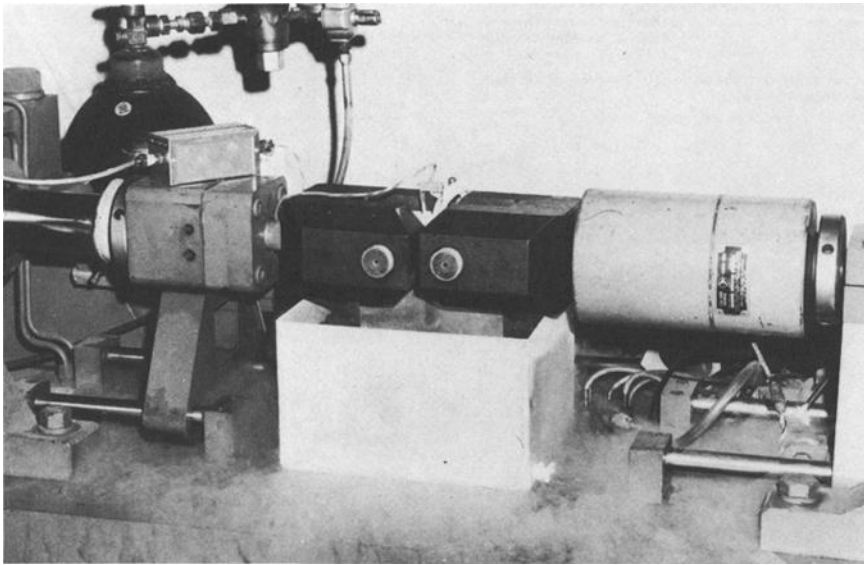


FIG. 7—Test setup for compact tension fracture toughness specimens at -320°F .

where

P_5 = load at 5 percent secant offset, lb,

B = thickness of specimen, in.,

W = width of specimen, in., and

a = crack length, in.

In all tests, a K_{\max} was also calculated using the foregoing relationship, except that P_{\max} , the maximum load developed by the specimen, was substituted for P_5 .

Notch Bend Specimens—The notch bend specimens were fatigue precracked in Alcoa Laboratories' 50 000-lb structural fatigue machines. The cracks were initiated at about $20 \text{ ksi}\sqrt{\text{in.}}$, and extended to the appropriate lengths at about $16 \text{ ksi}\sqrt{\text{in.}}$, as for the compact tension specimens. After precracking, the specimens were tested in inverted simple three-point bending (that is, center point load on the bottom) in a 300 000-lb Amsler testing machine; the test setup is shown in Fig. 8. The inverted position was employed so that the crack opening displacement gage could be mounted on the top of the specimen. The tests at -260 and -320°F were made in exactly the same manner as those at room temperature, except that (a) for -260°F , the specimens were immersed in LN_2 until the center-thickness temperature reached -270°F , then removed from the LN_2 and allowed to warm while enveloped in the vapor of boiling LN_2 until the

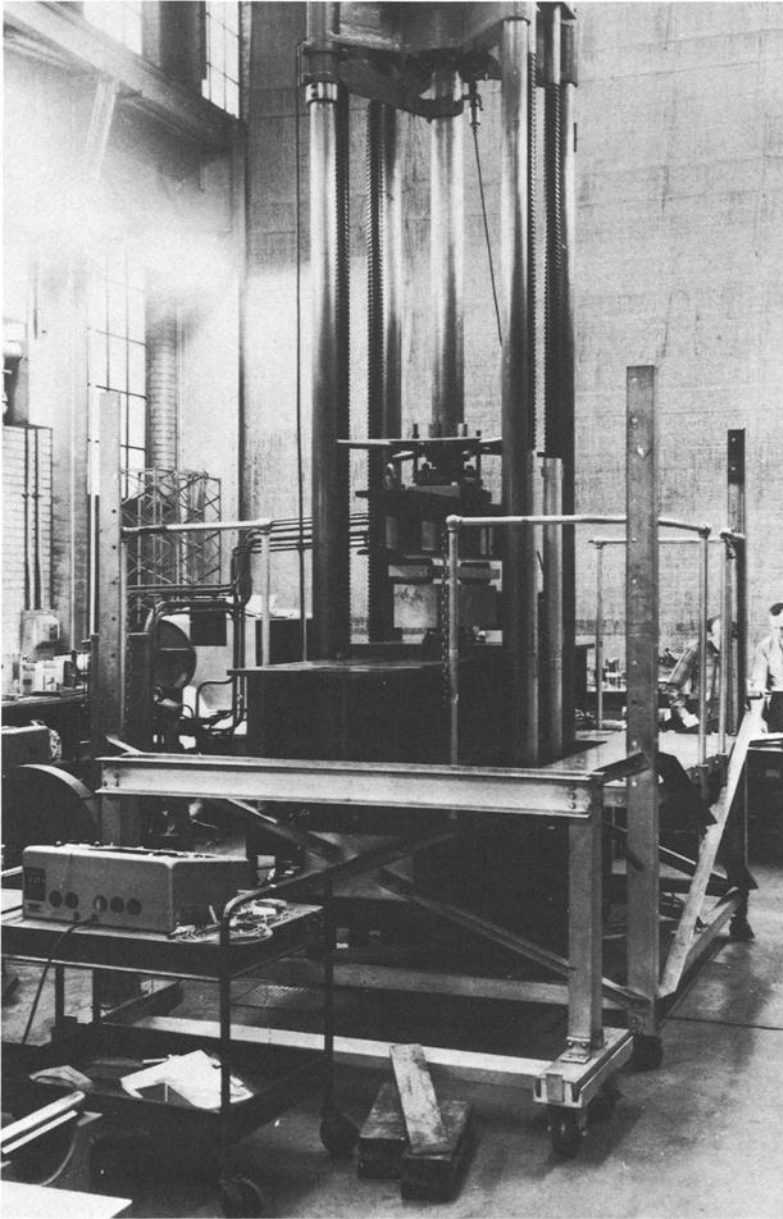


FIG. 8—Overall view of the test setup for 7.7-in. notch bend fracture toughness specimens.

center and surface temperatures were stabilized at $-260 \pm 5^\circ\text{F}$ and, (b) for -320°F , the specimens were immersed almost completely in a tank of LN_2 , such that only the upper surface and the displacement gage were above the LN_2 level. The temperature of each specimen was allowed to stabilize 30 min before testing.

In each test, load-crack opening displacement curves were plotted on an X - Y plotter, and the curves were analyzed as required by ASTM Method E 399, a 5 percent secant offset line was constructed, and, if certain basic requirements were met, a K_Q value (candidate value of K_{Ic}) was calculated by the following equation[17]:

$$K_Q = \frac{P_5 S}{B W^{3/2}} \left[2.9 \left(\frac{a}{W} \right)^{1/2} - 4.6 \left(\frac{a}{W} \right)^{3/2} + 21.8 \left(\frac{a}{W} \right)^{5/2} - 37.6 \left(\frac{a}{W} \right)^{7/2} + 38.7 \left(\frac{a}{W} \right)^{9/2} \right]$$

where

P_5 = load at 5 percent secant offset, lb,

S = span length, in.,

B = thickness of specimen, in.,

W = width of specimen, in., and

a = crack length, in.

In each test, a K_{\max} value was also calculated, using the foregoing equation but substituting the maximum load, P_{\max} for P_5 .

Large Edge-Notched Specimen—The large edge-notched specimen was precracked by fatigue loading in Alcoa Laboratories' structural fatigue machines at a stress intensity of about $10 \text{ ksi}\sqrt{\text{in.}}$ and a stress ratio of +0.1. About 2 000 000 cycles were required to grow the crack about 1.5 in. from the crack starter notch. Following fatigue precracking, the specimen was fractured in the Southwark 3 000 000-lb testing machine; the specimen is shown in the cleaves in Fig. 9.

During the test, load-displacement curves as in Figs. 10 and 11 were obtained on X - Y plotters, using two measurements of displacement. In one case (Fig. 10), clip gages were mounted in integrally machined knife edges in the crack starter slot, and, as the test progressed, successively larger gages were installed to obtain a complete curve through the maximum load point. In the other case (Fig. 11), the displacement of the cleaves (load-points) was obtained with a string-displacement meter. To supplement these data, periodic visual observations were made of surface crack lengths.

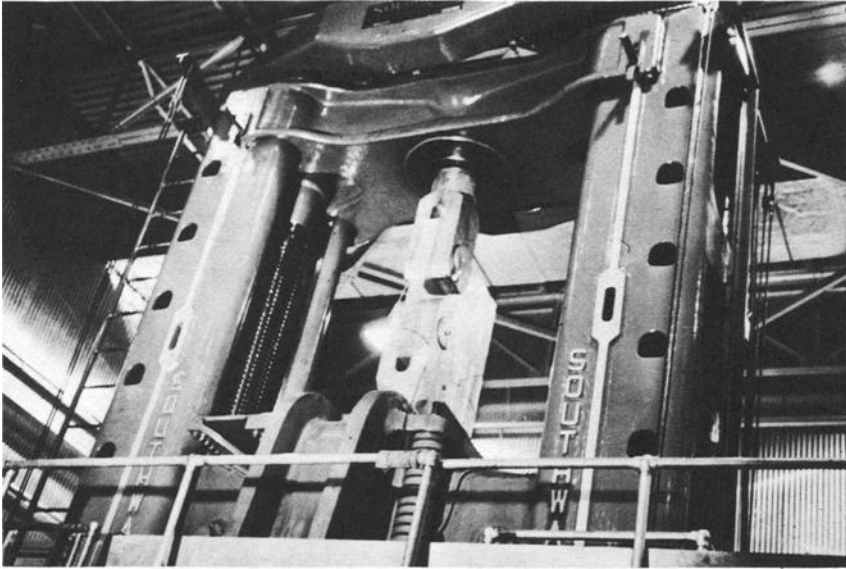


FIG. 9—Setup for fracturing edge-notched specimen in Southwark 3 000 000-lb testing machine.

Following the test, the original crack length was measured on the fracture surface, and the maximum nominal net-section stress, the maximum stress intensity, and the work done (energy absorbed) in producing the fracture were calculated.

The stress intensity relationship utilized in calculating precracking and fracture conditions was that in Fig. 8 of Ref 18. No plastic zone correction was used in the calculations.

Results

Tension Tests

The individual and average results of the tension tests of 1/2-in. diameter tension specimens from the 5083-O plate and 5183 welded panels are shown in Tables 3 and 4, respectively.

The tensile and yield strengths of the 7.0-in. plate (Table 3) are 1 to 7 ksi above those of the 7.7-in. plate, the biggest difference being in the short-transverse (S-T) tensile strength. The strengths in the longitudinal and long-transverse directions are generally quite similar, while the strengths in the short-transverse direction are generally 5 to 15 percent lower. Elongations are highest in the longitudinal direction and lowest in the short-transverse direction, with the latter being about 1/4 to 2/3 of the values in the longitudinal direction.

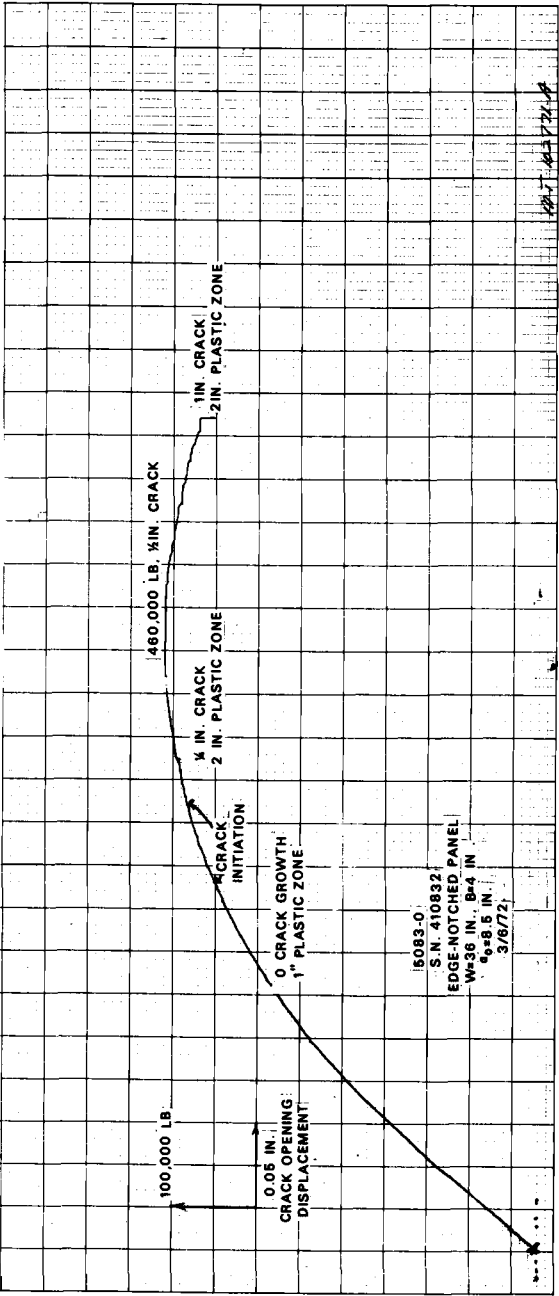


FIG. 10—Load versus crack-opening displacement curve for 4-in. edge-notched fracture toughness specimen.

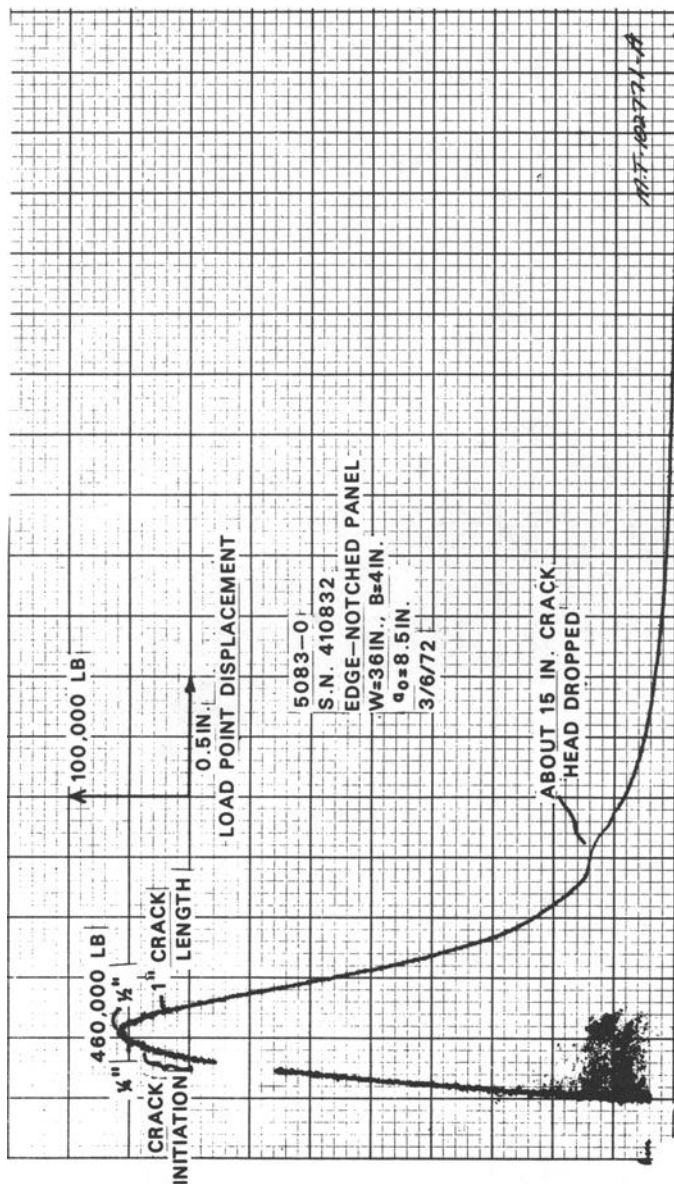


FIG. 11--Load versus load-point displacement curve for 4 in. edge-notched fracture specimen.

TABLE 3—Tensile properties of some thick 5083-0 plate at room temperature, -260 and -320° F.

Specimen Thickness, in.	Location in Thickness	Temperature, °F	Longitudinal (L-T)				Long-Transverse (T-L)				Short-Transverse (S-L)			
			Tensile Strength, ksi	Yield Strength, ksi	Elongation in 4D, %	Reduction of Area, %	Tensile Strength, ksi	Yield Strength, ksi	Elongation in 4D, %	Reduction of Area, %	Tensile Strength, ksi	Yield Strength, ksi	Elongation in 4D, %	Reduction of Area, %
7.0	T/4, T/2 ^a	RT	45.0	19.7	24.2	34	45.0	20.8	18.8	21	42.6	20.4	11.2	12
		-260	54.4	21.6	33.0	39	56.4	23.8	24.0	24	46.8	22.6	10.0	11
		-320	59.8	22.5	37.5	35	60.0	23.6	24.5	21	47.8	22.8	9.5	11
7.7	center	RT	41.1	18.7	15.0	14	38.0	17.5	14.0	14	35.6	16.8	10.0	11
		-320	54.3	21.1	15.0	19	50.9	...	15.5	17	45.8	19.6	11.7	13
	midway	RT	39.6	17.6	22.2	27	39.4	18.1	17.5	21
		-320	55.4	20.5	26.0	26	52.6	20.8	19.5	21
	surface	RT	41.2	18.4	24.8	29	39.3	18.0	17.2	16
		-320	57.7	21.0	36.8	33	53.6	20.4	21.5	20
Minimum values 5.001 to 7.000 7.000 to 8.000		RT	37	15	14
		RT	36	14	12

^a T/4 for L-T, T-L; T/2 for S-L.^b RT = room temperature.^c Not obtained; extensometer did not function properly.

TABLE 4—Tensile properties of 5183 welds in 7.0 and 7.7-in. 5083-0 plate.

Thickness, in.	Orientation in Weld	Location in Thickness	Room Temperature					-260°F					-320°F				
			Tensile Strength, ksi	Yield Strength, ksi	Elonga- tion in 4D, %	Reduction of Area, %	Tensile Strength, ksi	Yield Strength, ksi	Elonga- tion in 4D, %	Reduction of Area, %	Tensile Strength, ksi	Yield Strength, ksi	Elonga- tion in 4D, %	Reduction of Area, %	Tensile Strength, ksi	Yield Strength, ksi	Elonga- tion in 4D, %
7.0	cross weld fusion zone	center	43.7	25.0	16.2	23	56.2	29.8	19.0	22	60.3	30.1	19.0	18			
		midway	38.4	22.8	12.7	12	49.2	26.2	11.0	16	49.4	26.2	9.8	14			
7.7	cross weld	center	35.8	22.5	6.5	20	57.0	27.3	15.0	18			
		midway	39.8	20.9	18.2	30	57.2	24.4	25.0	29			
	parallel	surface	40.4	21.6	17.5	26	53.8	24.2	20.5	23			
		center	43.8	24.5	23.5	31	58.0	28.1	15.5	18			
	fusion zone	midway	43.3	24.2	22.5	29	58.0	28.1	15.5	18			
		center	41.1	24.4	15.5	19	55.6	27.7	15.0	17			
heat affected zone		midway	41.3	23.1	16.5	25	58.7	26.9	20.5	21			
		surface	42.2	23.1	21.0	26	59.3	27.0	23.5	25			
		center	39.9	19.7	14.0	19	51.5	25.8	10.5	12			
		midway	39.7	18.5	22.0	31	56.4	21.1	31.5	29			

This is normal for aluminum alloy plate. Even in the short-transverse direction, the elongations are relatively high, ranging from 9.5 to 11.7 percent. There is little variation in strength through the thickness, but elongations are lowest at the center and highest near the surfaces.

At -320°F , the tensile strengths and tensile yield strengths in the longitudinal and long-transverse directions average about 35 and 15 percent, respectively, greater than the comparable room temperature values; in the short-transverse direction the differences are generally smaller. For the one lot evaluated at -260°F , the tensile strengths are 2 to 10 percent lower than at -320°F , while the yield strengths were nearly equal to the values at -320°F . The elongation and reduction of area values at -260 and -320°F are as great as or greater than the corresponding room temperature values, the only exception being for the 7.0-in. plate in the short-transverse direction, but even in this case the lowest value is relatively high, 9.5 percent, as noted previously.

At -260 and -320°F as at room temperature, the properties of the 7.0 and 7.7-in. plate are a little lower than those of thinner plate[2-9]; this is to be expected with plate of this great thickness because of the differences in working during fabrication, a fact also indicated by the lower specified minimum values for the thicker plate[11].

The tensile properties of the welds (Table 4) are generally equal to or greater than those of the plain plate, at all temperatures. The tensile and joint-yield strengths across the weld at both room temperature and at -320°F are slightly lower than those parallel to the weld. The strengths in the fusion and heat-affected zones are lowest, though even the lowest values are equal to or greater than the short-transverse properties of the parent metal. It is particularly noteworthy that, though there is some variation, the values of elongation and reduction in area of the weldment are generally as great as or greater than those of the parent material.

Tear Tests

The results of the tear tests are shown in Table 5 for the plain plate and in Table 6 for the welds; unit propagation energies are summarized in Fig. 12.

For both the plain material and the welds, the tear-yield ratios (tear strength/yield strength) and unit propagation energies in all three directions and at room temperature (RT), -260 and -320°F are extremely high, and indicate that both parent metal and weld are extremely tough. The fact that all tear-yield ratios are equal to or greater than 2.0 indicates that these materials have a great capability for plastically deforming in the presence of a severe stress raiser and, therefore, great resistance to crack initiation. The unit propagation energies show more directionality than the tear-yield ratios; typical of the case for aluminum alloys, the energies are highest in the longitudinal direction (L-T) and

TABLE 5—Tear resistance of some thick 5083-0 plate at room temperature, -200 and -320°F.

Thickness, in.	Location	Temper- ature, °F	Longitudinal (L-T)				Long-Transverse (T-L)				Short-Transverse (S-L)			
			Tear Strength, ksi	Tear Strength, Yield Strength	Energy Required to Initiate a Crack, in-lb	Unit Propagation Energy, in-lb/in. ²	Tear Strength, ksi	Tear Strength, Yield Strength	Energy Required to Initiate a Crack, in-lb	Unit Propagation Energy, in-lb/in. ²	Tear Strength, ksi	Tear Strength, Yield Strength	Energy Required to Initiate a Crack, in-lb	Unit Propagation Energy, in-lb/in. ²
7.0	T/4, T/2 ^a	RT ^b	51.4	2.61	49.8	1075	49.1	2.35	37.0	830	44.2	2.16	26.0	500
		-260	60.8	2.81	68.4	1355	57.2	2.41	52.5	1080	49.8	2.20	30.6	590
7.7	center, T/2	-320	59.4	2.64	67.6	1440	57.6	2.44	45.8	1250	48.4	2.12	24.8	590
		RT	43.6	2.33	36.8	755	40.0	2.29	27.1	550	37.8	2.25	18.5	475
	midway, T/4	-320	53.8	2.55	60.0	990	48.3	2.42	39.9	765	44.4	2.26	28.1	605
		RT	44.0	2.38	44.1	830	41.4	2.27	31.1	625	38.2	2.27	17.6	525
	surface	-320	53.6	2.61	69.0	1125	49.4	2.38	46.6	790	46.4	2.36	34.0	590
		RT	45.0	2.45	39.7	885	41.0	2.28	29.6	730
		-320	54.6	2.60	66.0	1160	48.6	2.38	44.2	755

^a T/4 for L-T, T-L; T/2 for S-L.^b RT = room temperature.

TABLE 6—Results of tear tests of 5183 welds in thick 5083-0 plate.

Position	In Thickness	Designation ^a	Room Temperature				-260°F				-320°F			
			Tear Strength, ksi	Yield Strength	Energy Required to Initiate a Crack, in-lb	Unit Propagation Energy, in-lb/in. ²	Tear Strength, ksi	Yield Strength	Energy Required to Initiate a Crack, in-lb	Unit Propagation Energy, in-lb/in. ²	Tear Strength, ksi	Yield Strength	Energy Required to Initiate a Crack, in-lb	Unit Propagation Energy, in-lb/in. ²
Deposited metal	T/2	CNT	60.0	2.40	69	980	69.8	2.34	95	1380	62.2	2.05	45	965
	Through weld	CNP	56.8	2.27	50	910	70.0	2.35	89	1360	64.7	2.13	46	1015
	Cross weld	CTP	60.1	2.45	84	1375	77.8	2.71	134	1255
	Along weld	CTP	52.6	2.17	45	1090	64.2	2.24	67	940
Fusion zone	T/2	FNT	50.0	2.22	39	690	60.5	2.22	62	1010
	Through weld	FNT	59.0	2.59	61	960	68.3	2.61	70	1275	69.6	2.66	77	1335
	T/4	FNT	47.8	2.29	38	855	57.4	2.35	58	1265 ^b
	T/4	FNP	58.8	2.58	56	880	64.1	2.45	61	1260	65.4	2.50	60	1025
Cross weld	T/2	FNP	48.9	2.00	29	430 ^c	63.0	2.27	49	725 ^c
	Along weld	FTP	55.5	2.40	67	1270 ^b	57.1	2.12	51	825
Heat affected Parent metal (T-S)	T/2	HNT	46.9	2.38	38	830	58.1	2.61	70	1265
	T/4	HNT	47.4	2.56	49	840	56.3	2.67	72	1253 ^b

^a Legend for welds (plain plate per ASTM E 399):

T = heat affected zone, H = heat affected zone, and F = fusion zone.

S = center of weld, C = center of weld, T = through.

Second letter designates direction of principal stress at crack tip with respect to weld: P = parallel, N = normal, and T = through.

Third letter designates direction of crack growth.

^b Diagonal fracture^c Propagated largely through short-transverse direction in parent plate.

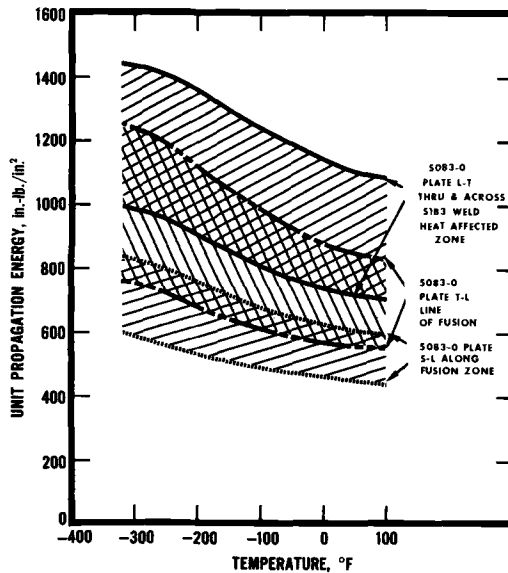


FIG. 12—Unit propagation energies in thick 5083-0 plate and welded panels.

lowest in the short-transverse (S–L) direction. The values for welds range from nearly equal to to above the corresponding orientations for the plain plate.

Since one of the principal uses of such data is to rate materials, it is appropriate to compare the average unit propagation energies for the 5083-0 plate and 5183 welds with those for some other aluminum alloys used in structural and aerospace applications as follows (room temperature)[16]:

Alloy and Temper	Unit Propagation Energy, in·lb/in. ²		
	L-T	T-L	S-L
2014-T651	270	180	...
2024-T351	730	500	...
2024-T851	200	120	...
6061-T651	850	790	...
7075-T651	230	150	...
7075-T7351	395	250	...
5083-0	850	730	500
5183 welds		(all orientations)	
Deposited metal		1090	
Fusion zone		865	
Heat-affected zone		835	

Such a comparison shows that the 5083-0 plate and 5183 welds are significantly tougher than alloys such as 7075-T7351, which are used in extremely critical aerospace applications. Even in the short-transverse direction, the values are as high as for many of the alloys in the longitudinal direction.

It is also particularly noteworthy that at -320°F the indexes were about as high as or higher than those at room temperature, as shown by the following average ratios:

Alloy and Temper	Temperature, $^{\circ}\text{F}$	Unit Propagation Energy, $\text{in}\cdot\text{lb}/\text{in.}^2$		
		L-T	T-L	S-L
5083-0	RT	850	730	500
	-320	1280	1020	590
5183 welds (Avg of all tests at 4 orientations)	RT -320	Weld Deposit	Fusion Zone	Heat- Affected Zone
		1090	865	830
		1065	985	1260

From the few comparisons available, the toughness of both the plain plate and the welds at -260°F ranges from almost as great as or greater than at -320°F . Thus, 5083-0 plate and 5183 welds retain their very high toughness to very low temperatures. From the similarity of results at -260 and -320°F , and published data for intermediate temperatures[2-9], it is clear that the toughness at -260°F may be taken to be just as high as at -320°F .

Fracture Toughness—Plane Strain

The results of the compact tension fracture toughness tests for the plain plate and welds at room temperature and at -320°F are shown in Table 7, and the results of the notch-bend fracture-toughness tests are shown in Table 8. The fracture surfaces of representative notch-bend specimens are shown in Figs. 13 and 14. There are three distinct regions shown in the photographs: (1) surface developed during the initial high-stress-intensity fatigue precracking, (2) surface developed during low-stress-intensity propagation of that fatigue crack to the final crack length for the K_{Ic} determination, and (3) failure surface created during the static K_{Ic} test.

A representative individual load-deformation curve from a notch-bend test at -320°F is reproduced in Fig. 15; the curves for all specimen types, orientations, and all locations in the parent alloy and in the weld were of the same type. In all

compact tension and notch-bend tests at room temperature, -260 and -320°F , a ductile tearing type of fracture was observed, with no evidence of any instability. The 5 percent offset line had no intrinsic value in indicating crack growth, as indicated by the gradual curvature of the load-crack opening displacement (COD) curves, and valid values of K_{Ic} could not be determined. The 5083-0 plate and the 5183 welds were so tough that the specimens simply were not large enough to develop sufficient stored elastic strain energy to cause self-sustaining, rapid crack growth. Even the 7.7-in. specimens were not thick enough to force plane-strain conditions on these materials; in fact, from the K_{max} values, it would be estimated from ASTM Method E 399[17] that specimens greater than 12 in. in thickness and 24 in. in width would be required to do so.

While values of K_{max} are not a recognized measure of the toughness, they and the specimen strength ratios support indications from the tear and notch tension tests that the toughness of the 5083-0 plate and 5183 welds at -260 and -320°F is as high as or higher than at room temperature. As shown in Fig. 16, the K_{max} values are about 15 percent higher at -320°F than at room temperature, and the K_{max} values for 5183 welds are comparable to those for 5083-0 in the L-T or T-L orientations.

Although no direct measurements of K_{Ic} could be obtained, it is of interest to use the combined data from the various toughness tests to make the best engineering estimate of what K_{Ic} may be for 5083-0 and 5183 welds. It should be noted that no evidence of unstable crack growth at elastic stresses was observed, and yet it is useful to speculate as to the conditions, if any, under which it might occur, so that conservative limiting crack sizes can be calculated.

		Projected K_{Ic} , ksi $\sqrt{\text{in.}}$	
		Room Temperature	-320°F
5083-0 plate	L-T	50	60
	L-S	55	60
	T-L and T-S	45	50
	S-L and S-T	35	40
5183 welds	across or through	50	60
	along root pass	35	45

From trends in other fracture data, the toughness at -260°F may be taken to be essentially equal to that of -320°F [2-9,19].

Rice et al[20-22] have recently proposed the J-integral as a means of estimating the fracture toughness of materials from appreciably smaller

TABLE 7—Results of compact-tension fracture toughness tests of some 7.7-in.-thick 5083-0 plate and 5183 welds.

Temperature, °F	Specimen Orientation ^a	Yield Strength, ^b ksi	Dimensions, in.		Crack Length, <i>a</i> _o , in.	Valid <i>K</i> _{Ic} Determined ^c	Maximum Load, <i>P</i> , lb	<i>K</i> _{max} , ksi √in.
			Thickness, <i>B</i>	Width, <i>W</i>				
RT ^d	L-S	16.8	1.800	6.006	3.199	no	20 200	48.7
			1.800	6.004	3.276	no	19 250	48.4
	T-S	18.1	1.800	6.001	3.311	no	16 175	41.6
			1.800	6.001	3.209	no	16 750	40.7
	S-T	16.8	1.800	6.001	3.238	no	14 750	36.4
			1.800	5.999	3.196	no	14 925	36.0
-320	L-S	19.6	1.800	6.005	3.243	no	21 250	52.5
			1.800	6.006	3.239	no	24 100	59.4
	T-S	20.8	1.800	6.004	3.291	no	20 325	51.6
			1.800	6.004	3.227	no	18 050	44.2
	S-T	19.6	1.800	6.000	3.237	no	16 950	41.8
			1.800	6.003	3.225	no	17 100	41.8

RT	CPT	24.2	Welded Panels		no	23 000	60.2
			1.800	6.008			
-320	CPT	24.2	1.800	6.003	no	16 375	55.8
			1.800	6.001	no	17 450	36.9
	CTP	24.2	1.800	6.002	no	16 750	34.6
			1.800	6.018	no	22 100	49.6
	FNT	20.8	1.800	6.017	no	22 200	48.5
			1.800	6.000	no	19 400	65.3
	CTP	28.7	1.800	6.003	no	20 400	63.4
			1.800	6.003	no	20 250	47.5
	FNT	21.2	1.800	6.002	no	20 700	43.6
			1.800	6.003	no	26 550	74.6
			1.800	6.016	no	26 850	73.3

^a Legend for welds (plain plate per ASTM E 399):

First letter designates crack tip location: C - center of weld, H - heat-affected zone, and F - fusion zone.

Second letter designates direction of principal stress at crack tip with respect to weld: P - parallel, N - normal, and T - through.

Third letter designates direction of crack growth.

^b Offset equals 0.2 percent; gage length 2 in.

^c Excess plasticity due to high toughness of 5083-0 and 5183 welds prevented valid K_{IC} measurement.

^d RT = room temperature.

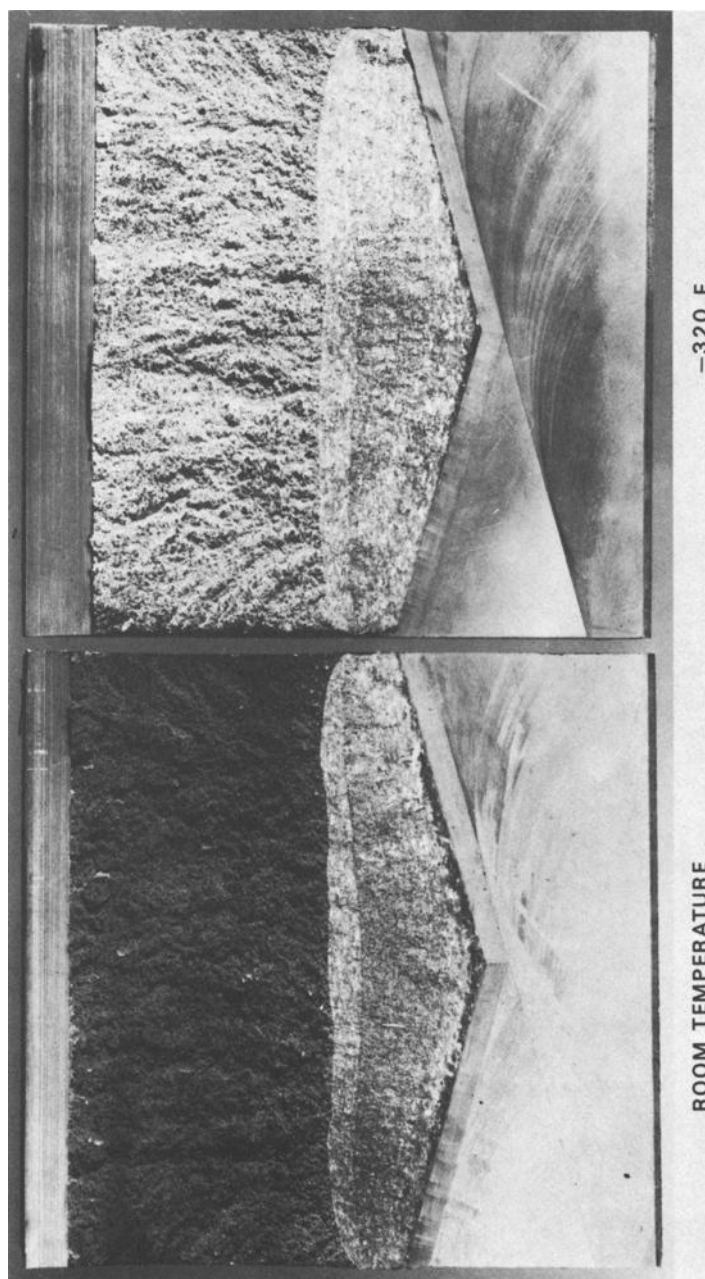


FIG. 13—Fracture surfaces of 7.7-in. notch bend fracture toughness specimens (TS-orientation) from 7.7-in.-thick plain 5083-0 plate (S-410801) (about $\times 0.6$).

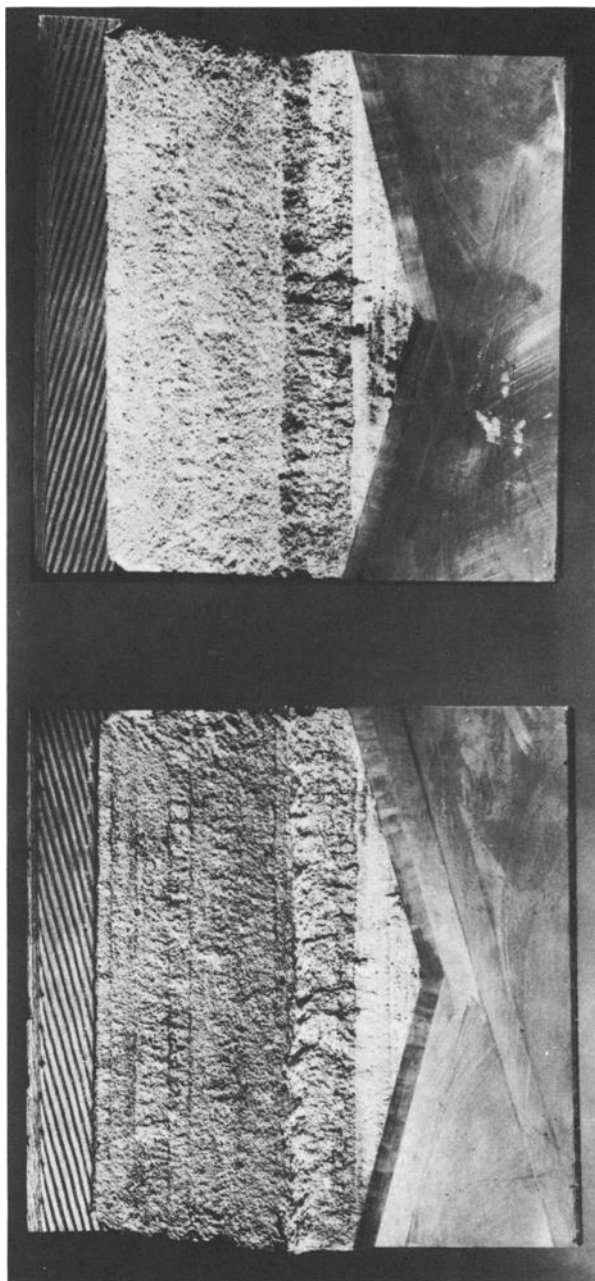


FIG. 14—Fracture surfaces of 7.7-in. notch bend fracture toughness specimens (FNT-orientation) from groove welded 7.7-in.-thick 5083.0 plate welded with 5183 IG electrode with the gas consumable electrode method testing at room temperature (S-410801) (about $\times 0.6$).

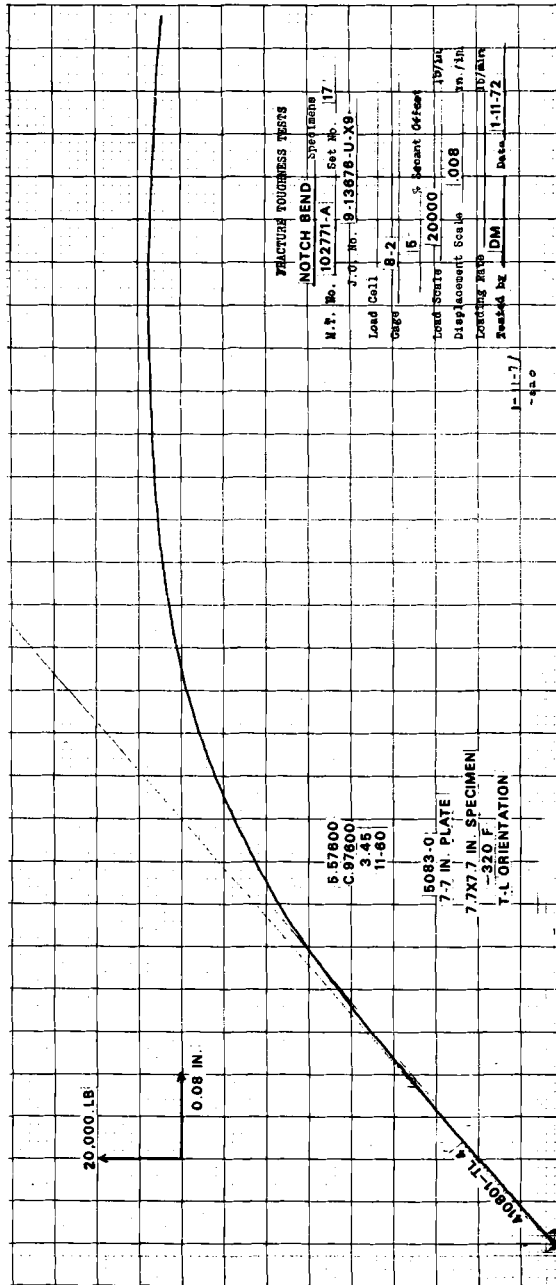


FIG. 15--Representative load versus crack opening displacement curves from notch bend test at -320°F .

specimens than required in compliance with ASTM methods. While the measurements taken in the notch bend tests in this program were not ideal for use with the J-integral method, some approximations can be made utilizing the load-displacement curves and Paris' single curve approximation that:

$$J_{Ic} = \frac{2fMd\theta}{b} \text{ or } J_{Ic} = \frac{P\Delta}{b} \left[1 + 0.036 \left(\frac{P}{P_L} \right)^2 \right]$$

where

J_{Ic} = toughness index, corresponding to G_{Ic} , in·lb/in.²;

M = bending movement in bend specimen, in·lb;

$d\theta$ = angle change of crack;

b = remaining ligament, in. = $W - a$;

Δ = displacement of load points in tension test, in.;

P = load at measurement point, lb; and

P_L = maximum load, lb.

With approximations of θ from the COD measurements from the bend tests and of Δ from similar data from the compact tension tests, it is possible to make gross estimates of J_{Ic} , the critical plane strain value of J , and from this calculate the equivalent K_{Ic} , namely,

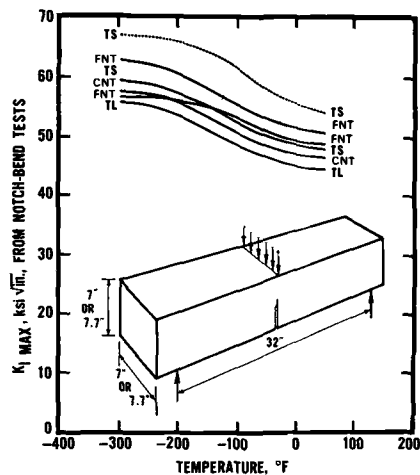


FIG. 16—Results of notch bend fracture toughness tests of 5083-0 plate and 5183 welds.

$$K_{Ic} = (E J_{Ic})^{1/2}$$

Estimates of K_{Ic} obtained in this manner range from 50 to 100 ksi $\sqrt{\text{in.}}$, dependent upon the assumed θ -COD and Δ -COD relationships, and for purposes of this paper will be taken solely to indicate that the conservative estimates of K_{Ic} just mentioned are reasonable.

Fracture Toughness—Mixed Mode

The load versus crack-opening displacement and load versus load-point displacement curves are shown in Figs. 10 and 11, respectively. The critical data from the test are as follows:

Maximum load, $P_{\max} = 460\,000$ lb

Original crack length, $a_o = 8.50$ in.

Crack length at maximum load, $a_{\max} \approx 9.0$

Energy to maximum load = 79 000 in·lb

Energy to fracture specimen = 186 000 in·lb

Unit propagation energy = 1720 in·lb/in.²

It is apparent from the curves in Figs. 10 and 11 that no crack instability developed, and that the specimen fractured by ductile tearing. The fact that net section yielding took place is confirmed by a calculation of the net section stress at maximum load

$$\sigma = \frac{P_{\max}}{B(W-a)^2} (4W - 2a) = \frac{460\,000}{4(36-9)^2} (4.36 - 2.9) = 19.9 \text{ ksi}$$

Thus, even in this very large specimen and under the very severe conditions of this test, the 4-in.-thick 5083-0 plate had the capability to deform plastically, yield, and fracture by ductile tearing.

Under those conditions, it is not possible to calculate a precise and valid value of K_c , but a lower bound K_c may be estimated from the maximum stress intensity developed by the specimen, namely [18]

$$K_{\max} = \frac{Pa^{1/2}}{BW} Y = \frac{(460\,000)3}{4.36} (10.6) = 102 \text{ ksi}\sqrt{\text{in.}}$$

No plastic zone correction on crack length was used; if it had been, the K_{\max} would have been about 15 to 25 percent higher.

Thus it appears that the K_c value for 4 in. 5083-0 plate in the transverse direction is in the same range as that for 1/2 to 2-in. plate [3,5], and may be substantially in excess of 100 ksi $\sqrt{\text{in.}}$. As with all other toughness indexes, it would be expected to be (a) even higher in the longitudinal direction, and (b) at least as high at -260 and -320°F as at room temperature.

It is also interesting to note from the energy values measured that despite the great size of the specimen, the unit energy required to initiate and propagate a crack ($1720 \text{ in} \cdot \text{lb/in.}^2$) is even greater than that in the small (0.1 in. thick) tear specimens ($800 \text{ to } 1200 \text{ in} \cdot \text{lb/in.}^2$), added evidence of the extreme toughness of this material.

As indicated earlier, Rice et al [20-22] have proposed the J-integral concept for the determination of fracture toughness based upon analysis of data for smaller specimens than required by a nominal linear elastic analysis. Paris' approximation of J procedure may be applied readily to the mixed-mode fracture toughness test described in this section, since displacement of the load points was measured. From Paris:

$$J_c = \frac{P\Delta}{b} \left[1 + 0.036 \left(\frac{P}{P_L} \right)^2 \right]$$

where

J_c = toughness index, corresponding to G_c , $\text{in} \cdot \text{lb/in.}^2$;

P = load at measurement point, lb;

P_L = maximum load, lb;

Δ = load point displacement, in.; and

b = remaining ligament, in. = $W - a$.

At maximum load, $J_c \approx 2380 \text{ in} \cdot \text{lb/in.}^2$, for which the corresponding K_c would be $154 \text{ ksi}\sqrt{\text{in.}}$.

Because of the newness of this concept, and the fact that it is as yet unproven, this will be taken only to be further evidence of the high toughness of the 5083-0, and that the use of $100 \text{ ksi}\sqrt{\text{in.}}$ in crack size calculation is a conservative procedure.

Conclusions

1. The exceptionally high toughness of thick 5083-0 plate and 5183 welds at room temperature, -260 and -320°F is demonstrated by the results of large-scale fracture toughness testing. No evidence of a fracture instability at elastic stresses was observed, even in K_{Ic} tests of 7.7-in.-thick notched bend specimens and in a K_c test of a 4-in.-thick and 44-in.-square edge-notched tension panel. Ductile tearing was observed in all cases with panels as thick as or thicker than those for critical structures such as LNG tanks.

2. Although the foregoing conclusions indicate that the application of fracture mechanics to the design of 5083-0 tanks is inappropriate, some conservative engineering estimates of K_{Ic} and K_c have been made from the results of the fracture tests. Those values are as follows:

	Orientation	Projected K_{IC} , ksi $\sqrt{\text{in.}}$	
		Room Temperature	-320° F
5083-0	L-T	50	60
	L-S	55	60
	T-L and T-S	45	50
	S-L and S-T	35	40
5183 welds	across or through	50	60
	along root pass	35	45
		Projected K_C , ksi $\sqrt{\text{in.}}$	
		Room Temperature	-320° F
5083-0 plate	T-L, and across or through 5183 welds	100	100

3. All available data confirm that the fracture toughness of 5083-0 plate and 5183 welds at -260°F is as high as or higher than at -320°F.

References

- [1] Howard, J. L., *Marine Technology*, Vol. 9, No. 3, July 1972, pp. 281-291.
- [2] Kaufman, J. G. and Wanderer, E. T., *Machine Design*, 11 Nov. 1965.
- [3] Kaufman, J. G., Holt, Marshall, and Wanderer, E. T., "Aluminum Alloys for Cryogenic Temperatures," presented at the Cryogenic Engineering Symposium of the Canadian Chemical Conference, Toronto, Ont., Canada, 7 June 1967.
- [4] Nelson, F. G., Kaufman, J. G., and Holt, Marshall, *Metals Engineering Quarterly*, Vol. 6, No. 1, Feb. 1966, pp. 48-54; also *Welding Journal*, Vol. 45, No. 7, July 1966, pp. 321s-329s.
- [5] Nelson, F. G., Kaufman, J. G., and Wanderer, E. T. *Advances in Cryogenic Engineering*, Vol. 15, 1970, pp. 91-101.
- [6] Lake, R. L., DeMoney, F. W., and Eiber, R. J., *Advances in Cryogenic Engineering*, Vol. 13 1968, pp. 278-293.
- [7] Nelson, F. G., Kaufman, J. G., and Wanderer, E. T., *Advances in Cryogenic Engineering*, Vol. 14, 1969, pp. 71-82.
- [8] Kaufman, J. G., Bogardus, K. O., and Wanderer, E. T., *Advances in Cryogenic Engineering*, Vol. 7, 1961, pp. 478-489.
- [9] Rice, L. P., Campbell, J. E., and Simmons, W. F., *Advances in Cryogenic Engineering*, Vol. 8, 1962, pp. 671-677.
- [10] Kelsey, R. A., Nordmark, G. E., and Clark, J. W., this symposium, pp. 159-185.
- [11] *Aluminum Standards and Data*, third edition, Jan. 1972, The Aluminum Association, New York.
- [12] Standard Specification for Aluminum-Alloy Sheet and Plate (Designation: B 209-72a), 1972 *Annual Book of ASTM Standards*, Part 6, pp. 110-141.
- [13] Section VIII (Pressure Vessels) and IX (Welding Qualifications), ASME Boiler and Pressure Vessel Code, 1971 Edition.
- [14] Standard Methods of Tension Testing of Metallic Materials (Designation: E 8-69), 1972 *Annual Book of ASTM Standards*, Part 31, pp. 195-214.
- [15] Standard Recommended Practice for Tension Testing of Wrought-Aluminum and Magnesium Alloy Products (Designation: B 557-72), 1972 *Annual Book of ASTM Standards*, Part 6, pp. 514-516.

- [16] Kaufman, J. G. and Holt, Marshall, "Fracture Characteristics of Aluminum Alloys," Aluminum Company of America, ARL Technical Paper No. 18, 1965.
- [17] Standard Method of Test for Plane-Strain Fracture Toughness of Metallic Materials (Designation: E 399-72), *1972 Annual Book of ASTM Standards*, Part 31, pp. 955-974.
- [18] Brown, W. F., Jr., and Srawley, J. E., *Plane Strain Crack Toughness Testing of High Strength Metallic Materials*, *ASTM STP 410*, American Society for Testing and Materials, 1967.
- [19] Kaufman, J. G. and Holt, Marshall, *Advances in Cryogenic Engineering*, Vol. 10, 1965, pp. 77-85.
- [20] Begley, J. A. and Landes, J. D. in *Fracture Toughness*, *ASTM STP 514*, American Society for Testing and Materials, 1972, pp. 1-20.
- [21] Landes, J. D. and Begley, J. A. in *Fracture Toughness*, *ASTM STP 514*, American Society for Testing and Materials, 1972, pp. 24-39.
- [22] Bucci, R. J., Paris, P. C., Landes, J. D., and Rice, J. R. in *Fracture Toughness*, *ASTM STP 514*, American Society for Testing and Materials, 1972, pp. 40-69.

R. A. Kelsey,¹ G. E. Nordmark,¹ and J. W. Clark¹

Fatigue Crack Growth in Aluminum Alloy 5083-0 Thick Plate and Welds for Liquefied Natural Gas Tanks

REFERENCE: Kelsey, R. A., Nordmark, G. E., and Clark, J. W., "Fatigue Crack Growth in Aluminum Alloy 5083-0 Thick Plate and Welds for Liquefied Natural Gas Tanks," *Fatigue and Fracture Toughness—Cryogenic Behavior, ASTM STP 556*, American Society for Testing and Materials, 1974, pp. 159-185.

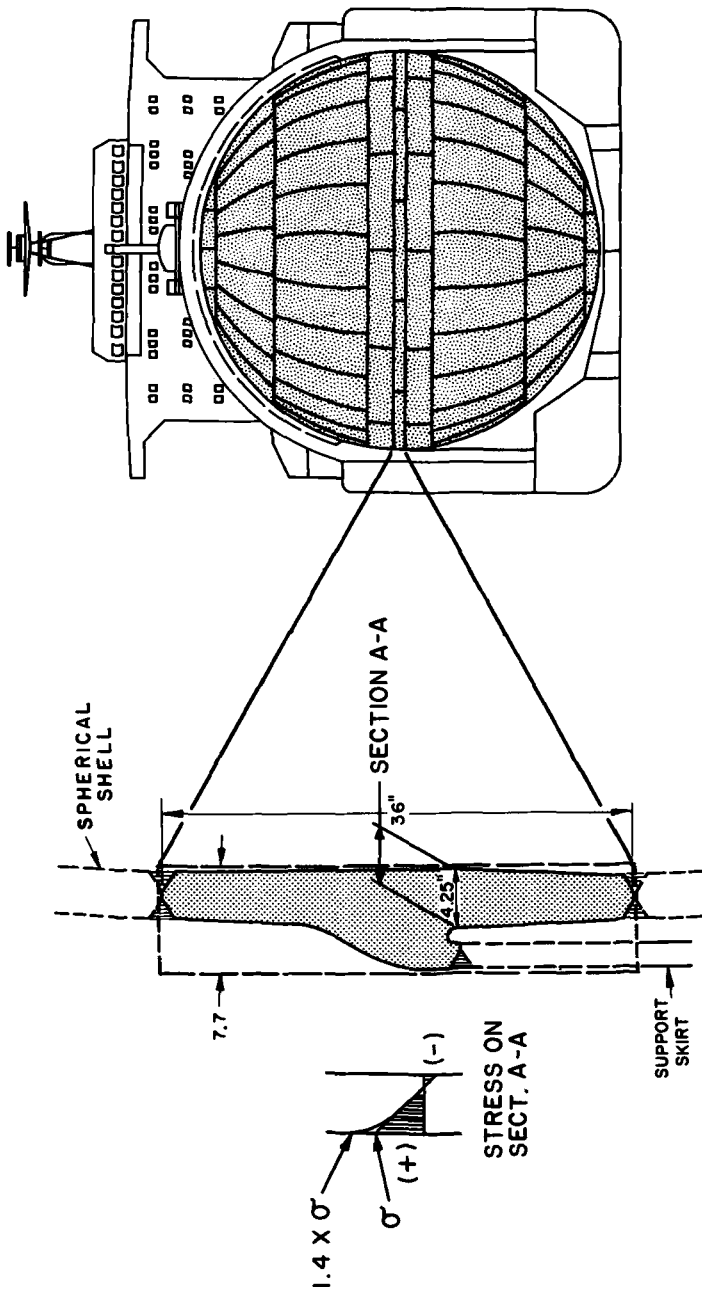
ABSTRACT: Data are presented on fatigue crack growth rates in thick plate of aluminum alloy 5083-0 for spherical liquefied natural gas cargo tanks. The investigation included: (1) determination of fatigue crack growth rates at room temperature and -320°F ; (2) comparison of fatigue crack growth in welds with that in parent material; (3) establishment of the rate and direction of growth of surface flaws under tension and combined tension and bending; and (4) comparison of the rate of growth of surface flaws in plates under spectrum loading with calculated rates based on data from constant amplitude loading of compact tension specimens.

KEY WORDS: fracture properties, aluminum, plates, welds, cryogenics, crack propagation, fatigue (materials), temperature, surfaces, tension, bending, amplitude, loading, spectra, tanks (containers)

Aluminum alloy 5083-0 is used widely in cryogenic applications because of its excellent low-temperature properties[1,2].² Until recently regulatory bodies have not required a consideration of fatigue crack growth in the design of such tanks, so data of this kind have been relatively limited[3,4]. However, designers are now being asked to predict whether possible flaws, which may be introduced during fabrication, will grow and cause leaks, and whether there is any danger of failure of the tanks. In addition, new designs[5] (Figs. 1 and 2) utilize aluminum alloy 5083-0 plate up to 7.7 in. thick, much thicker than the plate for which

¹ Engineering associate, engineer, and manager, respectively, Engineering Design Division, Alcoa Laboratories, Aluminum Company of America, New Kensington, Pa. 15068.

² The italic numbers in brackets refer to the list of references appended to this paper.



EQUATORIAL RING
MACHINED FROM 7.7-IN. 5083-O PLATE

FIG. 1—Liquefied natural gas spherical tank in ship hull (tank inside diameter equals 118 ft).

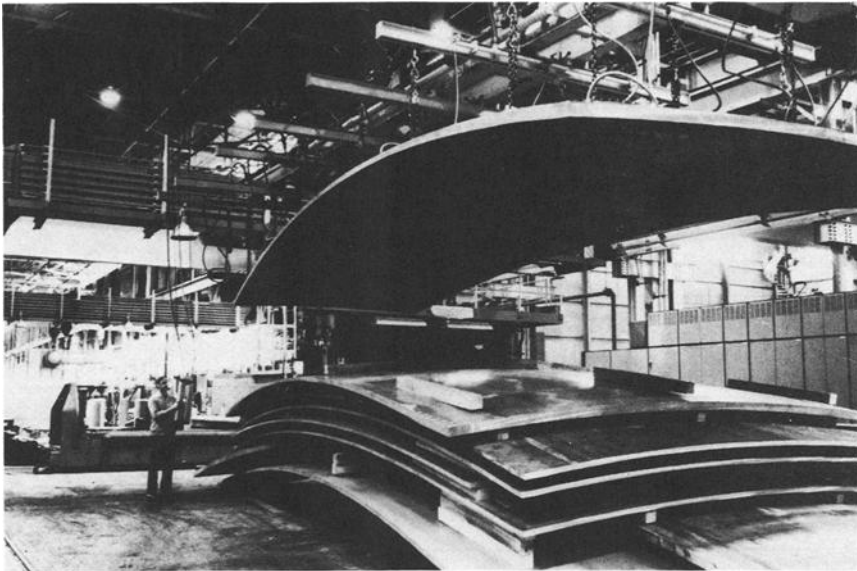


FIG. 2—Aluminum alloy 5083-0 trapezoidal segments for liquefied natural gas sphere formed by the Alcoa 570 process.

data were previously available. Therefore, an investigation was undertaken at Alcoa Laboratories, sponsored in part by Quincy Shipbuilding Division of General Dynamics Corporation, to establish fatigue crack growth data for 7.7-in.-thick plate of alloy 5083-0 and weldments in this plate made with alloy 5183 filler wire. Another part of this investigation, which was concerned with mechanical properties and fracture toughness of the plate and welds at various temperatures, is reported elsewhere[6].

The work described in this paper was aimed at: (1) establishing fatigue crack growth rates for thick 5083-0 plate, both at room temperature (RT) and at -320°F ; (2) comparing fatigue crack growth in welds with that in parent plate; (3) establishing the rate and direction of growth of surface flaws under tension and under combined tension and bending; and (4) comparing the rate of growth of surface flaws with calculated rates based on data from compact tension specimens.

Material

The tensile properties and chemical composition of the parent material are shown in Table 1, which also lists tensile strengths of the weld joints. Welds were made by the automatic gas metal arc process, using alloy 5183 filler wire. Typical welding procedures are summarized in Table 2. Note that some plates

TABLE 1—*Properties of 7.7-in. alloy 5083-0 plate and 5183 welds.*

Longitudinal Tensile Properties of Parent Material			
	Tensile Strength, ksi	Yield Strength, ksi	Elongation in 4D, %
Min, 7.001 to 8.000 in. ^a	41.2 36	18.4 14	21.4 12
Cross-Weld Tensile Properties (reduced-section specimens)			
Specimen Identification	Tensile Strength, ksi	Location of Fracture	
1	40.7	line of fusion	
2	41.7	line of fusion	
3	38.7	line of fusion	
Avg	40.4		
Weld qualification value ^b	36.0		
Chemical Composition of Parent Material			
Elements	Composition Limits ^a		
Silicon	0.40 max		
Iron	0.40 max		
Copper	0.10 max		
Manganese	0.30 to 1.0		
Magnesium	4.0 to 4.9		
Chromium	0.05 to 0.25		
Zinc	0.25 max		
Titanium	0.15 max		

^a *Aluminum Standards and Data*, 1972-1973 edition, The Aluminum Association.^b Section IX, ASME Boiler and Pressure Vessel Code, 1971 edition.

were welded in the full 7.7 in. thickness, whereas others were machined from 7.7-in. plate to a thickness of 1.5 or 1.8 in. before welding. Note also that some of the compact tension (CT) specimens were taken from alloy 5183 welds in 7.0-in. alloy 5083-0 plate.

Compact Tension Specimens

The CT specimens used to obtain basic fatigue crack growth data were oriented in the 7.7-in. plate and welds as shown in Fig. 3. These specimens were subjected to +1/3 stress ratio³ loadings in a 15 kip Krouse fatigue machine. The

³ Stress ratio: $R = (\text{minimum stress})/(\text{maximum stress})$

TABLE 2—Summary of typical welding procedures for preparing alloy 5183 welds in alloy 5083-0 plate.

(Double Vee, 60 deg included angle, GMA DCRP process)

Variable	Plate Thickness, in.		
	1.5 and 1.8 ^a	7.0	7.7
Electrode diameter, in.	1/16	1/16	1/16
Position	flat	vertical	vertical
Interpass temperature, °F (max)	150	150	150
Gas flow, ft ³ /h	80 (60 He + 20 Ar)	70 (50 He + 20 Ar)	80 (60 He + 20 Ar)
Welding current, A	240 to 260	220 to 250	230 to 260
Welding voltage, V	26 to 29	29 to 31	24 to 28
Welding speed, in./min	18	20 to 22	20 to 30
No. of passes	29 or 36	413	476 to 646

^a Machined from 7.7-in. plate.

room temperature tests were made in air having a relative humidity of 10 percent or less, since moisture would be low in the environment of a liquefied natural gas (LNG) cargo tank. To obtain crack propagation at cryogenic temperatures, an insulated chamber surrounding the specimen and fixtures was kept filled with liquid nitrogen (LN₂). When taking crack length readings, the LN₂ level was lowered to just below the crack. Thermocouple readings showed that a temperature of -320°F was maintained on the test section.

Fatigue cracks were initiated in the test specimens at higher stresses, or larger stress ranges than the test loads, and then the cracks were propagated about 0.10 in. at test loads before propagation measurements were taken.

Crack propagation was measured using a magnifying glass and a 0.05-in. grid printed on a plastic film overlay attached to the specimen. On specimens tested at low temperature and on some of the specimens tested at room temperature, the grid was photographically printed directly on the specimens.

The rate of fatigue crack propagation, da/dN , was determined from the crack length, a , versus number of cycles, N , data by fitting a second degree polynomial to three successive points, a_{i-1} , a_i , and a_{i+1} , with the derivative da_i/dN , being evaluated at the intermediate point only [7].

Fatigue crack growth data were obtained for values of ΔK in the range of 8 to 20 ksi $\sqrt{\text{in.}}$ Crack growth data versus ΔK are plotted in Figs. 4 to 9 and summarized in Table 3. Also shown in the figures are the curves giving the best fit to the test data for Forman's equation [8]:

$$\frac{da}{dN} = \frac{C(\Delta K)^n}{(1-R)K^* - \Delta K} \quad (1)$$

where

C and n = constants determined by least squares analysis of the crack propagation data,

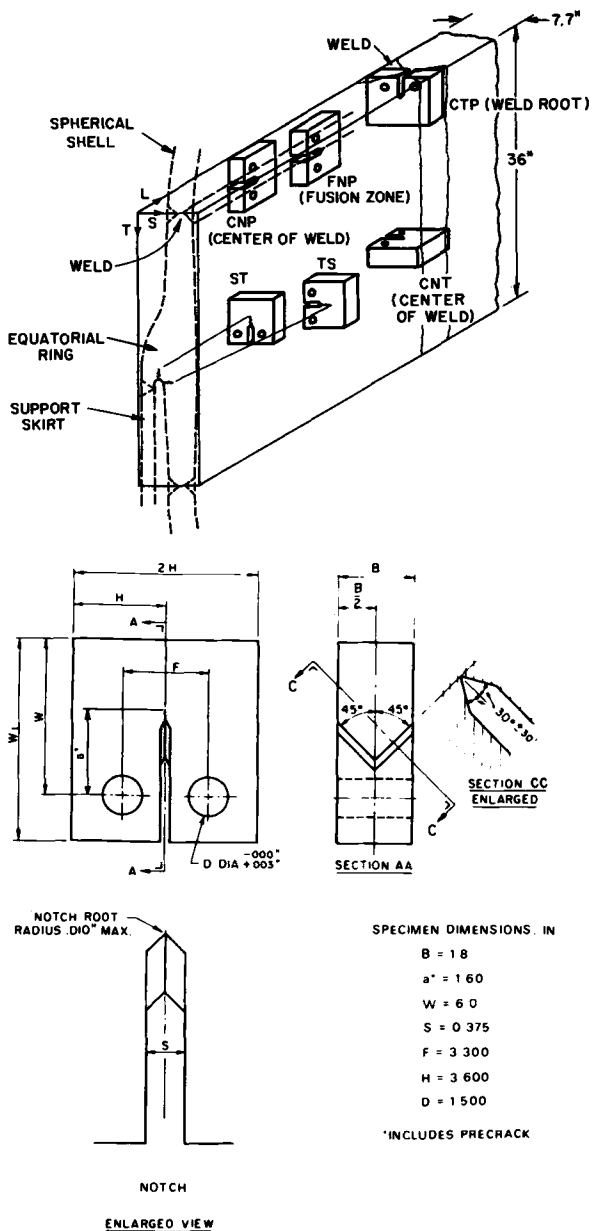


FIG. 3—Orientations of CT specimens in 7.7-in. alloy 5083-0 plate and alloy 5183 welds.

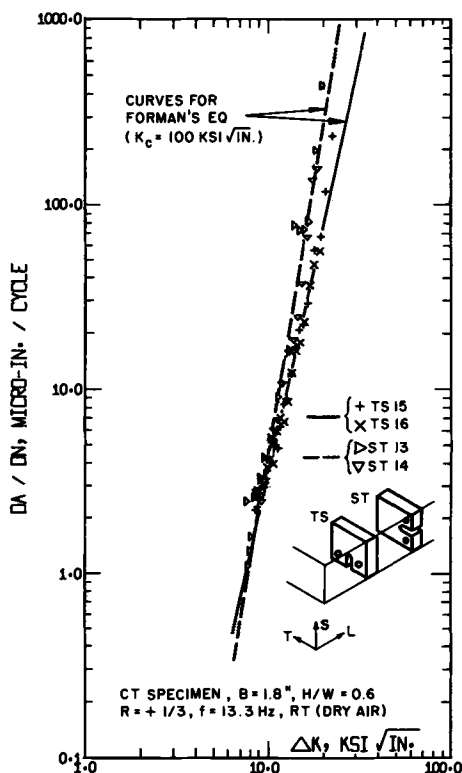


FIG. 4—Fatigue crack propagation in 7.7-in. aluminum alloy 5083-0 plate.

R = stress ratio, and

K^* = critical stress intensity for unstable crack growth.

Forman's equation was fitted to the test data by using K^* equal to either K_C or K_{IC} to provide equations representing growth under plane-stress or plane-strain conditions in the higher ΔK range. There is one difficulty with this approach. The use of either K_C or K_{IC} in the equation is intended to adjust the upper end of the curve to predict rapid fracture at the appropriate value of stress intensity. However, the curves derived using K_C or K_{IC} also differ from each other at the lower end (small ΔK values), where presumably the curve should not be affected by the ultimate mode of fracture. The constants C and n for Forman's equation for the various specimens are listed in Table 3.

The following comparisons of growth rate data can be made within the ΔK range tested:

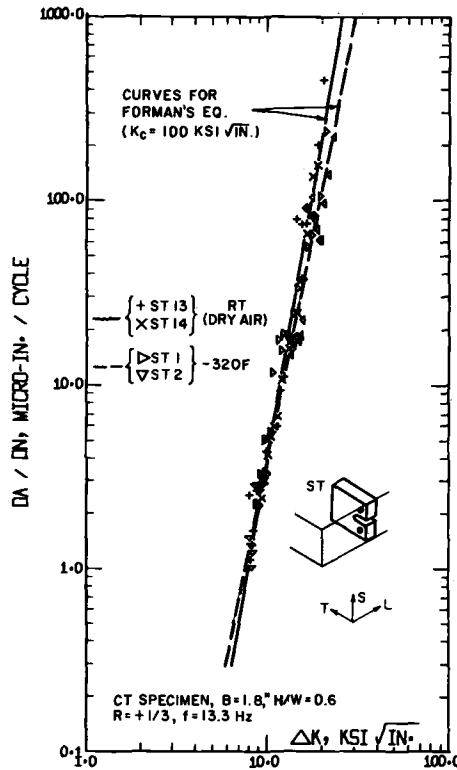


FIG. 5—Effect of temperature on fatigue crack propagation in 7.7-in. aluminum alloy 5083-0 plate.

1. In the parent material, growth rate at the high end of the ΔK range is slightly faster in the short-transverse (S-T) than in the long-transverse (L-T) direction (Fig. 4).

2. In the S-T direction of the parent material the growth rate at -320°F is slightly slower in the upper ΔK range than the growth rate at room temperature (Fig. 5).

3. Crack growth along the root of the weld (Fig. 6) is similar to that in the parent material in the S-T direction (Fig. 4).

4. There is a significant variation in growth rate as cracks growing through the welds in the thick plate (center of weld (CNT) direction) passed through the root of the weld (Fig. 7).

5. Except for the region where the crack passes through the root of the weld, the growth rate through welds in 7.7-in. material (Fig. 7) is similar to that measured along the welds in 1.8-in. material (Fig. 9).

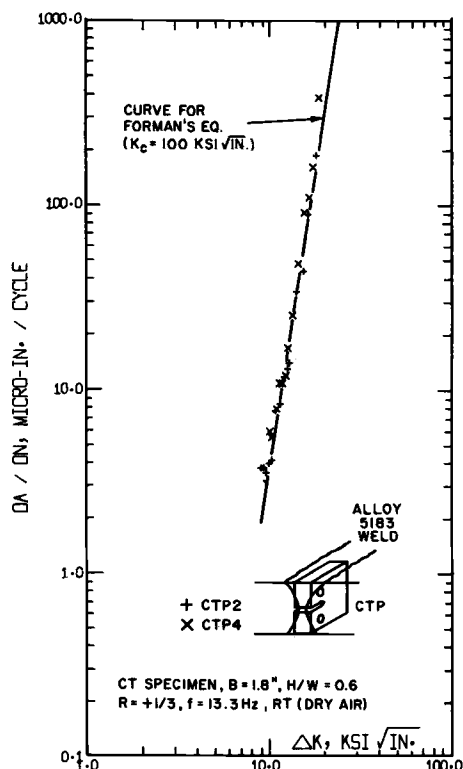


FIG. 6—Fatigue crack propagation in welded 7.7-in. aluminum alloy 5083-0 plate.

6. Crack growth rate through the weld in the 7.7-in. plate is similar at room temperature and at -320°F (Fig. 8), except for the region where the crack passes through the root of the weld, where the growth rate was somewhat slower at -320°F .

7. In welds in the 1.8-in. material the growth rate along the midwidth of the weld is similar to that measured along the edge of the weld (Fig. 9).

8. Finally, the average crack growth rate for the weld specimens is similar to that for the parent material.

Figures 7 and 9 show "upper bound" Forman's equations that give conservative crack growth predictions in comparison to most of the data of this investigation.

A previous investigation[3] of fatigue crack growth rate in alloy 5083-0 reported a significantly slower growth rate at -150°F than at room temperature.

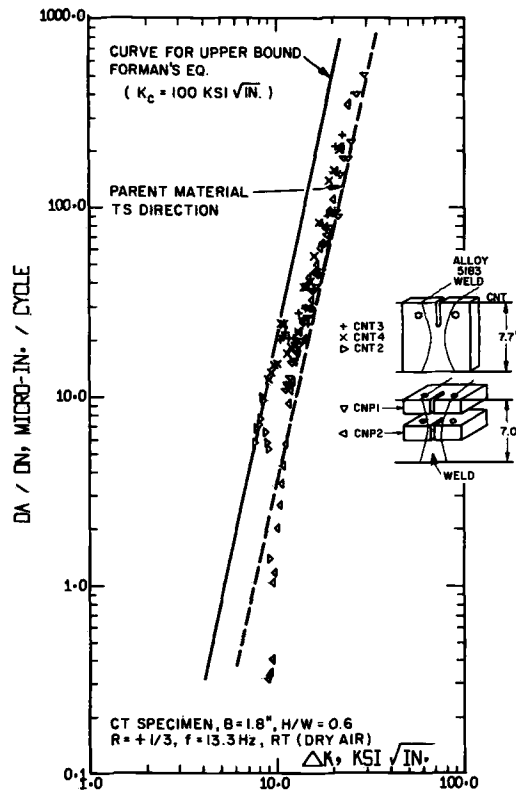


FIG. 7—Fatigue crack propagation in welded 7.0 and 7.7-in. aluminum alloy 5083-0 plate.

Although not reported, it may be assumed that room-temperature tests were made in air at ambient humidity. It has been shown[9] that fatigue crack propagation rate of aluminum alloys decreases with decreasing humidity. Thus, the small effect of temperature in the present investigation may be attributed to the fact that the room-temperature tests were made in low-humidity air (10 percent or less relative humidity).

Surface-Flawed Plate Specimens

Fatigue tests of welded 5083-0 plates, not included in this paper, have indicated that it is highly unlikely that a fatigue crack would initiate in an LNG cargo tank at the stress levels expected in service. Nevertheless, the designers of such tanks raise questions such as: supposing there were a flaw large enough to

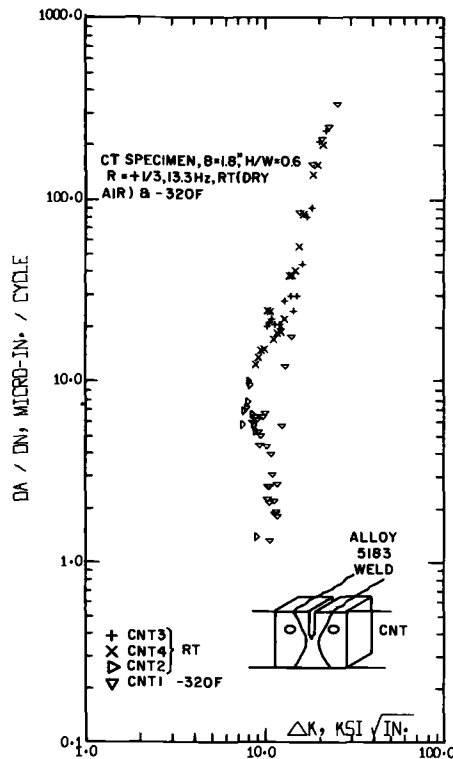


FIG. 8—Effect of temperature on fatigue crack propagation in welded 7.0 and 7.7-in. aluminum alloy 5083-O plate.

initiate a fatigue crack, would the crack grow through the tank, causing a leak which could be detected and repaired, or would it grow around the tank, perhaps reaching catastrophic proportions before it could be detected? If the crack did penetrate the tank, how fast would it grow after that? The question of whether the crack would penetrate the tank wall is of particular interest in connection with the equatorial ring, since this section is subjected to combined tension and bending so that the stress on the inner face of the tank wall is compressive, as shown in Fig. 1. Residual welding stresses are another factor that might tend to cause a crack to go around the tank rather than through the wall, since these stresses tend to be tensile on the surface and compressive near the midthickness of multipass welds [10].

Figure 10 shows the types of specimens used to study growth of surface cracks. Due to capacity limitations of available fatigue testing equipment, these specimens were loaded with the aid of a W12 by 133 steel beam, which was

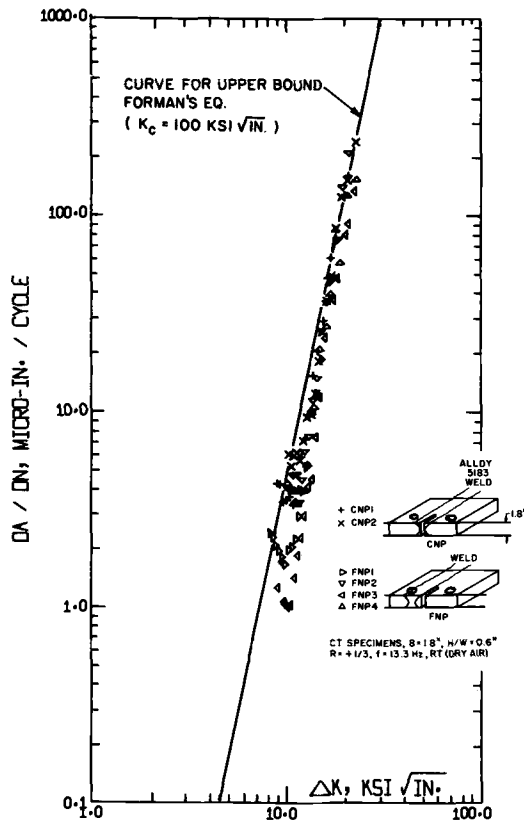


FIG. 9—Fatigue crack propagation in welded 1.8-in. material from 7.7-in. aluminum alloy 5083-0 plate.

supported on a 28-ft span and loaded at two points 18 in. on either side of the center line with the aid of a hydraulically operated, servocontrolled 20 000-lb jack. The specimens were bolted to the top flange of the steel beam, which was cut away for a distance of 20 in. at the center. Thus, the specimens, in effect, replaced the top flange.

Six surface-flawed specimens were tested as shown in Table 4. Two specimens (1 and 2) were subjected to essentially axial stress and four specimens (3 to 6) were subjected to a combined tension and bending loading. The latter specimens contained a groove and center eccentricity designed to produce a stress distribution simulating that on Section A-A of the equatorial ring (Fig. 1). The stress concentration caused by the groove was 1.4. The neutral axis was located 1/6 of the thickness from the back face.

TABLE 3—Fatigue crack growth test program, data location, and Forman equations (compact tension specimens).

Specimen No.	Test Temperature	Orientation (see Fig. 3)	Maximum Load, kips ^d		da/dN versus ΔK Plot	Forman Equation Constants ^e					
			Specimen A	Specimen B		$K^* = K_c = 100$		$K^* = K_{Ic} = 45$			
						C	n	C	n		
TS15&16	RT	TS	9.9	9.9	Fig. 4	1.58	$\times 10^{-8}$	4.13	2.37	$\times 10^{-8}$	3.51
ST13&14	RT	ST	9.0	9.9	4	0.0617	$\times 10^{-8}$	5.62	0.00882	$\times 10^{-8}$	5.96
ST1&2	-320	ST	9.9	12.0	5	0.563	$\times 10^{-8}$	4.64	0.780	$\times 10^{-8}$	4.04
CTP2&4	RT	CTP	10.5	12.0	6	0.0271	$\times 10^{-8}$	5.93	0.0373	$\times 10^{-8}$	5.34
CNT3&4	RT	CNT&CNP	12.0	10.5	7	4.50	$\times 10^{-8}$	3.93	13.48	$\times 10^{-8}$	3.02
CNT2 ^a			8.7	9.8							
CNP1&2 ^a			12.3								
CNT1 ^a	-320	CNT	8.9	...	8	3.02	$\times 10^{-8}$	4.03	8.26	$\times 10^{-8}$	3.13
CNP1&2 ^b	RT	CNP ^c	10.5	12.0	9	0.304	$\times 10^{-8}$	4.76	0.633	$\times 10^{-8}$	4.02
FNP1&2 ^b	RT	FNP ^c	9.9	12.0	9	0.0593	$\times 10^{-8}$	5.22	0.108	$\times 10^{-8}$	4.52
FNP3&4			10.5	12.0							

^a Specimens from 5183 welds in 7.0-in. alloy 5083-0 plate. Welding procedures were similar to those used for 7.7-in. plate (Table 2). Referring to Fig. 3, Specimen Nos. CNT1 and CNT2 had $H = 3.36$ in. and $W = 5.600$ in.

^b Welds parallel to rolling direction—all other welds perpendicular to rolling direction.

^c Welds in 1.8-in.-thick material machined from 7.7-in. plate. All other welds made in 7.0 or 7.7-in. plate.

^d Load ratio = (minimum load/maximum load) = 1/3. Specimen A is the first listed specimen and Specimen B the second.

^e $da/dN = [C(\Delta K)^n] / [(1 - R)K^* - \Delta K]$

where $K^* = K_c = 100$ ksi $\sqrt{\text{in.}}$ for plane stress or $K^* = K_{Ic} = 45$ ksi $\sqrt{\text{in.}}$ for plane strain [6].

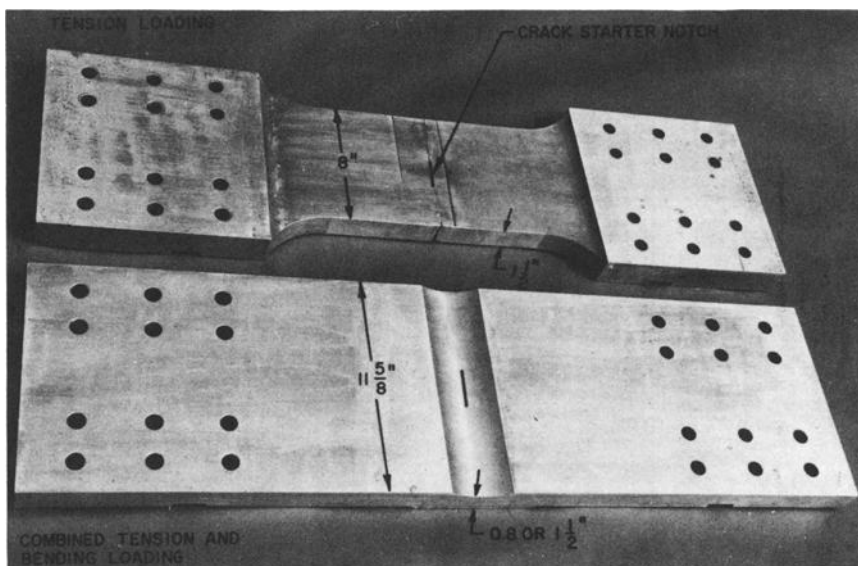


FIG. 10—Surface-flawed specimens for fatigue crack growth studies.

The flaws were made by electrical discharge machining. All six specimens were precracked by fatigue loading, generally using a load range greater than the test loading. After cracking initiated, loadings were reduced so that the maximum stress was within the range applied in the test program and the crack propagated by at least a few hundredths of an inch before the test program was initiated. Crack length at the surface was measured with the aid of dye penetrant, using a hundredths scale and a magnifying glass. Crack depth corresponding to various crack lengths was determined after the test by examination of beach marks on the fracture surface.

The 20-year stress spectrum used as a basis for the test program for the tension specimen is shown in Fig. 11 and that for the outside surface of the specimens subjected to combined tension and bending is shown in Fig. 12. In the tests, the stress spectra were approximated by block loadings of seven stress levels, σ_1 to σ_7 , as shown in Fig. 13. The loading pattern for a typical test day consisted of three load programs. Because the order of loading can affect the rate of propagation[11], half of the loads in a block were applied in ascending and half in descending order. Each program had enough loadings of σ_6 to σ_1 levels to represent two years' continuous service. It should be noted that in actual service the tanks would probably not be loaded more than half the time. Therefore, two years of continuous service is equivalent to four years of actual service.

TABLE 4—Summary of tests of surface-flawed specimens.

Specimen No.	Test Section, in.	Flaw Size			Flaw Location	Type	Loadings ^e				"Years" of Simulated Continuous Service Required for Crack Penetration
		Initial		Depth, in.			Initial Loadings		Subsequent Loadings		
		Length, in.	Depth, in.				No. of Block ^a Loadings	Stress Spectrum	No. of Block ^a Loadings	Stress Spectrum	
1	1 1/2 × 8	2.00	0.10	2.53	0.80	center of dressed weld bead	tension	constant load cycle, 0 to 9 kai (45 000 cycles)			
2	1 1/4 × 8	2.00	0.10	2.17	0.27	edge of weld bead	tension	8	design ^b	...	16
3	1 1/4 × 11 1/8	2.00	0.10	2.28	0.83	parent metal	tension-bending	5	design ^c	19	1.33 × design
4	1 1/4 × 11 1/8	0.30	0.10	0.73	0.32	parent metal	tension-bending	46	1.33 × design ^c	...	92
5	0.80 × 11 1/8	2.00	0.10	2.37	0.43	parent metal	tension-bending	7	design ^c	11	design ^d
6	1 1/4 × 11 1/8	2.00	0.10	2.36	0.54	transverse to longitudinal weld	tension-bending	10	design ^c	17	1.33 × design

^a See Fig. 13. One "block" is intended to simulate the loadings that would be encountered in 2 years of continuous service.^b See Fig. 11.^c See Fig. 12.^d Test loads reduced 5 times in proportion to loss in area after crack broke through to back surface.^e With the exception of Specimen 5, tests were made at constant load rather than constant stress amplitude. As a result, stresses increased as the crack grew. After the crack penetrated the thickness of Specimen 5, the load was decreased in proportion to the crack size so as to maintain a constant gross stress amplitude.

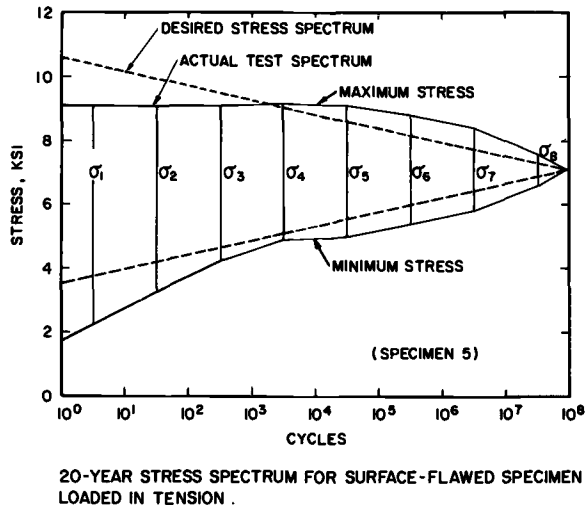


FIG. 11—Twenty year stress spectrum for surface-flawed specimen loaded in tension.

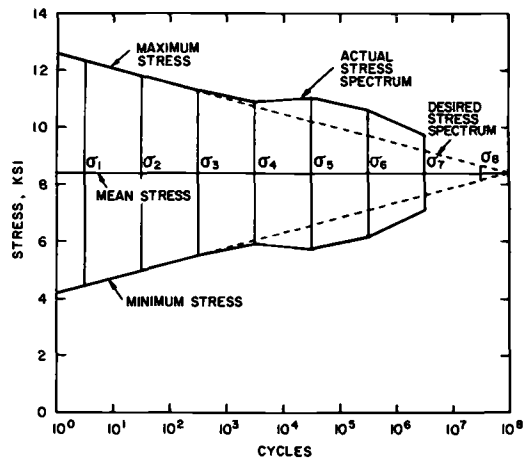


FIG. 12—Typical 20 year stress spectrum for surface-flawed specimens loaded in combined tension and bending.

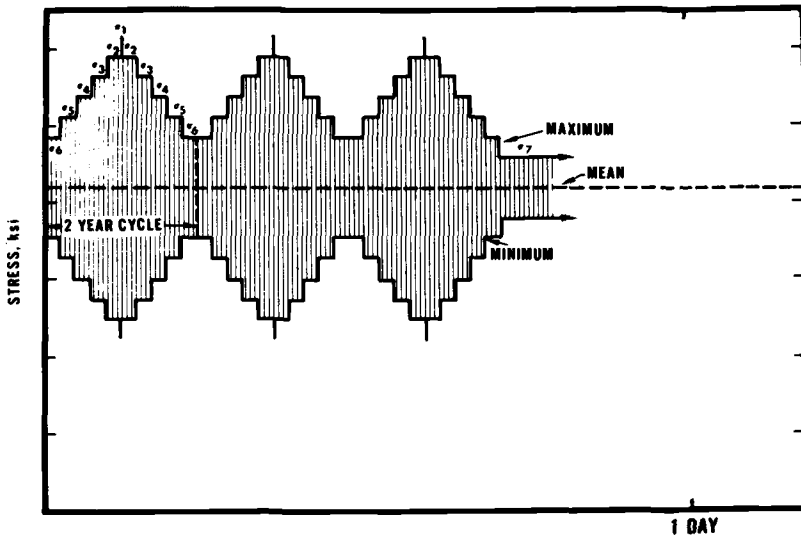


FIG. 13—Typical daily load cycling for crack propagation test of surface-flawed specimens.

Loadings at the σ_7 level were not expected to cause crack propagation, except perhaps when the cracks had grown to large size. Nevertheless, stresses at this level were applied (usually overnight or on weekends) to check whether propagation occurred. In most cases the lack of propagation was confirmed, so the total number of loadings applied at this stress level was not necessarily as large as the proportionate amount shown in Figs. 11 and 12. However, in some cases, it was found that propagation was taking place at the σ_7 level, even though the crack size was fairly small. This unexpected behavior led to a check of dynamic effects in the loading apparatus, and it was found that the actual stresses in the specimens were appreciably higher at the more rapid rates of loading used for the smaller load amplitudes than had been indicated by static measurements. This load amplification is a result of the rate of loading approaching the natural frequency of the loading system (about 20 Hz for the first mode). Actual stress spectrums applied are shown in Figs. 11 and 12. Since the loads applied were more severe than intended, the results are conservative.

In the case of Specimen 2, the maximum desired stress could not be reached for loadings σ_1 to σ_3 , so the range of stress was increased by an amount calculated using Forman's equation to produce an equivalent amount of crack propagation. Figure 11 shows the resulting stress history, including dynamic effects.

Another factor tending to make the results conservative is that the tests were

made at constant load rather than constant stress amplitude (except for the test of Specimen 5). As a result, the stresses increased as the cracks grew. This increase in stress was checked by occasional strain measurements as the tests progressed.

Figures 14 and 15 are photographs of typical fracture surfaces, and curves depicting the test results are shown in Figs. 16 to 21. The basis for the calculated values shown in the figures will be discussed later in the paper.

In all cases the fatigue cracks propagated through the specimens, despite the presence of compressive stresses on one face or residual welding stresses. For the tension specimens, the ratio of crack length to depth at break-through was about four. For the tension-bending specimens, this ratio was about six. This ratio was probably larger than it would be in an actual tank because the relatively narrow width of these specimens tended to increase the stresses on the side where the crack was longer.

Another point that can be noted from the tests is that crack propagation was very slow. The years of continuous "service" required for a crack to penetrate the thickness are shown in Table 4. For the 1.5-in.-thick specimens simulating the stress distribution in the equatorial ring of a spherical tank, far more than 20 years of service were required to cause crack penetration, even though loads were increased over service values by one third and there were the additional increases in stress due to increasing crack area and dynamic effects. Even for Specimen 5, with an initial crack depth of 0.43 in. in a thickness of only 0.8 in., 14 years of service were needed to cause penetration.

Predicting Growth of Cracks Under Spectrum Loading

One of the purposes of this investigation was to determine whether the growth of cracks under complex stress conditions and spectrum loading can be predicted approximately from the results of constant load amplitude tests on compact tension specimens. Such a correlation is highly desirable in order to be able to predict the behavior of full size tanks in service. For this purpose, a method of calculation was developed based on accepted procedures available in the literature, which were combined and modified to apply to the particular test specimens used in this investigation. A computer program was written to perform the calculations.

The computer program to predict propagation of part-through cracks in the test specimens is based on several assumptions regarding the shape of the crack, the stress intensity factor, and the rate of propagation. The crack is assumed to be semi-elliptical in shape with its major axis lying in the surface of the plate. The following expression derived by Irwin[12] was used as a basis for calculating the stress intensity, K , for a semi-elliptical surface flaw

$$K = 1.12\sigma\sqrt{\pi a/Q} [\sin^2 \beta + (a/c)^2 \cos^2 \beta]^{1/4} \quad (2)$$

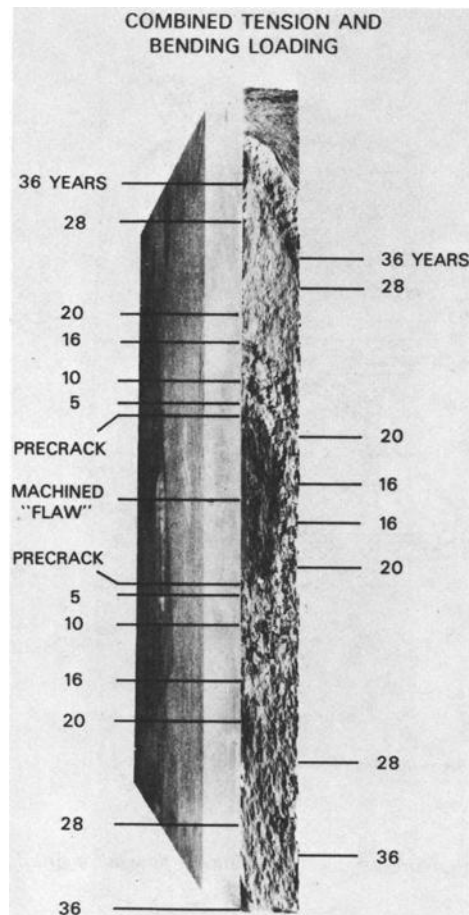


FIG. 14—Fracture surface of Specimen 5.

where

σ = stress normal to the crack,

a = crack depth,

c = one half the crack length,

β = location along the crack front at which K is being calculated, and

Q = plasticity and flaw shape parameter determined from the formula

$$Q = \phi^2 - 0.212 \left(\frac{\sigma}{\sigma_{ys}} \right)^2 \quad (3)$$

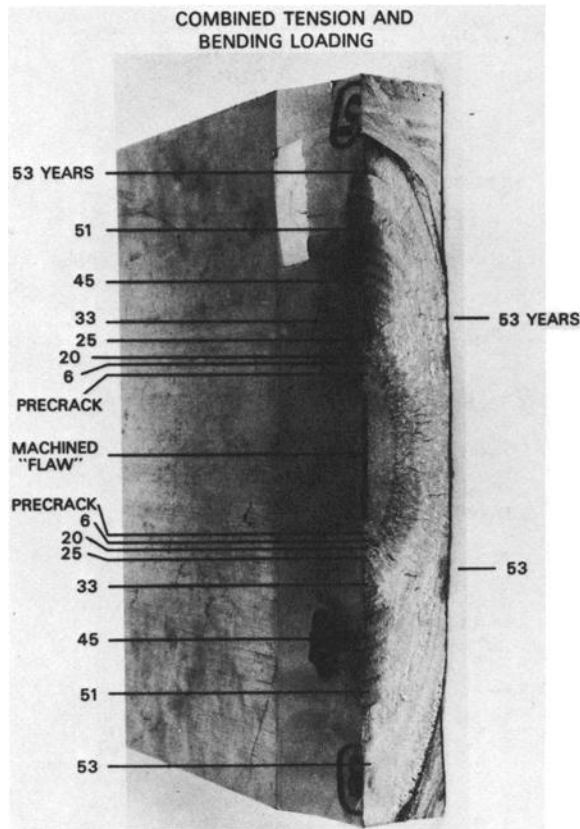


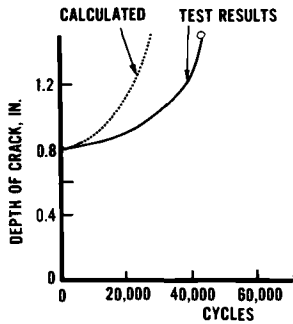
FIG. 15—Fracture surface of Specimen 6 flaw in longitudinal weld.

$$\phi = \int_0^{\pi/2} \sqrt{1 - \left(\frac{c^2 - a^2}{c^2} \right) \sin^2 \theta} d\theta \quad (4)$$

σ_{ys} represents the yield strength. In the cases where $\sigma > \sigma_{ys}$, the value of σ/σ_{ys} is set equal to 1.

The constant 1.12 in Eq 2 was used by Irwin as a stress intensity magnification factor and accounts for the influence of the front surface on shallow cracks. For deep cracks it is necessary to include the influence of the back surface in the magnification factor. If the combined front and back surface

CONSTANT LOAD CYCLE-TENSION
TEST SECTION: 1 1/2 X 8-IN.



CALCULATIONS MADE USING FORMAN'S
EQUATION FOR CT CNT AND CNP SPECIMENS
WITH $K'=K_c=100 \text{ ksi}\sqrt{\text{in}}$ FOR SURFACE
GROWTH AND $K'=K_{IC}=45 \text{ ksi}\sqrt{\text{in}}$ FOR
DEPTH GROWTH

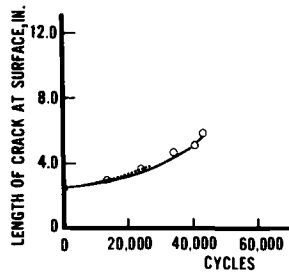


FIG. 16—Specimen 1: propagation of surface crack at center of alloy 5183 weld in alloy 5083-0 plate.

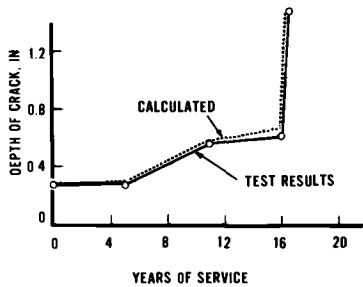
magnification factor is denoted as M^* , at the bottom of the crack, where $\beta = 90$ deg, Eq 2 may be expressed as

$$K = M^* \sigma \sqrt{\frac{\pi a}{Q}} \quad (5)$$

and at the ends of the crack (plate surface), where $\beta = 0$ deg, Eq 2 becomes

$$K = 1.12 \sigma \sqrt{\left(\frac{\pi a}{Q}\right) \left(\frac{a}{c}\right)} \quad (6)$$

SPECTRUM LOADING-TENSION
TEST SECTION: 1 1/2 X 8-IN.



CALCULATIONS MADE USING FORMAN'S
EQUATION FOR CT FNP SPECIMENS WITH
 $K'=K_c=100 \text{ ksi}\sqrt{\text{in}}$ FOR SURFACE
GROWTH AND TS SPECIMENS WITH
 $K'=K_{IC}=45 \text{ ksi}\sqrt{\text{in}}$ FOR DEPTH GROWTH.

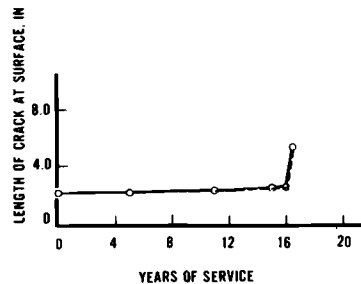


FIG. 17—Specimen 2: propagation of surface crack at edge of alloy 5183 weld in alloy 5083-0 plate.

SPECTRUM LOADING - TENSION AND BENDING
TEST SECTION: 1 1/2 X 11-5/8 IN.

CALCULATIONS MADE USING FORMANS
EQUATION FOR CT TS SPECIMENS WITH
 $K^* = K_{IC} = 100 \text{ ksi}\sqrt{\text{in}}$ FOR SURFACE GROWTH
AND $K^* = K_{IC} = 45 \text{ ksi}\sqrt{\text{in}}$ FOR DEPTH
GROWTH

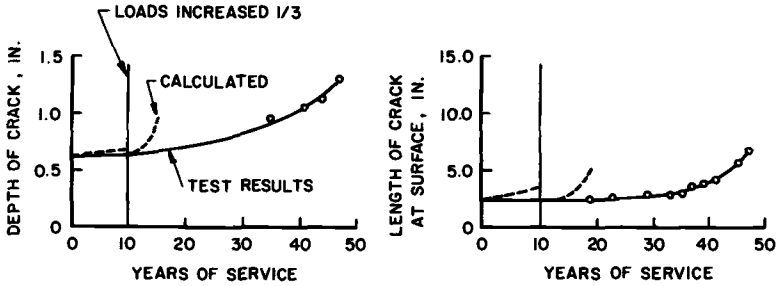


FIG. 18—Specimen 3: propagation of surface crack in alloy 5083-0 plate.

A constant value of 1.12 is used here because the variation of the magnification factor with aspect ratio is too small to warrant adjustment.

For plates in tension the elastic magnification factor, M^*_T , selected for predicting surface flaw growth was that proposed by Kobayashi and Moss [13]. To facilitate computer programming, use was made of the following polynomial approximation derived by Collipriest and Ehret [14]

$$\begin{aligned}
 M^*_T = & 1 + [0.091 + 0.1014(a/t) - 1.606(a/t)^2 + 15.81(a/t)^3 \\
 & - 76.2(a/t)^4 + 197.9(a/t)^5 - 276.9(a/t)^6 + 195.9(a/t)^7 \\
 & - 54.13(a/t)^8] \times [1.433 - 5.305(a/2c) + 6.81(a/2c)^2 \\
 & + 26.42(a/2c)^3 - 109.4(a/2c)^4 + 106.77(a/2c)^5]
 \end{aligned} \quad (7)$$

SPECTRUM LOADING - TENSION AND BENDING
TEST SECTION: 1 1/2 X 11-5/8 IN.

CALCULATIONS MADE USING FORMANS
EQUATION FOR CT TS SPECIMENS WITH
 $K^* = K_{IC} = 100 \text{ ksi}\sqrt{\text{in}}$ FOR SURFACE GROWTH
AND $K^* = K_{IC} = 45 \text{ ksi}\sqrt{\text{in}}$ FOR DEPTH
GROWTH

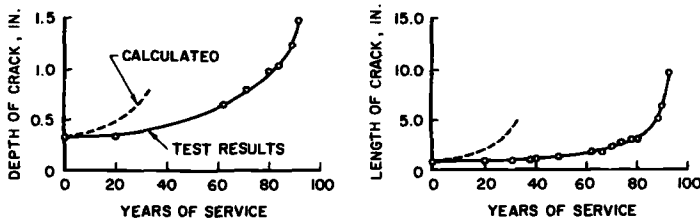


FIG. 19—Specimen 4: propagation of surface crack in alloy 5083-0 plate.

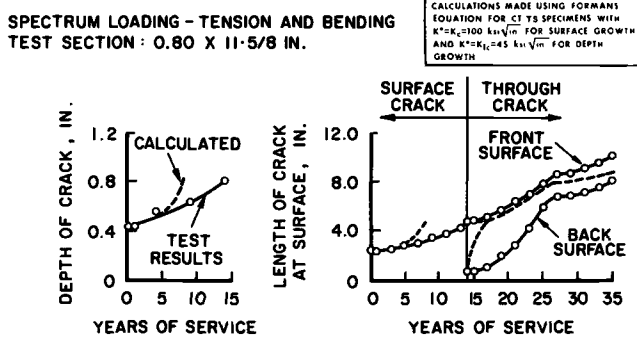


FIG. 20—Specimen 5: propagation of surface crack in alloy 5083-0 plate.

For plates in bending, the elastic magnification factors, M^*_B , derived by Smith[15] were used. In the computer calculations the value of M^*_B was determined by linear interpolation and extrapolation from a table of values of the magnification factors.

The surface-flawed specimens of this investigation were relatively narrow, so that, as the crack grew, its area became a relatively large proportion of the total cross-sectional area. In the absence of a more precise method for taking into account the effect of finite width for part-through cracks, the applied stress for the specimens with part-through cracks was multiplied by an area factor (f_A) of the form

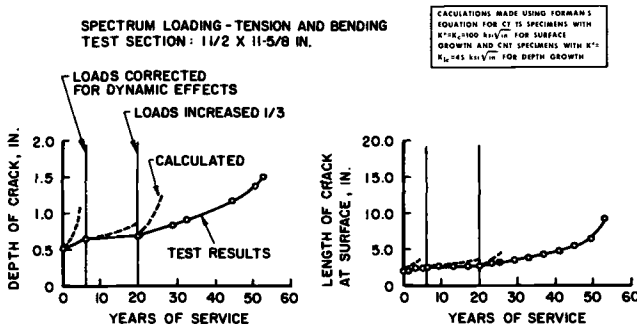


FIG. 21—Specimen 6: propagation of surface crack transverse to alloy 5183 butt weld in alloy 5083-0 plate.

$$f_A = \frac{A_T}{A_T - A_C} \quad (8)$$

where

A_T = total area and

A_C = area cracked.

The stress intensity factor for a through crack in an infinitely wide plate is given by

$$K = \sigma\sqrt{\pi c} \quad (9)$$

For a finite-width plate [16]

$$K = \sigma\sqrt{\pi c} \sec\left(\frac{\pi c}{W}\right)^{1/2} \quad (10)$$

The data for Specimen 5, in which cyclic loading was continued after crack breakthrough, show that the crack length increases much faster at the back surface than at the front surface. To account for this phenomenon, crack growth after breakthrough was handled using a method proposed by Collipriest [14], in which the front surface crack length ($2c_F$) is held constant and the back surface crack length ($2c_B$) allowed to grow under cyclic stress until its length equals that of the front surface crack. Then the crack is assumed to grow as a straight through crack, and K is calculated from Eq 10. Since no method was known to the authors on how to handle growth of a through crack in a plate in bending, calculations were made of crack growth in Specimen 5 using a stress assumed to be equal to the average tensile stress on the specimen.

Various studies [17,18] have shown that there is a limiting value of ΔK below which crack propagation does not occur. For these calculations this limiting value was assumed to be 2 ksi $\sqrt{\text{in.}}$ and independent of stress ratio.⁴

Given the initial crack size and the stress spectrum, the program uses a linear cumulative growth model to estimate crack growth by multiplying the propagation rate by the number of cycles at each stress level. Propagation rates are recalculated for each stress level and, within each level, at intervals of 1 cycle or 0.01 N_i cycles, whichever is greater. N_i represents the number of cycles at the i^{th} stress level. These calculations are repeated for successive programs until failure is detected. A failure is said to have occurred when either crack dimension exceeds the corresponding specimen dimension or when ΔK exceeds $(1 - R)K^*$.

⁴ Subsequent tests at Alcoa Laboratories have confirmed the findings of Ref 19 that threshold ΔK varies with stress ratio.

Predicted Flaw Growth in Test Specimens

Calculated crack growth is shown along with the test data for the surface-flawed specimens in Figs. 16 to 21. As noted in the figures, Forman's equation for the compact tension specimen which most closely represented the location and direction of crack growth in the plate specimens was used in calculating crack growth in the surface-flawed specimens. In these calculations, Forman's equation with $K^* = K_c$ was used to predict growth along the plate surface, and Forman's equation with $K^* = K_{Ic}$ was used to predict flaw growth through the depth.

The calculated growth rates of part-through cracks in the surface-flawed specimens were either quite conservative or were in close agreement with the test data. Figure 20 shows that for a through crack, when the front surface crack length was assumed to remain constant, the calculated growth rate at the back surface was much faster than that observed in the tests. The fact that the back surface was nominally under compression, whereas the calculations for the through crack assumed a uniform tension equal to the average tensile stress on the specimens probably contributed to this variance. The calculated and measured crack growth rates at the front surface are in fairly good agreement.

In the calculations for Specimens 1, 3, 5, and 6, the major portion of the crack growth occurred for the stress cycles which combined low ΔK 's, high stress ratios and a large number of cycles. The tests of compact tension specimens in this investigation did not produce crack growth in the low ΔK range. However, some other investigations (see Ref 14, Fig. 5) suggest that the Forman's equation is probably quite conservative in this range.

There are four other factors which may account for differences between the calculated and measured crack growth rates in the surface-flawed specimens: (1) it is known that a high-low loading sequence can cause a period of delay in crack growth, and that a low-high sequence can cause a transient acceleration in crack growth[11] (net effect of the low-high and high-low sequence, used in the block loadings of this investigation, may have been to retard crack growth relative to that measured in the compact tension specimens, which had a constant load amplitude); (2) finite width correction factor, Eq 8, may be too conservative; (3) there does not appear to be general agreement on the proper magnification factors to apply to part-through cracks; and (4) no corrections were made for plastic zone size in calculating stress intensity factors for the compact tension specimens or the surface-flawed specimens.

Despite the differences just noted, the method of calculation described in this paper gave sufficiently satisfactory results that it was used to estimate the behavior of possible fatigue cracks in full sized LNG cargo tanks. The results indicated that there is a large margin of safety against the occurrence of leaks, but if leaks should occur there would be plenty of time to find them and make repairs before any more serious failure occurred.

Summary and Conclusions

The results of this investigation of fatigue crack growth in aluminum alloy 5083-0 plate and welds made with 5183 filler wire can be summarized as follows:

1. Fatigue crack growth data obtained from compact tension specimens taken from plate and welds up to 7.7-in.-thick indicate relatively little effect of the following variables: parent plate versus weld metal, direction of stressing versus direction of rolling, and room temperature versus -320°F .

2. In tests of specimens with surface flaws, either welded or not welded, subjected to either direct tension or combined tension and bending with one face in compression, the fatigue cracks progressed entirely through the specimen. This means that in an LNG cargo tank, any cracks propagating from the surface would go through the tank, causing a detectable leak before reaching catastrophic proportions.

3. Crack growth in surface-flawed specimens subjected to spectrum loading simulating the stress conditions expected in an LNG cargo tank was extremely slow, with many "years" of simulated service required to cause appreciable crack growth.

4. Calculations of the growth of surface flaws in the specimens subjected to spectrum loading, based on the results of tests of compact tension specimens under constant loading, were either conservative (that is, the calculated growth rates were faster than the actual growth rates) or they agreed closely with the experimental growth rates.

Much work remains to be done in evaluating the factors affecting fatigue crack growth and the use of these data in predicting crack growth during cyclic loading of structures subjected to complex loadings. To this end, the following work is underway at the Alcoa Laboratories:

1. Evaluation of various formulas for characterization of fatigue crack growth over the entire ΔK range and the use of these formulas for predicting cyclic crack growth of surface flaws under spectrum loading.

2. Measurement of crack growth rate for various stress ratios in low ΔK range. Determination of threshold for fatigue crack growth.

3. Measurement of fatigue crack growth in thicker specimens. Alcoa is sponsoring tests at Det Norske Veritas in Norway to measure growth of surface flaws in specimens $3\frac{1}{4}$ in. thick by 35 in. wide.

4. Tests are underway to study the effect of metallurgical structures on fatigue crack initiation and propagation.

5. Evaluation of the effect of porosity on fatigue crack growth in weldments.

6. Determination of fatigue crack growth in corrosive environments.

References

- [1] Kaufman, J. G. and Wanderer, E. T., *Machine Design*, 11 Nov. 1965.
- [2] Kaufman, J. G., Holt, Marshall, and Wanderer, E. T., "Aluminum Alloys for Cryogenic Temperatures," presented at the Cryogenic Engineering Symposium of the Canadian Chemical Conference, Toronto, Ont., Canada, 7 June 1967.
- [3] Loushin, L. L., Lamberton, W. J., and Palmer, A. J., "An Application of Fracture Mechanics to Safe Life Design in Cryogenic Pressure Vessels," Esso Research & Engineering Company Report No. EE.26ER.70, 24 Aug. 1970, presented at the 4th National Symposium on Fracture Mechanics, 1970, Pittsburgh, Pa.
- [4] Tafuri, J. C. and Roberts, R., "Fatigue-Crack Growth Rates and Fracture Toughness Study of Welded Aluminum Alloy 5083," ASME Paper No. 70-WA/PVP-5, presented at Winter Annual Meeting, American Society of Mechanical Engineers, 29 Nov.-3 Dec. 1970, New York, N. Y.
- [5] Kvamsdal, R. S. and Howard, J. L., "Moss Rosenberg's Spherical Tank LNG-Carrier," LNG-LPG Conference, London, 21-22 March 1972.
- [6] Kaufman, J. G., Nelson, F. G., and Wygonik, R. H., this symposium, pp. 125-158.
- [7] Jaske, C. E., Feddersen, C. E., and Davies, K. B., "Analysis of Fatigue, Fatigue-Crack Propagation, and Fracture Data," 19 May 1972 Quarterly Report, Contract NAS1-11344, Battelle-Columbus Laboratories, Columbus, Ohio.
- [8] Forman, R. G., Kearney, V. E., and Engle, R. M., *Journal of Basic Engineering, Transactions*, American Society of Mechanical Engineers, Sept. 1967.
- [9] Nordmark, G. E. and Kaufman, J. G., *Engineering Fracture Mechanics*, Vol. 4, 1972, pp. 193-204.
- [10] Kelsey, R. A., *Supplement to the Welding Journal*, Vol. 50, No. 12, Dec. 1971, pp. 507s-514s.
- [11] Crooker, T. W., "Basic Concepts for Design Against Structural Failure by Fatigue Crack Propagation," NRL Report 7347, Naval Research Laboratory, 13 Jan. 1972.
- [12] Irwin, G. R., *Journal of Applied Mechanics*, Dec. 1962.
- [13] Kobayashi, A. S. and Moss, W. L. in *Proceedings*, Second International Conference on Fracture, Brighton, England, 13-18 April 1968, pp. 31-45.
- [14] Colli priest, J. E., Jr., and Ehret, R. M., "Computer Modeling of Part-Through-Crack Growth," Space Division, North American Rockwell, Report No. SD72-CE-0015A, July 1972, revised Sept. 1972.
- [15] Smith, F. W., "Stress Intensity Factors for Semi-Elliptical Surface Flaw," Boeing Company Structural Development Research Memorandum No. 17, Aug. 1966.
- [16] Brown, W. F., Jr., and Scrawley, J. E., *Plane Strain Crack Toughness Testing of High Strength Metallic Materials*, ASTM STP 410, Dec. 1967; discussion by Feddersen, pp. 77-79.
- [17] Hudson, C. M. and Scardina, J. T., "Effect of Stress Ratio on Fatigue-Crack Growth in 7075-T6 Aluminum-Alloy Sheet," NASA Langley Station, Hampton, Va., presented at the National Symposium on Fracture Mechanics, 19-21 June 1967.
- [18] Speidel, M. O., Blackburn, M. J., Beck, T. R., and Feeney, J. A., "Corrosion-Fatigue and Stress-Corrosion Crack Growth in High-Strength Aluminum Alloys, Magnesium Alloys, and Titanium Alloys, Exposed to Aqueous Solutions," Boeing Scientific Research Laboratory, Seattle, Wash., paper presented at International Conference on Corrosion Fatigue, University of Connecticut, 14-18 June 1971.
- [19] Schmidt, R. A. and Paris, P. C. in *Progress in Flaw Growth and Fracture Roughness Testing*, ASTM STP 536, American Society for Testing and Materials, 1973, pp. 79-94.